Modelling the Combustion of Explosives

Sally Said

A dissertation submitted in partial fulfillment
of the requirements for the degree of
Doctor of Philosophy
of
University College London.

Department of Mathematics
University College London

March 29, 2023

I, Sally Said, confirm that the work presented in this thesis is my own. Where information has been derived from other sources, I confirm that this has been indicated in the work.

Abstract

When an explosive burns, gaseous products are formed as a result. The interaction of the burning solid and gas is not well understood. More specifically, the process of the gaseous product heating the explosive is yet to be explored in detail. The present work does much to fill that gap using mathematical modelling: this aims to track the temperature profile in the explosive and the response of the gas.

This work begins by modelling single step reactions using the simple Arrhenius model. An alternative asymptotic approach is also employed. There is close agreement between results from the full reaction-diffusion problem and the asymptotic problem. The model is then extended to include three step reaction kinetics, where we again apply asymptotic analysis. Further work includes of gas being incorporated in the existing model with temperature and pressure distributions considered. We also consider the effects of the gas on the solid explosive temperature. This is achieved by first allowing the gas to heat the boundaries of the solid. Later we incorporate internal heating of the solid by the gas into the model. An asymptotic approach is also considered here and successfully captures the behaviours of interest. Finally, we address a second heating method; mechanical stimulus provided by a wedge-like squeezing of an explosive material. Here sensitive effects within thin shear layers are predicted. The study finds major events take place in thin boundary layers, a highlight which holds for mechanical as well as thermal events.

Impact Statement

The impact of the research undertaken in this thesis is intended to address human safety concerns, in particular the storage and safe handling of explosives. High Explosives (HEs) store energy which can have disastrous effects if released accidentally. Thus safe handling and storage of HEs is a matter of utmost concern. When a HE is subjected to significant heating it reacts, i.e. it burns to form gaseous products. The interaction of the burning solid and gaseous products formed is not well understood. More specifically, the process of the gaseous product heating explosives is yet to be explored in detail. The present work, in collaboration with the Atomic Weapons Establishment (AWE), does much to fill that gap using mathematical modelling: this aims to track the temperature and volume profiles, as well as pressure distributions in the explosive and the gas response. HEs provide a low mass source of massive energy release, but this stored energy can pose a major hazard and even cause disaster if accidentally released. There is a long and sad history of serious accidents that have resulted from both mechanical and thermal abnormal and unexpected loadings of diverse severities. Therefore, safety is paramount in the handling and storage of explosives. Understanding the circumstances in which an explosive can ignite, burn and detonate is essential if we are to predict the severity of likely hazards and understand the associated risks. Understanding the time to detonation of an explosive is essential if we are to avoid disasters from occurring. The work presented in this thesis successfully tracks the heat flow within an explosive material over time. One of the most significant contributions of the research outlined herein, however, is a model which aims to fill the gap in understanding of solid-gas interaction by considering the heating effects of the gas within the solid

explosive. This model tracks the temperatures of both the solid and gas and allows for feedback and internal heating of the solid by the gas which is produced.

Another significant contribution of the work presented here is an alternative approach to solving these otherwise numerically difficult and expensive problems, using asymptotic methods. This methodology allows us to solve problems which would otherwise be extremely computationally expensive. The method also works successfully on the physical parameters supplied by AWE which standard numerical methods did not handle well due to the extreme nature of the physical parameters.

Acknowledgements

The work presented in this thesis is the result of a collaboration between Atomic Weapons Establishment (AWE) and University College London (UCL). I would like to thank my supervisor Professor Frank Smith for his expertise, patience and guidance. His constant support throughout the process has made this possible. I would also like to thank my supervisor Dr John Curtis for sharing his industry expertise. He always offered unique insights and perspective as well as a wide range of literature which enriched the quality of the research. I am extremely grateful to both my supervisors for the time and effort they have invested in me and the research.

A special thanks goes to AWE without whom this project would not have been possible. Thanks also goes to colleagues at AWE; specifically Dr Caroline Handley for her continued interest in the research and the opportunity to present it at specialist conferences. I would also like to thank both AWE and UCL for their financial support to complete my research.

Contents

List of Figures

List of Tables

Chapter 1

Introduction

1.1 Motivation & Literature Review

When a fuel of some sort is burnt, it combines with oxygen in a chemical reaction to release energy. Most of this energy is released in the form of heat, although some energy is released as sound. Other products released from such chemical reactions are often gases. Reactions of this form are known as combustion reactions, which are also referred to as burning or deflagration. The rate of the reaction affects the type of burn; for example, rapid reactions usually lead to explosions and slower reactions often lead to burns.

Explosives may be classified as either low or High Explosives (HEs), depending on burn rate. HEs themselves, which are of most interest to this thesis, can be further categorised into primary, secondary and tertiary HEs. Most primary explosives readily detonate through thermal stimulus as they are extremely sensitive. The detonation of primary explosives is often used as a detonation device for secondary explosives [2]. Similarly secondary explosives can be used to detonate tertiary explosives. Unfortunately, however, understanding the time to detonation of the secondary explosive is much more complex as there are often large time delays due to their insensitivity to heat or shock. A detailed discussion on the technology of explosives can be found in [2, 3], where the physical processes involved in explosives are explored in detail. This includes an insight into the chemical processes which occur as well as the mechanics of the burning process and detonation. We should mention in passing here that parts of our Introduction are based on the joint paper [4] by the author with Smith and Curtis.

Combustion reactions are used in everyday applications such as heating, cooking, vehicles, manufacturing and to produce electricity. Unfortunately, combustion processes are not always possible to manage safely [2], [3] and their behaviours are tough to predict. This is an extremely important problem when considering and dealing with the combustion of explosives.

The high cost and danger of experimentation has necessitated the modelling of scenarios of potential danger. The combustion process may be modelled using the heat conduction equation, also referred to as the diffusion equation, together with a reaction term. The present work, following the works of [5–9] for example, begins by including a one-step Arrhenius reaction. Following the work of [1], we extend the model to include a more physically realistic three-step reaction. The great flexibility and power of hydrocode packages implementing finite element and difference methods [10, 11] has made them the natural choice to address this need. However, the use of these codes has often revealed that localised effects arise that are hard to resolve with standard computation meshes; often shear bands or local regions of extreme heating are observed. The question thus arose: could mathematical analysis and/or new sophisticated adaptive methods offer further advances both in understanding the governing physics and chemistry, and in achieving improved computational models?

Let us attempt to summarise our current understanding of the processes happening in a reacting high explosive. HEs may be distinguished from other types by their capability to detonate rather than burn if sufficient stimulus is applied to them. Under lesser stimuli, they may burn [12] and the resulting reaction can diminish, remain steady, or grow to more violent deflagration or even to detonation, where the stored explosive energy is released in times typically of the order of nanoseconds. What is governing these very diverse outcomes?

It is established that, when a HE is subject to significant heating as a result of either mechanical dissipation caused by accidental severe deformation or direct heating from a heat source, it begins to react. The solid material reacts, i.e. burns to form high pressure gaseous products [5, 13–16]. As the reaction proceeds more and more gas is formed. The porosity of the explosive increases and as more and more surface area becomes exposed the reaction can accelerate and propagate with the increasing porosity and permeability [17] until all the explosive is consumed or until some mechanism releases the pressure and the reaction is quenched. Violent reaction or even disastrous detonation can be achieved in some cases. We believe that it is fair to say that the interplay between the burning (and thereby disintegrating) solid matrix and gaseous products is still ill-understood. Plainly there are confined locations where flames may be interacting with flames from nearby surfaces, probably in highly complex ways. A recent paper [18] on gas effects, a paper which came to our notice after completion of the present study explores solid-gas interaction.

Baer and Nunziato [19] and subsequent workers have explored the two-phase problem of reacting solid and gaseous products from a macroscopic continuum viewpoint, but detailed treatments of the internal burning process and of how the hot gas heats the explosive up are lacking. The problem is compounded by the complexity of modern heterogeneous explosives in which crystals of pure HE are embedded in polymer binders, which themselves can be reactive. The creation and propagation of flames in this type of explosive have not been modelled in detail; the computational costs would be prohibitive even were this possible. Therefore, burn models in current use are generally empirically based macroscopic models rather than being based upon first principles. Their calibration often depends on the experiment or geometry being modelled. That being so, we asked ourselves the question [4]: ‘Would it be possible to gain deeper understanding of the physical processes at work in real HEs by looking at scenarios with idealised geometries lending themselves to analytical modelling?’

We believe this is a question worthy of attention and the present work reports one research line taken in attempting to answer. We additionally comment that the recent advances in additive manufacturing of explosives provide enhanced motivation for the investigation of idealised explosive geometries [20], which are becoming realisable in practice while being potentially more amenable to mathematical modelling [7, 9, 21, 22]. The modelling to be used herein is based on a continuum assumption.

The primary objective of this research is to gain a fundamental understanding of how explosives burn. This can be achieved by investigating idealised problems in which the important parameters can be easily identified. Thus the work here begins by modelling a one-dimensional slab of inert explosive material.

The HERMES (High Explosive Response to MEchanical Stimulus) model which is well described in [23], does not depend explicitly on temperature; it models the onset and progression of an explosive reaction. It is well known however that the combustion process of explosives is temperature driven, and this in itself is motivation for building the current model independently. AWE are interested in improving capabilities and alternative ways to predict the violence of reactions in which gas is included by looking at alternative approaches. The HERMES code cannot predict well mechanical responses arising from thermal origins, whereas the work presented here is a step towards doing so.

Modelling the combustion of explosives is a topic which has been studied for several decades and has received a lot of attention in recent years, see [7, 21, 22, 24]. It is widely accepted that the combustion process occurs in several stages which need to be studied. In particular the process of burning to detonation, or the deflagration-to-detonation transition (DDT) [19, 25] is one which is not yet fully understood due to the complex chemistry involved. Understanding the DDT process is highly important for the development, as well as the safe handling and storage of explosives [2, 3, 21]. Again, the present thesis aims to contribute towards filling the gap here.

There have been various theories on the mechanisms which drive the DDT process; Groocock et al [12] suggest the formation of shock waves ultimately result in detonation, see also [24, 26, 27]. McGuire and Tarver [1] use a thermal conduction model to predict the time to detonation compared with reciprocal temperature. It is well documented in the literature [28] that the time to detonation using a single-step

Arrhenius reaction model or two-step reaction models cannot be predicted accurately. The authors of [1] use experimental data to predict the time to detonation for several confined explosives, namely HMX, RDX, TATB and TNT. The reaction of explosives can be broken down into three processes, which are: endothermic reactions, slightly exothermic reactions and extremely exothermic reactions. McGuire and Tarver [1] model these processes using a three step chemical decomposition model for four explosives. The times to detonation are compared and are accurately predicted and verified against experimental results.

In the background also, several works, including [1, 28, 29] for example, have modelled the one-dimensional time to explosion (ODTX). Breshears [7] agreed with Tarver et al [1], with their chemical reaction model capturing the fundamentals of ODTX experiments. Supporting literature is in [30–35]. Baer and Nunziato [19] developed a multiphase mixture model of solid grains and gas to describe the combustion process. The authors of [19] modelled the DDT process in reactive granular materials, with a specific focus on HMX. Numerical results in this work using the method of lines were found to be in agreement with experimental observations. The effects of particle size of the grains as porosity were also briefly explored. See also the background papers [13, 36–54]. Curtis [55] investigated a spigot air gap model. It is notable that the current slab model of the present thesis could be used to further the work in [55], thus acting as a potential application of the current model. Howe et al [29] investigated the multiphase treatment of ODTX in HMX spheres with constant boundary temperature. The time taken for each sample to explode is recorded. A recent paper by Curtis, which is yet to be published, on two-phase effects is one of the papers we will be examining in order to consider the later stages of any significant fluid flow involved (see also Baer and Nunziato [19]).

Certain major features of the thesis should be emphasised at this point. Thus, partly to repeat, the main work we have done (to be described herein) that is novel is exemplified by the present studies on interactive gas effects, on an alternative thermomechanical approach, on understanding the likely influences of complex chemistry and on the usage of a new asymptotic treatment created during the current research. The work of the thesis is something of a new departure but it has also been put into the context of existing literature and research efforts above, for example concerning the improvement of capabilities in industry and also concerning gaps in understanding described earlier. The major issues surrounding the topic of interest here are likewise raised earlier, in regard to gaseous products heating explosives and the influences of several reactants in particular as well as the quantitative determination of such important features. The relationship between the different papers cited above in our survey of relevant literature is rather mixed and patchy in some respects but it seems clear that the ones of prime concern for the present thesis are [1, 5, 6, 56]. Furthermore the current work is believed to shed valuable new light on the significant research gaps described earlier, for example by means of the use of a novel asymptotic approach and by the development of a novel model for gaseous products and interaction. The resulting help to industry (AWE) is via the new codes concerned with temperature and reactants, and comparisons, with several other helpful aspects being detailed near the beginning of the introduction.

The thesis work makes use of numerical simulations and asymptotic analysis in attempting to predict the temperatures and the time scales involved, including reactant effects and, later on, gaseous interactions. The maximum temperature reached and the time taken to reach that maximum from given initial conditions are of special interest. The aspects of explosions that are to be modelled thus include the (high) temperatures attained and any reactant behaviour as well as gaseous production and feedback. The main justification for, and perhaps the need for, asymptotic analysis here rather than simulation packages such as Comsol [57] lies in the extreme values which turn out to be present for certain key parameters, such as 10^{-25} or so when written in reasonable non-dimensional terms. The physical processes being examined in the thesis centre on the triggering of reactions which become ultimately very strong ones whose effects on temperature are to increase its rate of change very positively.

To end this part of the introduction we propose the basic research questions that will determine or at least guide the author's work following on directly from the present thesis. The research questions will clearly draw upon the work accomplished to date as described in this thesis. These questions or issues address the following:

- the evolution of the temperature under various different conditions;
- the influence of reactants and their properties;
- gaseous interaction effects on the evolution;
- the time scales and other physical scales involved.

Our aims, then, include gaining further insight, providing comparisons or alternatives for direct computation and adding to the portfolio of methodologies available in this area [58].

1.2 Structure of thesis

The general structure of the thesis is divided into three main parts. Part I consisting of chapters 2–4, which considers the basic reaction-diffusion model with alternative asymptotic treatment. The work in part I has been published in [4].

Part II of the thesis is made up of chapter 5–9 and focusses on the incorporation of gas into the model. Finally part III, which can be considered a stand-alone piece of work, considers an alternative method of stimulus, namely mechanical heating.

Starting with part I, chapter 2 describes the model of interaction evolving between thermal diffusion effects in one spatial dimension and a single reactant [5–9], along with a computational study. Here reference is made to ODTX (One dimensional time to explosion methods) [6, 19, 25, 28] and HMX (octogen explosive) for which the values of certain parameters in the model turn out to be significantly small or large. This leads on to an investigation of asymptotic properties presented in chapter 3 accompanied by comparisons with the direct computations. Chapter 4 then addresses the evolution between thermal diffusion and three reactants [1] computationally followed by corresponding asymptotic analysis and comparisons. Part II of the thesis focusses on the incorporation of gas into the existing model. In this part of the thesis, we begin by introducing the treatment of gas as a discrete model before extending this to a continuous framework in chapter 5. Next in chapter 6 we consider the effects of feedback in the system by allowing the temperature of the gas produced to heat the explosive externally. In chapter 7 we consider an alternative model to that presented in chapter 6 by allowing feedback from the gas both internally and externally. This is achieved through allowing the densities of both the solid and gas to vary. We seek insight from asymptotic treatment here. Based on this, chapter 8 allows for internal heating within the system. Here we work purely in an asymptotic framework while in chapter 9 we repeat the analysis for the fully dimensional problem using both mild and physical parameters.

Part III of the thesis considers work which is, in one sense, separate to the previous two parts. Here chapter 10 briefly considers mechanical stimulus as opposed to the thermal heating which has been considered throughout the thesis. In another sense, however, there is close connection to the previous parts. We find that the main behaviour takes place in the thin boundary layers, despite the mechanical treatment as opposed to the thermal one presented in parts I and II. The aim here is that the overall large-scale model is eventually to involve not only fluid dynamics bus also heat production, reaction and interaction; to some extent chapter 10 is preparation for such a large-scale model. Finally, general conclusions and future work are presented in chapter 11.

Part I

Reaction-Diffusion

Chapter 2

One-reactant problem and computational properties

The problem area of concern here arises as follows. A simple configuration is considered, with a slab of solid explosive confined at one end with a burning surface at the other end. A layer of hot gas is adjacent to the burning surface, itself confined by a non-conducting wall opposite to the burning surface. See figure 2.1. Modelling the wall as non-conducting is believed to be more relevant in practice than the fixed temperature case, although in the present work we take the constant temperature case because it is simpler and clearer. When the hot gas is assigned a temperature value that is in the vicinity of the activation temperature for the explosive, this acts as a trigger for the ignition of the explosive. Classical heat conduction [30, 59, 60] in the explosive is one feature with a significant role in the model here.

We then enhance the model by considering the effects of adding a reaction term to the heat conduction equation [61]. To begin modelling the reaction-diffusion process, we consider the simple and well-known Arrhenius reaction equation [2].

The Arrhenius equation [1] is used to calculate the effect of a change in temperature on reaction rates. It is commonly used to calculate chemical reactions, particularly in heat induced problems such as ours. The combustion of explosives depends heavily on chemical processes which take place. Heating and impact both can trigger a reaction process which leads to significant burning, and they are the main two reasons why an explosive combusts. Once the temperature reaches a cer-

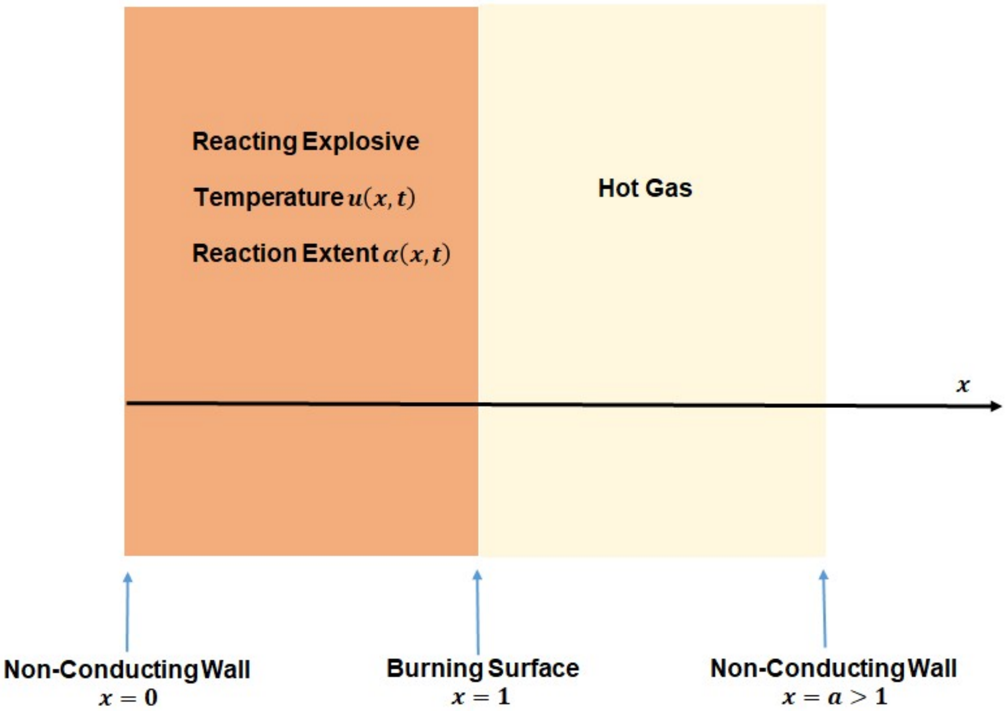

Figure 2.1: Schematic of the solid explosive (left) and hot gas (right).

tain level, commonly known loosely as the critical temperature, the reaction process becomes significantly large. When the reaction has started, the speed of the reaction increases as the temperature increases. The Arrhenius reaction equation has been used in several explosives models including [5] and is given by

$$k = A\exp(-E/Ru), \tag{2.1}$$

where k is the reaction rate constant which expresses the relationship between the concentration of reactants and reaction rate, u is the temperature, E is the activation energy required for the reaction, R is the universal gas constant and A is the frequency factor, which is also known as the pre-exponential constant.

Following the works of [5, 61, 62], for example, we consider a variation of (2.1). Namely, we consider the reaction α with rate such that $k \to \frac{\frac{\partial \alpha}{\partial t}}{(1-\alpha)}$ which mimics the general form (2.1) but varies with time t and represents a finite amount of combustible material. The reaction rate is restricted by the term $(1-\alpha)$, which represents the fraction of unreacted material remaining. In other words $0 \leq \alpha(x,t) \leq 1$ for all spatial positions $x \in D$ and $t \in T$ where $\alpha = 0$ is the initial state (unreacted) and $\alpha = 1$ is the final state (fully reacted). Here $T = [0, T_{max}]$, where T_{max} is the period of time over which we model the event, and D is the bounded spatial domain, which can be taken as $[-1,1]$ without loss of generality by working with x/a and κ/a^2 for a domain $[-a,a]$, where the diffusion coefficient κ is defined below. We use the reflected geometry to avoid the requirement to impose a zero flux condition for simplicity. However, if we did adhere to $x \geq 0$ we would need to impose that condition, but might reduce the computational time.

We now consider the reaction-diffusion PDE

$$\rho c_v \frac{\partial u}{\partial t} = \kappa \frac{\partial^2 u}{\partial x^2} + \rho \Omega \frac{\partial \alpha}{\partial t}, \tag{2.2}$$

with the reaction term given by

$$\frac{\partial \alpha}{\partial t} = A(1-\alpha)\exp\left(-\frac{E}{Ru}\right), \tag{2.3}$$

where the constant Ω is the heat of reaction. Equations (2.2) and (2.3) combine to form a non–linear coupled system of PDEs for $u(x,t)$ and $\alpha(x,t)$.

Here ρ, c_v, κ, Ω, R, E and A are dimensional parameters with realistic values and units listed in table 2.1. The typical boundary and initial conditions are

Table 2.1: Physical parameters used in model.

Parameter with units	**Symbol**	**Value**
Conductivity (W/m/K)	κ	0.44
Specific Heat (J/kg/K)	c_v	1255.0
Density (kg/m^3)	ρ	1800.0
Heat of Reaction (J/kg)	Ω	$5.0208e6$
Molar Gas Constant (J/mol/K)	R	8.314
Activation Energy (J/mol)	E	$2.2e5$
Pre-exponential Constant (s^{-1})	A	$5.011872336e19$
Wall temperature $^\circ K$	B	570
Initial solid temperature $^\circ K$	C	293

$$u(-1,t) = u(1,t) = B, \quad \text{for } 0 < t \leq T_{\max}, \tag{2.4a}$$

$$u(x,0) = C, \quad \text{for } x \in D, \tag{2.4b}$$

where quite realistic temperature values are $B = 570$ (activation temperature), $C = 293$ (room temperature) say. This spatially symmetric scenario with constant boundary and initial temperatures is to be generalized later, whereas the initial value of α is taken to be zero in all the present studies.

Given the extremely large dimensional values appearing in table 2.1 and in the conditions 2.4a,2.4b we turn to a non-dimensional form of the governing equations and conditions and note a need for caution concerning numerical results at this stage. To deal with the parameters, then, we introduce the non-dimensional variables $\bar{t}$ and $\bar{u}$ that satisfy

$$t = A^{-1}\bar{t}, \qquad u = \frac{E}{R}\bar{u}, \tag{2.5a}$$

having recognised the fact that A is likely to be responsible for main changes in u and α happening on different time scales and that $\frac{E}{R}$ is relatively large. There is no need to scale α since it is already non-dimensional and $\mathscr{O}(1)$.

The substitutions lead to the non-dimensional system of PDEs

$$\frac{\partial \bar{u}}{\partial \bar{t}} = \bar{\kappa}\frac{\partial^2 \bar{u}}{\partial x^2} + \bar{\Omega}\frac{\partial \alpha}{\partial \bar{t}}, \tag{2.6a}$$

$$\frac{\partial \alpha}{\partial \bar{t}} = (1-\alpha)\exp\left(-\frac{1}{\bar{u}}\right), \tag{2.6b}$$

where from table 2.1 the non-dimensional parameters present now are $\bar{\kappa} := \frac{\kappa}{\rho c_v A} \approx 10^{-25} \ll 1$, and $\bar{\Omega} := \frac{\Omega R}{c_v E} \approx 0.15$. The boundary and initial conditions also need scaling and are given by

$$\bar{u}(-1,t) = \bar{u}(1,t) = \bar{B}, \quad \text{for } 0 < \bar{t} \leq T_{\max}, \tag{2.7a}$$

$$\bar{u}(x,0) = \bar{C}, \quad \text{for } x \in D, \tag{2.7b}$$

where $\bar{B} := \frac{RB}{E} \approx 0.02$ and $\bar{C} := \frac{RC}{E} \approx 0.01$. We note that the initial condition for

α remains unchanged of course and that quite extreme parameter values are still present, particularly the $\bar{\kappa}$ value.

Numerical solutions were sought first, using a semi-implicit scheme of second-order accuracy in x, t. This adopts three-point backward differencing in t and three-point centred differencing in x. The discretisation replaces (2.2)–(2.3) by

$$\begin{aligned} -\mu U_{j-1,i+1} + (3+2\mu)U_{j,i+1} - \mu U_{j+1,i+1} &= 4U_{j,i} - U_{j,i-1} + \dots \\ \dots + 2\Delta t \frac{A\Omega}{c_v}(1-2\alpha_{j,i}+\alpha_{j,i-1}) &\exp\left(-\frac{E}{R(2U_{j,i}-U_{j,i-1})}\right), \end{aligned} \tag{2.8a}$$

$$\alpha_{j,i+1} = \frac{2A\Delta t \exp\left(\frac{-E}{RU_{j,i+1}}\right) + 4\alpha_{j,i} - \alpha_{j,i-1}}{3 + 2A\Delta t \exp\left(\frac{-E}{RU_{j,i+1}}\right)}, \tag{2.8b}$$

and it acts similarly on the form (2.6a),(2.6b). Here i, j refer to time t and space x respectively, with grid sizes Δt, Δx, the arrays $U_{j,i}$, $\alpha_{j,i}$ represent discretised u, α and $\mu = r\frac{2\Delta t}{(\Delta x)^2}$, where $r = \frac{\kappa}{\rho c_v}$. We remark that, to keep the scheme quasi-linear at each new time step, lagging of terms in the exponential effects in (2.8a), (2.8b) is present. For example in the exponential effect in (2.8a) the expression $(2U_{j,i} - U_{j,i-1})$ is used in place of $U_{j,i+1}$ and preserves the desired second-order accuracy. The parameter values involved are of much interest. The fairly realistic values in practice shown in table 2.1 are potentially quite extreme values; indeed we investigate the influences of a quite wide range of values of the parameters below.

In fact cautiously obtaining and then considering the computational solutions is felt to be very desirable for mild, less mild and realistic cases. We defer further discussion of the realistic cases such as in table 2.1 until later chapters. Figures 2.2-2.6 show the numerical results for mild cases. They exhibit a number of interesting features. There is analytically a classical similarity solution [56] with spatial thickness of order $t^{1/2}$ holding in each thin edge layer at small time astride each wall, a property which is captured satisfactorily by the current numerical scheme. One can see evidence of thin edge layers emerging also as κ or $\bar{\kappa}$ is decreased. These layers however continue to apply over a considerable time range. The numerical results further produce overshoots in temperature which become more pronounced and linger more (see figure 2.6) as $\bar{\kappa}$ is decreased for example, whereas α increases monotonically towards unity in every case. We see in addition some pronounced differences in the apparent time scales typical of the temperature and α in the results. These are to be considered analytically later. The results in figures 2.2–2.6 are only showing spatially symmetric cases but non-symmetric ones, presented in figure 2.7, display similar trends.

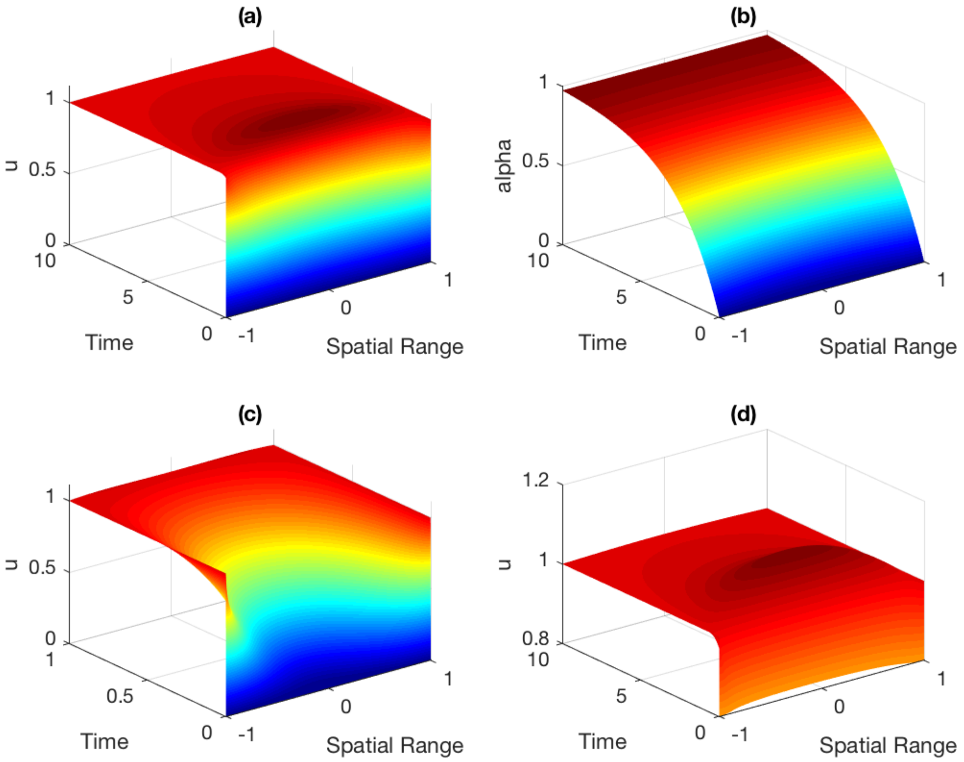

Figure 2.2: The finite difference solution to u (figure (a)) and α (figure (b)) in the coupled system of PDEs (2.2) and (2.3) using a second–order implicit scheme. We chose $T_{\max} = 10$ with $\Delta x = 0.05$ and $\Delta t = 0.01$. Here $\rho, c_v, \kappa, \Omega, A, E, R$ are set to unity. Also $B = 45$ and $C = 15$ (in non-dimensional terms, $\bar{\Omega} = 1, \bar{\kappa} = 1, \bar{B} = 1$ and $\bar{C} = 15$). On the bottom left (figure (c)) we plot the solution for small time $t = 0$ to $t = 1$ to show the rise of the temperature, u. Notice how the inclusion of a reaction term causes the temperature profile to surpass the temperature value at the boundary before plateauing (figure (d)).

We found the realistic case with the values of table 2.1 to be a very difficult one to compute reliably in view of, for example, a sensitivity observed in the results for α as the spatial step was varied. In contrast, when we use milder parameter values

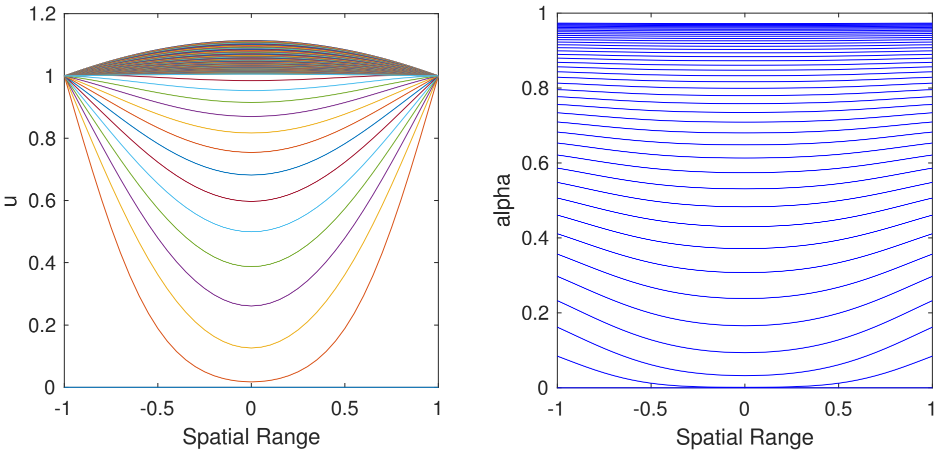

Figure 2.3: Solutions to u and α over the spatial range x for fixed values of t. Here we have used the same parameters and temperature conditions as in figure 2.2.

such as $E = 10$ and $A = 200$ with the boundary and initial conditions (2.4a)-(2.4b) with $B = 45$, $C = 15$ then the finite difference approximation of α is insensitive to the same choices of spatial step. The profiles of these solutions are given in figure 2.4. A further set of results for even milder values of the parameters is presented in figures 2.5, 2.6, pointing to the use of asymptotic analysis below.

To address the very small parameter $\bar{\kappa}$ that features in the scaled PDE, we add a different approach. It can be shown through asymptotic expansions of $\bar{u}$ and α that by equating the coefficients of like powers of $\bar{\kappa}$ and taking $\mathscr{O}(1)$ terms only, the term $\frac{\partial^2 \bar{u}}{\partial x^2}$ is unlikely to have any substantial effect for a long time, except near the boundaries, since the reaction term dominates. Hence, asymptotically, the problem can now be viewed as the interaction of two problems: a problem in thin wall layers at both ends of the domain and a problem in a core.

The view just mentioned in regard to the emergence of two problems accom-

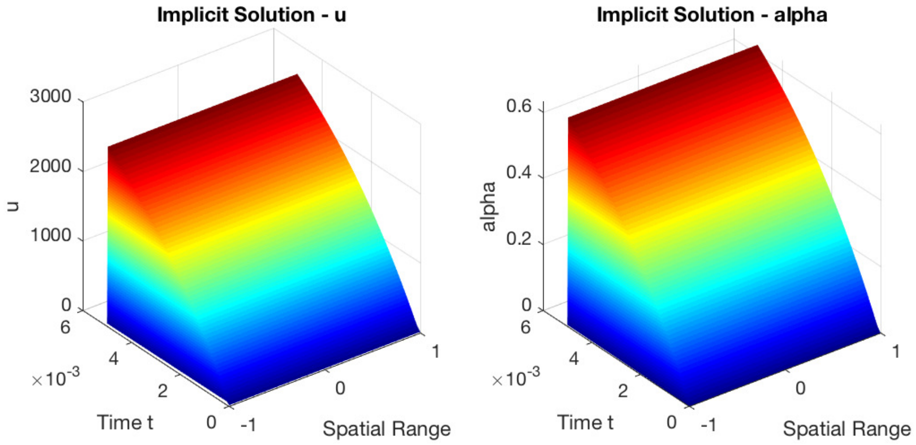

Figure 2.4: The numerical finite difference solutions to u (left) and α (right) satisfying the PDEs (2.2)–(2.3) using a second–order semi implicit scheme with mild physical parameters. Here $\rho = 1800$, $c_v = 1255$, $\kappa = 0.44$, $\Omega = 5.0108 \times 10^6$, $A = 200$, $E = 10$, $R = 8.314$, $B = 45$ and $C = 15$. In non-dimensional terms, $\bar{\Omega} \approx 3319.505, \bar{\kappa} \approx 9.7 \times 10^{-10}, \bar{B} \approx 37.413$ and $\bar{C} \approx 12.471$.

panied by distinct regions is especially supported by the numerical results for the single-reactant cases shown in figures 2.5-2.7, where figure 2.7 admits spatial non-symmetry. The physics represented here as κ is decreased is associated with the relatively low diffusion in the system, over the main time scale of the reaction fraction, which indicates that only the initial temperature distribution affects the core temperature and reaction significantly over that time scale. The results in the figures, which are for parameter values even milder than those introduced in figures 2.2-2.4, confirm clearly the appearance of a core in the majority of the domain and thin wall layers near the boundaries even for values of κ for example that are small but, in a sense, not extremely so. This suggests that an asymptotic approach (as described in the following chapter) will be fruitful over a wide range of the parameter space.

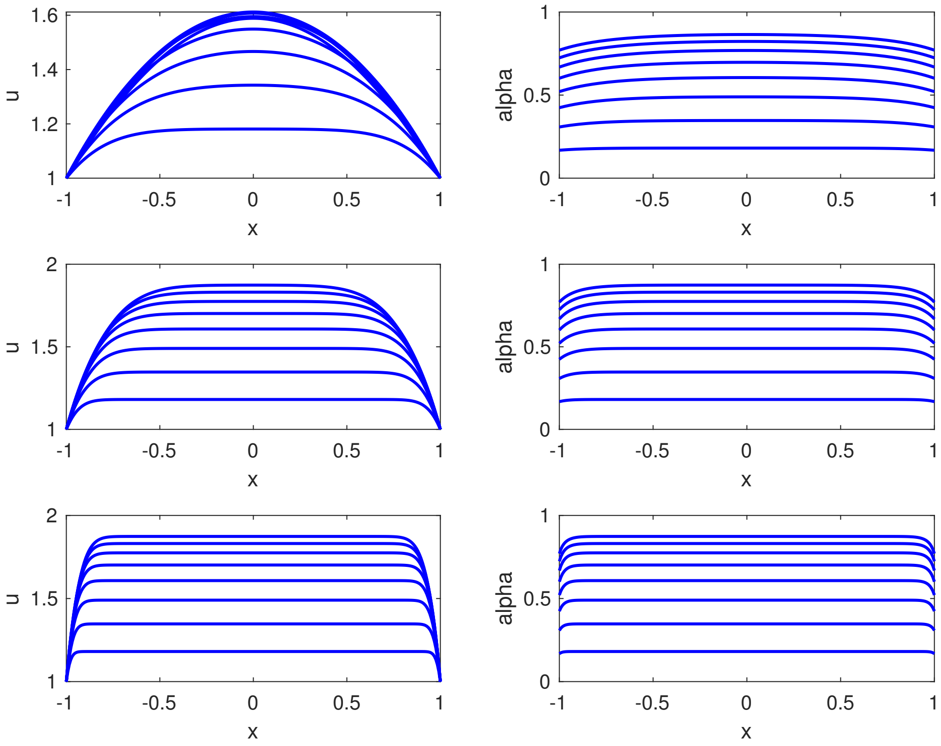

Figure 2.5: The numerical results for u and α satisfying equations (2.2)–(2.3) with very mild parameter values $E = R = A = \rho = \Omega = c_v = B = C = 1$ and $\kappa = 0.1, 0.01, 0.001$ (top to bottom). In non-dimensional terms, $\bar{\Omega} = 1, \bar{B} = 1, \bar{\kappa} = 0.1, 0.01, 0.001$ (top to bottom) and $\bar{C} = 1$.

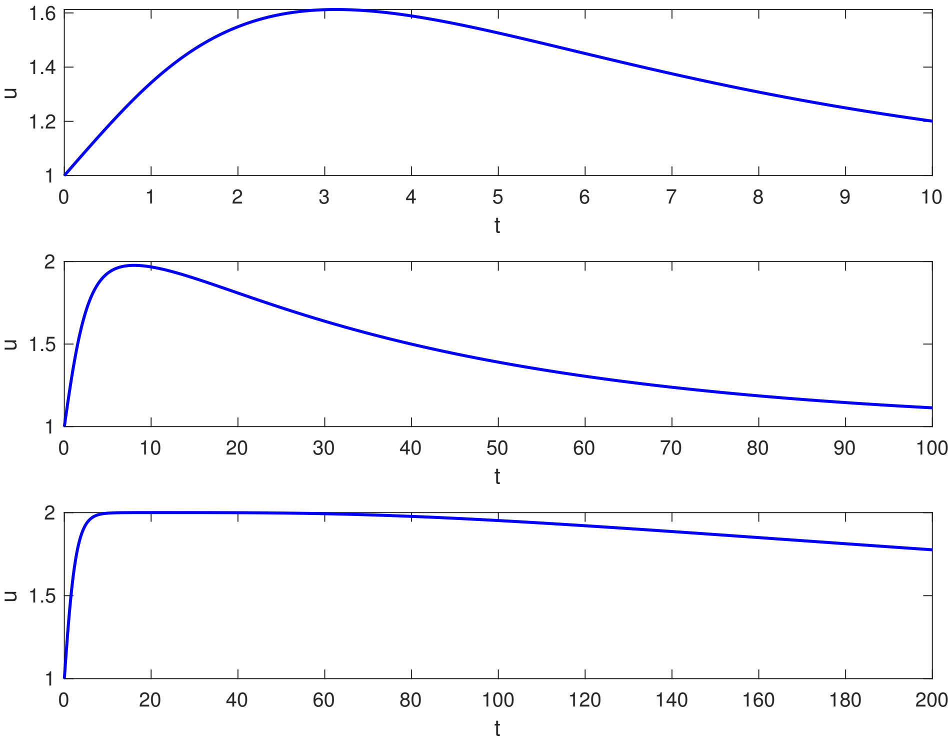

Figure 2.6: The numerical results for u at $x = 0$ satisfying equations (10.2)–(2.3) with very mild parameter values $E = R = A = \rho = \Omega = c_v = B = C = 1$ and $\kappa = 0.1, 0.01, 0.001$ (top to bottom). Overshoot is clearly seen for all cases here and lasts longest for the lowest κ value.

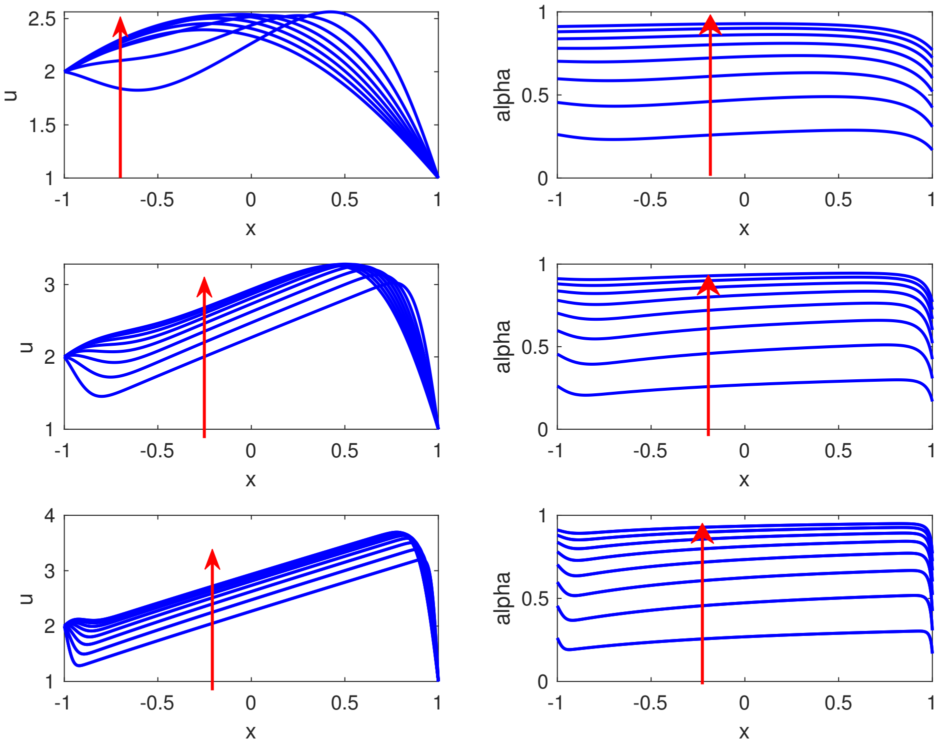

Figure 2.7: The numerical results for u, α for the non-symmetric case satisfying equations (2.2)–(2.3) with very mild parameter values $E = R = A = \rho = \Omega = c_v = 1$ and $\kappa = 0.1, 0.01, 0.001$ (top to bottom). The temperature u, with boundary conditions $u(-1,t) = 2$ and $u(1,t) = 1$, is shown for fixed values of $t = 0$ to $t = 4$ in steps of $1/2$, where the red vertical arrows indicate time increasing. Here the initial temperature is given by $C(x) = x + 2$.

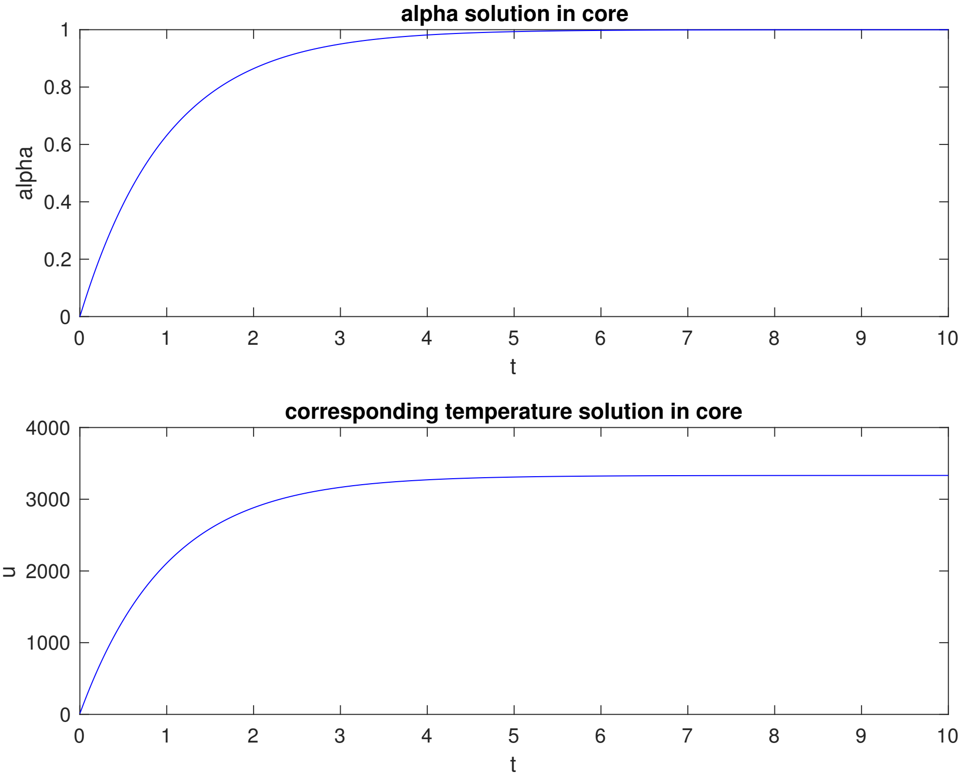

alpha solution in core

corresponding temperature solution in core

Figure 2.8: The solutions α (top) and u (bottom) in the core satisfying equation (3.5).

2.1 Summary of chapter

The work presented in this chapter is believed to fill some of the gap in understanding concerned with interaction between solid material and chemical reaction during combustion, through detailed study of thermal and reactant properties. Single step reactions have been modelled first using a simple Arrhenius model. We introduced the physical parameters involved in the system as well as milder versions of these parameters for computational ease. In order to deal with the relatively small and extremely large parameter values we non-dimensionalised the coupled system and worked with the scaled variables $\bar{u}$ and $\bar{t}$.

Numerical solutions using a semi-implicit finite difference scheme which is second-order accurate were presented for the system of equations using mild parameter values. The analysis in this chapter confirms the appearance of a core region which occupies the majority of the domain as well as thin wall layers near the boundaries. This is explored further in the next chapter.

Chapter 3

Asymptotic analysis and comparisons

Guided by the numerical solution features above we seek extra insight by taking an asymptotic approach that in principle handles effectively the extreme parameter values. A core region, denoted by the subscript $_c$, covering most of the domain can be anticipated along with thin wall layers close to the boundaries. That distinction in spatial scale is found to persist for a considerable amount of time before change occurs. The initial condition on the temperature is taken to be constant for now but this is generalised later on.

3.1 Effects of $\bar{\kappa}$

The main evidently small parameter is $\bar{\kappa}$. Treating it as an asymptotically small parameter leads to two major time scales appearing as follows. The first time scale has $\bar{t}$ of $\mathcal{O}(1)$. Here in the core where $-1 < x < 1$ the variables $\bar{u}$, α are expected to be of order unity and so the expansions

$$\bar{u} = u_c + \dots, \tag{3.1a}$$

$$\alpha = \alpha_c + \dots \tag{3.1b}$$

are called for. Terms of equal orders in the non-dimensional governing equations 2.6 then yield a reduced system for the leading order quantities, namely

$$\frac{\partial \bar{u}_c}{\partial \bar{t}} = \bar{\Omega}\frac{\partial \alpha_c}{\partial \bar{t}}, \tag{3.2}$$

where

$$\frac{\partial \alpha_c}{\partial \bar{t}} = (1-\alpha_c)\exp\left(-\frac{1}{\bar{u_c}}\right). \tag{3.3}$$

The leading equation above admits the simple result that $\bar{u}_c - \bar{\Omega}\alpha_c$ is a function of x only but the initial condition of a constant u across the domain then establishes that function is constant. Therefore applying the initial conditions that $\bar{u_c}(x,0) = \bar{C}$ and $\alpha_c(x,0) = 0$ yields the relation

$$\bar{u_c}(x,\bar{t}) = \bar{\Omega}\alpha_c(x,\bar{t}) + \bar{C}, \tag{3.4}$$

for all $\bar{t}$ of $\mathscr{O}(1)$. We see in (3.4) that the temperature rises through local burning. Hence equation (3.3) becomes one for α_c alone,

$$\frac{d\alpha_c}{d\bar{t}} = (1-\alpha_c)\exp\left(-\frac{1}{\bar{\Omega}\alpha_c + \bar{C}}\right). \tag{3.5}$$

Note that since the initial condition $\alpha_c(x,0) = 0$ is independent of x, (3.2) as it stands is also independent of x and essentially represents a non-linear ODE for α_c that is valid for $-1 < x < 1-$. We remark in passing here that x-dependence in the initial conditions at $t = 0$ which can be reflected in $\bar{C}$ in (3.4), (3.5) and similarly $\alpha(x,0)$ being given functions of x will be discussed later. Clearly the diffusive term involving a double x-derivative is negligible in the core at this level and no boundary condition is applied. The ODE (3.5) is non-trivial to solve and so we use ODE45 in MATLAB to integrate numerically. The core reaction α_c may then be substituted back into (3.4) to determine the leading order temperature $\bar{u_c}$ in the core.

In figure 2.8 we plot the core solutions $\bar{u_c}$ and α_c that satisfy (3.3) and (3.2), respectively, using the mild parameter values $E = 10$ and $A = 200$ as well as $C = 15$ which is required for the initial condition of $\bar{u_c}$. The asymptotic analysis is still formally valid using these mild parameters since the corresponding value of $\bar{\kappa}$ is still exceptionally small. We use mild parameters for now so that in a sense we may check (see figure 3.1) the asymptotic analysis against the finite difference solutions given in chapter 2, before proceeding to employ the full parameter values of table 2.1. Further details on the effects of treating $\bar{\Omega}$ as a large parameter are given in a subsection below. It is worth noting that the characteristics of the core with mild parameters and physical parameters are likely to be different because the parameters change not only the boundary layer but also the behaviour of the core. Results for other parameter values are given in the next subsection.

Wall layers are necessary partly because the core equations have no spatial dependence and represent in effect only initial value problems. As a result, the loss of the derivative term in x means that the underlying boundary conditions in (2.7a) cannot be satisfied in the core, in the general case. We seek an accompanying solution to the core solutions by considering the system (2.6) near the boundaries. To handle the extreme parameter $\bar{\kappa}$ we set, in the left-hand thin wall layer,

$$x = -1 + \bar{\kappa}^{1/2}\bar{x} \tag{3.6}$$

and expand

$$\bar{u} = \bar{u}_e(\bar{x},\bar{t}) + \ldots, \tag{3.7a}$$

$$\alpha = \alpha_e(\bar{x},\bar{t}) + \ldots. \tag{3.7b}$$

Substitution into (2.6) implies that the governing equations are

$$\frac{\partial \bar{u}_e}{\partial \bar{t}} = \frac{\partial^2 \bar{u}_e}{\partial \bar{x}^2} + \bar{\Omega}\frac{\partial \alpha_e}{\partial \bar{t}}, \tag{3.8a}$$

$$\frac{\partial \alpha_e}{\partial \bar{t}} = (1-\alpha_e)\exp\left(-\frac{1}{\bar{u}_e}\right), \tag{3.8b}$$

in the wall layer. (For the most realistic cases described earlier the edge layer is remarkably thin, having an approximate non-dimensional thickness of order 10^{-12} from (3.6). The validity of the continuum model may become questionable there for such cases. Further discussion on this is presented in 11.) It is notable that since at present the core problem is independent of x, the solutions at the inside edges of the wall layers are valid across the entire core. In other words, the solutions $\bar{u}_e$ and α_e satisfying (3.8) coincide with the core solutions at $\bar{x} = \infty$ effectively. We therefore

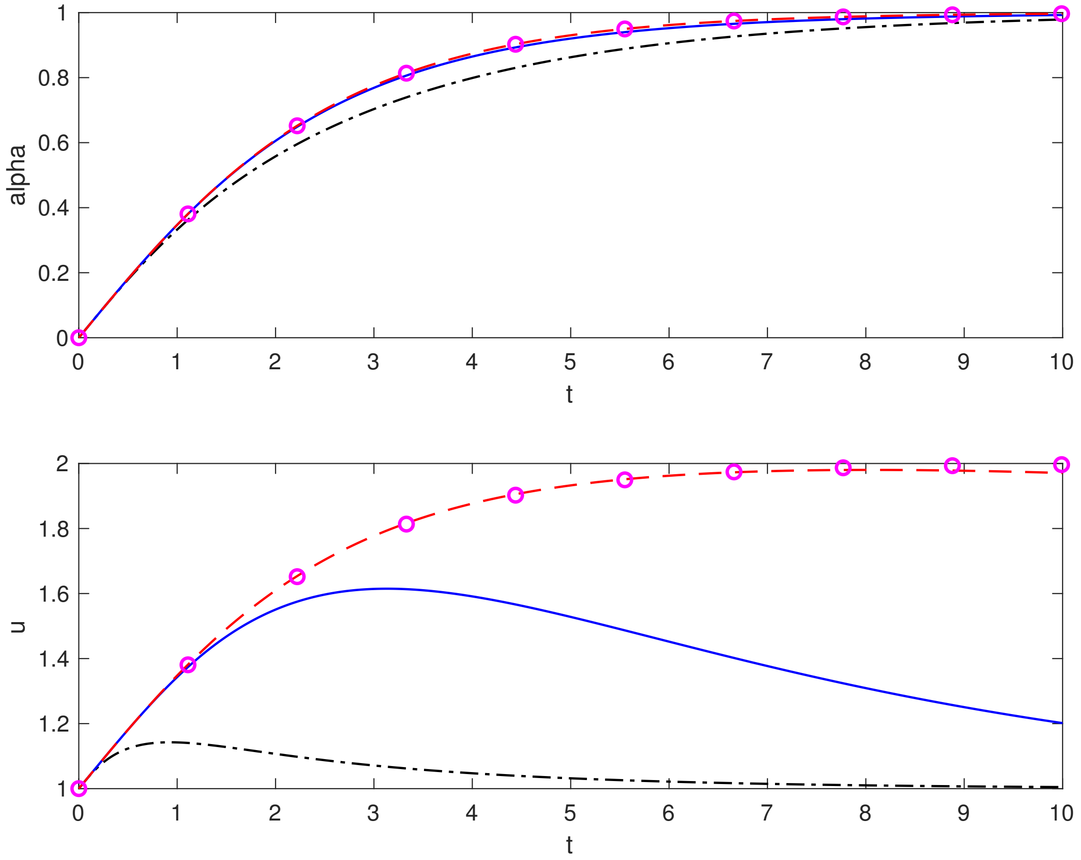

Figure 3.1: Comparison of core (round markers) and full solutions for varying $\kappa = 1, 0.1, 0.01$ (represented by the dot–dashed black, solid blue and dashed red lines, respectively).

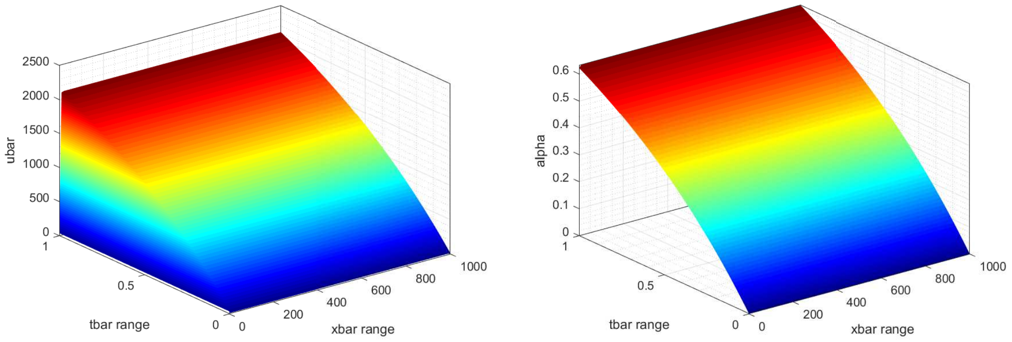

(a) $\bar{u}_e$ **(b)** α_e

Figure 3.2: The wall-layer solutions $\bar{u}_e$ and α_e satisfying (3.8) using a second-order numerical scheme with the mild parameters $E = 20$; $A = 200$; $C = 15$ and $B = 45$.

subject (3.8) to the boundary conditions

$$\bar{u}_e(\infty,\bar{t}) = \bar{u}_c, \quad \alpha_e(\infty,\bar{t}) = \alpha_c.$$

It also holds that

$$\bar{u}_e(0,\bar{t}) = \bar{B}, \tag{3.9}$$

and, as before, the boundary solution for α_e at the wall can be determined by solving the second equation in (3.8) using the condition (3.9). That

$$\alpha_e(0,\bar{t}) = 1 - \exp\left(-\bar{t}\exp\left(-\frac{1}{\bar{B}}\right)\right), \tag{3.10}$$

at the wall. We also have the initial conditions

$$\bar{u}_e(\bar{x},0) = \bar{C}, \qquad \alpha_e(\bar{x},0) = 0, \qquad 0 < \bar{x} < \infty.$$

Again we note that there is a similarity solution for small times $\bar{t}$ near $\bar{x} = 0$, [56]. To solve the system (3.8) we use the finite difference schemes of chapter 2. Typically we took $0 \leq \bar{x} \leq 1000$, to ensure the spatial domain was large enough to demonstrate the true solution behaviour. In figure 3.2 we plot the numerical solutions to $\bar{u}_e$ and α_e using the mild parameters $E = 20$; $A = 200$; $C = 15$ and $B = 45$. In figure 3.3 we compare the full non–asymptotic solutions given in figure 2.4 (top) with the present asymptotic wall solutions (bottom). Note that to compare these solutions directly we must scale u and $T_{\max}$ in figure 2.4 by $\frac{R}{E}$ and A respectively. We observe that the solutions not on the boundary (which is ultimately what we are interested in, since we do not know them a priori) match almost perfectly.

At sufficiently large times $\bar{t}$ the wall layer solution acquires a similarity form. This is because the core temperature and α_e both asymptote to constants then, in particular with the core temperature being $\bar{C} + \bar{\Omega}$ and α_e being unity to a first approximation, and on the other hand the sidewall temperature $\bar{B}$ is taken to be constant. So in the wall layer $\bar{u}_e$ is expected to be of $\mathscr{O}(1)$ and α_e is anticipated as

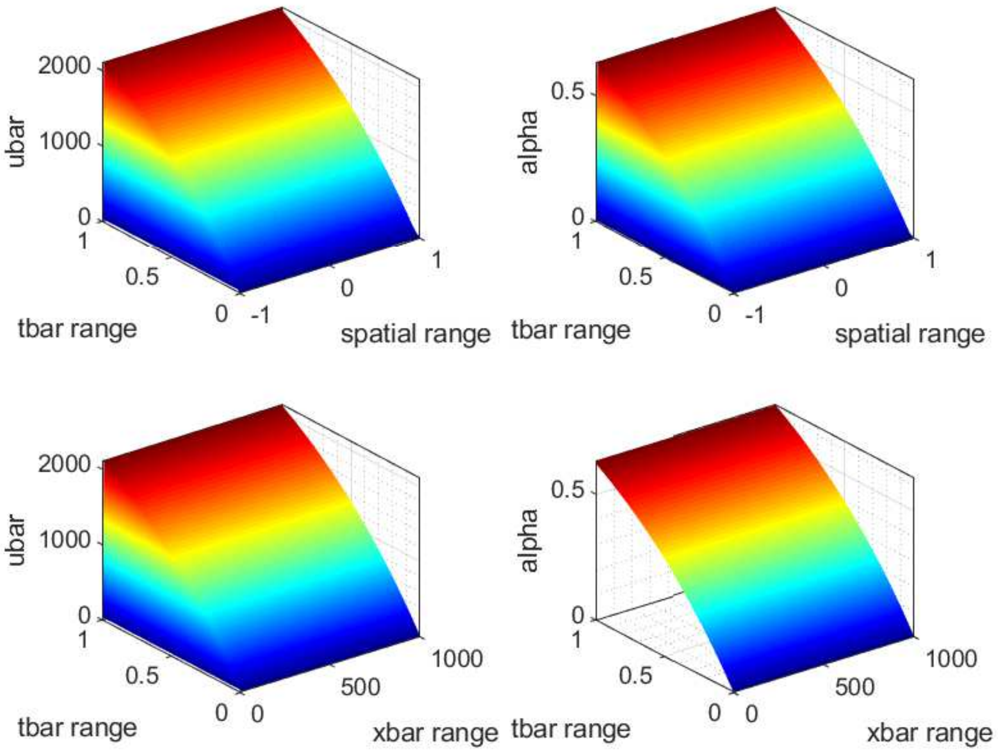

Figure 3.3: Comparison of solutions u and α for the full system (top) corresponding to equations (2.2), (2.3) and the wall-layer (bottom) solutions corresponding to equation (3.8).

being unity with only an exponentially small correction in view of (3.8b). The orders of magnitude involved then suggest that the $\bar{x}$ scale grows as $\bar{t}^{1/2}$, leading to the expression

$$\bar{u}_e = f_1(\xi) + \ldots, \quad \alpha_e = 1 + f_2(\xi) + \ldots \tag{3.11}$$

where $\xi = \bar{x}/\bar{t}^{1/2}$ is of order unity and the function f_2 is exponentially small. Substituting into (3.8) we obtain the equation $-\frac{1}{2}\xi f_1' = f_1''$ for $f_1(\xi)$, with no influence retained now from the reaction effects. The equation is a classical thermal one and yields the solution

$$f_1(\xi) = (\bar{C} + \bar{\Omega} - \bar{B})I^{-1} \int_0^{\hat{\xi}} \exp\left(-\frac{1}{4}\hat{\xi}^2\right) d\hat{\xi} + \bar{B}. \tag{3.12}$$

Here $I = \pi^{1/2}$.

The second major time scale arises because on a longer time scale the wall layers penetrate into the core and become one with it. The wall layer thickness increases like $\bar{t}^{1/2}$ and so makes its presence felt in the core over a long time scale $\bar{t}$ of order $\bar{\kappa}^{-1}$, from the scalings above, specifically in (3.7a). The evolution at that stage takes the form

$$\bar{u} = \mathscr{O}(1), \quad \alpha = 1 + \varepsilon, \tag{3.13}$$

$$x = \mathscr{O}(1), \quad \bar{t} = \bar{\kappa}^{-1}\hat{t} \tag{3.14}$$

over the entire domain, where 'ε' denotes an exponentially small term. The governing equation (2.6a) thus reduces to the classical thermal one

$$\frac{\partial \bar{u}}{\partial \hat{t}} = \frac{\partial^2 \bar{u}}{\partial x^2} \tag{3.15}$$

while (2.6b) gives only effects of higher order. The boundary and initial conditions for (3.15) are

$$\bar{u} = \bar{B} \quad \text{at } x = \pm 1 \quad \text{for } \hat{t} > 0, \tag{3.16}$$

$$\bar{u} = \bar{C} + \bar{\Omega} \quad \text{at } \hat{t} = 0^{+} \quad \text{for } |x| < 1. \tag{3.17}$$

The problem can be transformed to one solved in Carslaw and Jaeger [56], showing similarity behaviour near each wall at early times but a steady state of $\bar{u}$ equal to $\bar{B}$ being approached at late times. The initial (core) temperature can clearly be substantially larger than the steady-state temperature over this time scale. Moreover the complete behaviour of the temperature $\bar{u}$ is seen to be on a different (longer) time scale than the reaction rate α.

3.2 Effects of other parameters ($\bar{\Omega}$, $\bar{C}$, $\bar{B}$).

Although $\bar{\kappa}$ is by far the most extreme parameter the small typical values of the scaled initial temperature $\bar{C}$ and the scaled reaction constant $\bar{\Omega}$ still play important roles in the core of the interaction. Numerical solutions obtained for ($\bar{\Omega}$, $\bar{C}$) values of $(1,0.1)$, $(0.1,1)$, $(0.1,0.1)$, $(10,1)$, $(1,1)$ are shown in figure 3.4(a)-(e) respectively.

Suppose first that $\bar{C}$ is small and $\bar{\Omega}$ is $\mathscr{O}(1)$. Then in the core equation (3.5) the right-hand side, when plotted as a function of α_c, is exponentially small of order $c = \exp(-1/\bar{C})$ at zero α_c but rises rapidly as α_c increases to $\mathscr{O}(\bar{C})$ and it asymptotes towards unity as α_c increases further. The influence of the $(1-\alpha_c)$ term then gradually reduces the right-hand side over a slower scale. The function $d\bar{t}/d\alpha_c$ therefore decreases rapidly from its initial exponentially large value at zero α_c to unity when α_c becomes larger than $\mathscr{O}(\bar{C})$ but still small. Clearly α_c as a function of time begins small, of order $\bar{C}$, and remains so for a considerable time. This slow effect on the reaction when the initial temperature is small makes sense physically. The main evolution of α_c into an $\mathscr{O}(1)$ quantity occurs when time $\bar{t}$ is exponentially large,

$$\bar{t} = \exp\left(\frac{1}{\bar{C}}\right) + \bar{\bar{t}} \tag{3.18}$$

with $\bar{\bar{t}}$ being of $\mathscr{O}(1)$ and the governing equation then becoming

$$\frac{d\alpha_c}{d\bar{\bar{t}}} = (1-\alpha_c)\exp\left(-\frac{1}{\bar{\Omega}\alpha_c}\right). \tag{3.19}$$

See figure 3.4(a). The march back in time corresponds to α_c being small, such that (3.19) gives, after some working,

$$\alpha_c \sim \bar{\Omega}^{-1}(\ln|\,\bar{\bar{t}}\,|)^{-1} \tag{3.20}$$

which confirms the slow progress of the evolution. The march forward in time is effectively displayed in figure 3.4(a), giving rise to α_c tending to unity at large $\bar{\bar{t}}$.

Secondly, if on the other hand $\bar{C}$ is of order unity but $\bar{\Omega}$ is small as in figure 3.4(b) then the contribution $\bar{\Omega}\alpha_c$ in (3.5) simply plays a negligible part throughout the interaction. The governing equation reduces to a linear ODE for α_c to leading order and the form

$$\alpha_c = 1 - \exp(-c\bar{t}) \tag{3.21}$$

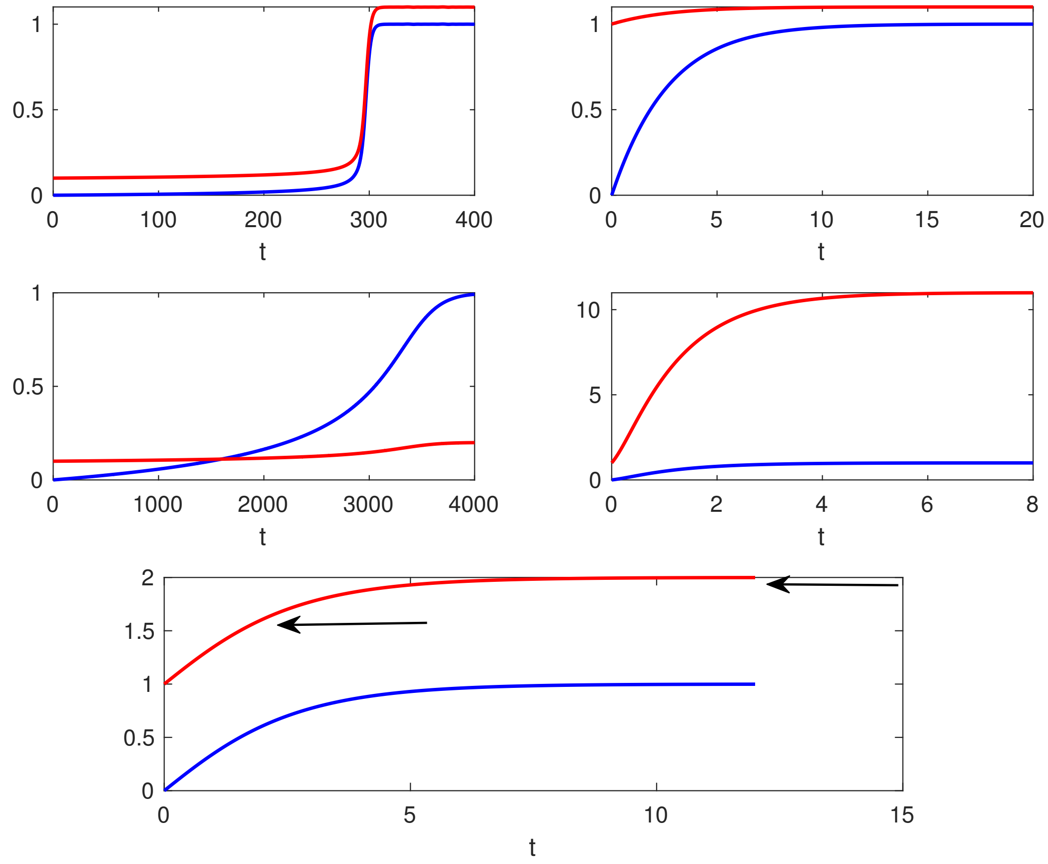

Figure 3.4: Core solutions $\bar{u}_c$ (red) and α_c (blue) corresponding to equation (3.19) as parameters $(\bar{\Omega}, \bar{C}) = (1, 0.1), (0.1, 1), (0.1, 0.1), (10, 1), (1, 1)$, (left to right - top to bottom). In the bottom figure, the arrows represents the highest and mid-values of the temperature $\bar{u}_c$.

describes the solution, where $c = \exp(-1/\bar{C})$ is now a given $\mathscr{O}(1)$ constant in the present case of $\bar{C}$ being uniform. The time scale in terms of $\bar{t}$ thus remains of order unity. The low reaction rate here means physically that the core temperature remains constant to leading order.

Thirdly, if $\bar{C}$ and $\bar{\Omega}$ are both small as in figure 3.4(c) and of order Δ, say $\Delta(\bar{\bar{C}}, \bar{\bar{\Omega}})$ respectively, then again consideration of the graph of the function $d\bar{t}/d\alpha_c$ is helpful. Its initial value is large, being $1/c$, and the function remains large and positive through the entire interaction, reaching an exponentially large minimum value of

$$\bar{\bar{\Omega}}\Delta^{-1}(\bar{\bar{C}}+\bar{\bar{\Omega}})^{-2}\exp(\Delta^{-1}(\bar{\bar{C}}+\bar{\bar{\Omega}})^{-1}), \tag{3.22}$$

at the value

$$\alpha_c = 1 - \frac{\Delta(\bar{\bar{C}} + \bar{\bar{\Omega}})^2}{\bar{\bar{\Omega}}}, \tag{3.23}$$

i.e. near the end of the reaction. Hence the time $\bar{t}$ taken for the reaction to be completed such that α_c grows from zero to unity is exponentially large again. The physical sense is similar to that in the case of (3.18)-(3.20) concerning relatively slow reaction.

By contrast, if either or both of $\bar{C}$ and $\bar{\Omega}$ is or are large then the representative scale $\bar{t}$ remains $\mathscr{O}(1)$, with α_c given by $1-\exp(-\bar{t})$ and the scaled temperature $\bar{u}_c$ given by

$$\bar{u}_c = \bar{C} + \bar{\Omega}(1 - \exp(-\bar{t})). \tag{3.24}$$

An example is shown in figure 3.4(d). The maximum temperature $\bar{C} + \bar{\Omega}$ is approached at times $\bar{t}$ which are large but not as large as in the cases of (3.18)-(3.20) and (3.23).

The effect of the sidewall temperature $\bar{B}$ is felt only in the wall layer, at least for times $\bar{t}$ of order unity because the core is unaffected to leading order by diffusion in x. This is discussed further now. The case of relatively small $\bar{B}$, corresponding to a relatively low temperature imposed at the wall, is also of some mathematical concern although of little likely relevance to real application. Since any $\bar{u}$ of $\mathscr{O}(1)$ leads to α_e tending to unity at large $\bar{t}$ the similarity solution (3.11)-(3.12) still holds then for most ξ values but with the inner boundary condition of $\bar{u}(= f_1$ to leading order) equalling $0+$ at $\xi = 0+$ and $\bar{u}$ tending linearly to zero with ξ. Hence if $\bar{B} = \varepsilon\hat{B}$ say with ε being small and $\hat{B}$ of order unity then there is a sublayer close to the wall where ξ, $\bar{u}$ are both $\mathscr{O}(\varepsilon)$ and $\bar{u}$ is affected by the low wall temperature. The second stage where $\hat{t}$ is $\mathscr{O}(1)$ is perhaps clearer to analyse. Here the majority of the domain is governed by (3.15)-(3.17) but subject to $\bar{u} \to 0+$ as $x \to -1+$ and similarly as $x \to 1-$. So the behaviour

$$\bar{u} \sim (x+1)\beta(\hat{t}) \qquad \text{at } x = -1+ \tag{3.25}$$

is expected near the left-hand wall where β is an order-unity function of $\hat{t}$ determined by the forward-marching solution of (23)-(25). Essentially the same response occurs at the right-hand wall. The function $\beta(\hat{t})$, and indeed the entire $\bar{u}(x,\hat{t})$ solution, tends to zero at large times $\hat{t}$, while at small times $\beta(\hat{t})$ is large, varying as $\hat{t}^{-1/2}$. Near the wall on the other hand a sublayer is present in which

$$\bar{u} = \varepsilon\hat{u} + \dots, \qquad \alpha = \hat{\alpha} + \dots, \qquad \text{with } x = -1 + \varepsilon\hat{x} \tag{3.26}$$

where $\hat{\alpha}$ is non-trivial because of the low wall temperature. The governing equations (2.6a),(2.6b) in this sublayer reduce to

$$\frac{\partial^2\hat{u}}{\partial\hat{x}^2} = 0, \tag{3.27a}$$

$$\bar{\kappa}\frac{\partial\hat{\alpha}}{\partial\hat{t}} = (1-\hat{\alpha})\exp\left(-\frac{1}{\varepsilon\hat{u}}\right). \tag{3.27b}$$

Here (3.27a) gives, on matching with (3.25),

$$\hat{u} = \hat{a}(\hat{t}) + \hat{x}\beta(\hat{t}), \tag{3.28}$$

with $\hat{a} = \hat{B}$ independently of $\hat{t}$ due to the wall condition. The balance in (3.27b) which is akin to those operating in (3.18) - (3.24) is associated with a critical size of ε being

$$\varepsilon = -G/(\ln\bar{\kappa}), \tag{3.29}$$

with G being an $\mathscr{O}(1)$ positive constant and a critical temperature being reached at which

$$\hat{u} = G^{-1} + \varepsilon u_1 + \dots \tag{3.30}$$

where (3.27b) becomes at leading order

$$\frac{\partial\hat{\alpha}}{\partial\hat{t}} = (1-\hat{\alpha})\exp(G^2 u_1(\hat{x},\hat{t})). \tag{3.31}$$

The form (3.31) containing $\mathscr{O}(1)$ quantities ensures, when combined with (3.28),(3.30), that $\hat{\alpha}$ tends to unity as time increases over the present scale.

3.3 Comparisons

The asymptotic description in the previous two subsections appears to capture all the major trends of the full solutions as κ or $\bar{\kappa}$ is decreased and hence the major trends for the realistic case also in which κ and $\bar{\kappa}$ are extremely small. The main quantitative comparisons are shown by means of the arrows displayed in figure 3.4(e) as well as the round markers in figure 3.1, for the same case. To clarify, the arrows in figure 3.4(e), which indicate the maximum temperature value reached and the time taken for the temperature to attain the average of its maximum and its initial value, tend to confirm the agreement seen in figure 3.1. See also the comparisons presented in figure 3.3. Overall the analysis is seen to 'work' for values of $\bar{\kappa}$ below about 0.01 say and hence for the extremely small $\bar{\kappa}$ values of the realistic setting.

Further it is notable that the maximum temperature attained can be predicted in analytical form very readily from the core responses: the maximum is

$$\bar{u}_{max} = \bar{\Omega} + \bar{C} \tag{3.32}$$

in non-dimensional terms. This is because of the result (3.4) in the core when α_c tends to unity at the completion of the reaction. In dimensional terms (3.32) yields

$$u_{c,max} = 3840°K \tag{3.33}$$

for the maximum, based on the parameters ($\bar{C}$, $\bar{\Omega}$, E/R) being (0.01, 0.15, 24000) as representative values from table 2.1. The predicted maximum temperature in (3.32), (3.33) is independent of the imposed wall temperatures and is of much potential interest.

3.4 Summary of chapter

Motivated by the insights gained from chapter 2, in this chapter we considered an alternative approach to the numerical one presented in chapter 2 to solve the system. A treatment by direct numerical simulation of the fully coupled system involved has been complemented by a treatment founded on asymptotic analysis, with the predictions from the two approaches being found to agree closely in quantitative terms.

We also examined here the effects of the main parameter which was identified, $\bar{\kappa}$, as well as other parameters of interest, namely; $\bar{\Omega}, \bar{C}, \bar{B}$.

Finally, we note that under this framework, the long-term behaviour of $\bar{u}$ is observed on a different (longer) time scale than the reaction rate α.

Chapter 4

Computational properties for three reactants

A multi-kinetic reaction process is now introduced into the model to provide an improved representation of the physical and chemical processes that may occur in practice. See [2] for further detail of the model. Following the work of [1], [6] for example we consider here a three–step reaction to model better the endothermic and exothermic chemical processes.

It is widely accepted within the literature that the chemical process can be described by following three processes which dictate the time to detonation. These are given by equations (4.1)–(4.4) below and can be described as follows

$$A\ to B\ to 2C \rightarrow D.$$

Here A is the explosive product and the process $A \rightarrow B$ is described by equation (4.2) which captures the endothermic state of the reaction process. Similarly $B \rightarrow 2C$ represents the slightly exothermic state of the reaction and is modelled by equation (4.3). Finally $2C \rightarrow D$ represents the exothermic process within the reaction, given by equation (4.4) where the squared term is a result of the $2C$ which represents two products being created in the reaction process. D is the final product, given by equation (4.5).

The diffusion process with a three-step reaction present is described by

$$\begin{aligned}\rho c_v \frac{\partial u}{\partial t} &= \kappa \frac{\partial^2 u}{\partial x^2} \\ &+ N_A Q_1 Z_1 \exp\Big(-\frac{E_1}{Ru}\Big) + N_B Q_2 Z_2 \exp\Big(-\frac{E_2}{Ru}\Big) + N_C^2 Q_3 Z_3 \exp\Big(-\frac{E_3}{Ru}\Big). \qquad (4.1)\end{aligned}$$

Coupled with (4.1) are the following ODEs governing the rates of change of the reactions N_A, N_B, N_C respectively,

$$\dot{N_A} = -\frac{N_A Z_1}{\rho} \exp\Big(-\frac{E_1}{Ru}\Big), \qquad (4.2)$$

$$\dot{N_B} = \frac{N_A Z_1}{\rho} \exp\Big(-\frac{E_1}{Ru}\Big) - \frac{N_B Z_2}{\rho} \exp\Big(-\frac{E_2}{Ru}\Big), \qquad (4.3)$$

$$\dot{N_C} = \frac{N_B Z_2}{\rho} \exp\Big(-\frac{E_2}{Ru}\Big) - \frac{N_C^2 Z_3}{\rho} \exp\Big(-\frac{E_3}{Ru}\Big), \qquad (4.4)$$

and

$$N_A + N_B + N_C + N_D = 1. \qquad (4.5)$$

Here the dots denote derivatives with respect to time. The constants Q_1–Q_3 in the reactant equations stand for the heats of reaction whereas E_1–E_3 are the corresponding activation energy constants of the reactions and Z_1–Z_3 are the corresponding pre-exponential constants. Table 4.1 presents a list of realistic values for the parameters here.

The boundary and initial conditions for $u(x,t)$ are set as in (2.4a), while the initial conditions on the reactants are

$$(N_A, N_B, N_C) = (1, 0, 0) \quad at \quad t = 0. \qquad (4.6)$$

That leaves our task then as solving (4.1)-(4.4) subject to (2.4a), (4.6). No boundary conditions need to be set on the reactant quantities because of the absence of spatial derivatives in the balances (4.2)-(4.4). The value of N_A at the boundary where $u = u_A$

can be obtained directly from integration of (4.2) and application of (4.6) as

$$N_A = \exp\left(-\frac{Z_1}{\rho} \frac{t}{\exp\left(\frac{E_1}{Ru_A}\right)} \right). \tag{4.7}$$

Hence N_B is given by solving (4.3) combined with (4.7) to yield

$$N_B = \frac{A\exp\left(-A\frac{t}{\exp(C)} + D\right)}{B\exp(C) - A\exp(D)} - \frac{A\exp(D)}{B\exp(C) - A\exp(D)} \exp\left(-B\frac{t}{\exp(D)}\right), \tag{4.8}$$

where $A = \frac{Z_1}{\rho}$, $B = \frac{Z_2}{\rho}$, $C = \frac{E_1}{Ru_A}$ and $D = \frac{E_2}{Ru_A}$. This is shown graphically in figure 4.1, while N_C then stems from (4.4) with (4.7), (4.8), giving the numerical solution presented in figure 4.2. These two figures are for the relatively mild parameter values shown in table 4.2 together with the boundary condition $u_A = 45$ which again is comparatively mild.

The computational approach of chapter 2 was extended and adapted for the present task. Second-order accuracy in time and space and appropriate lagging were notable features again. Results are plotted in figure 4.3. More realistic cases will be re-addressed in section 11 after the discussion of analytical properties in the following section.

Table 4.1: Additional parameters used in ODTX model for HMX explosive assuming multi-step kinetics as in [1], converted into SI units.

Parameter with units	Symbol	Value
Heat of first reaction (J/kg)	Q_1	$-4.2e5$
Heat of second reaction (J/kg)	Q_2	$1.26e6$
Heat of third reaction (J/kg)	Q_3	$5.04e6$
Activation Energy of first reaction (J/mol)	E_1	$2.21e5$
Activation Energy of second reaction (J/mol)	E_2	$1.85e5$
Activation Energy of third reaction (J/mol)	E_3	$1.43e5$
First Pre-exponential Constant (kg m^{-3} s^{-1})	Z_1	$1.4e24$
Second Pre-exponential Constant (kg m^{-3} s^{-1})	Z_2	$1.9e19$
Third Pre-exponential Constant (kg m^{-3} s^{-1})	Z_3	$1.5e15$

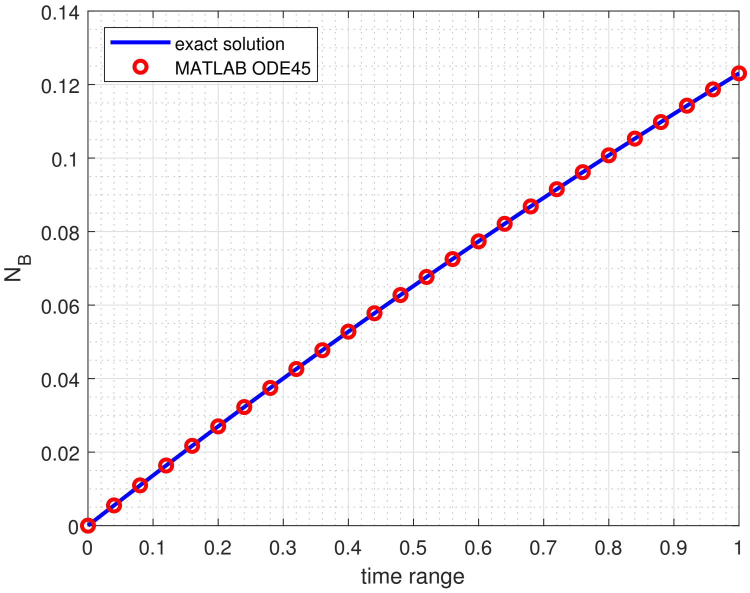

Figure 4.1: The numerical approximation (using `ODE45` in MATLAB) compared with the analytical solution of Equation (4.3)

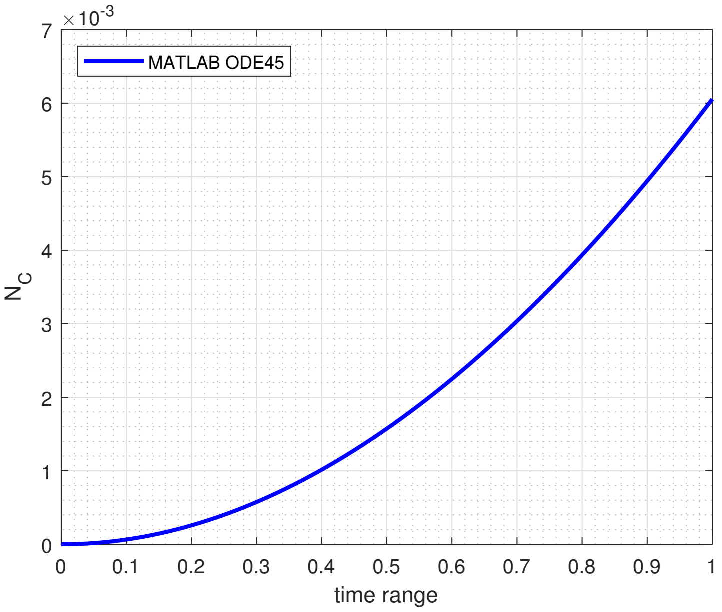

Figure 4.2: The numerical approximation (using `ODE45` in MATLAB) of Equation (4.4)

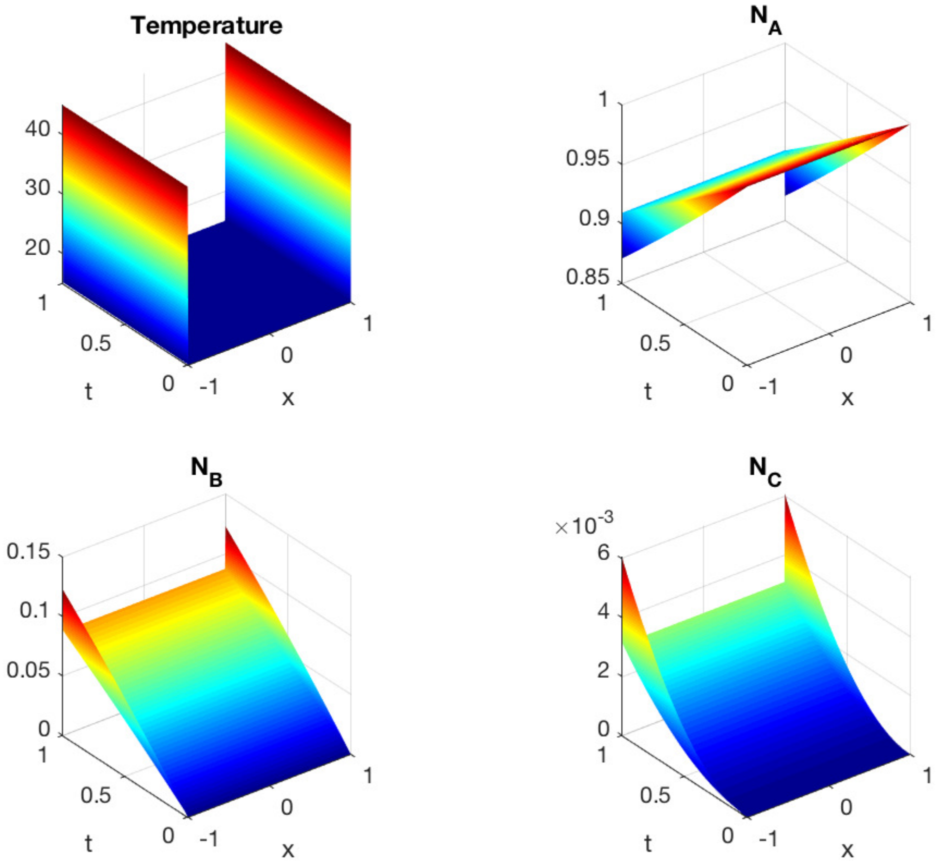

Figure 4.3: The numerical solutions u, N_A, N_B and N_C satisfying (4.1)–(4.4), using a second–order numerical scheme, with the relatively mild parameters supplied in table 4.2.

Table 4.2: Mild parameters used in analysis of chapter 4, 4.1.

Parameter with units	**Symbol**	**Value**
Heat of first reaction (J/kg)	Q_1	-10
Heat of second reaction (J/kg)	Q_2	20
Heat of third reaction (J/kg)	Q_3	30
Activation Energy of first reaction (J/mol)	E_1	70
Activation Energy of second reaction (J/mol)	E_2	60
Activation Energy of third reaction (J/mol)	E_3	50
First Pre-exponential Constant (kg m^{-3} s^{-1})	Z_1	300
Second Pre-exponential Constant (kg m^{-3} s^{-1})	Z_2	200
Third Pre-exponential Constant (kg m^{-3} s^{-1})	Z_3	100
Pre-exponential Constant (s^{-1})	A	200

4.1 Analytical solutions and comparisons for three reactants

Turning to asymptotic analysis for the multi-kinetics interactions we observe that in effect Q_n, Z_n terms here replace the $\rho\Omega$ and A terms in the one reactant case in chapter 2 and the N's here correspond to the reactant α in the single reactant case. We use the same scalings as before in chapter 3, that is we set $t = A^{-1}\bar{t}$ and $u = \frac{E}{R}\bar{u}$ and expand the solution. In addition, to account for the new parameters $Z_n = A\bar{Z}_n\rho$ and $E_n = E\bar{E}_n$, we choose E_2 as a representative value of E to try to ensure $\bar{Z}_n \sim \mathscr{O}(1)$, $\bar{E}_n \sim \mathscr{O}(1)$, $N_n \sim \mathscr{O}(1)$ and $x \sim \mathscr{O}(1)$ to begin. We have again used mild values of E_n, Z_n and A in the first instance, see table 4.2 for exact values. With the scalings above, the controlling equations become

$$\frac{\partial \bar{u}}{\partial \bar{t}} = \bar{\kappa}\frac{\partial^2 \bar{u}}{\partial x^2} + N_A\bar{\Omega}_1 \exp\Big(-\frac{\bar{E}_1}{\bar{u}}\Big) + N_B\bar{\Omega}_2 \exp\Big(-\frac{\bar{E}_2}{\bar{u}}\Big) + N_C^2\bar{\Omega}_3 \exp\Big(-\frac{\bar{E}_3}{\bar{u}}\Big), \tag{4.9}$$

$$\frac{dN_A}{d\bar{t}} = -N_A\bar{Z}_1 \exp\Big(-\frac{\bar{E}_1}{\bar{u}}\Big), \tag{4.10}$$

$$\frac{dN_B}{d\bar{t}} = N_A\bar{Z}_1 \exp\Big(-\frac{\bar{E}_1}{\bar{u}}\Big) - N_B\bar{Z}_2 \exp\Big(-\frac{\bar{E}_2}{\bar{u}}\Big), \tag{4.11}$$

$$\frac{dN_C}{d\bar{t}} = N_B\bar{Z}_2 \exp\Big(-\frac{\bar{E}_2}{\bar{u}}\Big) - N_C^2\bar{Z}_3 \exp\Big(-\frac{\bar{E}_3}{\bar{u}}\Big), \tag{4.12}$$

where $\bar{\kappa} = \frac{\kappa}{\rho c_v A}$ which when using the full parameter values gives us $\bar{\kappa} \approx 3.8863e-27$ and $\bar{\Omega}_n = Q_n\bar{Z}_n\left(\frac{R}{c_v E_2}\right)$, for $n = 1,2,3$. When using relatively mild parameter values we have instead $A = 200$, $\bar{\kappa} = 9.7388^{-10}$. Thus $\bar{\kappa}$ is the most extreme parameter in both cases, using the full parameter values and milder values. Hence we base our asymptotic analysis on $\bar{\kappa} << 1$ as before in chapter 3. We proceed by again separating the problem into a core and wall layers with equations describing the behaviour in each.

The core problem is reduced for small $\bar{\kappa}$ to equation (4.9) with a negligible $\frac{\partial^2 \bar{u}}{\partial x^2}$ term, as before in chapter 3. Hence, it follows that the quasi-ODE

$$\frac{d\bar{u}}{d\bar{t}} = N_A\bar{\Omega}_1 \exp\Big(-\frac{\bar{E}_1}{\bar{u}}\Big) + N_B\bar{\Omega}_2 \exp\Big(-\frac{\bar{E}_2}{\bar{u}}\Big) + N_C^2\bar{\Omega}_3 \exp\Big(-\frac{\bar{E}_3}{\bar{u}}\Big), \tag{4.13}$$

holds in the core, and we have the following ODEs for the reactants N_A, N_B and N_C,

$$\frac{dN_A}{d\bar{t}} = -N_A\bar{Z}_1 \exp\Big(-\frac{\bar{E}_1}{\bar{u}}\Big), \tag{4.14}$$

$$\frac{dN_B}{d\bar{t}} = N_A\bar{Z}_1 \exp\Big(-\frac{\bar{E}_1}{\bar{u}}\Big) - N_B\bar{Z}_2 \exp\Big(-\frac{\bar{E}_2}{\bar{u}}\Big), \tag{4.15}$$

$$\frac{dN_C}{d\bar{t}} = N_B\bar{Z}_2 \exp\Big(-\frac{\bar{E}_2}{\bar{u}}\Big) - N_C^2\bar{Z}_3 \exp\Big(-\frac{\bar{E}_3}{\bar{u}}\Big). \tag{4.16}$$

Equations (4.13)-(4.16) can readily be solved numerically subject to the following initial conditions at $\bar{t} = 0$,

$$N_A(x,0) = 1, \tag{4.17a}$$

$$N_B(x,0) = N_C(x,0) = 0, \tag{4.17b}$$

$$\bar{u}(x,0) = \bar{C}, \quad \bar{C} = \frac{RC}{E_2} \qquad \text{for } x \in D. \tag{4.17c}$$

In figure 4.4, the ODEs (4.13)-(4.16) have been solved using the relatively mild parameter values in table 4.1.

In the wall layers the same scaling as that in chapter 3 applies, so that $x = -1 + \bar{\kappa}^{1/2}\bar{x}$ at the left-hand wall and similarly at the right-hand wall. This reduces equation (4.9) to the form

$$\frac{\partial \bar{u}}{\partial \bar{t}} = \frac{\partial^2 \bar{u}}{\partial x^2} + N_A\bar{\Omega}_1 \exp\Big(-\frac{\bar{E}_1}{\bar{u}}\Big) + N_B\bar{\Omega}_2 \exp\Big(-\frac{\bar{E}_2}{\bar{u}}\Big) + N_C^2\bar{\Omega}_3 \exp\Big(-\frac{\bar{E}_3}{\bar{u}}\Big), \tag{4.18}$$

independently of $\bar{\kappa}$. To solve the reduced system comprising (4.18) with (4.10)-(4.12) computationally we developed a finite difference scheme based closely on those of chapters 2–4. Results for the wall layer are presented in figure 4.5 where we have used the relatively mild parameter values of table 4.2.

Comparisons given in figure 4.6 between the above asymptotic solution and the full numerical solution tend to indicate fair agreement for the milder parameter range of Table 4.2. These comparisons also indicate significant computational savings using the asymptotic approach.

Further analysis of the core proves to be helpful. Thus (4.13)-(4.16) imply that

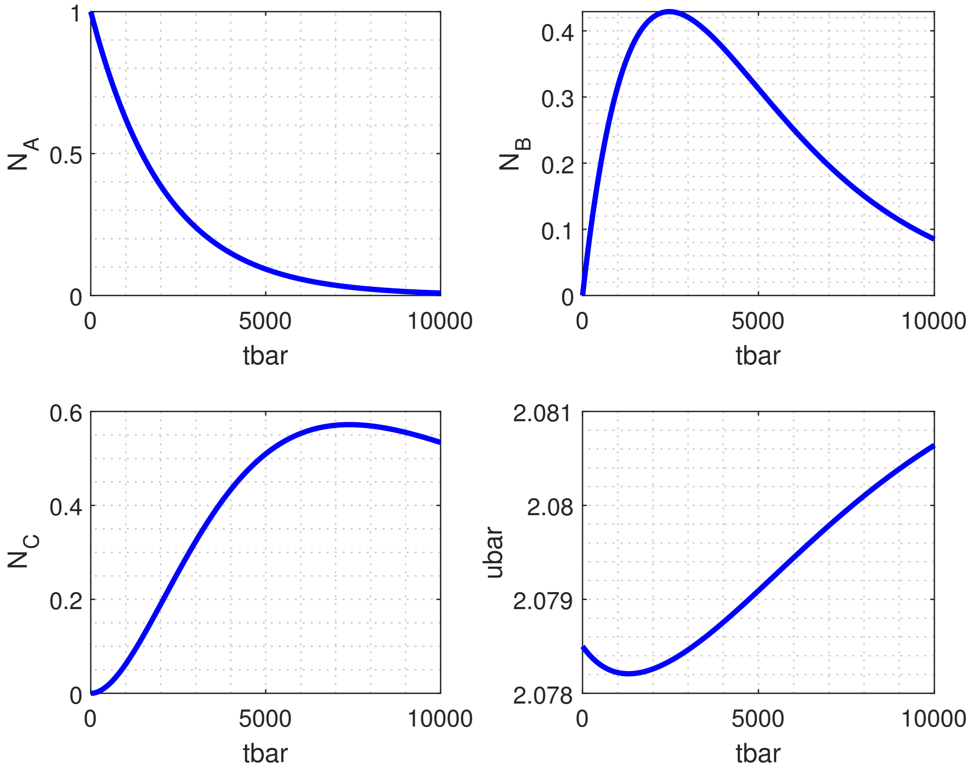

Figure 4.4: The numerical solutions (using `ODE45` in MATLAB) to $\bar{u}$, N_A, N_B and N_C satisfying Equations (4.13)-(4.16) in the core with relatively mild parameter values supplied in Table 4.2.

a certain non–trivial linear combination of the left–hand sides sums to zero and so on integration $\bar{u}$ can be expressed in terms of the reactions in the form

$$\bar{u} = a_1(1 - N_A) - a_2 N_B - a_3 N_C + \bar{C}. \tag{4.19}$$

Here the initial conditions in (4.17), which include $\bar{C}$, determine the constant of integration and the constant coefficients are given by

$$a_n = \sum_{(n,3)} \frac{\bar{\Omega}_n}{\bar{Z}_n} \tag{4.20}$$

for $n = 1,2,3$. We are left with four equations (4.14)-(4.16), (4.19) for N_A, N_B, N_C, $\bar{u}$. Sample solutions of this nonlinear system presented in figure 4.7 show (N_A, N_B, N_C) starting as $(1,0,0)$ in line with (4.17) and eventually tending to $(0,0,0)$ at suf-

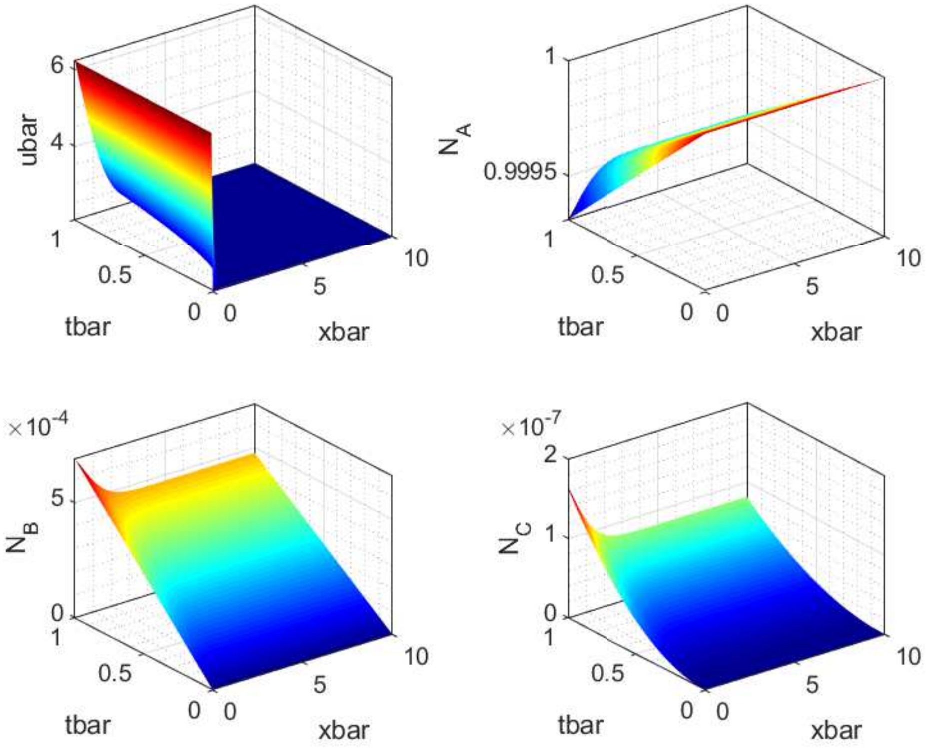

Figure 4.5: The wall solutions $\bar{u}$, N_A, N_B and N_C satisfying (4.18), with the mild parameters supplied in Table 4.2. Note that the $\bar{x}$ range has been truncated to facilitate a numerical implementation.

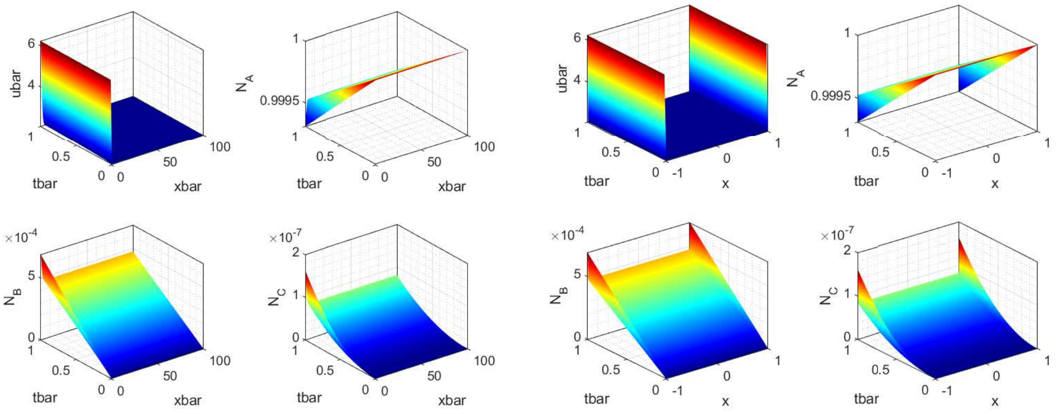

(a) Wall layer solution with mild parameters

(b) Full numerical solution with mild parameters

Figure 4.6: Finite difference solutions to the full non–asymptotic problem shown (right) and the asymptotic wall problem (left) using the mild parameters in table 4.2. For the non–asymptotic problem we set $\bar{T}_{\max} = 1$. In order to compare the solutions directly we multiply the non asymptotic u by $\frac{R}{E}$.

ficiently large times, with $\bar{u}$ increasing monotonically along with other interesting behaviour during the evolution.

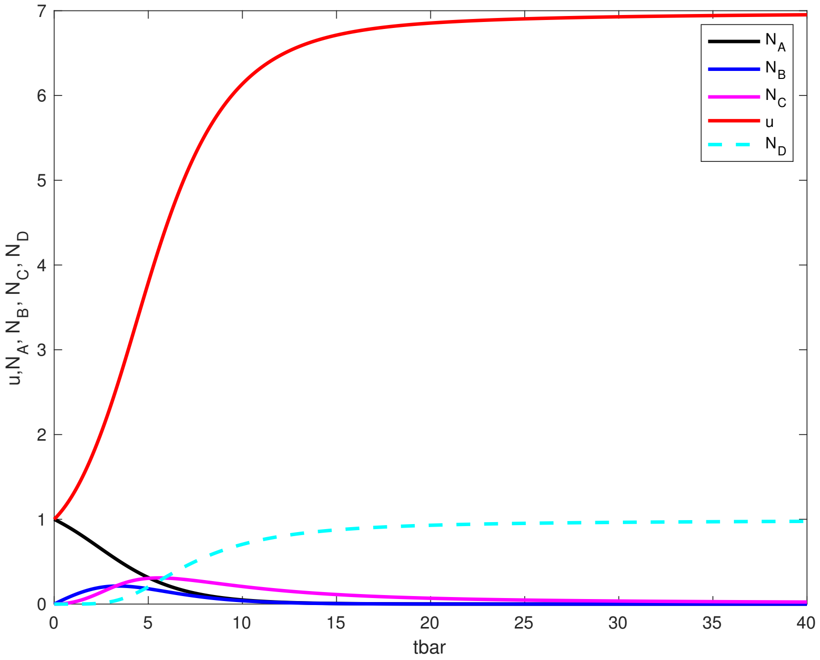

Figure 4.7: The numerical approximation to Equations (4.5), (4.14)-(4.16), (4.19). Here the values $\bar{D} = 1$, $dt = 0.005$, $\bar{\Omega}_1 = 1$, $\bar{\Omega}_2 = 2$, $\bar{\Omega}_3 = 3$, $\bar{Z}_1 = 0.5$, $\bar{Z}_2 = 1$, $\bar{Z}_3 = 1.5$, $\bar{E}_1 = 1.5$, $\bar{E}_2 = 1$, and $\bar{E}_3 = 0.5$ have been used.

A phase-plane view is also useful here. It follows from treating N_B, N_C as functions of N_A by virtue of eliminating $\bar{t}$ explicitly from (4.14)-(4.16) through division to yield the two equations

$$\frac{dN_B}{dN_A} = -1 + \bar{Z}_{21} N_B N_A^{-1} \exp\left(\frac{\bar{E}_{12}}{\bar{u}}\right), \tag{4.21}$$

$$\frac{dN_C}{dN_A} = -\bar{Z}_{21} N_B N_A^{-1} \exp\left(\frac{\bar{E}_{12}}{\bar{u}}\right) + \bar{Z}_{31} N_C^2 N_A^{-1} \exp\left(\frac{\bar{E}_{13}}{\bar{u}}\right), \tag{4.22}$$

with constants $\bar{Z}_{21} = \bar{Z}_2/\bar{Z}_1$, $\bar{Z}_{31} = \bar{Z}_3/\bar{Z}_1$, $\bar{E}_{12} = \bar{E}_1 - \bar{E}_2$, $\bar{E}_{13} = \bar{E}_1 - \bar{E}_3$. The system is uncoupled in the sense that (4.21) together with (4.19) acts to determine N_B and then (4.22) with (4.19) determines N_C in principle. The value of N_A is taken to start at unity and decrease monotonically to zero. Solutions of (4.21), (4.22) with (4.19) are displayed in figure 4.8 as $N_B(N_A)$, $N_C(N_A)$, $\bar{u}(N_A)$ plots and in figure 4.9 in the

$N_B - N_C$ plane. Subsequently from these solutions $\bar{u}$ can be found from (4.19) and the time-dependence can be found by addressing (4.14) as an equation for $\bar{t}$ as a function of N_A.

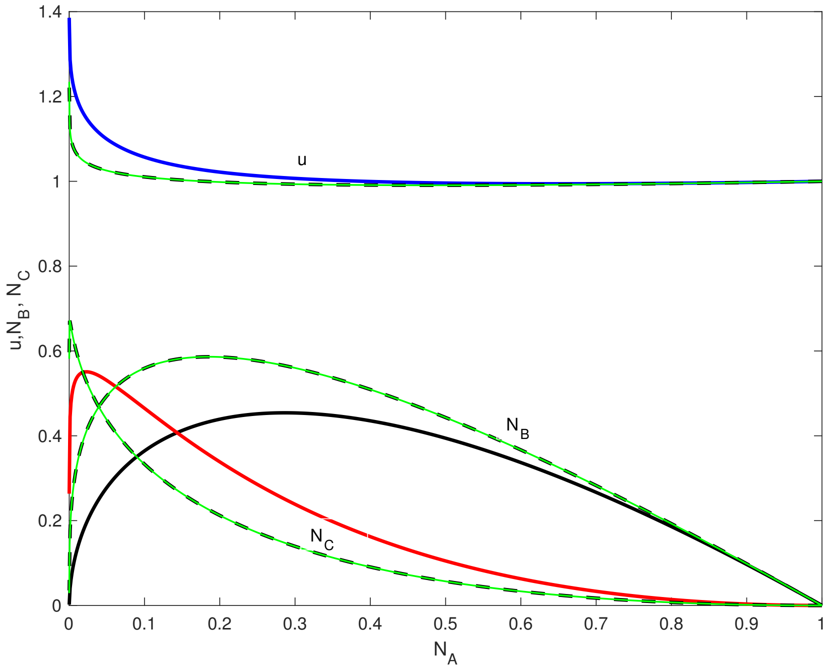

Figure 4.8: The numerical approximation to Equations (4.19), (4.21), (4.22) for two cases; case 1 is where $\bar{Z}_{21} = 0.4$ and $\bar{Z}_{31} = 0.16$ displayed by the solid lines (blue, red and black) and case 2 is where $\bar{Z}_{21} = 0.2$ and $\bar{Z}_{31} = 0.04$ displayed by the green lines. In both cases $\bar{D} = 1$, $\bar{E}_{12} = 0.46$, $\bar{E}_{13} = 1$, $a_1 = 0.5$, $a_2 = 0.53$ $a_3 = 0.43$ and $dN_A = 0.000005$. The dashed lines represent an accuracy check where the effective numerical step dN_A is halved.

There are seven independent parameters in the phase plane of (4.21), (4.22), namely

$$(a_1, a_2, a_3, \bar{C}, \bar{E}_{12}, \bar{Z}_{21}, \bar{Z}_{31})/(\bar{E}_{13}), \tag{4.23}$$

or combinations thereof, and in the numerical work leading to the above figures we took those parameters to be very mild in value. The alternative of singling out $\bar{E}_{12}$ instead of $\bar{E}_{13}$ would also cover the entire parameter space at issue but in a different way and with equivalent results. We set $\bar{E}_{13}$ equal to unity in the numerical study without loss of generality because here only the ratios of coefficients matter. By

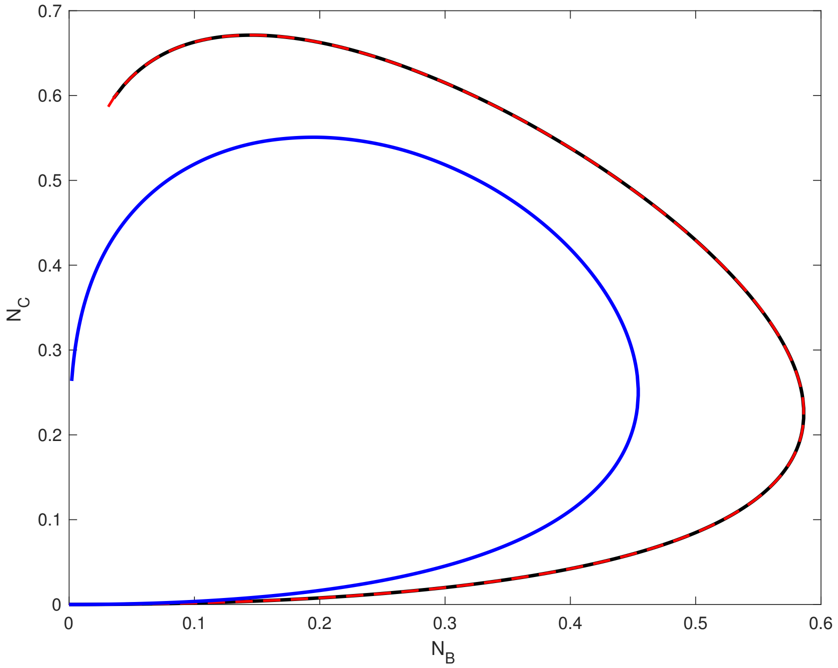

Figure 4.9: The numerical approximation to Equations (4.19), (4.21), (4.22) for two cases; case 1 is where $\bar{Z}_{21} = 0.4$ and $\bar{Z}_{31} = 0.16$ represented by the solid blue line and case 2 is where $\bar{Z}_{21} = 0.2$ and $\bar{Z}_{31} = 0.04$ represented by the solid red line. In both cases $\bar{D} = 1$, $\bar{E}_{12} = 0.46$, $\bar{E}_{13} = 1$, $a_1 = 0.5$, $a_2 = 0.53$ $a_3 = 0.43$ and $dN_A = 0.000005$. Here the dashed black line demonstrates an accuracy check where dN_A has been halved.

contrast, typical numerical values of the parameters for the realistic case mentioned earlier turn out to be

$$(0.498, 0.533, 0.427, 1, 0.462, 1.36e-5, 1.070e-9), \tag{4.24}$$

approximately. The small values of $\bar{Z}_{21}$, $\bar{Z}_{31}$ here suggest consideration of an asymptotic analysis, guided by the insight provided in the single reactant case of chapter 3. Taking $\varepsilon = \bar{Z}_{21}$ as small and $\bar{Z}_{31}$ as of order ε^2 we find that there are at least three distinct parts of the N_A range to discuss for (4.21), (4.22). For the majority of the range where N_A is of order unity the solution expands as

$$N_B = N_{B0} + \varepsilon N_{B1} + \ldots, \tag{4.25}$$

$$N_C = \varepsilon N_{C1} + \ldots, \tag{4.26}$$

$$\bar{u} = \bar{u}_0 + \varepsilon \bar{u}_1 + \ldots, \tag{4.27}$$

where $\bar{u}_0 = (1-N_A)(a_1-a_2)+\bar{C}$. Substitution into (4.19), (4.21), (4.22) gives successively

$$N_{B0} = 1 - N_A, \tag{4.28}$$

$$\frac{dN_{B1}}{dN_A} = (1-N_A)N_A^{-1}\exp\left(\frac{\bar{E}_{12}}{(a_1-a_2)(1-N_A)+\bar{C}}\right), \tag{4.29}$$

$$\frac{dN_{C1}}{dN_A} = -\frac{dN_{B1}}{dN_A}, \tag{4.30}$$

$$\bar{u}_1 = -a_2 N_{B1} - a_3 N_{C1}. \tag{4.31}$$

The numerical value of $\bar{u}_0$ at $N_A = 0.5$ is 0.985, which is suitably close to the computational finding in figure 4.8. The trends of (4.28)-(4.30) are similarly close to those in the figure; for example the perturbation in N_B about the straight line (4.28) is nearly equal and opposite to the curve of N_C indicated by (4.30). The next significant part of the range (apart from a benign region where N_A is of order ε) occurs when N_A is exponentially small such that

$$N_A = \exp\left(\frac{-r}{\varepsilon}\right) \quad \text{with } N_B \text{ of } \mathscr{O}(1). \tag{4.32}$$

Here the variable r is typically $\mathscr{O}(1)$. Integration of (4.21) and matching to (4.25) with (4.28) at small r, gives us the solution

$$N_B = \exp(-c_1 r), \tag{4.33}$$

at leading order, where $c_1 = \exp\left(\frac{\bar{E}_{12}}{a_1-a_2+\bar{C}}\right)$ is an $\mathscr{O}(1)$ constant. The N_B solution therefore tends to zero as N_A tends to zero over this scale (when r tends to infinity), in the form $N_A^{c_1\varepsilon}$, a form which agrees with the balance in (4.21). The corresponding N_C however is given by $1 - N_B$ and so tends to unity then. This leads to the final part of the N_A range in which N_A is even smaller, specifically

$$N_A = \exp\left(-\frac{s}{\varepsilon^2}\right) \quad \text{with } N_C \text{ of } \mathscr{O}(1). \tag{4.34}$$

Here we find that the leading–order solution matching to that of the previous part of the range at small s values is

$$N_C = \frac{c_5}{(s + c_5)}, \tag{4.35}$$

where $c_5 = \exp\left(-\frac{\bar{E}_{13}}{a_1 - a_2 + \bar{C}}\right)$ approximately is an $\mathscr{O}(1)$ positive constant. The N_C solution now tends to $0+$ as N_A tends to zero over this scale (when s tends to infinity), in the form $c_5/(-\varepsilon^2 \ln(N_A))$, a form which is in balance with (4.22). The slowness of the approach of N_C to zero here compared with that for N_B is notable. The trends in (4.32)-(4.35) are consistent with the computational results for N_B, N_C in figure 4.8 at small N_A values. The associated time dependence follows from inversion of (4.14); for instance the first part of the N_A range ends with

$$N_A \propto \exp\left(-\frac{\bar{Z}_1 \bar{t}}{c_6}\right) \quad \text{as } \bar{t} \to \infty, \tag{4.36}$$

with $c_6 = \exp\left(-\frac{\bar{E}_1}{a_1 - a_2 + \bar{C}}\right)$ being a known $\mathscr{O}(1)$ positive constant.

The analytical trends above are consistent with the full computational properties. In addition the result (4.19) implies that the maximum of $\bar{u}$ is $a_1 + \bar{C}$; in dimensional terms this gives for representative realistic conditions

$$\bar{u}_{c,max} = 4685 \text{ degrees } K, \tag{4.37}$$

which again is of potential interest.

4.2 Summary of chapter

In this chapter the model presented in chapter 2 was extended to include three step reactions and again the combination of simulation and asymptotic analysis, presented in chapter 3, was applied, yielding close agreement between results from the full reaction-diffusion problem and those from the asymptotic problem using a mild set of parameters. This concludes the part of the thesis containing work on the reaction-diffusion problem with a focus on heat flow. The next part of the thesis considers the effects of gas produced on the system.

Part II

Gas Treatment

Chapter 5

Gas Treatment

The treatment of gas effects generated in the present explosive context forms an important part of our future work. The current purely thermal analytical models in use at AWE and elsewhere do not account for the treatment of gas produced; once gas has been formed it is neglected. In a physically realistic case on the other hand, the hot gas which is produced by the reaction drives the temperature. The current work sets out to incorporate the treatment of gas which is produced into our model. Some of the detailed modelling and analysis required to account for gas produced has been done below. We show some preliminary results in this chapter and in later chapters. First we consider a simple discrete model of gas flow and thermal gas-solid interactions, then extend to a continuous model. We also consider the combustion case in later sections.

Here we use discrete physical reasoning with the aim of constructing a basic model. Consider two gases occupying the two regions above in figure 5.1, one gas in each compartment. The line separating the gases is treated as an infinitely thin membrane which prevents mixing or interaction of the two gases from taking place. Here $P_{1,0}$ denotes the initial pressure, $V_{1,0}$ denotes the initial volume occupied by the gas, and $T_{1,0}$ denotes the initial temperature. The first subscript refers to gas 1 or gas 2 and the second subscript refers to the initial time, $t = 0$. We assume that the pressure $P_{1,0} > P_{2,0}$. The mass of the first gas is defined by $M_1 = \rho_{1,0}V_{1,0}$, where ρ represents the density, and the mass of the second gas is defined by $M_2 = \rho_{2,0}V_{2,0}$.

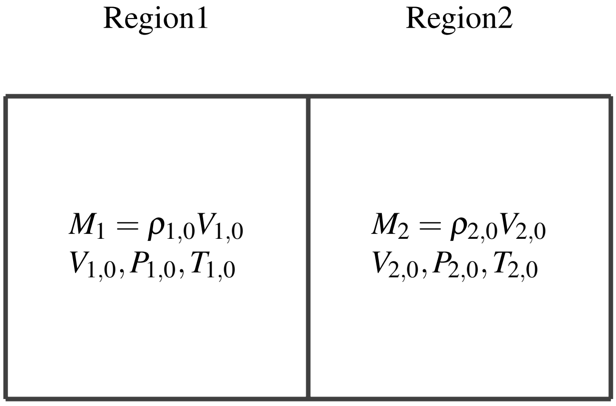

Figure 5.1: Gases occupying two regions separated by an interface. Here region 1 represents gas which already exists at time t and region 2 represents newly created gas.

After some time, the interface is removed and the gas mixes uniformly. This results in M_1 spreading slightly and M_2 compressing slightly, since $P_{1,0} > P_{2,0}$. This distributes the pressure and temperature such that $P_{1,1} = P_{2,1}$ and $T_{1,1} = T_{2,1}$, but $V_{1,1} > V_{2,1}$ as the volumes become unequal in general.

Since the total volume of gas is preserved however, we have

$$V_{1,0} + V_{2,0} = V_{1,1} + V_{2,1}, \tag{5.1}$$

i.e. the total volume of gas at the initial stage (first stage) in figure 5.1 is equal to the total volume of gas in the next stage (second stage); the total volume does not change.

We use the ideal gas equation next, describing the behaviour of a gas under certain conditions, to model the gas motion in each volume in the first instance. Thus

$$PV = nRT,$$

where P is the pressure, V is the volume, R is the universal gas constant, T is the temperature and n, the number of moles of gas is given by $n = \frac{\text{mass}}{\text{molecular weight}}$ or equivalently $n = \frac{\text{M}}{M_w}$. In the schematic 5.1 above, the ideal gas law describing the gas, occupying the first region can be written as

$$P_{1,0}V_{1,0} = n_1RT_{1,0}, \tag{5.2}$$

where $n_1 = \frac{M_1}{M_{w_1}}$ in the initial stage. Similarly the state of the second gas, also depicted in figure 5.1, can be described by

$$P_{2,0}V_{2,0} = n_2RT_{2,0}, \tag{5.3}$$

where $n_2 = \frac{M_2}{M_{w_2}}$.

In the second stage, we have one pressure P and one temperature T for both gases and the constant R remains the same. Hence we have

$$PV_{1,1} = n_1RT, \tag{5.4}$$

$$PV_{2,1} = n_2RT \tag{5.5}$$

for the first and second gas respectively. We may assume, for now, that $n_1 = n_2$ and therefore following from equations (5.2)-(5.3) we have

$$\frac{PV_{1,1}}{T} = \frac{P_{1,0}V_{1,0}}{T_{1,0}}, \tag{5.6}$$

$$\frac{PV_{2,1}}{T} = \frac{P_{2,0}V_{2,0}}{T_{2,0}} \tag{5.7}$$

for the first and second gas respectively. We make the assumption that the amount of heat in the box confining the gases in figure 5.1 is preserved. Assuming the specific heat, c_i, remains constant, the heat generated by the first gas is described by $c_1M_1(T - T_{1,0})$, where c_1 is the specific heat of the first gas and $(T - T_{1,0})$ is the rise in temperature. Similarly the heat generated by the second gas is described by $c_2M_2(T - T_{2,0})$. Assuming there is no heat added, the total heat generated is zero, giving

$$c_1M_1(T - T_{1,0}) + c_2M_2(T - T_{2,0}) = 0. \tag{5.8}$$

We now have six equations, (5.1)-(5.5) and (5.8), for the six unknowns; $V_{1,1}$, $V_{2,1}$,P,

T, $P_{1,0}$ and $P_{2,0}$. We can determine $P_{1,0}$ and $P_{2,0}$ by rearranging equations (5.2) and (5.3) respectively such that

$$P_{1,0} = \frac{n_1 R T_{1,0}}{V_{1,0}}, \tag{5.9}$$

$$P_{2,0} = \frac{n_2 R T_{2,0}}{V_{2,0}}. \tag{5.10}$$

From equations (5.4) and (5.5) we have

$$n_1 R = \frac{P V_{1,1}}{T}, \quad \text{and} \quad n_2 R = \frac{P V_{2,1}}{T}. \tag{5.11}$$

We can write $R(n_{1,0} + n_{2,0}) = \frac{PV_{1,1}}{T} + \frac{PV_{2,1}}{T}$; making use also of equation (5.1) this can be written as

$$\frac{P}{T} = \frac{R(n_1 + n_2)}{(V_{1,0} + V_{2,0})}. \tag{5.12}$$

From equation (5.8) we obtain the temperature solution

$$T = \frac{c_1 M_1 T_{1,0} + c_2 M_2 T_{2,0}}{(c_1 M_1 + c_2 M_2)}. \tag{5.13}$$

Clearly this solution is a weighted average, the weighting being the heat capacity. By substituting (5.13) into equation (5.12), we get an expression for the pressure P given by

$$P = \frac{R(n_1 + n_2)(c_1 M_1 T_{1,0} + c_2 M_2 T_{2,0})}{(V_{1,0} + V_{2,0})(c_1 M_1 + c_2 M_2)}. \tag{5.14}$$

The volumes $V_{1,1}$ and $V_{2,1}$ follow as

$$V_{1,1} = \frac{n_1 R T}{P} = \frac{n_1 (V_{1,0} + V_{2,0})}{n_1 + n_2},$$
$$V_{2,1} = \frac{n_2 R T}{P} = \frac{n_2 (V_{1,0} + V_{2,0})}{n_1 + n_2},$$

from equations (5.11) and (5.12).

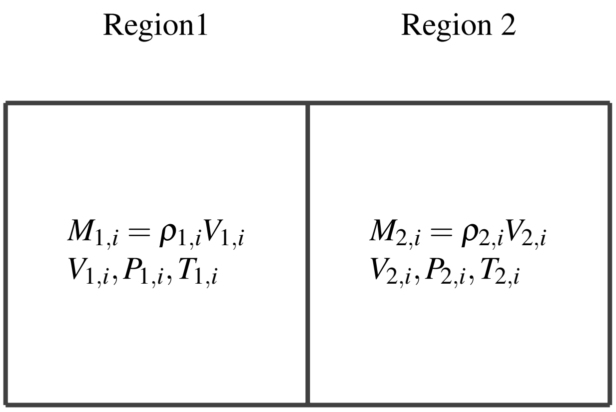

Figure 5.2: Gases occupying two regions separated by an interface at an initial stage i.

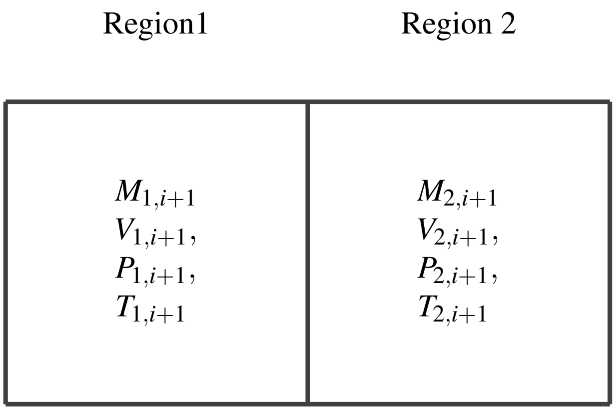

Figure 5.3: Gases occupying two regions separated by an interface at a stage $i+1$.

5.1 Discrete Model

The discrete scheme, derived in the discrete physical reasoning above, may be initialised using the initial conditions given in table 5.1.

We may update the quantities as follows:

$$M_{1,i} = \rho_1 A \left(\int_{-x_0}^{x_0} \frac{\partial \alpha}{\partial t} dx \right) \Delta t, \tag{5.15}$$

where Δt is small, α is the extent of reaction (see details in the earlier chapter 2), A is the specific surface area and x_0 is the boundary of the domain. Hence $V_{1,i} = M_{1,i}/\rho_1$. We may now update $T_{1,i}$ using the following expression for $T_{1,i} = T_{AV,i}$,

$$T_{AV,i} = \frac{\int_{-x_0}^{x_0} \frac{\partial \alpha}{\partial t} u(x,t) dx}{\int_{-x_0}^{x_0} \frac{\partial \alpha}{\partial t} dx},$$

Table 5.1: Initial conditions used in discrete scheme analysis. Values supplied by AWE.

Parameter	**Initial Value**
$V_{1,0}$	0.01×10^{-6}
$\rho_{1,0}$	1800
$M_{1,0}$	$1800 \times 0.01 \times 10^{-6}$
$T_{1,0}$	2000
$n_{1,0}$	34.2×10^{-3}
$P_{1,0}$	5.6868×10^{10}
$V_{2,0}$	0.1×10^{-6}
$\rho_{2,0}$	372
$M_{2,0}$	$0.2 \times 1860 \times 0.1 \times 10^{-6}$
$T_{2,0}$	600
$n_{2,0}$	34.2×10^{-3}
$P_{2,0}$	1.7060×10^{9}

where $u(x,t)$ is the temperature in the solid, and hence,

$$\begin{aligned} T_{2,i+1} &= \frac{c_1 M_{1,i} T_{AV,i} + c_2 M_{2,i} T_{2,i}}{c_1 M_{1,i} + c_2 m_{2,i}}, \\ &= \frac{M_{1,i} T_{AV,i} + M_{2,i} T_{2,i}}{M_{1,i} + M_{2,i}}, \end{aligned}$$

for $c_1 = c_2$. Thus we may update the quantities in our discrete scheme using the following relations:

$$M_{2,i+1} = M_{1,i} + M_{2,i}, \tag{5.16}$$

$$V_{2,i+1} = V_{1,i} + V_{2,i}, \tag{5.17}$$

$$n_{2,i+1} = n_{1,i} + n_{2,i}, \tag{5.18}$$

$$\rho_{2,i+1} = \frac{M_{2,i+1}}{V_{2,i+1}}, \tag{5.19}$$

$$T_{2,i+1} = \frac{M_{1,i} T_{AV,i} + M_{2,i} T_{2,i}}{M_{1,i} + M_{2,i}}, \tag{5.20}$$

$$P_{2,i+1} = \frac{n_{2,i+1} R T_{2,i+1}}{V_{2,i+1}}. \tag{5.21}$$

where $V_{1,i} = M_{1,i}/\rho_1$ and $M_{1,i}$ is given by equation (5.15).

Numerical solutions of the discrete system above are presented in figure 5.4, showing volume V_2, temperature T_G, mass M_2 and pressure P_2 versus time and temperature U and reaction fraction α versus x. The apparent near-saturation after rapid temporal evolution of the solutions is notable. The numerical solutions presented here are the gas quantities from region 2 of figure 5.2, where these quantities have been introduced by the reaction and have mixed with those from region 1.

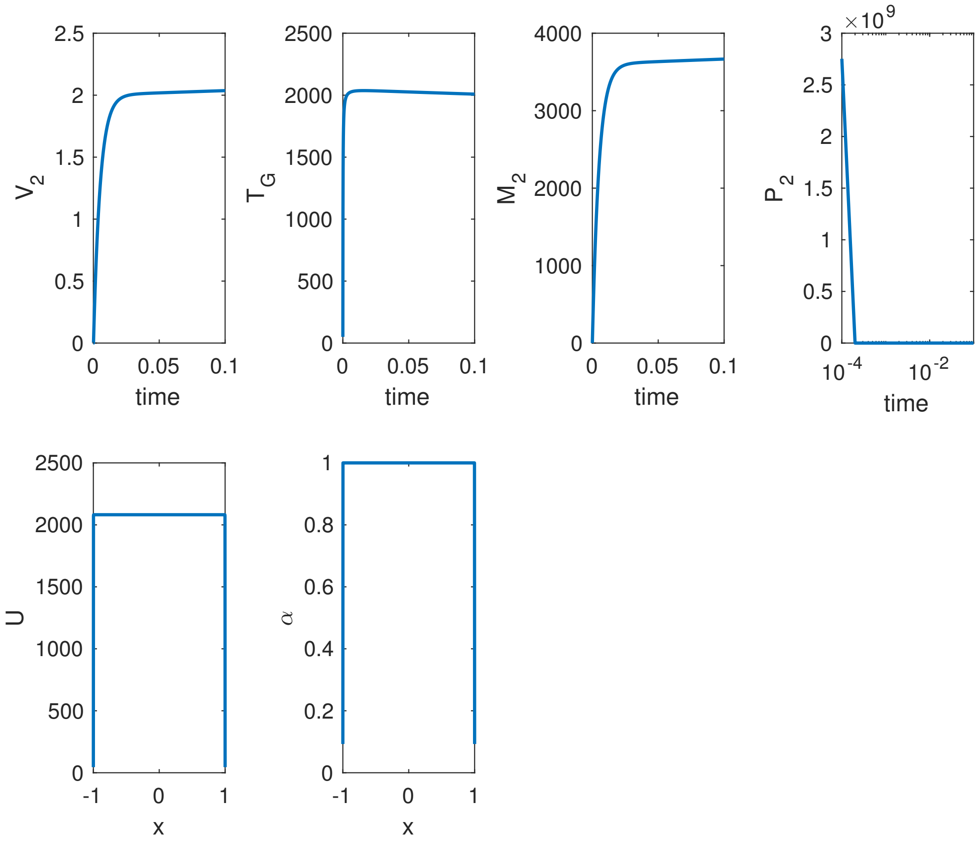

Figure 5.4: Discrete model solutions to equations (5.16)–(5.21) using mild parameters. Here T_G represents $T_2(i+1)$ and U and α represent the solid temperature and extent of reaction.

5.2 Analysis for Differential Scheme

In this section we build on the analysis in section 5.1 and extend the model from discrete form to differential form. The box on the top right hand side of figure 5.5 represents the original quantities at time t. We may calculate the quantities in the top left hand side box of figure 5.5, which represent the change in quantities, using the equations described below. To begin, the total mass of gas created, which we later

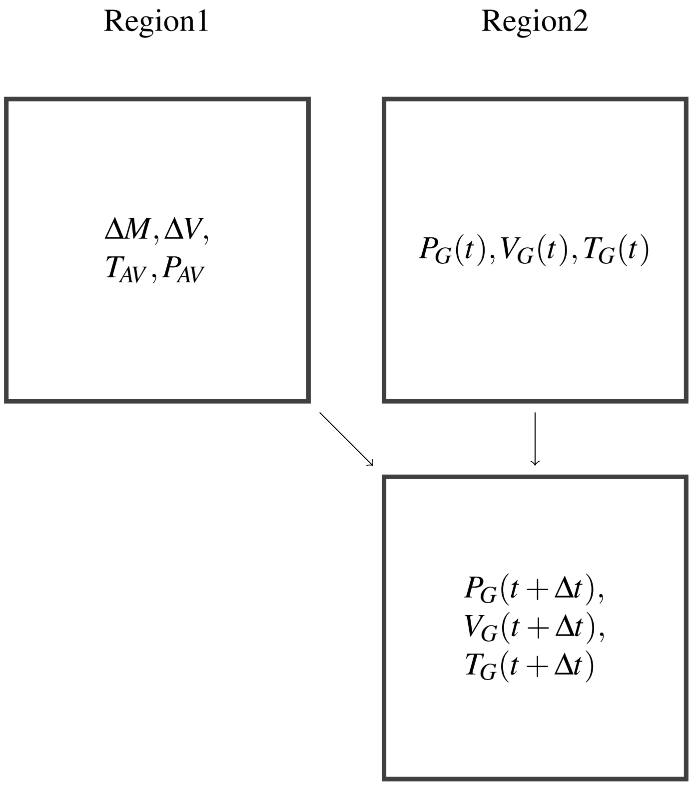

Figure 5.5: Gas and solid occupying two regions separated by an interface. The lower box on the right hand side is calculated by combining the top two boxes.

use to calculate the volume of new gas created and hence the average temperature and pressure of the gas, can be calculated using

$$\Delta M(t) = \rho_1 A \left[\int_{-x_0}^{x_0} \frac{\partial \alpha}{\partial t} dx \right] \Delta t. \tag{5.22}$$

Hence the volume of new gas created in the time Δt uses equation (5.22) such that

$$\Delta V(t) = \frac{\Delta M(t)}{\rho_1}, \tag{5.23}$$

and the average temperature of gas being generated in the solid is given by

$$T_{AV}(t) = \frac{\int_{-x_0}^{x_0} \frac{\partial \alpha}{\partial t} u(x,t) dx}{\int_{-x_0}^{x_0} \frac{\partial \alpha}{\partial t} dx}. \tag{5.24}$$

Finally, the average pressure of the gas within the solid is given by

$$P_{AV}(t) = \frac{\Delta n R T_{AV}(t)}{\Delta V(t)}, \tag{5.25}$$

which is derived from the ideal gas law. Recall that α represents the extent of reaction and u represents the temperature of the solid. The quantities shown in the bottom right hand side box of figure 5.5 are calculated by combining the existing quantities (shown on the top right hand side of figure 5.5) with those created (shown on the top left hand side of figure 5.5). The volume of gas at time $t+\Delta t$ can be found using

$$V_G(t+\Delta t) = \Delta V(t) + V_G(t), \tag{5.26}$$

and the temperature at time $t+\Delta t$ is given by

$$T_G(t+\Delta t) = \frac{c_1 m_1(t) T_{AV}(t) + c_2 m_2(t) T_G(t)}{c_1 m_1(t) + c_2 m_2(t)}, \tag{5.27}$$

where we assume $c_1 = c_2$ to begin and m_1 and m_2 are given by $m_1(t) = \rho_1 \Delta V(t)$, and $m_2(t) = \rho_2 V_G(t)$. The pressure of the gas at time $t+\Delta t$ is given by

$$P_G(t+\Delta t) = \frac{n(t+\Delta t) R T_G(t+\Delta t)}{V_G(t+\Delta t)}. \tag{5.28}$$

Finally, we have the following system of eight equations to solve for the eight unknowns, $\Delta M(t), \Delta V(t), T_{AV}(t), P_{AV}(t), V_G(t+\Delta t), m_2(t), T_G(t+\Delta t), P_G(t+\Delta t)$, at each time step.

$$m_1(t) = \Delta M(t) = \rho_1 A \left(\int_{-x_0}^{x_0} \frac{\partial \alpha}{\partial t} dx \right) \Delta t, \tag{5.29}$$

$$\Delta V(t) = \frac{\Delta M(t)}{\rho_1}, \tag{5.30}$$

$$T_{AV}(t) = \frac{\int_{-x_0}^{x_0} \frac{\partial \alpha}{\partial t} u(x,t) dx}{\int_{-x_0}^{x_0} \frac{\partial \alpha}{\partial t} dx}, \tag{5.31}$$

$$P_{AV}(t) = \frac{\Delta n R T_{AV}(t)}{\Delta V(t)}, \tag{5.32}$$

$$V_G(t+\Delta t) = \Delta V(t) + V_G(t), \tag{5.33}$$

$$m_2(t) = M(t) = \rho_2 V_G(t), \tag{5.34}$$

$$T_G(t+\Delta t) = \frac{m_1(t) T_{AV}(t) + m_2(t) T_G(t)}{m_1(t) + m_2(t)}, \tag{5.35}$$

$$P_G(t+\Delta t) = \frac{n(t+\Delta t) R T_G(t+\Delta t)}{V_G(t+\Delta t)}. \tag{5.36}$$

We note here that we can anticipate the Δt terms will usefully be replaced by dt terms leading to derivatives. This will be taken up in the next model which is described in section 5.3. In the set of equations above, P_{AV} is redundant, i.e. it is not needed for any further calculations, nor is it a quantity in which we are interested at the moment. Similarly $P_G(t+\Delta t)$ is not required for further calculations, but it is a quantity we are interested in calculating. We also have

$$\begin{aligned} m_2(t+\Delta t) &= m_2(t) + m_1(t), \\ &= M(t) + \Delta M(t), \end{aligned}$$

and

$$n_2(t+\Delta t) = n(t) + \Delta n(t),$$

which can be updated such that $n(t) = \frac{M(t)}{M_W}$ i.e. the number of moles of gas at a given time t is equal to the mass $M(t)$ at time t over the molecular weight M_W which is constant. Similarly, $\Delta n(t) = \frac{\Delta M(t)}{M_W}$, that is the change in n at time t, given by $\Delta n(t)$

is equal to the change in mass at time t, $\Delta M(t)$ over the molecular weight M_W. In this model and the previous model, we have treated $n_1(t)$ and $n_2(t)$ as constants. Figure 5.6 shows the solutions to equations (5.29)–(5.36), where we are calculating

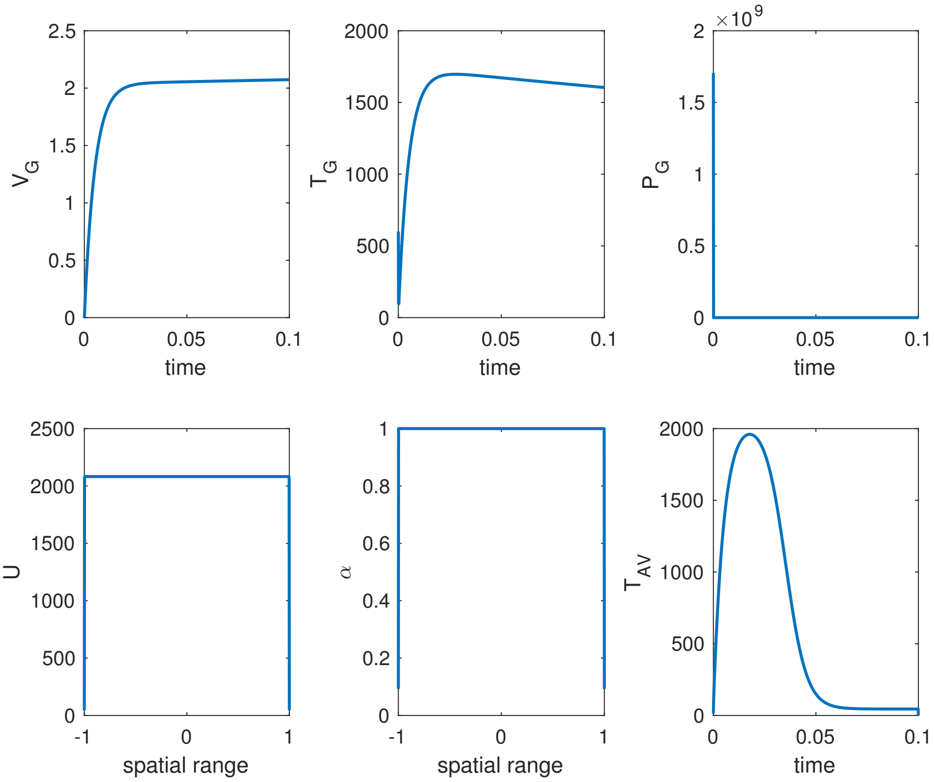

Figure 5.6: Sequential scheme solutions to gas equations (5.29)–(5.36) in section 5.2.

the gas quantities but not yet incorporating any feedback into the system. Beginning from left to right, top to bottom, we observe that the volume of gas V_G exceeds the maximum volume 2 by a small amount. A similar overshoot is found analytically in subsequent sections. We also notice a dip in the gas temperature T_G. The pressure of gas P_G drops rapidly whilst the temperature of the solid u appears to vary only on the boundaries. The extent of reaction α increases to unity as expected. Finally the average temperature of the solid peaks at approximately $2000K$ as a result of the maximum solid temperature u, after which it drops down to $45K$ (the solid boundary condition).

5.3 Continuous Gas model

We now consider the issue of turning the gas-effect discrete form from section 5.2 into a differential-equations formulation. This is achieved simply by taking the limit, in the discrete formulation, as the discrete time step tends a strictly vanishingly small element dt. This limit process yields the system

$$\frac{dV_G(t)}{dt} = A\int_{-x_0}^{x_0} \frac{\partial \alpha}{\partial t} dx, \tag{5.37}$$

$$\frac{dM(t)}{dt} = \rho_1 \frac{dV_G(t)}{dt}, \tag{5.38}$$

$$T_{AV}(t) = \frac{\int_{-x_0}^{x_0} \frac{\partial \alpha}{\partial t} u(x,t)dx}{\int_{-x_0}^{x_0} \frac{\partial \alpha}{\partial t} dx}, \tag{5.39}$$

$$P_{AV}(t) = \frac{\Delta n R T_{AV}(t)}{\Delta V(t)}, \tag{5.40}$$

$$m_1(t) = \rho_1 \frac{dV_G}{dt}\Delta t, \tag{5.41}$$

$$m_2(t) = \rho_2 V_G(t), \tag{5.42}$$

$$\frac{dT_G(t)}{dt} = \frac{1}{m_2(t)}\bigg(T_{AV}(t) - T_G(t)\bigg)\frac{dM(t)}{dt}, \tag{5.43}$$

$$P_G(t) = \frac{nRT_G(t)}{V_G(t)}, \tag{5.44}$$

where we compute $V_G(t)$ at small time using the numerical approximation below, since at $t = 0$, $V_G(t) = 10^{-7}$

$$V_G(t) = \frac{dV_G(t-\Delta t)}{dt}\Delta t + V_G(t-\Delta t),$$

and equation (5.43) follows from equation (5.35). In (5.41) m_1 represents a small increment and in (5.40) likewise, Δn and ΔV are small increments.

As in section 5.2, P_{AV}, P_G and m_1 are redundant. We may solve equation (5.43) for T_G (in terms of other quantities) both numerically and analytically using the classical integrating factor method as follows. We begin by rewriting equation (5.43) as

$$\frac{dT_G}{dt} = k_2(t) - k_1(t)T_G(t), \tag{5.45}$$

where $k_1(t) = \frac{\frac{dM(t)}{dt}}{m_2(t)}$ and $k_2(t) = k_1(t)T_{AV}(t)$, where $T_{AV}(t)$ is given by equation(5.39). Thus we have

$$\frac{dT_G}{dt} + k_1(t)T_G(t) = k_2(t). \tag{5.46}$$

Multiplying through by the integrating factor $\mu(t) = \exp(\int_0^t k_1(t)dt)$ gives

$$\begin{aligned}
\mu(t)\frac{dT_G}{dt} + \mu(t)k_1(t)T_G(t) &= \mu(t)k_2(t), \\
(\mu(t)T_G(t))\prime &= \mu(t)k_2(t), \\
\mu(t)T_G(t) + c &= \int_0^t \mu(t)k_2(t)dt, \\
T_G(t) &= \frac{\int_0^t \mu(t)k_2(t)dt - c}{\mu(t)}.
\end{aligned}$$

Applying the initial condition $T_G(0)$ to the above yields $c = -T_G(0)$ and thus

$$T_G(t) = \frac{\int_0^t \mu(t)k_2(t)dt + T_G(0)}{\mu(t)}. \tag{5.47}$$

This solution (5.47) is shown in figure 5.7 (left). Alternatively, we may approximate $T_G(t)$ using a finite difference approximation, presented in figure 5.7 (right). To approximate T_G at time t, we take the weighted average of the previous time points and approximate the derivative using a backwards difference in time. After discretising equation (5.43) then expanding and simplifying, we are left with

$$T_G(t) = \frac{T_G(t-1)\left(\frac{1}{\Delta t} - \frac{\frac{dM(t)}{dt}}{2m_2(t)}\right) + \frac{\frac{dM(t)}{dt}}{m_2(t)}T_{AV}(t)}{\left(\frac{1}{\Delta t} + \frac{\frac{dM(t)}{dt}}{2m_2(t)}\right)}.$$

We observe close agreement in figure 5.7 between the results of the methods used. Similarly, we may solve for $V_G(t)$ using more than one method. The methods used are outlined immediately below and results are displayed in figure 5.8. Firstly, we may integrate equation (5.37) numerically. The result of this

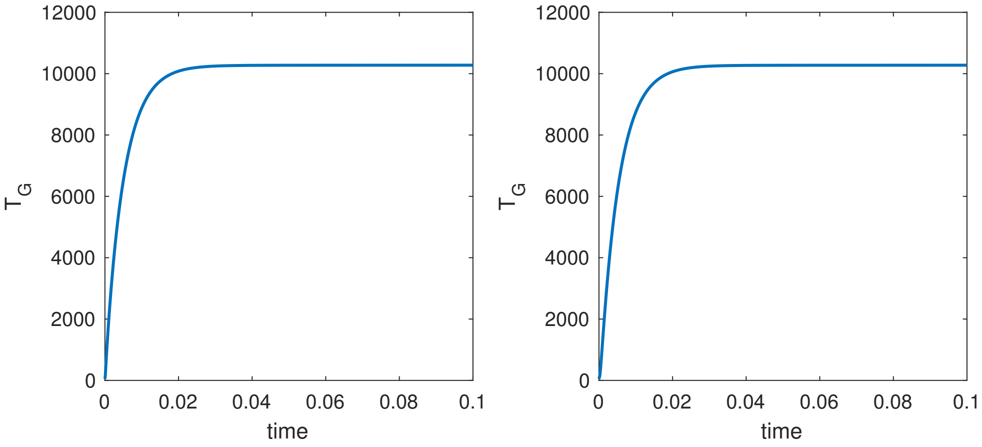

Figure 5.7: Comparison of $T_G(t)$ solutions using the integrating factor method (left) and the finite difference approximation (right). Here $T_G(0) = 50$.

method is shown in figure 5.8 on the left. Secondly, we may approximate $V_G(t)$ by $V_G(t) = \frac{dV_G(t-1)}{dt}\Delta t + V_G(t-1)$, which we initialise using the initial condition $V_G(0) = 0.1 \times 10^{-6}$. This is shown in the middle plot of figure 5.8. Lastly, we may integrate such that $V_G(t) = A\int_{-x_0}^{x_0} \alpha(x,t)dx + V_G(0)$ shown in figure 5.8 on the right. We observe close agreement between the results of the three methods used to compute $V_G(t)$ in figure 5.8.

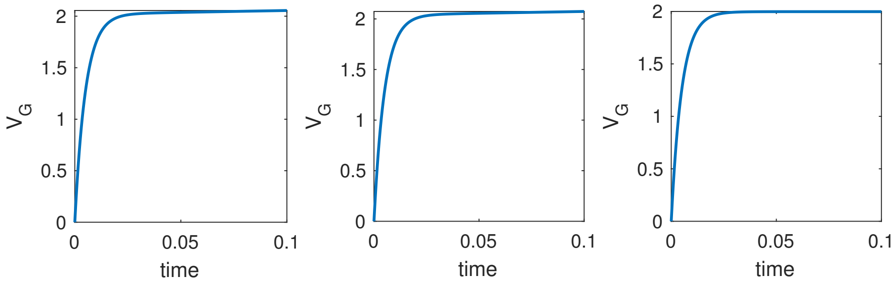

Figure 5.8: Comparison of $V_G(t)$ solutions to equation (5.37) using three different methods; numerical integration, finite difference approximation and analytical integration (outlined above).

We now solve equations (5.37)–(5.44), where (5.37) and (5.43) have been solved (above) using a finite difference approximation. The numerical solutions are presented in figure 5.9, with the results being given in SI units.

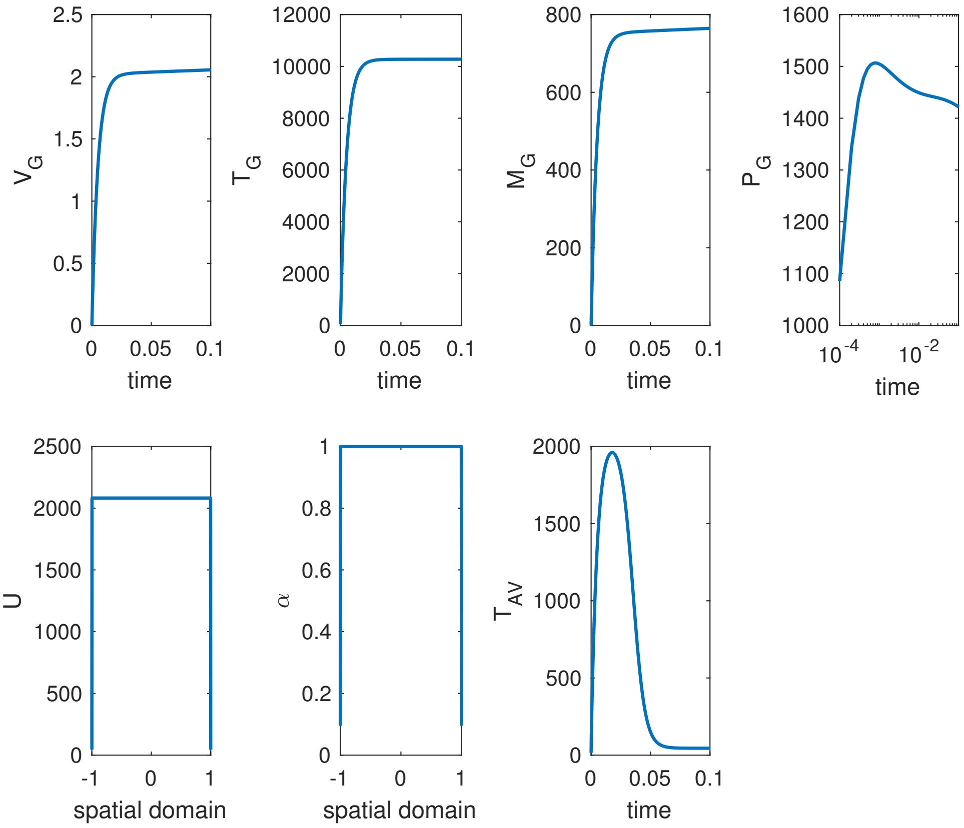

Figure 5.9: Solutions of the differential equations (5.37)–(5.44) solved using mild parameter values.

5.4 Summary of chapter

The progress made in this chapter has been concentrated on introducing the treatment of gas into the model. We began by considering a discrete formulation as a starting point and later converted this to a continuous framework. Comparison of the discrete and continuous schemes has been made for the same physical scenario in the gas treatment. As the discretisation is made finer the two models should converge to the continuous result. The next step to improve the model is to incorporate feedback between gas and solid, an aspect which we consider in the following chapter.

Chapter 6

Feedback

In this chapter we introduce some feedback between the gas and the solid. The gas which is produced by the reaction is at a temperature different from that which is heating the solid on the boundaries. We expect the gas produced to be hotter than the boundary temperatures and therefore we anticipate an accelerated reaction rate. To incorporate some feedback, we begin by using the temperature of the gas calculated in our continuous scheme (equation (5.47)) as a boundary condition on the solid problem. This heats the solid on the boundaries as the temperature of the gas varies with time t. This is implemented by prescribing the temperature of the gas $T_G(t)$ as the solid boundary condition(s).

To examine the effects of the gas we may compare figure 5.9 with figure 6.1 where mild parameters have been used in both cases; the solutions here were obtained using the numerical techniques of the previous chapters. We observe the temperatures of both the gas and the solid become much higher when feedback is incorporated. The pressure of the gas is also much higher. The volume of gas remains virtually unchanged as expected.

When including feedback from the gas temperature in the solid calculations with physical parameter values, as shown in figure 6.2, the numerical scheme breaks down (so far). Concerning this breakdown we now examine the effects on the volume of gas, V_G, of gradually increasing the pre-exponential constant parameter A. From figure 6.3 it is clear to see that for milder values of A the numerical scheme copes well. However as A tends to its true value, the numerical scheme breaks down

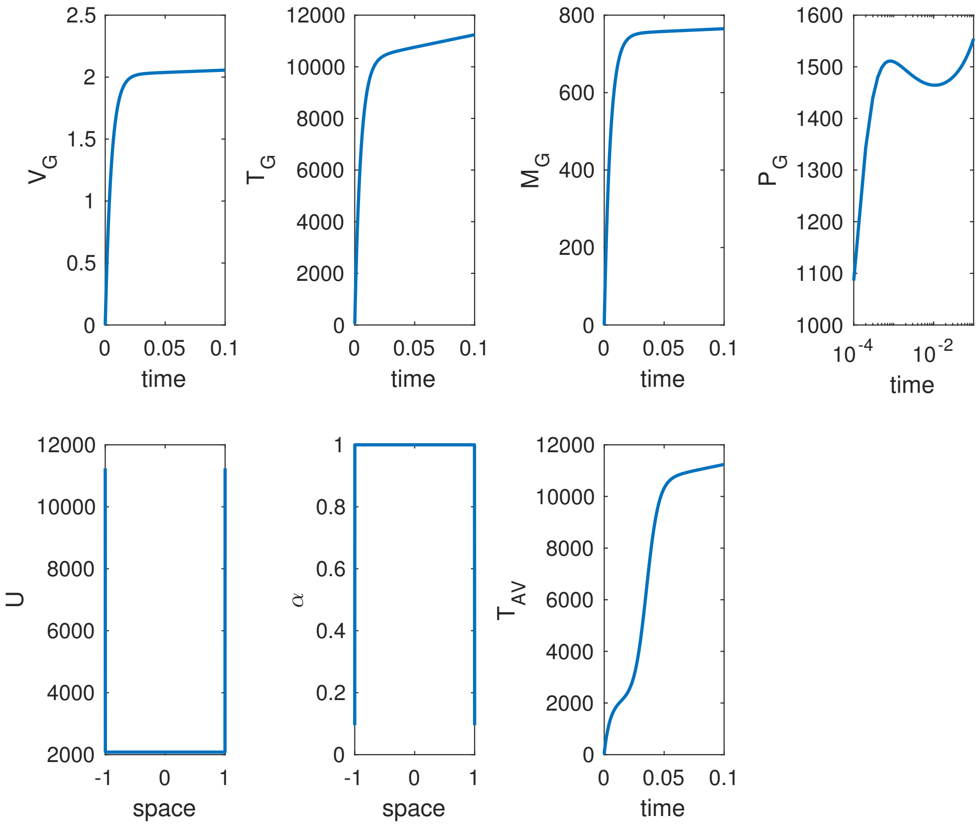

Figure 6.1: Differential equations solutions with feedback from gas to solid using mild parameters.

and Δt requires increasing refinement. There is qualitatively little change between the second and third column of results in figure 6.3 for varying Δt and hence we focus our attention on refining the spatial discretisation, Δx.

In figure 6.4 we observe the effects of the spatial discretisation on the solution, resulting in convergence with finer spatial discretisation. Figure 6.5 provides a focussed view of the results shown in figure 6.4. Comparing the bottom plot in figure 6.4 with the plot in the third row, second column of figure 6.3 (where we have used the same Δt, E and A values, but Δx has changed) we observe great improvement in the solution. Unfortunately, for the true value of $A \approx 5 \times 10^{19}$ we would need to refine both the spatial and temporal discretisations $\Delta x, \Delta t$ beyond standard computing capabilities.

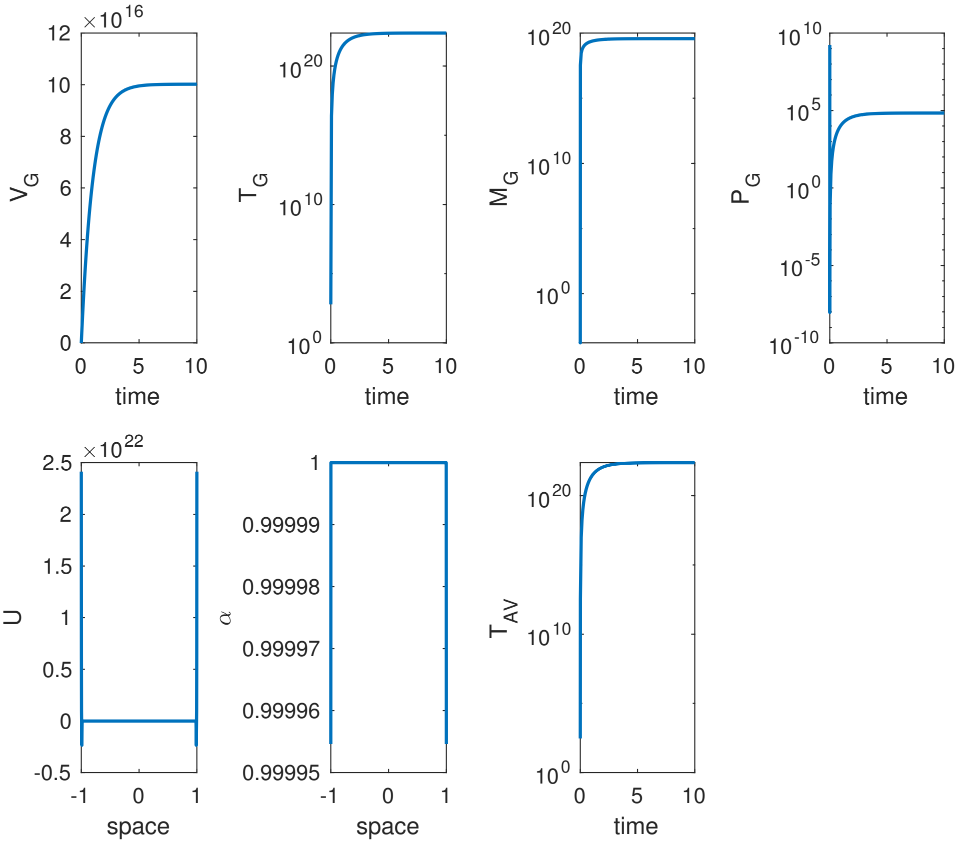

Figure 6.2: Differential equations solutions with feedback from gas to solid using physical parameters.

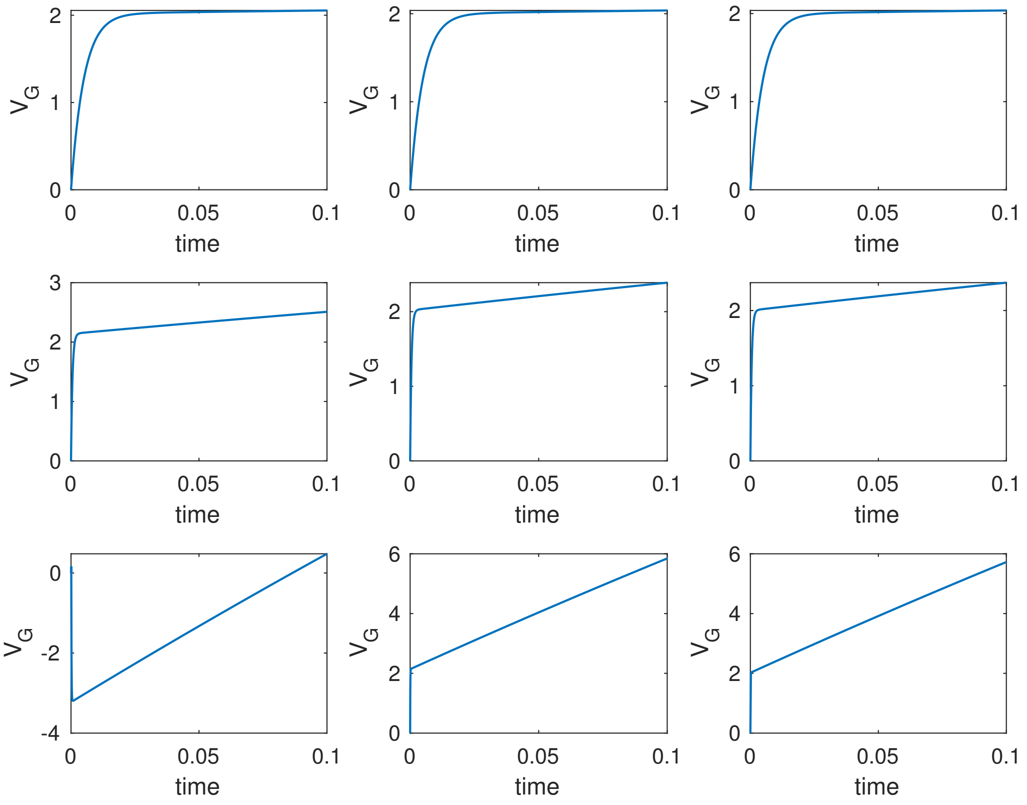

Figure 6.3: The volume of gas V_G for varying Δt and parameter value A representing the pre-exponential constant. Here Δt varies from $\Delta t = 0.0001, 0.00001, 0.000001$ (left to right column) and A varies from $A = 200, 2000, 20000$ (top to bottom row). Here we have fixed $E = 10$ and $\Delta x = 0.002$.

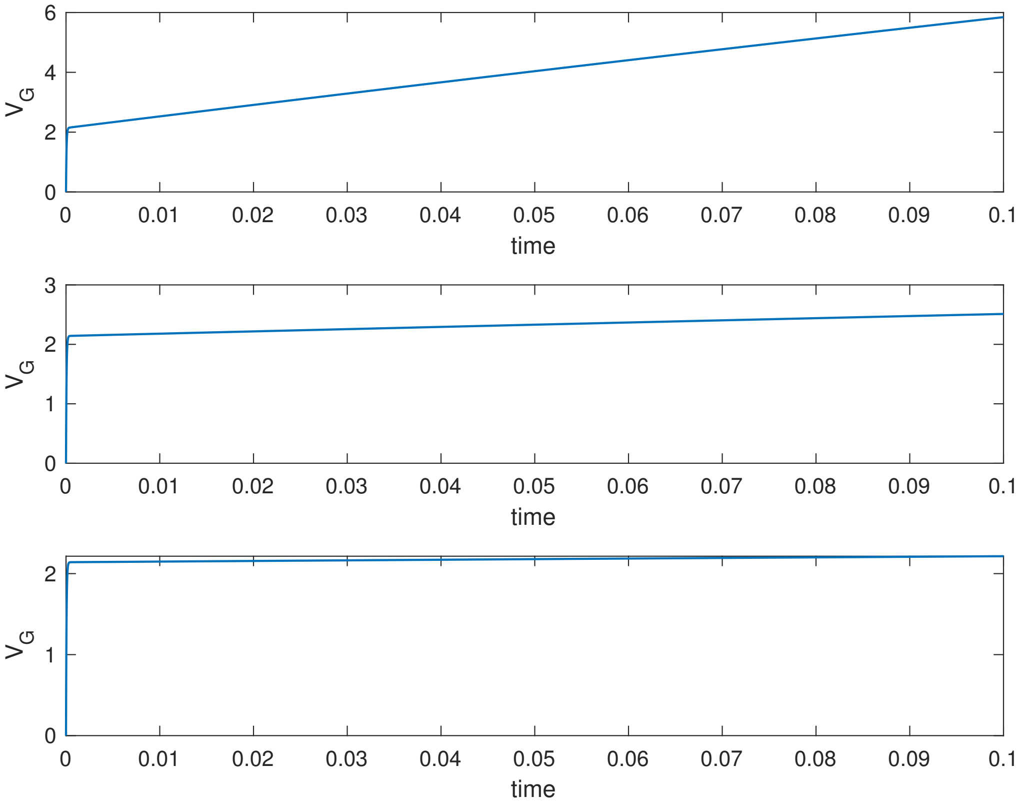

Figure 6.4: The volume of gas V_G for varying (decreasing) Δx. Here Δx varies from $\Delta x = 0.002, 0.0002, 0.00004$ (top to bottom) and $A = 20000$, $E = 10$, $\Delta t = 0.00001$ are fixed.

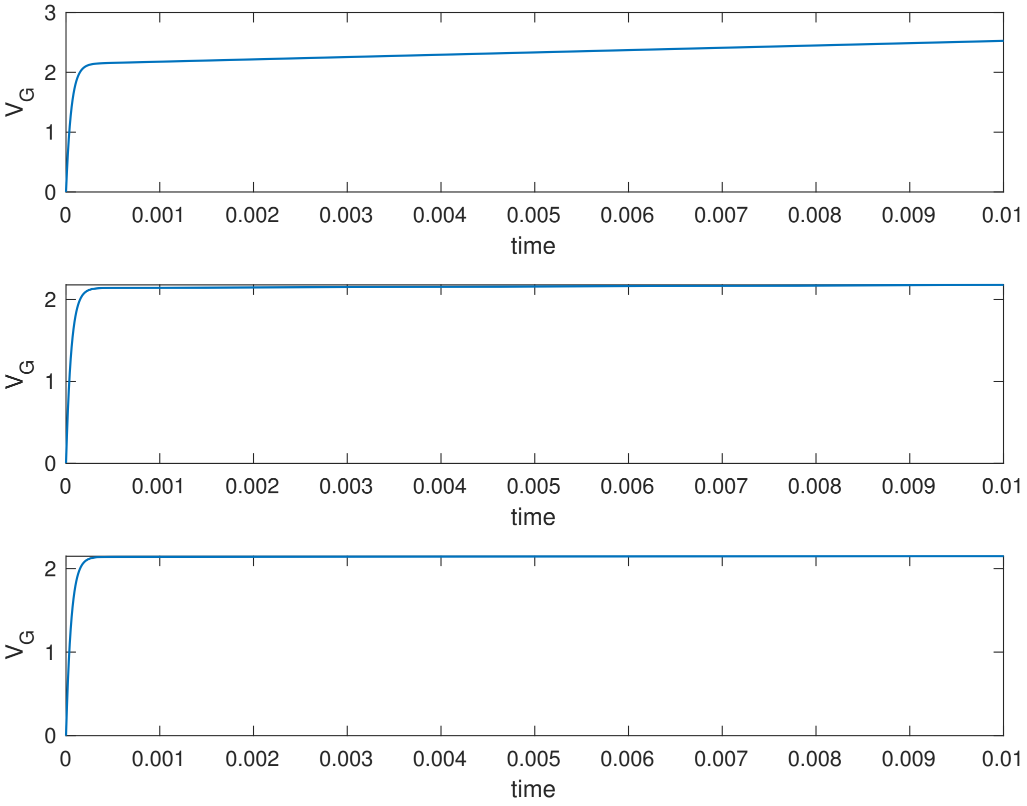

Figure 6.5: The volume of gas V_G for varying (decreasing) Δx. Here Δx varies from $\Delta x = 0.002, 0.0002, 0.00004$ (top to bottom) and $A = 20000$, $E = 10$, $\Delta t = 0.00001$ are fixed.

6.1 Moving Boundary

As the solid burns, more and more gas is created until eventually the entire domain becomes filled with gas once all of the solid explosive has been burnt up. This is demonstrated in the schematic 6.6.

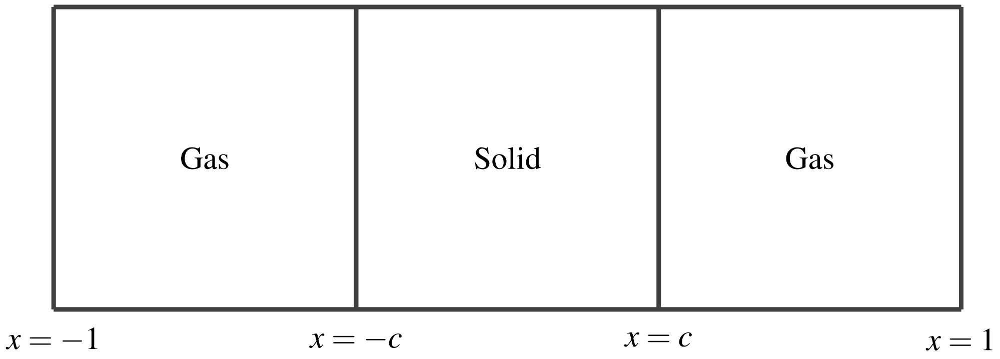

Figure 6.6: Gases occupying two regions (for the symmetric case) with a solid explosive, separated by an interface at some stage *i*.

Here the entire domain over which the problem is modelled is shown by $x = \pm 1$ and $x = \pm c$ represents the boundaries of the solid. The gas which is created occupies the space between $x = \pm 1$ and $x = \pm c$. These boundaries $c(t)$ are functions of time t since the position of the boundaries of the solid move as the reaction progresses and the solid is burnt up. To model this we transform the problem using the following simple transformation: $x = c\bar{x}$. Under this transformation $\bar{x} \in (-1,1)$ and $x \in (-c,c)$. Applying this transformation to the double x derivative in the governing equations

$$\rho c_v \frac{\partial u}{\partial t} = \kappa \frac{\partial^2 u}{\partial x^2} + \rho\Omega \frac{\partial \alpha}{\partial t}, \qquad \frac{\partial \alpha}{\partial t} = A(1-\alpha)\exp\left(-\frac{E}{Ru}\right),$$

gives

$$\rho c_v \frac{\partial u}{\partial t} = \frac{\kappa}{c^2} \frac{\partial^2 u}{\partial \bar{x}^2} + \rho\Omega \frac{\partial \alpha}{\partial t}, \qquad \frac{\partial \alpha}{\partial t} = A(1-\alpha)\exp\left(-\frac{E}{Ru}\right). \tag{6.1}$$

At time $t = 0$, $x = \bar{x}$ and the position of the boundary is given by $c(0) = \pm 1$.

At a given time t, we chose to calculate the position of the boundary $c(t)$ using

$$c(t) = 1 - \frac{V_G(t)}{2}. \tag{6.2}$$

We may now update the continuous scheme presented in section 5.3 such that the governing equations become

$$\frac{dV_G(t)}{dt} = A\int_{-c}^{c} \frac{\partial\alpha}{\partial t} dx, \tag{6.3}$$

$$\frac{dM(t)}{dt} = \rho_1 \frac{dV_G(t)}{dt}, \tag{6.4}$$

$$T_{AV}(t) = \frac{\int_{-c}^{c} \frac{\partial\alpha}{\partial t} u(x,t)dx}{\int_{-c_0}^{c_0} \frac{\partial\alpha}{\partial t} dx}, \tag{6.5}$$

$$\frac{dT_G(t)}{dt} = \frac{1}{m_2(t)}\left(T_{AV}(t) - T_G(t)\right)\frac{dM(t)}{dt}. \tag{6.6}$$

Here we have used $m_1(t) = \rho_1 \frac{dV_G}{dt}\Delta t$ and $m_2(t) = \rho_2 V_G(t)$. We may use equations (6.3)–(6.6) to calculate the average pressure of gas which is given by $P_{AV}(t) = \frac{nRT_{AV}(t)}{V_G(t)}$, as well as the pressure of the gas, given by

$$P_G(t) = \frac{nRT_G(t)}{V_G(t)}. \tag{6.7}$$

We note that in the updated system presented in this section, the integrals are evaluated over $(-c, c)$ since this is now the domain which is spanned by the solid explosive.

In the results in figure 6.7, we observe that despite the extremely high temperature of the gas, shown by the figure labelled T_G, the low diffusivity of heat in the solid means that the temperature u of the solid prevents the temperature of the gas from penetrating the solid. Thus we can conclude that the initial temperature of the solid affects the majority of the solid slab's temperature. We also observe from figure 6.7 that the position of the moving boundary c (which we expect to start at $x = \pm 1$ and eventually reach the centre of the slab $x = 0$ once all of the solid has been burnt) does not reach $x = 0$ as expected. This, along with the fact that the vol-

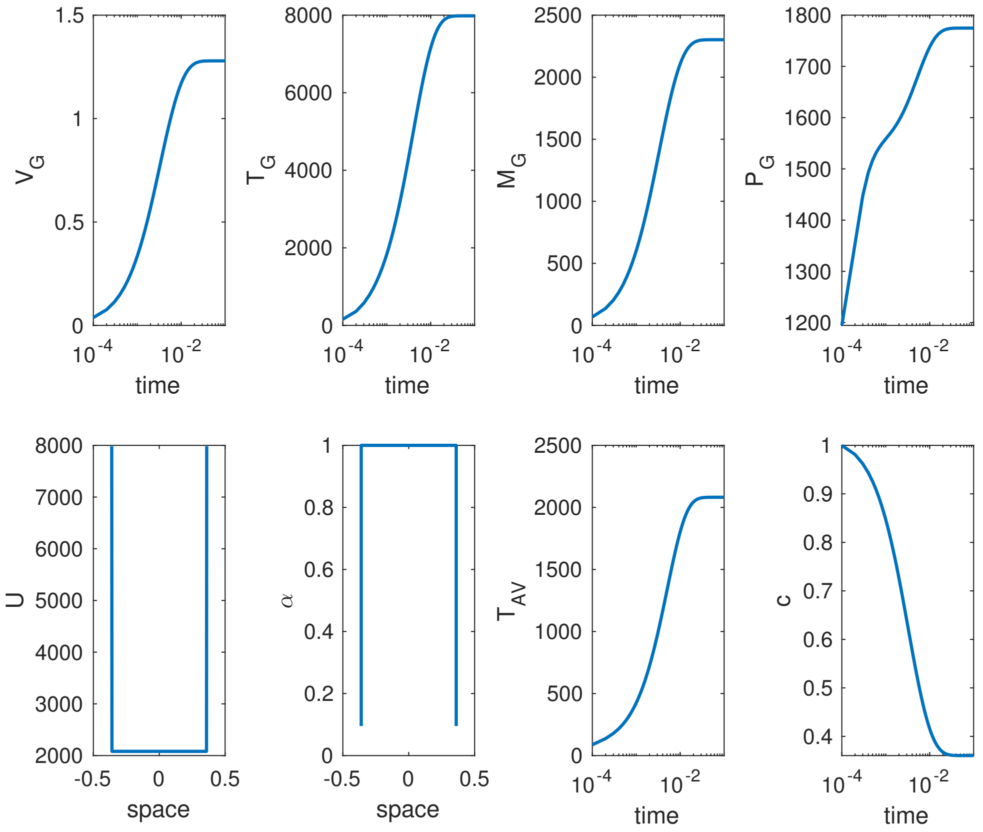

Figure 6.7: Differential equations solutions to equations (6.2)–(6.7), where $t = t_{\text{max}}$ in the plots representing U and α.

ume of gas V_G shown here does not reach 2, suggests there could be an issue with the way in which the problem is being modelled.

In figure 6.8 we plot $U^*(x,t)$, where

$$U^*(x,t) = \begin{cases} u(x,t), & \text{for } x \in [-c(t), c(t)], \forall t \\ T_G(t), & \text{otherwise.} \end{cases} \tag{6.8}$$

Figure 6.8 shows the boundaries of the solid tending towards zero from the left and right as the solid is burnt. The temperature of the gas increases as the solid is being used up. Figure 6.9 represents the extent of the reaction α^* at fixed times where

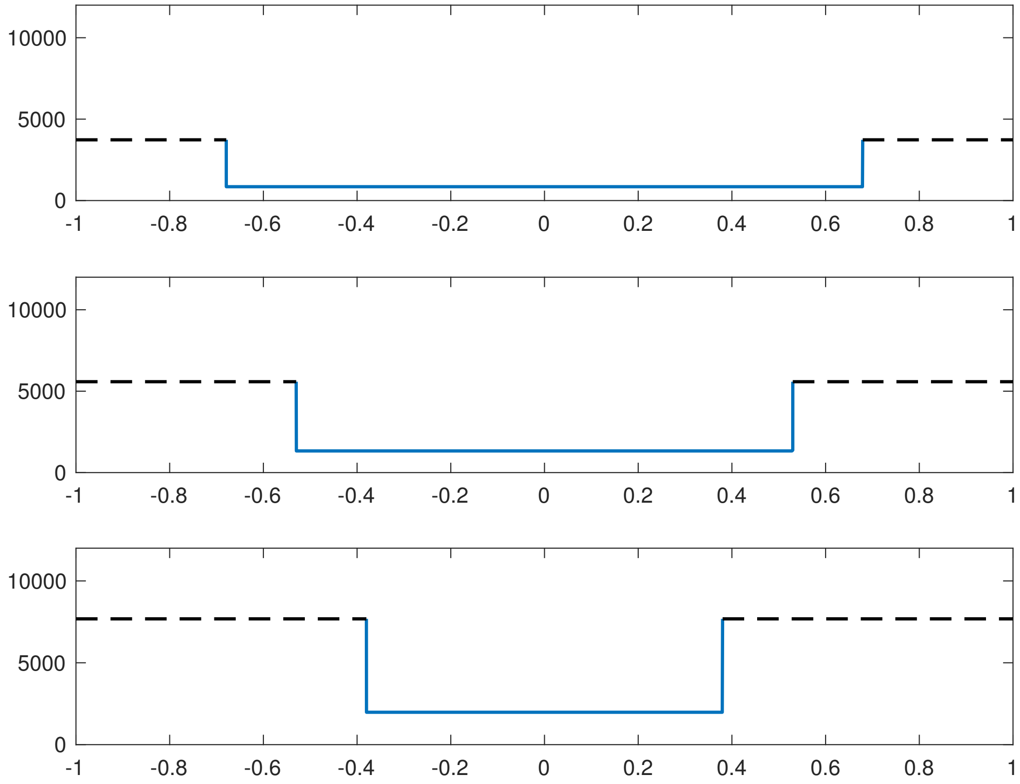

Figure 6.8: Plot of U^* where $U^* = U^*(x,t)$. Temperatures of gas (black dashed lines) and solid (blue solid lines) at fixed times $t = 0.02, 0.04, 0.06$.

$$\alpha^*(x,t) = \begin{cases} \alpha(x,t), & \text{for } x \in [-c(t), c(t)], \forall t \\ 1, & \text{otherwise.} \end{cases} \tag{6.9}$$

Here we plot $\alpha^*(x,t) = 1$ to represent a fully reacted product, i.e. there is no reaction in the gas region.

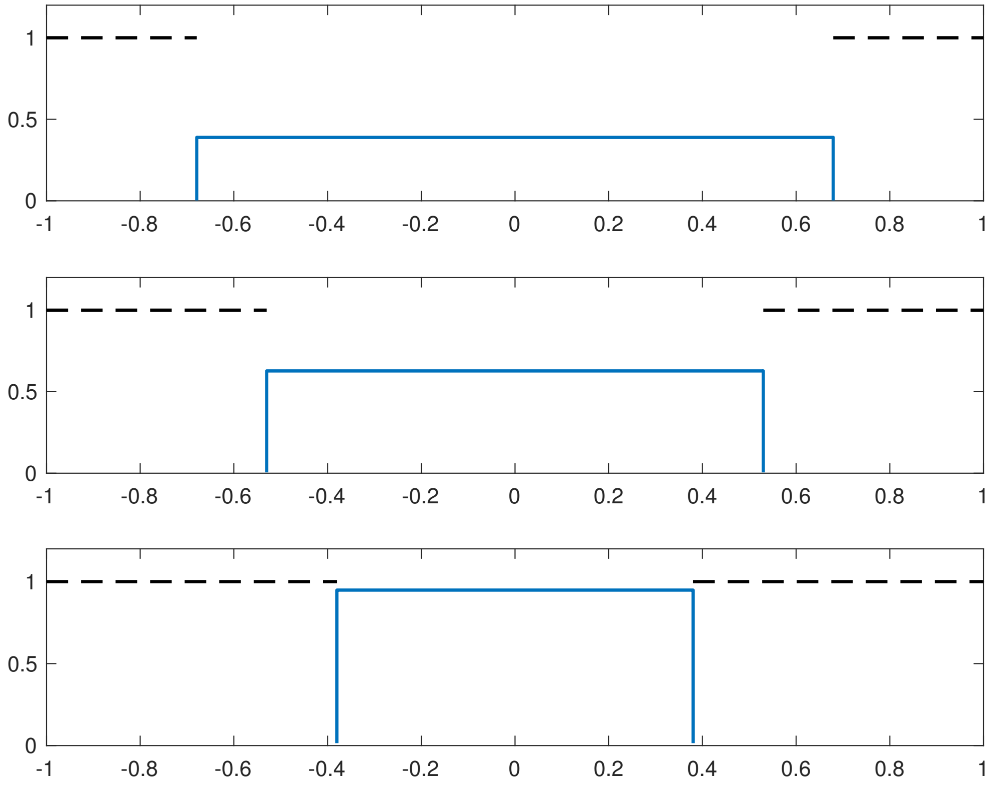

Figure 6.9: The extent of reaction $\alpha^* = \alpha^*(x,t)$ at fixed times $t = 0.02, 0.04, 0.06$ in the gas regions (black dashed lines) and in the solid (blue solid lines).

6.2 Asymptotic Analysis

Motivated by the numerical inaccuracy and difficulties faced in the previous section (section 6.1), we seek an alternative approach using asymptotic analysis. Recall the governing equations

$$\rho c_v \frac{\partial u}{\partial t} = \kappa \frac{\partial^2 u}{\partial x^2} + \rho \Omega \frac{\partial \alpha}{\partial t}, \tag{6.10}$$

$$\frac{\partial \alpha}{\partial t} = A(1-\alpha)\exp\left(-\frac{E}{Ru}\right); \tag{6.11}$$

after applying the transformations $u = \frac{E}{R}\bar{u}$ and $t = A^{-1}\bar{t}$ and neglecting the diffusion term as justified in previous chapters, equation (6.10) becomes $\frac{\partial \bar{u}}{\partial \bar{t}} = \bar{\Omega}\frac{\partial \alpha}{\partial \bar{t}}$. The latter is equivalent to

$$\bar{u} = \bar{\Omega}\alpha + \bar{C}, \tag{6.12}$$

in the core region (which occupies the majority of the slab), since we omit spatial dependence. We also apply the transformations $\bar{C} = \frac{R}{E}C$, where C is the initial temperature condition, and $\bar{\Omega} = \frac{\Omega R}{C_v E}$ to the governing equations. This implies that equation (6.11) becomes

$$\frac{d\alpha}{d\bar{t}} = (1-\alpha)\exp\left(-\frac{1}{\bar{\Omega}\alpha + \bar{C}}\right), \tag{6.13}$$

after substituting equation (6.12). Considering the gas effects of the system, the continuous equations derived in section 5.3, now scaled and without spatial dependence, become

$$\begin{aligned}
\frac{dV_G(t)}{d\bar{t}} &= A\int_{-c}^{c}\frac{\partial\alpha}{\partial\bar{t}}dx, && (6.14)\\
&= 2A\frac{\partial\alpha}{\partial\bar{t}}c(t), && (6.15)\\
\frac{dM(t)}{d\bar{t}} &= \rho_1\frac{dV_G(t)}{d\bar{t}}, && (6.16)\\
&= 2\rho_1 A\frac{\partial\alpha}{\partial\bar{t}}c(t). && (6.17)
\end{aligned}$$

Note here that as $\frac{\partial\alpha}{\partial\bar{t}} \to 0$ over time, both $\frac{dV_G(t)}{d\bar{t}} \to 0$ and $\frac{dM(t)}{d\bar{t}} \to 0$ which implies that V_G and M_G approach their maximum values. The average temperature of the solid becomes

$$\begin{aligned}
T_{AV}(t) &= \frac{\int_{-c}^{c}\frac{\partial\alpha}{\partial\bar{t}}u(t)dx}{\int_{-c}^{c}\frac{\partial\alpha}{\partial\bar{t}}dx}, && (6.18)\\
&= \frac{2\frac{\partial\alpha}{\partial\bar{t}}u(t)c(t)}{2c(t)\frac{\partial\alpha}{\partial\bar{t}}} && (6.19)\\
&= u(t). && (6.20)
\end{aligned}$$

Moreover, the following approximations can be used numerically to calculate the quantities in the gas

$$V_G(t) = \frac{dV_G(t-\Delta t)}{d\bar{t}}\Delta t + V_G(t-\Delta t), \tag{6.21}$$

$$m_2(t) = \rho_2 V_G(t), \tag{6.22}$$

can be used to calculate various quantities in the gas. For example, we may calculate the average pressure in the solid using

$$P_{AV}(t) = \frac{nRT_{AV}(t)}{V_G(t)},$$

although this quantity is not needed for any further calculations here but could be of interest in terms of applications for example. The temperature of the gas is given by the following equation

$$\frac{dT_G(t)}{d\bar{t}} = \frac{1}{m_2(t)}\left(T_{AV}(t) - T_G(t)\right)\frac{dM(t)}{d\bar{t}}, \tag{6.23}$$

$$= \frac{2\rho_1 A \frac{\partial\alpha}{\partial\bar{t}} c(t)u(t)}{\rho_2 V_G(t)} - \frac{2\rho_1 A \frac{\partial\alpha}{\partial\bar{t}} c(t)T_G(t)}{\rho_2 V_G(t)}. \tag{6.24}$$

Note that equation (6.23) may be integrated analytically by restating the equation as

$$\frac{dT_G(t)}{d\bar{t}} = \frac{c_1 \frac{\partial\alpha}{\partial\bar{t}} c(t)u(t) - c_1 \frac{\partial\alpha}{\partial\bar{t}} c(t)T_G(t)}{V_G(t)},$$

giving the linear ordinary differential equation

$$\frac{dT_G(t)}{d\bar{t}} + k_1(t)T_G(t) = k_2(t), \tag{6.25}$$

where $c_1 = \frac{2\rho_1 A}{\rho_2}$, $k_1(t) = c_1 \frac{\frac{\partial\alpha}{\partial\bar{t}} c(t)}{V_G(t+\Delta t)}$ and $k_2(t) = k_1(t)u(t)$. After some work, we obtain

$$T_G(t) = \frac{\int_0^{\bar{t}} \exp\left(\int_0^{\bar{t}} c_1 \frac{\frac{\partial\alpha}{\partial\bar{t}} c(t)}{V_G(t)} d\bar{t}\right) c_1 \frac{\frac{\partial\alpha}{\partial\bar{t}} c(t)u(t)}{V_G(t)} d\bar{t} + T_G(0)}{\exp\left(\int_0^{\bar{t}} c_1 \frac{\frac{\partial\alpha}{\partial\bar{t}} c(t)}{V_G(t)} d\bar{t}\right)} \tag{6.26}$$

which may be integrated numerically. We may also calculate the pressure of the gas using

$$P_G(t) = \frac{nRT_G(t)}{V_G(t)}. \tag{6.27}$$

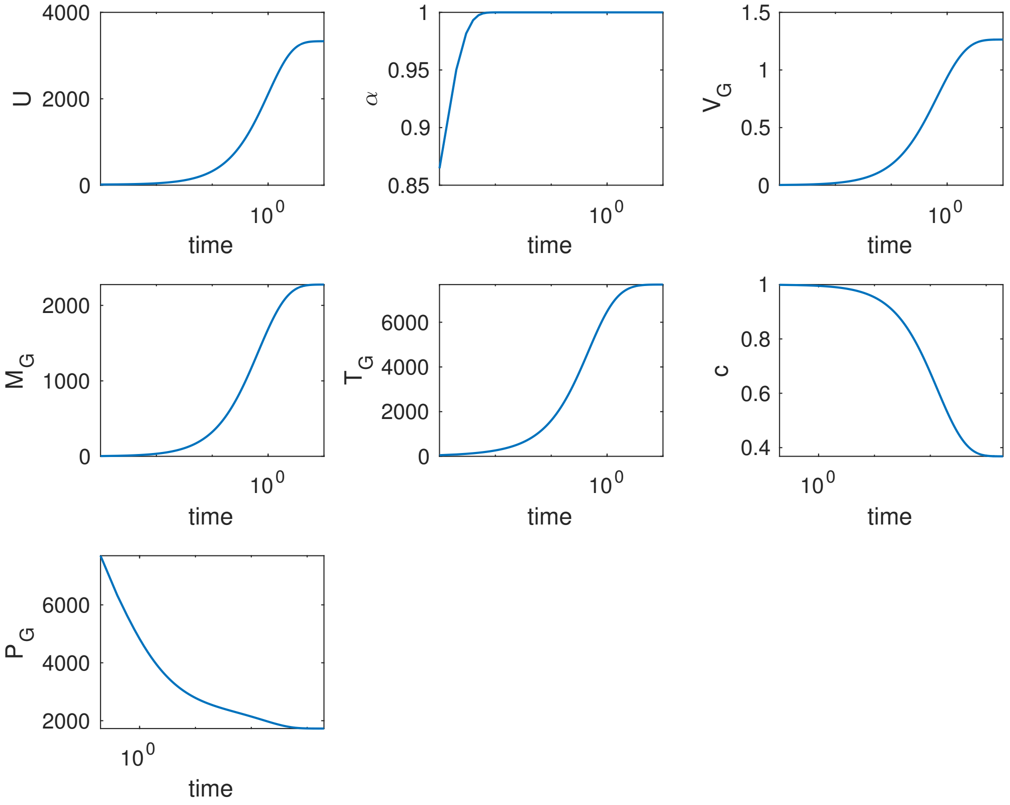

Figure 6.10: Solutions to equations (6.12)-(6.27).

6.3 Summary of chapter

In this chapter we considered the effects of incorporating feedback between the solid and gas. We began by tracking the temperature of the gas and using this as the solid boundary condition once the gas temperature has exceeded the prescribed solid boundary condition. Next in section 6.1, we considered the effects of a moving boundary on the system. As the solid explosive burns, gas occupies the region as the boundaries of the solid move inward (from $x = \pm 1$ to $x = 0$). We observe (figure 6.7) that the model does not successfully capture the behaviour of the system as expected. Finally, we explored an asymptotic approach, presented in section 6.2, to the problem with the moving boundary. We maintain the solid-gas feedback at the boundaries in this methodology. Although this approach proved more computationally efficient, the flaws of the model namely the volume of gas not reaching $V_G = 2$ as expected (presented in figure 6.10), are still present and cannot be resolved using this approach. We have $V_G'(t) = 2A\alpha'(t)c(t)$ in (6.15). Here $c(t) = (1 - \frac{V_G}{2})$ from (6.2). Hence we obtain

$$\frac{dV_G}{d\alpha} = A(2 - V_G). \tag{6.28}$$

The solution of this ODE subject to $V_G = 0$ at $\alpha = 0$ (i.e. time zero) is

$$V_G = 2(1 - exp(-A\alpha)). \tag{6.29}$$

Hence at large times (α tending to unity) we find

$$V_G \to 2(1 - exp(-A\alpha)). \tag{6.30}$$

This is always less than 2. In fact we can go further – if we put $A = 1$ into (6.30) then we are predicting V_G tending to 1.27 approximately: this value looks very close to the maximum value of V_G in figure 6.10. We can conclude that V_G not reaching 2 is truly a feature of the model in chapter 6 and it is a limitation of that model. The above findings act as a springboard for the new modelling addressed in the next chapter.

Chapter 7

Gas model 2 - varying density

The aim of this chapter is to understand the interplay between the gas and the solid. As the interaction takes place, hot gas is produced within the solid. Our first model, presented in chapter 6, accounts for hot gas affecting the temperature only at the sides of the solid. As described in chapter 6, this model proved to be unsuccessful. The logical next step is to allow the gas temperature to penetrate the entirety of the solid. One way to do this is to allow internal heating through porous effects. Alternatively, density reduction is another approach which we can consider.

In chapter 6, we attempted to include some feedback from gas to solid using a moving boundary approach. The results from this method were non-physical. In the present chapter we introduce varying densities which we then extend to include the ideal gas law in the system. To seek an internal or overall feedback effect on the solid explosive we will associate a gradual reduction in the solid density, $\rho_S(t)$, with an increase in the amount of gas. We then modify the density of the solid, keeping the spatial domain fixed between $-1 \leq x \leq 1$. As the reaction occurs, we modify the density, which leads to altered governing equations, and thus, with mass conservation, the equation for density will be solved in parallel with the equations for temperature u and reaction α.

7.1 Full problem

In this section we explore the effects of varying the densities of the solid and gas. At this stage we do not account for feedback of varying densities on the solid temperature u or reaction rate α. We consider a fixed density of gas to begin with where $\rho_G =$ constant. This leads to the same equations as those presented in chapter 6

$$V_G(t) = A\int_{-x_0}^{x_0} \alpha(x,t)dx, \tag{7.1}$$

$$V_S(t) = 2 - V_G(t), \tag{7.2}$$

$$\frac{dT_G(t)}{dt} = \frac{1}{m_2(t)}\Bigg(T_{AV}(t) - T_G(t)\Bigg)\frac{dM(t)}{dt}, \tag{7.3}$$

$$P_G(t) = \frac{nRT_G(t)}{V_G(t)}, \tag{7.4}$$

$$\rho_G = 372, \tag{7.5}$$

$$\rho_S(t) = \frac{M_T - \rho_G(t)V_G(t)}{V_S(t)}, \tag{7.6}$$

where $m_2(t) = M_G(t) = \rho_G(t)V_G(t+\Delta t) = \rho_G(t)\left(\frac{dV_G}{dt}\Delta t + V_G(t)\right)$ and $\frac{dM}{dt} = \rho_S(t)\left(\frac{dV_G}{dt}\right)$. Here we have ρ_G =constant and equation (7.6) is derived from the conservation of mass law

$$\rho_S(t)V_S(t) + \rho_G(t)V_G(t) = M_T, \tag{7.7}$$

where M_T represents the total mass (3600). The density of the solid has been redefined such that $\rho_1 = \rho_S$. Numerical results for the above system are presented in figure 7.1 We observe from figure 7.1 that the density of the solid increases, as opposed to decreasing as we would expect. We can assume for now that this is a direct result of setting the gas density ρ_G to be constant.

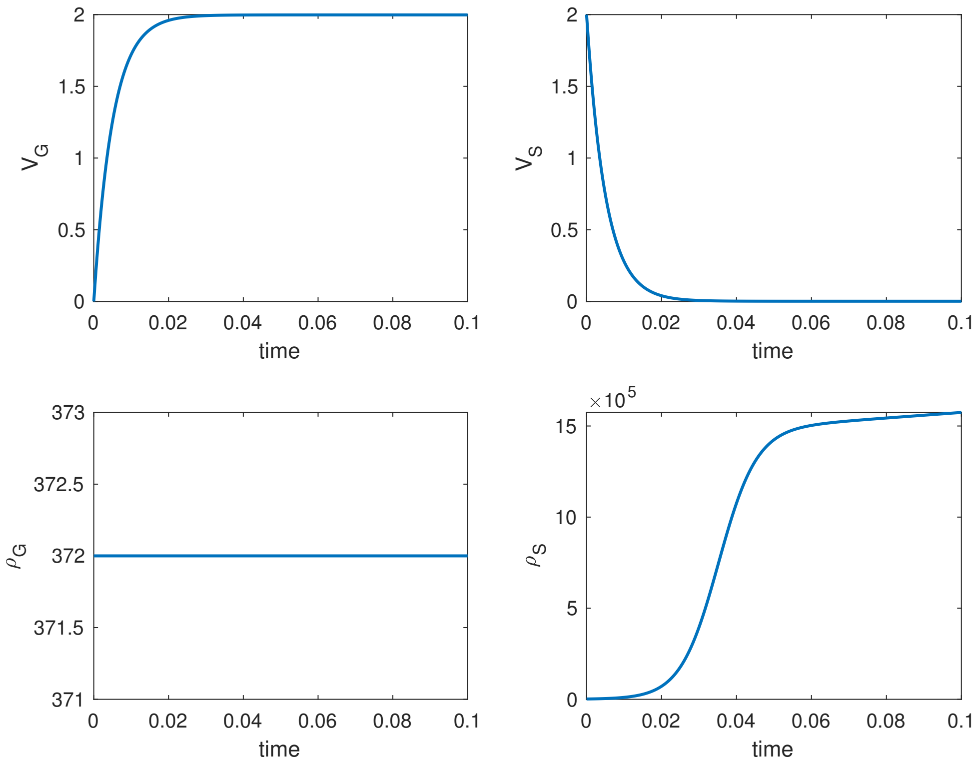

Figure 7.1: Plots of varying density, treating ρ_G as constant and updating $\rho_S(t)$ using the conservation of mass equation (7.6).

7.2 Varying density of gas

We now consider varying the density of the gas such that $\rho_G = \rho_G(t)$. Using the relationship of the ideal gas law

$$P_G(t) = c_1 \rho_G^{\gamma}(t), \tag{7.8}$$

where $\gamma = 1.4$ and c_1 is a constant to be determined, equation (7.8) can be rearranged to give an expression for $\rho_G(t)$ such that

$$\rho_G(t) = \left(\frac{P_G(t)}{c_1}\right)^{\frac{1}{\gamma}}. \tag{7.9}$$

Alternatively, we may use of our ideal gas law $PV = nRT$, and substitute this into (7.8) to get equation (7.9). Hence, our system of equations, with both densities of the solid and gas varying, becomes

$$V_G(t) = A\int_{-x_0}^{x_0} \alpha(x,t)dx, \tag{7.10}$$

$$V_S(t) = 2 - V_G(t), \tag{7.11}$$

$$\frac{dT_G(t)}{d\bar{t}} = \frac{1}{m_2(t)}\left(T_{AV}(t) - T_G(t)\right)\frac{dM(t)}{d\bar{t}}, \tag{7.12}$$

$$P_G(t) = \frac{nRT_G(t)}{V_G(t)}, \tag{7.13}$$

$$\rho_G(t) = \left(\frac{P_G(t)}{c_1}\right)^{\frac{1}{\gamma}}, \tag{7.14}$$

$$\rho_S(t) = \frac{M_T - \rho_G(t)V_G(t)}{V_S(t)}, \tag{7.15}$$

where $m_2(t)$ and and $\frac{dM}{dt}$ are the same as in section 7.1. Solving this system yields the results shown in figure 7.2. We note here that in figure 7.2, neither the density of the gas $\rho_G(t)$ nor the density of the solid $\rho_S(t)$ are behaving as expected. We would expect to see an increase in $\rho_G(t)$ as $\rho_S(t)$ decreases. In light of this, we now consider writing a decreasing function to vary the density of the solid $\rho_S(t)$ with the aim of improving the modelling. We choose

$$\rho_S(t) = \rho_S(0)\left(\frac{1}{1+\frac{t^2}{t_{max}^2}}\right), \tag{7.16}$$

with no spatial dependence in the model for simplicity and enhanced insight. Updating the density of the gas using (7.7) gives

$$\rho_G(t) = \frac{M_T - \rho_S(t)V_S(t)}{V_G(t)}. \tag{7.17}$$

The results of the algebraic decreasing function for $\rho_S(t)$ are shown in figure 7.3. We note that in figure 7.3, the density of the gas $\rho_G(t)$ seems to immediately increase to $\rho_G = 1800$ and remain constant for all t thereafter. This suggests that perhaps the density of the solid is not decreasing fast enough. To remedy this, we

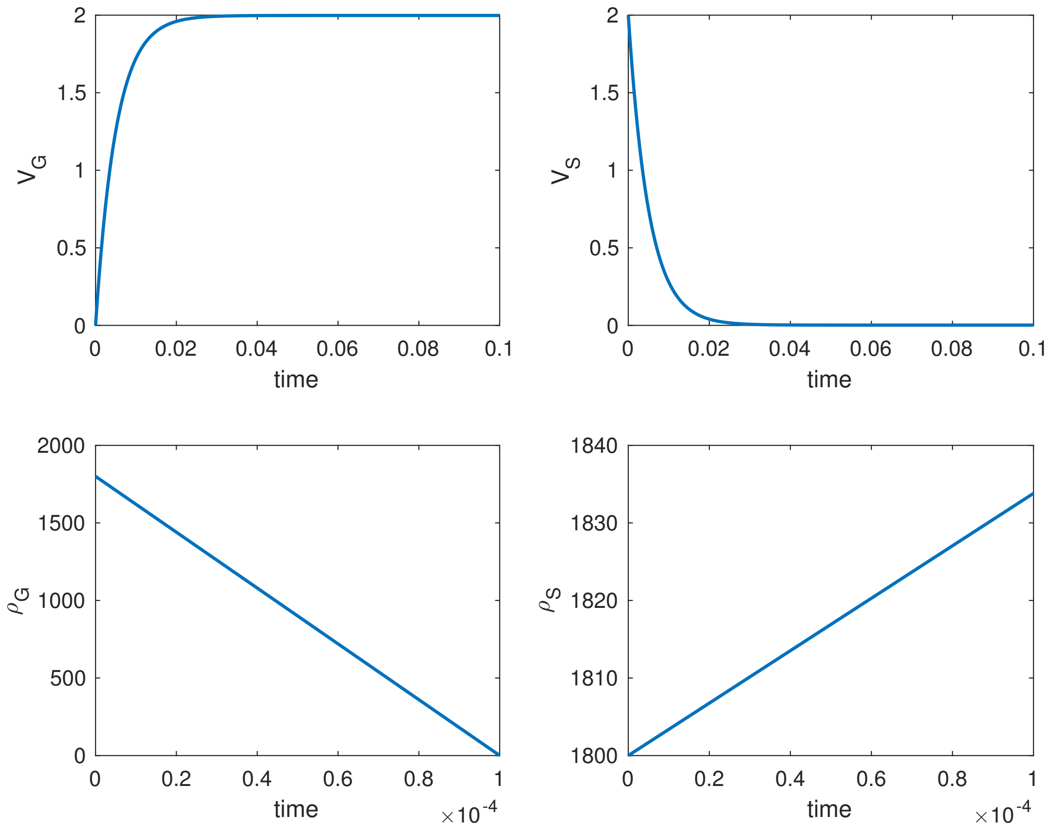

Figure 7.2: Varying densities ρ_G updated using equation (7.9) (ideal gas law) and ρ_S updated using equation (7.6) (conservation of mass).

implement the simple exponentially decreasing function

$$\rho_S(t) = \rho_S(0)e^{-t} \tag{7.18}$$

and update $\rho_G(t)$ using equation (7.17) as before. Results of this are shown in figure 7.4. From figures 7.3 and 7.4, we note that varying $\rho_S(t)$ in the specified ways (algebraically and exponentially) has little to no effect of the density of the gas $\rho_G(t)$, which remains virtually constant. These figures also verify the existence of a 'core' region in which any change in $\rho_G(t)$ maintains the order of the parameter $\bar{\kappa}$ i.e. $\bar{\kappa}$ remains small and thus we still see a visible core which is independent of $\bar{\kappa}$. We observe that the volumes of both the solid and gas, $V_S(t), V_G(t)$, displayed in figures 7.3 and 7.4, are largely unaffected by the densities. The above sections have

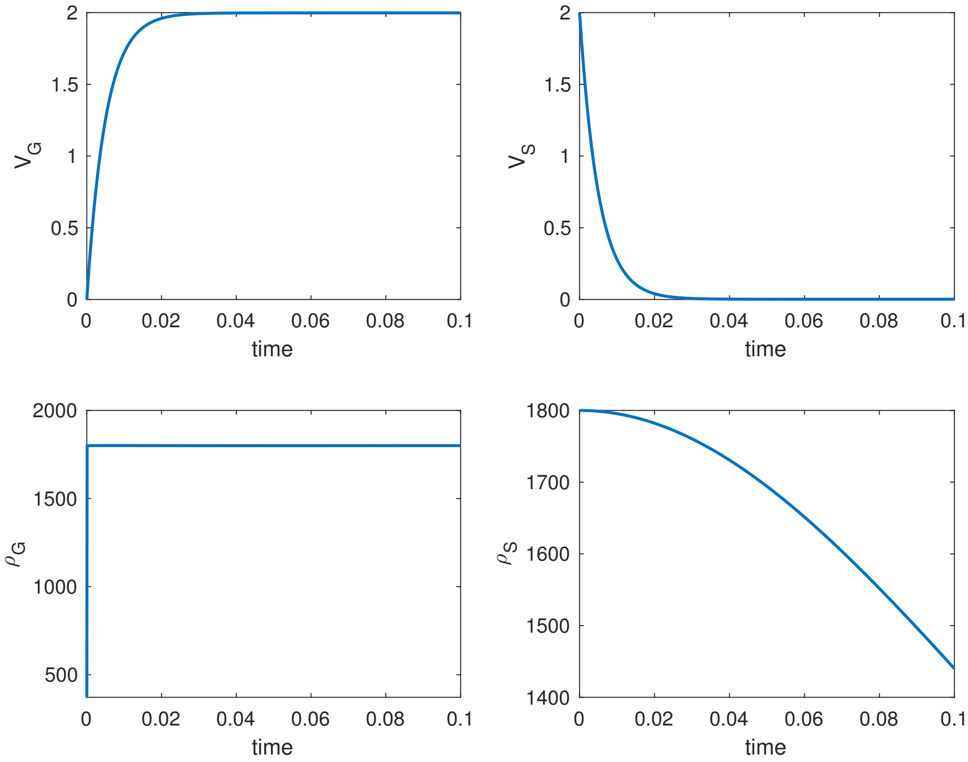

Figure 7.3: Varying densities $\rho_G(t)$ and $\rho_S(t)$ where $\rho_S(t)$ is updated using the algebraic function (7.16) and $\rho_G(t)$ is updated using equation (7.17).

shown the incorporation of feedback into the system is not straightforward, a point which serves as motivation for the following section.

Finally, we note here that in all of the cases presented above, the density of the solid $\rho_S(t)$ remains constant in the solid calculation i.e. we have not incorporated feedback into the solid temperature or reaction rate yet.

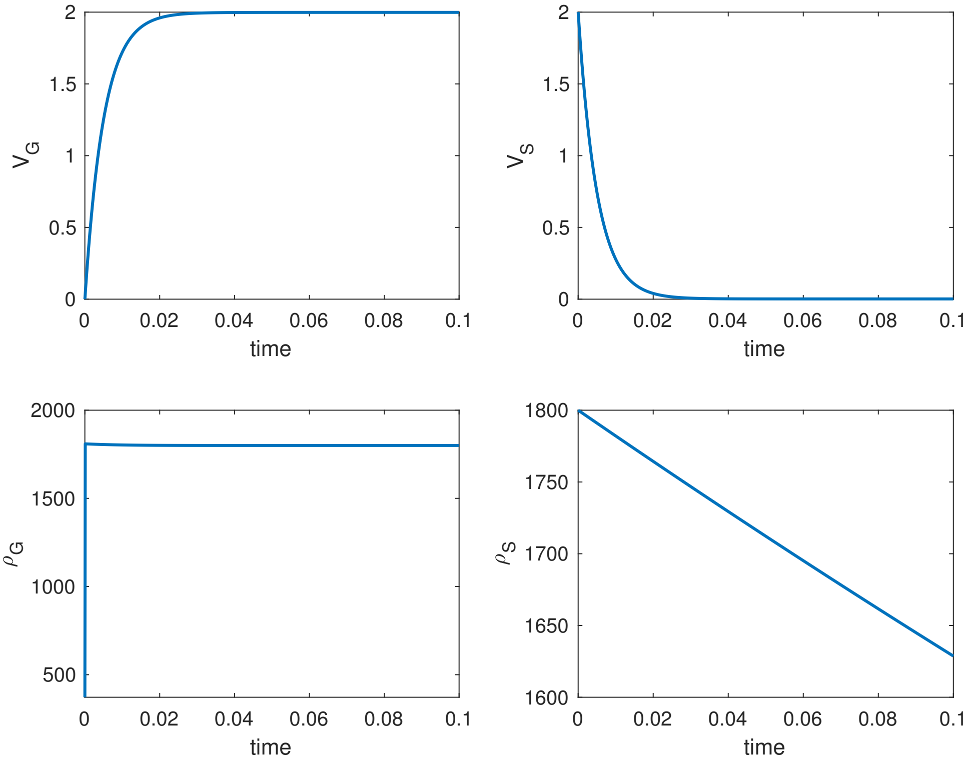

Figure 7.4: Varying densities $\rho_G(t)$ and $\rho_S(t)$ where $\rho_S(t)$ is updated using equation (7.18) and $\rho_G(t)$ is updated using equation (7.17).

7.3 Solid Feedback

In the previous section 7.2, we considered the effects of varying the densities of the solid and gas on the system without incorporating this as feedback in the solid. In reality, the density of the solid affects the temperature calculations of the solid and thus the reaction rate also. In this section we will investigate the effect that varying the densities of the solid and gas has on the solid calculations. Incorporating this feedback into the system of equations in section 7.2 leaves the following equations to be solved

$$
\begin{aligned}
\rho_S(t) c_v \frac{\partial u}{\partial t} &= \kappa \frac{\partial^2 u}{\partial x^2} + \rho_S(t) \Omega \frac{\partial \alpha}{\partial t}, && (7.19)\\
\frac{\partial \alpha}{\partial t} &= A(1-\alpha)\exp\left(-\frac{E}{Ru}\right), && (7.20)\\
V_G(t) &= A \int_{-x_0}^{x_0} \alpha(x,t)\,dx, && (7.21)\\
V_S(t) &= 2 - V_G(t), && (7.22)\\
\frac{dT_G(t)}{dt} &= \frac{1}{m_2(t)} \left(T_{AV}(t) - T_G(t) \right) \frac{dM(t)}{dt}, && (7.23)\\
P_G(t) &= \frac{nRT_G(t)}{V_G(t)}, && (7.24)\\
\rho_G(t) &= \left(\frac{P_G(t)}{c_1} \right)^{\frac{1}{\gamma}}, && (7.25)\\
\rho_S(t) &= \frac{M_T - \rho_G(t) V_G(t)}{V_S(t)}, && (7.26)\\
T_{AV}(t) &= \frac{\int_{-x_0}^{x_0} \frac{\partial \alpha}{\partial t} u(t)\,dx}{\int_{-x_0}^{x_0} \frac{\partial \alpha}{\partial t}\,dx}, && (7.27)\\
M_T &= M_S + M_G, && (7.28)
\end{aligned}
$$

where M_T represents the total mass of the system, while M_S and M_G represent the masses of the solid and gas respectively. Here (7.19) now includes the density of the solid $\rho_S(t)$ as a function of time whereas before, in section 7.2, this was treated as constant. Figure 7.5 shows the quantities calculated in the solid; starting from the top row, left to right, we can see the temperature of the solid u, plotted over the spatial range x and the extent of reaction α also plotted over the spatial range x. We observe that the temperature u increases slightly on the boundaries due to numerical error. From the top right plot we see that the volume of solid V_S which starts at $V_S = 2$ tends to zero as time (x-axis) goes on. This implies that the volume of solid, which initially occupies the whole domain, is replaced instead by gas (shown below in figure 7.6).

On the bottom row of figure 7.5, proceeding from left-to-right again, we see that the density of the solid ρ_S increases over time. To repeat, this is not realistic.

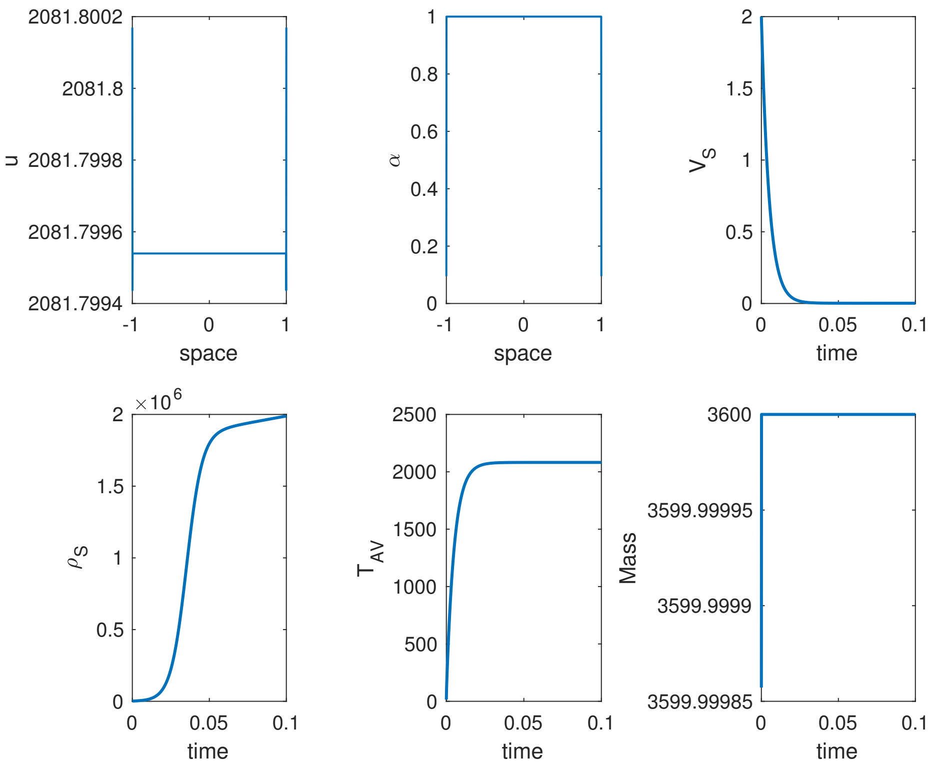

Figure 7.5: Solution to system of equations (7.19), (7.20), (7.22), and (7.26) – (7.28) using mild parameter values.

This agrees with what we observed in the previous section 7.2, figure 7.1. From the bottom-right plot, we observe that the mass of the system is conserved; as V_S tends to zero, at large times, the denominator in equation (7.26) approaches zero and noting the numerator does not tend to zero, we have the result $\rho_S \to \infty$.

In figure 7.6, we observe that $V_G \to 2$ as t increases, which corresponds to V_S tending to zero in figure 7.5. We also observe from figure 7.6 that ρ_G decreases, possibly as a result of ρ_S increasing in figure 7.5. On the bottom left, we see the temperature of the gas T_G, (which is closely related to the temperature of the solid u in figure 7.5), plateau at approximately $T_G = 2000$. Finally, on the bottom-right plot, the pressure of gas P_G, drops sharply at small time t. Here in figure 7.6 we are showing the same time range throughout the four sub-figures and the main density and pressure variations seem to be within a much shorter time scale.

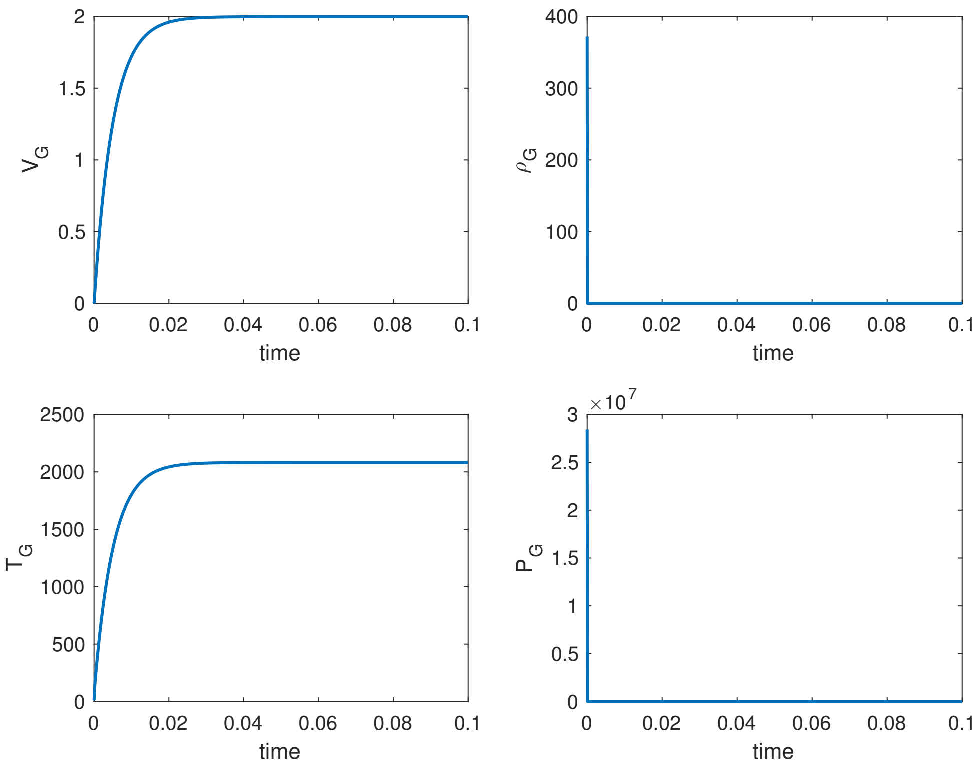

Figure 7.6: Solution to system of equations (7.21), (7.23)–(7.25) using mild parameter values.

7.4 Core problem

Motivated by the previous section 7.3, the model presented in this section is an improvement of that in section 6.2 in two main ways; firstly the volume of gas $V_G(t)$ now tends to 2, which is more physically realistic and secondly here we incorporate the varying densities into the model. Using the ideal gas law and conservation of mass, as in section 7.3 we now have the following system of equations (7.29)–(7.37) applying in the core where diffusion can be neglected.

$$\rho_S(\bar{t})C_v\frac{\partial \bar{u}}{\partial \bar{t}} = \rho_S(\bar{t})\Omega\frac{\partial \alpha}{\partial \bar{t}}, \tag{7.29}$$

$$\implies \bar{u} = \bar{\Omega}\alpha + \bar{C}, \tag{7.30}$$

$$\frac{d\alpha}{d\bar{t}} = (1-\alpha)\exp\left(-\frac{1}{\bar{u}}\right), \tag{7.31}$$

$$V_G(\bar{t}) = 2Ax_0\alpha(x,\bar{t}), \tag{7.32}$$

$$V_S(\bar{t}) = 2 - V_G(\bar{t}), \tag{7.33}$$

$$\frac{dT_G(\bar{t})}{d\bar{t}} = \frac{1}{m_2(\bar{t})}\left(\bar{u}(\bar{t}) - T_G(\bar{t})\right)\frac{dM(t)}{d\bar{t}}, \tag{7.34}$$

$$P_G(\bar{t}) = \frac{nRT_G(\bar{t})}{V_G(\bar{t})}, \tag{7.35}$$

$$\rho_G(\bar{t}) = \left(\frac{P_G(\bar{t})}{c_1}\right)^{\frac{1}{\gamma}}, \tag{7.36}$$

$$\rho_S(\bar{t}) = \frac{M_T - \rho_G(\bar{t})V_G(\bar{t})}{V_S(\bar{t})}, \tag{7.37}$$

where $m_2(\bar{t}) = \rho_G(\bar{t})V_G(\bar{t})$ and $\frac{dM(\bar{t})}{d\bar{t}} = \rho_S(\bar{t})\frac{dV_G(\bar{t})}{d\bar{t}}$. Here the bars denote scaled quantities. These have been scaled as before in earlier chapters. The numerical solution to equations (7.29)–(7.37) is shown in figure 7.7. In figure 7.7 the same time range is displayed throughout the four sub-figures. As stated earlier, the main density and pressure variations are within much shorter time scales. We chose to solve equation (7.34) using a finite difference approximation, presented in figure 7.7; however we note this can be solved for T_G using any one of three methods:

1. Integrating factor method - restating the equation in the correct form and solving analytically/numerically as usual.
2. Finite difference approximation - by discretising the equation as usual.
3. Substitution (discussed below).

These have been included for completeness and verification of numerical results used. Since we have an analytical expression for the temperature of the solid $\bar{u}$ in the core, we may manipulate equations (7.29)–(7.37) to reduce the system to a

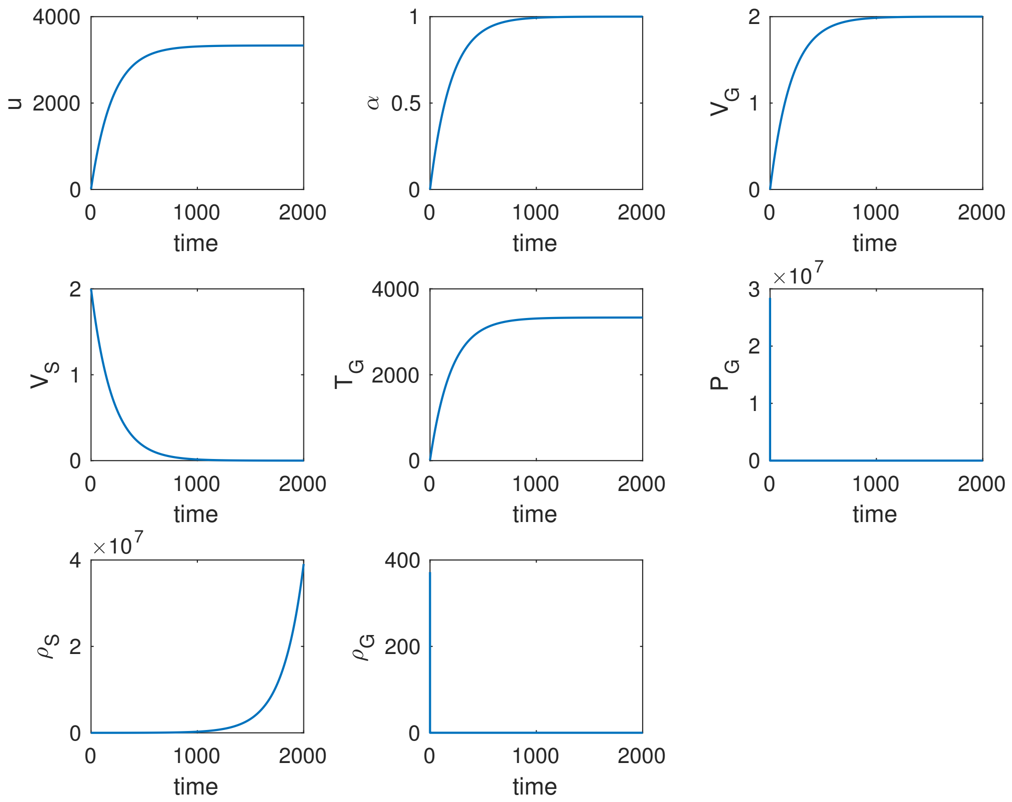

Figure 7.7: Solutions to equations (7.29)-(7.37) solved using mild parameter values.

single non-linear equation for $T_G(\alpha)$ which can be solved numerically. Equation (7.38) is obtained by substituting (7.32)–(7.33) and (7.35)–(7.37) into (7.34). This gives the expression

$$\frac{dT_G}{d\alpha} = (\bar{\Omega}\alpha + \bar{C} - T_G)\left(\frac{M_T - 2Ac_3\alpha^{1-1/\gamma}T_G^{1/\gamma}}{2c_3(1-A\alpha)\alpha^{1-1/\gamma}T_G^{1/\gamma}}\right), \tag{7.38}$$

where $c_3 = \left(\frac{nR}{2Ac_1}\right)^{1/\gamma}$, $c_1 = \frac{P_G(0)}{\rho_G(0)^\gamma}$ and $\gamma = 1.4$. From equation (7.38), we can see that as $t \to \infty$, $\alpha \to 1$ and thus $T_G \to \bar{\Omega} + \bar{C}$. As previously alluded to, the numerator in equation (7.26) may also tend to zero. To verify the numerator of equation (7.26) does not tend to zero it can be compared to the numerator in equation (7.38) such that

$$M_T - 2Ac_3\alpha^{1-1/\gamma}T_G^{1/\gamma} = M_T - \rho_G(t)V_G(t),$$

and hence $\rho_G V_G \to 2c_3(\bar{\Omega}+\bar{C})$ as $t \to \infty$ and $c_3 =$ constant. Below we have plotted this alternative method, using equation (7.38), for computing T_G using a root finder (`fzero` which uses a combination of bisection, secant and inverse quadratic interpolation methods to solve non-linear equations) implemented in `MATLAB`.

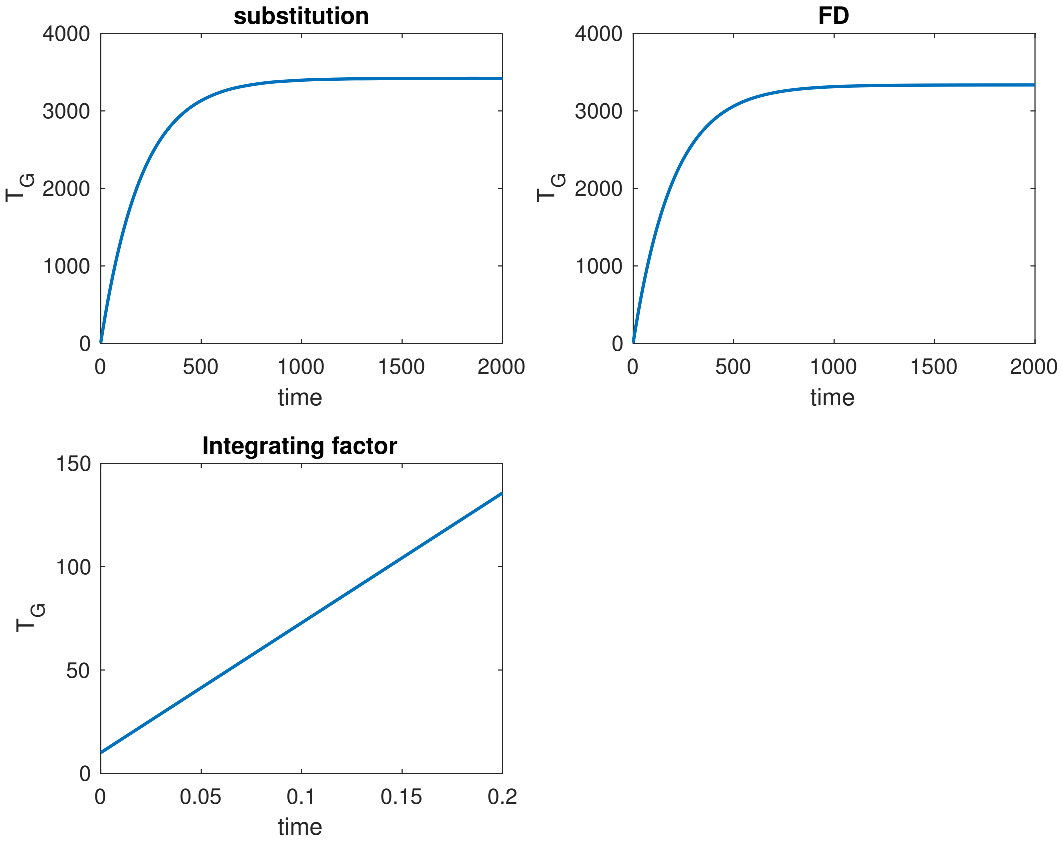

Figure 7.8: Solutions to equation (7.34) solved using a root finder, finite difference approximations and integrating factor methods (left to right, top to bottom).

In figure 7.8 the time range shown in the *Integrating factor* plot (bottom-right) is significantly shorter than that of the other two plots. This is because the analytical method becomes too sensitive for large times and becomes unstable. One clear benefit of the substitution method presented above is that we may consider small

α and thus small time t. From this we note that for $V_G(0) = 0$ both $P_G(0)$ and $\rho_G(0)$ are infinite, initially. We can use equation (7.38) to solve for $P_G(t)$ and $\rho_G(t)$ analytically for small times in order to overcome the initial infinite values. From (7.38), for $\alpha \ll 1$ we get

$$\frac{dT_G}{d\alpha} = (\bar{C} - T_G)\frac{M_T}{2c_3\alpha^{1-1/\gamma}T_G^{1/\gamma}} \tag{7.39}$$

If we take the expansion $T_G = b_0 + b_1\alpha^q + \ldots$ for $\alpha \ll 1$ then we get

$$qb_1\alpha^{q-1} = (\bar{C} - b_0)\frac{M_T}{2c_3\alpha^{1-1/\gamma}b_0^{1/\gamma}}. \tag{7.40}$$

Equating powers of α gives

$$\alpha^{q-1} = \frac{1}{\alpha^{1-1/\gamma}}, \implies q = 1/\gamma, \tag{7.41}$$

$$qb_1 = (\bar{C} - b_0)\frac{M_T}{2c_3b_0^{1/\gamma}}, \tag{7.42}$$

where b_0 represents the initial gas temperature and $\bar{C}$ represents the initial solid temperature. Hence, we have that initially, at small α and t,

$$P_G = \frac{nRT_G}{V_G} = \frac{nRb_0}{2A\alpha}, \tag{7.43}$$

$$\rho_G = \left(\frac{P_G}{c_1}\right)^{\frac{1}{\gamma}} = \left(\frac{nRb_0}{2Ac_1\alpha}\right)^q = c_3b_0^{\frac{1}{\gamma}}\alpha^{-\frac{1}{\gamma}}(\gg 1). \tag{7.44}$$

Comparisons of the full and core problems, using mild parameters, plotted in the same coordinates are shown below. We observe a high level of agreement between the two figures.

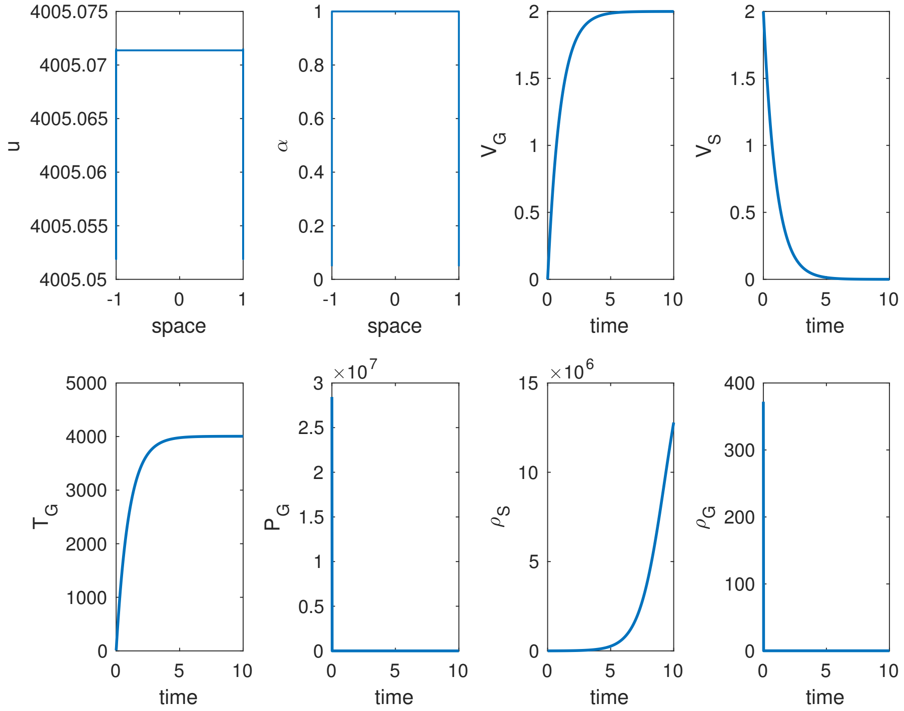

(a) Full problem

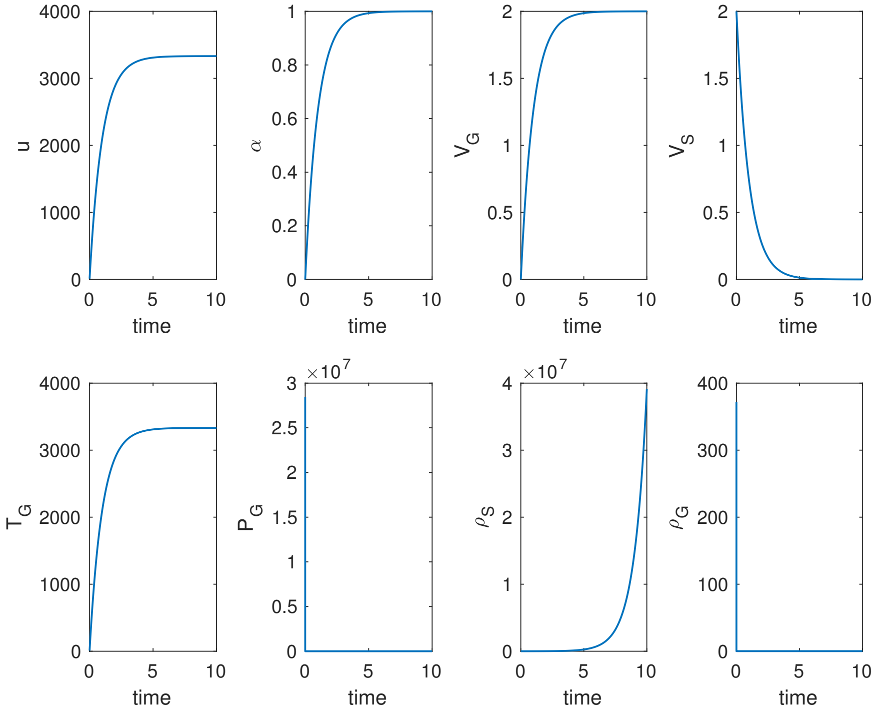

(b) Core problem

Figure 7.9: Comparison of full problem (figure (a) top) and core problem (figure (b) bottom) using mild parameter values.

7.5 Summary of chapter

In this chapter we improved and extended the model presented in chapter 6. We began by varying only the density of the solid and maintaining a constant gas density. This, although not physically accurate, provided a good starting point to consider varying both the density of the solid and gas. In section 7.1, we considered varying the density of the gas using the ideal gas law whilst varying the solid density through conservation of mass. This yielded some unexpected behaviour, for example an increase in the solid density, which led us to force the density of the solid to decrease and density of the gas to increase using strategically constructed algebraic expressions. This was a way in which we could test our model to ensure that the volumes were reaching the expected levels.

In section 7.3 we incorporated the varying densities into the solid calculations by allowing the density to vary within the solid temperature equation. This in turn had an effect on the extent of reaction and as a result the entire system of equations.

Finally, we allowed the densities to vary within the solid calculations in the asymptotic framework which is an extension of the model presented in section 6.2, chapter 6. A comparison of the full and asymptotic problems is presented, demonstrating close qualitative agreement between the two. This provides verification of the asymptotic approach which is easier to solve numerically and can occasionally produce analytical solutions.

In the next chapter we discuss internal heating of the solid by considering a constant gas temperature to begin with. We then vary the gas temperature with time and later consider the effects of parameters on the system using an asymptotic approach.

Chapter 8

Internal Heating

In this chapter we focus on heating the solid internally. Previously, in chapter 7 we only considered heating effects of the gas on the solid at the boundaries by allowing the gas temperature to heat the boundaries of the solid. Now we consider heating the solid internally as well as at the boundaries of the solid. The governing equations presented in earlier chapters only included one heating term, specifically the heat from the reaction represented by the term $\Omega \frac{\partial \alpha}{\partial t}$ in equation (7.19). In reality, there is heat being produced by the gas released from the reaction which penetrates the solid. This additional heat source can be represented by the term r_G say, where $r_G = \lambda_A H(T_G(t) - u(t))$. Here λ_A, [63] is the specific surface area of the gas/solid interface and H is the Robin heat transfer coefficient. Incorporating this additional heating term into the system, our governing equations become

$$\rho_S c_v \frac{\partial u}{\partial t} = \kappa \frac{\partial^2 u}{\partial x^2} + \rho_S \Omega \frac{\partial \alpha}{\partial t} + \lambda_A H(T_G(t) - u(t)), \tag{8.1}$$

$$\frac{\partial \alpha}{\partial t} = A(1-\alpha)\exp\left(-\frac{E}{Ru}\right). \tag{8.2}$$

The effect of internal heating is assumed to be spatially uniform throughout the solid. These form the basis for the studies in sections 8.1 - 8.4 below which consider, in succession, internal heating with constant gas temperature, internal heating with varying gas temperature, effects of the parameter $\bar{\lambda}\left(=\frac{\lambda_A H}{\rho_s c_v}\right)$, derived later, and finally, internal heating with both varying gas temperature as well as solid and gas densities. Section 8.5 provides a summary. We begin by treating the density of the solid, ρ_S, as constant and solve the system for u and α using mild parameter values given by table 8.1

Table 8.1: Mild parameters used in model.

Parameter with units	**Symbol**	**Value**
Conductivity (W/m/K)	κ	0.44
Specific Heat (J/kg/K)	c_v	1255.0
Heat of Reaction (J/kg)	Ω	$5.0208e6$
Molar Gas Constant (J/mol/K)	R	8.314
Activation Energy (J/mol)	E	10
Pre-exponential Constant (s^{-1})	A	200
Initial solid temperature $°K$	C	15
Number of moles of gas ($\frac{M}{mw}$)	n	0.0342
Specific surface area×Heat transfer coefficient	λH	1

8.1 Internal heating with constant gas temperature

First, motivated by the numerical and analytical findings in chapters 2 onwards we consider the (simpler) reduced problem in the core by scaling, such that equations (8.1) and (8.2) above become

$$\frac{\partial \bar{u}}{\partial \bar{t}} = \bar{\Omega}\frac{\partial \alpha}{\partial \bar{t}} + \bar{\lambda}(\bar{T_G} - \bar{u}(t)), \tag{8.3}$$

$$\frac{\partial \alpha}{\partial \bar{t}} = (1-\alpha)\exp\left(-\frac{1}{\bar{u}}\right), \tag{8.4}$$

respectively, where $\bar{\Omega} = \frac{\Omega R}{C_v E}$, $\bar{\lambda} = \frac{\lambda_A H}{\rho_S C_v A}$ and $\bar{T_G} = \frac{R}{E}T_G$. We set $\bar{T_G} =$ constant for all time and derive a numerical scheme for (8.3)–(8.4). For the first time step, following the initial condition, we derive the first order accurate finite difference scheme as follows

$$\frac{\partial \bar{u}}{\partial \bar{t}} = \frac{\bar{u}(\bar{t}) - \bar{u}(\bar{t}-\Delta\bar{t})}{\Delta\bar{t}},$$

which after some manipulating gives

$$\bar{u}(\bar{t}) = \frac{\bar{u}(\bar{t}-\Delta\bar{t}) + \bar{\lambda}\Delta\bar{t}\bar{T_G} + \Delta\bar{t}\bar{\Omega}(1-\alpha(\bar{t})\exp\left(-\frac{1}{\bar{u}(t-\Delta\bar{t})}\right)}{1+\bar{\lambda}\Delta\bar{t}}.$$

Here we have substituted (8.4) into (8.3) and taken $\lambda_A H = 1$ as an example such that $\bar{\lambda} = 2 \times 10^{-9}$, see table 8.2. We have also, as in previous sections lagged the exponential term such that $\bar{u}(\bar{t})$ is evaluated at the previous time step as $\bar{u}(\bar{t} - \Delta\bar{t})$ in the exponential. Similarly, we derive a first order scheme for α such that we get

$$\alpha(\bar{t}) = \frac{\alpha(t \bar{-} \Delta\bar{t}) + \Delta\bar{t} \exp\left(-\frac{1}{\bar{u}(\bar{t})}\right)}{1 + \Delta\bar{t} \exp\left(-\frac{1}{\bar{u}(\bar{t})}\right)}.$$

We note here that the exponential term is not lagged since $\bar{u}(\bar{t})$ has already been computed. Once we have used the first order schemes for α and $\bar{u}$ to initiate the numerical schemes, we may then implement second-order accurate schemes for $\bar{u}$ and α, which are given by

$$\begin{aligned}
\bar{u}(\bar{t}) &= \frac{4\bar{u}(\bar{t} - \Delta\bar{t}) - \bar{u}(\bar{t} - 2\Delta\bar{t}) + 2\Delta\bar{t}\bar{\lambda} T_G + 2\Delta\bar{t}\bar{\Omega}(1 - \alpha(\bar{t})) \exp\left(-\frac{1}{\bar{u}(\bar{t} - \Delta\bar{t})}\right)}{3 + 2\Delta\bar{t}\bar{\lambda}}, \\
\alpha(\bar{t}) &= \frac{2\Delta\bar{t} \exp\left(-\frac{1}{\bar{u}(\bar{t} - \Delta\bar{t})}\right) + 4\alpha(\bar{t} - \Delta\bar{t}) - \alpha(\bar{t} - 2\Delta\bar{t})}{3 + 2\Delta\bar{t} \exp\left(-\frac{1}{\bar{u}(\bar{t} - \Delta\bar{t})}\right)}.
\end{aligned}$$

We may solve equations (8.3) and (8.4) using the numerical schemes above, and hence calculate the volumes of both gas and solid in the core region using

$$V_G(t) = 2Ax_0\alpha, \tag{8.5}$$

$$V_S(t) = 2 - V_G(t), \tag{8.6}$$

as derived in section 7.4 of chapter 7. At this stage, we do not compute the gas pressure or densities since these rely on the gas temperature $\bar{T}_G$ which we have set to be constant; calculating these quantities with a constant gas temperature would not provide meaningful results. We observe from figure 8.1 the temperature of the solid is lower than expected (lower than those presented in figure 7.9a). This could be a result of a low (constant) gas temperature. Taking a range of values for $T_G = 10, 100, 500, 1000$ we observe in figure 8.2 the way in which the temperature of the gas affects the temperature profile of the solid through internal heating. We

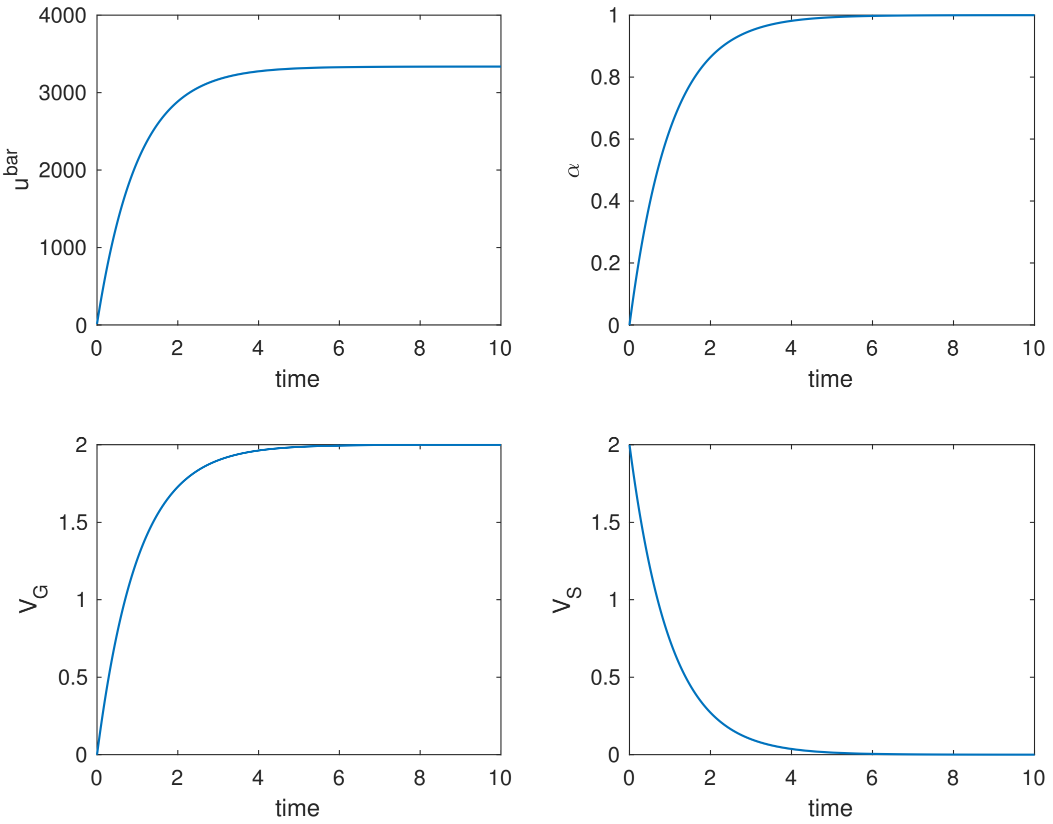

Figure 8.1: Solutions of equations (8.3) – (8.6), for a fixed gas temperature $\bar{T}_G = (R/E)T_G$ where $T_G = 10$ and mild parameter values with $\lambda H = 1$.

see from figure 8.2 that although the temperature of gas T_G was increased from $T_G = 10$ to $T_G = 1000$, the temperature peak barely changed. This suggests that we may need to consider varying the temperature of the gas over time such that $T_G = T_G(t)$. The extent of reaction α and volumes of both gas V_G, and solid V_S, are unaffected by the temperature of the gas T_G, which is due to the fact that the volumes depend on α. Although α depends on the temperature of the solid u, which depends on the temperature of the gas T_G, the influence of T_G on α (and thus V_G and V_S) is negligible and does not change qualitatively from figure 8.1.

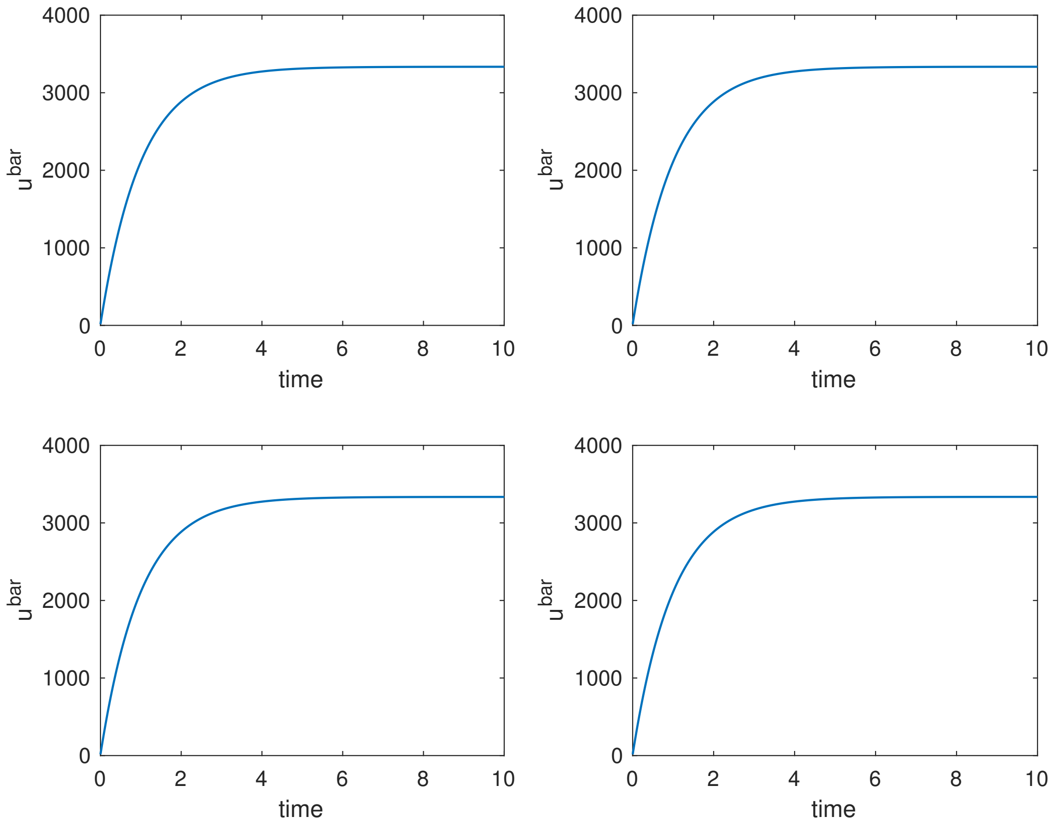

Figure 8.2: Solutions of solid temperature $\bar{u}$ for range of T_G values ranging from $T_G = 10$ (top left), $T_G = 100$ (top right), $T_G = 500$ (bottom left) and $T_G = 1000$ (bottom right). Here $\lambda H = 1$ is fixed and thus $\bar{\lambda} \approx 10^{-9}$.

8.2 Internal heating with varying gas temperature

In the previous section we investigated the effects of internal heating on the solid, and thus the effects on the extent of reaction and volumes of both gas and solid, by considering a constant temperature of gas. We now consider varying the temperature of the gas with time such that $\bar{T}_G = \bar{T}_G(t)$. This leads to a system of three equations to solve, specifically

$$\frac{\partial \bar{u}}{\partial \bar{t}} = \bar{\Omega}\frac{\partial \alpha}{\partial \bar{t}} + \bar{\lambda}(\bar{T}_G(\bar{t}) - \bar{u}(\bar{t})), \tag{8.7}$$

$$\frac{\partial \alpha}{\partial \bar{t}} = (1-\alpha)\exp\left(-\frac{1}{\bar{u}}\right), \tag{8.8}$$

$$\frac{d\bar{T}_G}{d\bar{t}} = \frac{\rho_S}{\rho_G V_G(t)}\left(\bar{u}(\bar{t}) - \bar{T}_G(\bar{t})\right)\frac{dV_G(t)}{d\bar{t}}, \tag{8.9}$$

where as in section 8.1 we have set the densities of both solid and gas as constants. In chapter 7 we derived equation (7.34) which we restate here as equation (8.9) which contributes to the internal heating of the solid.

Equation (8.9) follows from (7.34) where $T_{AV}(t) = \bar{u}(t)$ in the core and here ρ_S and ρ_G are constants. A first-order accurate scheme is derived using a backwards difference in time, which when rearranged gives the following schemes to update $\alpha(t)$, $\bar{u}(t)$ and $\bar{T}_G(t)$ respectively

$$
\begin{aligned}
\alpha(\bar{t}) &= \frac{\alpha(t\,\bar{-}\,\Delta\bar{t}) + \Delta\bar{t}\exp\left(-\frac{1}{\bar{u}(\bar{t}-\Delta\bar{t})}\right)}{1+\Delta\bar{t}\exp\left(-\frac{1}{\bar{u}(\bar{t}-\Delta\bar{t})}\right)},\\
\bar{u}(\bar{t}) &= \frac{\bar{u}(\bar{t}-\Delta\bar{t}) + \Delta\bar{t}\bar{\lambda}\bar{T}_G + \Delta\bar{t}\bar{\Omega}(1-\alpha(\bar{t})\exp\left(-\frac{1}{\bar{u}(t\,\bar{-}\,\Delta\bar{t})}\right)}{1+\Delta\bar{t}\bar{\lambda}},\\
\bar{T}_G(\bar{t}) &= \frac{\bar{T}_G(\bar{t}-\Delta\bar{t}) + \frac{\Delta\bar{t}\rho_S}{\rho_G V_G(t)}\frac{dV_G}{d\bar{t}}\bar{u}(\bar{t})}{1+\frac{\Delta\bar{t}\rho_S}{\rho_G V_G(t)}\frac{dV_G}{d\bar{t}}}.
\end{aligned}
$$

A second-order accurate scheme, which is implemented after the first time point, (derived using similar methods) for $\alpha(t)$, $\bar{u}(t)$ and $\bar{T}_G(t)$ is given below.

$$
\begin{aligned}
\alpha(\bar{t}) &= \frac{2\Delta\bar{t}\exp\left(-\frac{1}{\bar{u}(\bar{t}-\Delta\bar{t})}\right) + 4\alpha(\bar{t}-\Delta\bar{t}) - \alpha(\bar{t}-2\Delta\bar{t})}{3+2\Delta\bar{t}\exp\left(-\frac{1}{\bar{u}(\bar{t}-\Delta\bar{t})}\right)},\\
\bar{u}(\bar{t}) &= \frac{4\bar{u}(\bar{t}-\Delta\bar{t}) - \bar{u}(\bar{t}-2\Delta\bar{t}) + 2\Delta\bar{t}\bar{\lambda}\bar{T}_G + 2\Delta\bar{t}\bar{\Omega}(1-\alpha(\bar{t}))\exp\left(-\frac{1}{\bar{u}(\bar{t}-\Delta\bar{t})}\right)}{3+2\Delta\bar{t}\bar{\lambda}},\\
\bar{T}_G(\bar{t}) &= \frac{4\bar{T}_G(\bar{t}-\Delta\bar{t}) - \bar{T}_G(\bar{t}-2\Delta\bar{t}) + \frac{2\Delta\bar{t}\rho_S}{\rho_G V_G(t)}\frac{dV_G}{d\bar{t}}\bar{u}(\bar{t})}{3+\frac{2\Delta\bar{t}\rho_S}{\rho_G V_G(t)}\frac{dV_G}{d\bar{t}}}.
\end{aligned}
$$

We observe in figure 8.3 that the temperatures of the gas and solid are identical as is expected in the core region. From figure 8.3, we may conclude that the internal heating effects on the temperature of the solid thus far are negligible since figure 8.3 closely agrees with figure 7.9b which does not include an internal heating term. However, the agreement between figure 8.3 and figure 7.9b confirms that the method of incorporating internal heating into the system of equations has been successful and suggests the numerical schemes have been implemented well. The negligible

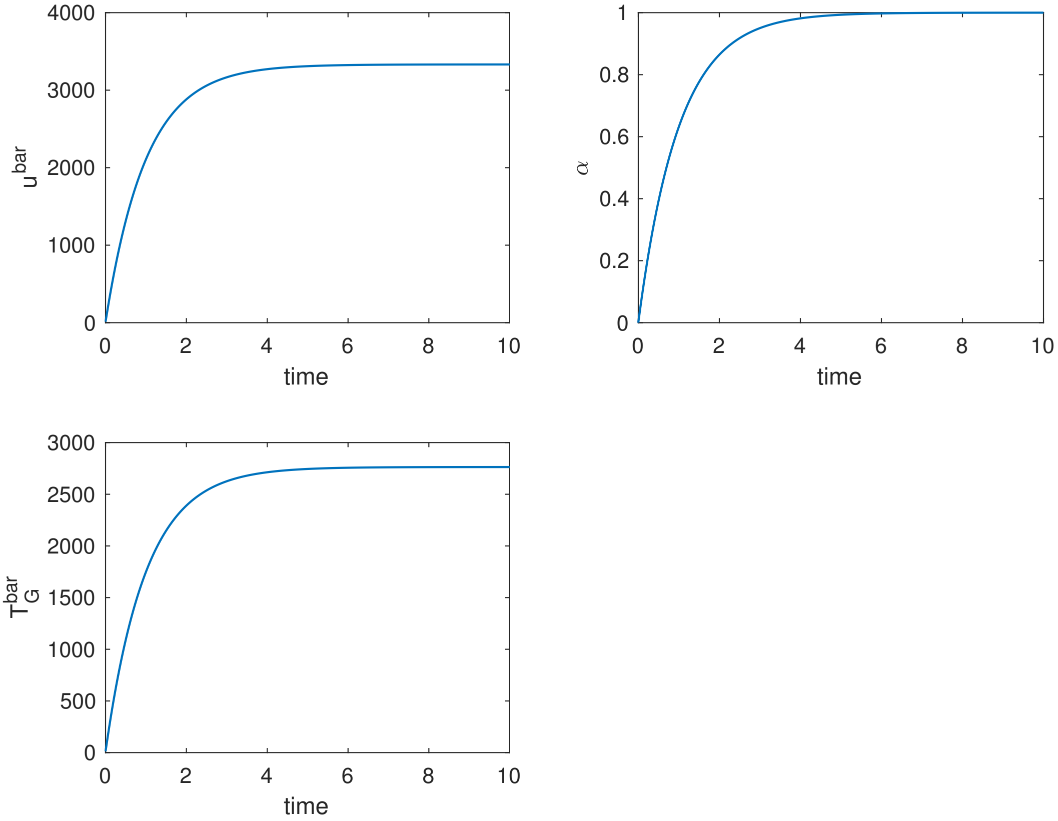

Figure 8.3: Solutions of equations (8.7)–(8.9) for mild parameter values. Here we have set $\lambda H = 1$ and $\bar{T}_G(0) = 10$.

effect of internal heating here (figure 8.3) could potentially be a result of the small $\bar{\lambda}$ term in equation (8.7), where $\bar{\lambda} \ll 1 (\approx \mathscr{O}(10^{-9}))$ for $\lambda H = 1$. We may test the effect of the parameter $\bar{\lambda}$ on the system by varying the numerator λH in $\bar{\lambda}$ whilst keeping the denominator $\rho_S C_v A$ fixed. Table 8.2 lists a range of λH values and their corresponding $\bar{\lambda}$ values. In reality the factor λH would need to be much larger than 10^{10} in order to balance the denominator of $\bar{\lambda}$ when using the physical parameter values, specifically that of $A = 10^{19}$ which dominates. In practice however, we cannot pick and choose the value of the specific surface area λ_A and hence the value of the coefficient λH, which means the term $\bar{\lambda}$ is small and internal heating is negligible in the current framework.

Taking the largest λH value of 10^{10} which results in $\bar{\lambda} = 2 \times 10^{-3}$, the effect on the internal heating of the solid is shown below in figure 8.4. Comparing figures

Table 8.2: Range of λH values and their corresponding $\bar{\lambda}$ values for otherwise mild parameters ($\rho_S = 1800$, $C_v = 1255$ and $A = 200$).

λH	$\bar{\lambda}$
1	2×10^{-9}
10	2×10^{-8}
100	2×10^{-7}
10^3	2×10^{-6}
10^4	2×10^{-5}
10^5	2×10^{-4}
10^6	2×10^{-3}
⋮	⋮
10^{10}	22.13

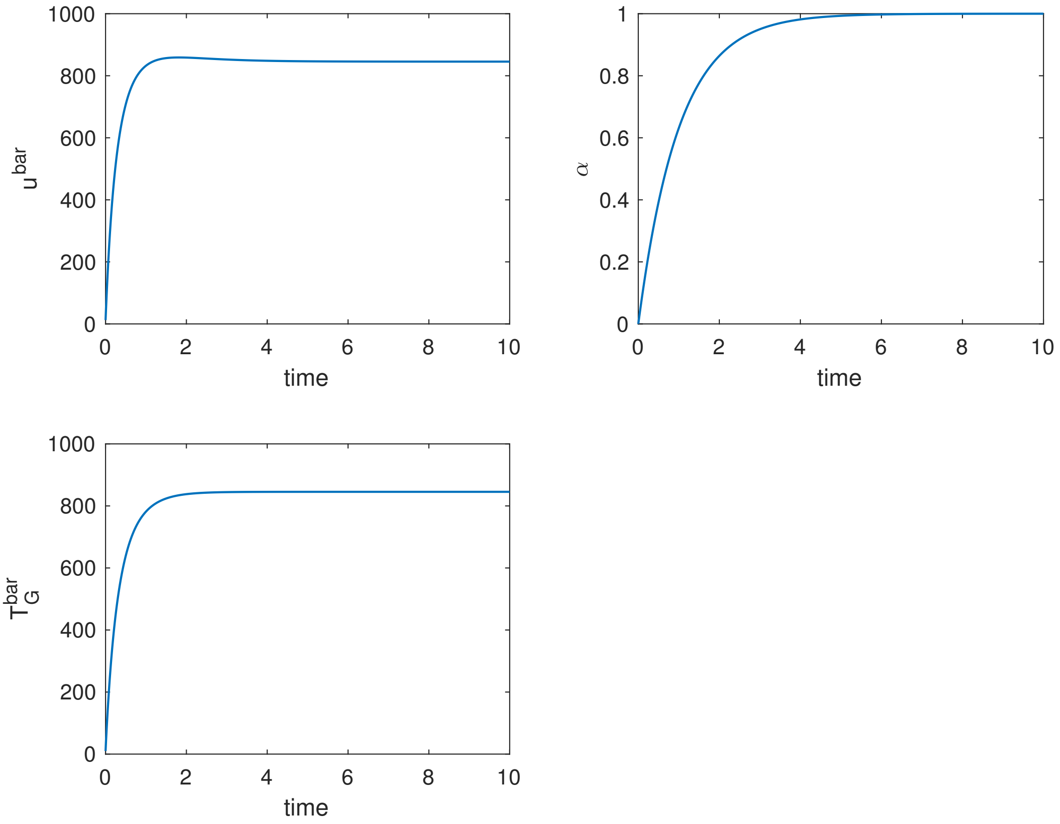

Figure 8.4: Solutions of equations (8.7)–(8.9) for $\bar{u}$, α and $\bar{T}_G$ respectively. Here we have used mild parameter values and set $\lambda H = 10^{10}$.

8.3 and 8.4, we observe that for larger λH values, and hence larger $\bar{\lambda}$ values, the temperatures of the gas and solid are lower than those with small λH values. To explore the relationship between λH values and temperature profiles, figure 8.5 displays the temperatures $\bar{u}$ and $\bar{T}_G$ as well as the extent of reaction α for increasing λH values. Here the green line corresponds to the largest λH value (shown in figure 8.4). We note that α remains unchanged for varying values of $\bar{\lambda}$.

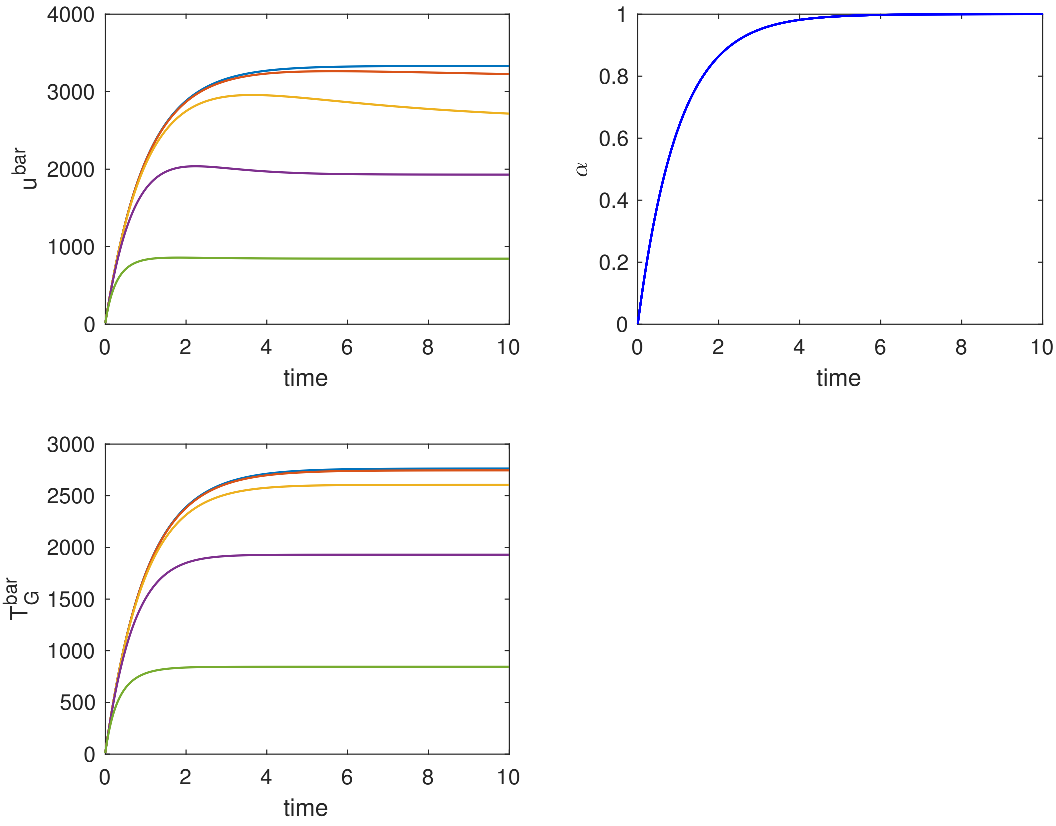

Figure 8.5: Solutions of equations (8.7)–(8.9) for $\bar{u}$, α and $\bar{T}_G$ respectively. Here we have used mild parameters with varying λH values starting at $\lambda H = 1$ (blue) and increasing to $\lambda H = 10^7$ (red) up to $\lambda H = 10^{10}$ (green).

Taking equations (8.7)–(8.9) for extremely mild parameter values, namely $\bar{\Omega} =$

1, $\bar{\lambda} = 1$ and $\rho_S = \rho_G = 1$ gives the system

$$\frac{\partial \bar{u}}{\partial \bar{t}} = \frac{\partial \alpha}{\partial \bar{t}} + \bar{T}_G(t) - \bar{u}(t), \tag{8.10}$$

$$\frac{\partial \alpha}{\partial \bar{t}} = (1-\alpha)\exp\left(-\frac{1}{\bar{u}}\right), \tag{8.11}$$

$$\frac{d\bar{T}_G}{d\bar{t}} = \frac{\frac{\partial \alpha}{\partial \bar{t}}}{\alpha(\bar{t})}\left(\bar{u}(\bar{t}) - \bar{T}_G(\bar{t})\right), \tag{8.12}$$

where we have set $\frac{dV_G(t)}{d\bar{t}} = 2A\frac{\partial \alpha}{\partial \bar{t}}$ and $V_G(\bar{t}) = 2A\alpha$. Hence, the numerical solution of equations (8.10)–(8.12), obtained using finite difference schemes, is presented in figures 8.6a-8.6b for different ratios of ρ_S/ρ_G. We observe from figures 8.6a-8.6b that as the ratio ρ_S/ρ_G increases, the temperature profiles $\bar{u}$ and $\bar{T}_G$ approach each other and peak quicker than for lower ρ_S/ρ_G ratios. The profile of the extent of reaction α remains virtually unchanged. This motivates the analytical study below.

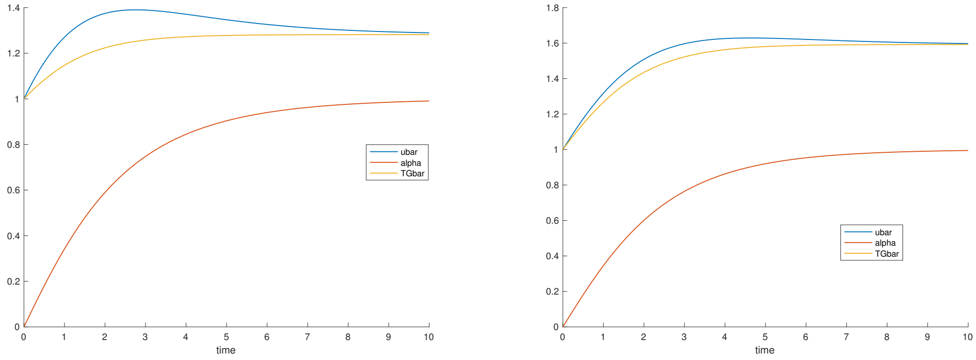

(a) $\bar{\Omega} = 1$, $\bar{\lambda} = 1$ and $\rho_S/\rho_G = 1$ **(b)** $\bar{\Omega} = 1$, $\bar{\lambda} = 1$ and $\rho_S/\rho_G = 5$

Figure 8.6: Solutions of equations (8.10)–(8.12) for different ρ_S/ρ_G ratios.

8.3 Asymptotic behaviour fr extreme values of $\bar{\lambda}$

Following the brief investigation on the effects of the coefficient $\bar{\lambda}$ in the previous section, we now consider the asymptotic behaviour of $\bar{\lambda}$ and the resulting effect on the system of equations which we restate below for convenience.

$$\frac{\partial \bar{u}}{\partial \bar{t}} = \bar{\Omega}\frac{\partial \alpha}{\partial \bar{t}} + \bar{\lambda}(\bar{T}_G(\bar{t}) - \bar{u}(\bar{t})), \tag{8.13}$$

$$\frac{\partial \alpha}{\partial \bar{t}} = (1-\alpha)\exp\left(-\frac{1}{\bar{u}}\right), \tag{8.14}$$

$$\frac{d\bar{T}_G}{d\bar{t}} = \frac{\rho_S}{\rho_G V_G(t)}\left(\bar{u}(\bar{t}) - \bar{T}_G(\bar{t})\right)\frac{dV_G(t)}{d\bar{t}}. \tag{8.15}$$

For the following cases which are presented in this section, we fix the quantities $\bar{\Omega} = 1$, $\rho_S = 1800$ and $\rho_G = 372$ such that the ratio $\frac{\rho_S}{\rho_G} \approx 5$. We also have here from previous working that $\frac{\frac{dV_G}{dt}}{V_G} = \frac{\frac{d\alpha}{dt}}{(\alpha+\varepsilon)}$ but with the non-negative constant ε being introduced to avoid a possible singularity at time zero where $V_G \approx 0$. However, if the temperatures $\bar{T}_G$ and $\bar{u}$ are equal at time zero then ε can be taken to be zero.

In figures 8.7 and 8.8, we demonstrate the effects of increasing and decreasing (respectively) the parameter $\bar{\lambda}$. We find in figures 8.7 and 8.8, that for small $\bar{\lambda}$ the effects of internal heating are negligible and for small $\bar{\lambda}$ values the temperatures of both solid and gas increase. For comparison, we show in figure 8.9 the effects of varying $\bar{\lambda}$ (by gradually increasing $\bar{\lambda}$), on the temperatures $\bar{u}$ and $\bar{T}_G$ as well as the extent of reaction α. Here $\bar{\lambda} = \frac{\lambda H}{\rho_S C_v A}$, where $\rho_S, C_v,$ and A are fixed and in order to vary $\bar{\lambda}$ the constant λH is changed.

8.3.1 $\bar{\lambda} \ll 1$

To investigate the asymptotic behaviour of the coefficient $\bar{\lambda}$ we consider first the effects of $\bar{\lambda} \ll 1$. There are two time scales $\bar{t}$ which arise if $\bar{\lambda}$ is small, $\bar{t} = \mathscr{O}(1)$ and $\bar{t} = \mathscr{O}\left(\frac{1}{\bar{\lambda}}\right)$; these are discussed in the sections below.

8.3.1.1 $\bar{t} = \mathscr{O}(1)$

Firstly, $\bar{t} = \mathscr{O}(1)$; we may solve the system (8.13)–(8.15) for small $\bar{\lambda}$ by setting $\bar{\lambda} = 0$ in equation (8.7) since to leading order we neglect the $\bar{\lambda}$ term, such that, after

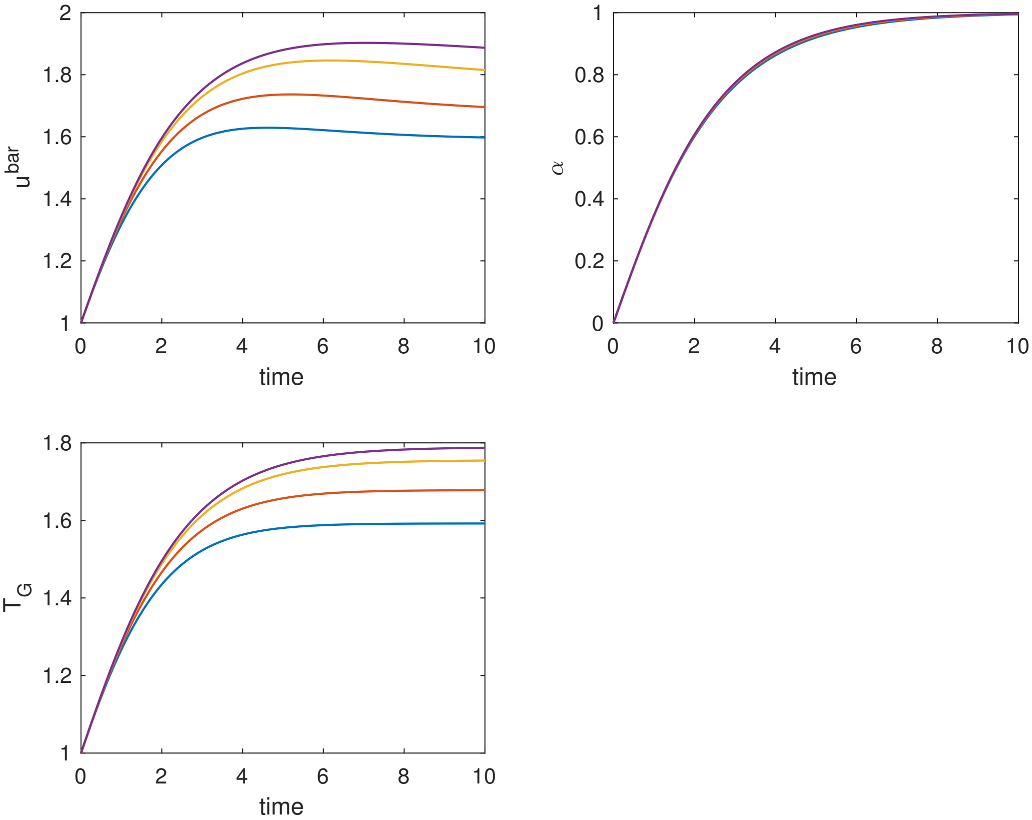

Figure 8.7: Solutions of equations (8.13)–(8.15) for $\bar{u}$, α and $\bar{T}_G$ respectively. Here we have used mild parameters with varying $\bar{\lambda}$ values starting at $\bar{\lambda} = 1$ (blue) and decreasing to $\bar{\lambda} = 0.1$ (purple). The parameter $\bar{\Omega} = 1$ is fixed, as is the ratio $\rho_S/\rho_G = 5$.

some work, we obtain

$$\bar{u} = \bar{\Omega}\alpha + \bar{C}, \tag{8.16}$$

$$\frac{\partial \alpha}{\partial \bar{t}} = (1-\alpha)\exp\left(-\frac{1}{\bar{u}}\right), \tag{8.17}$$

$$\frac{d\bar{T}_G}{d\bar{t}} = \frac{\rho_S}{\rho_G V_G(t)}\left(\bar{\Omega}\alpha + \bar{C} - \bar{T}_G(\bar{t})\right)\frac{dV_G(t)}{d\bar{t}}, \tag{8.18}$$

where $\bar{C}$ represents the initial solid temperature. The forms (8.16), (8.17) are exactly as in chapter 2. Since, in this case, $\rho_S = 1800$ and $\rho_G = 372$ are constants, equation

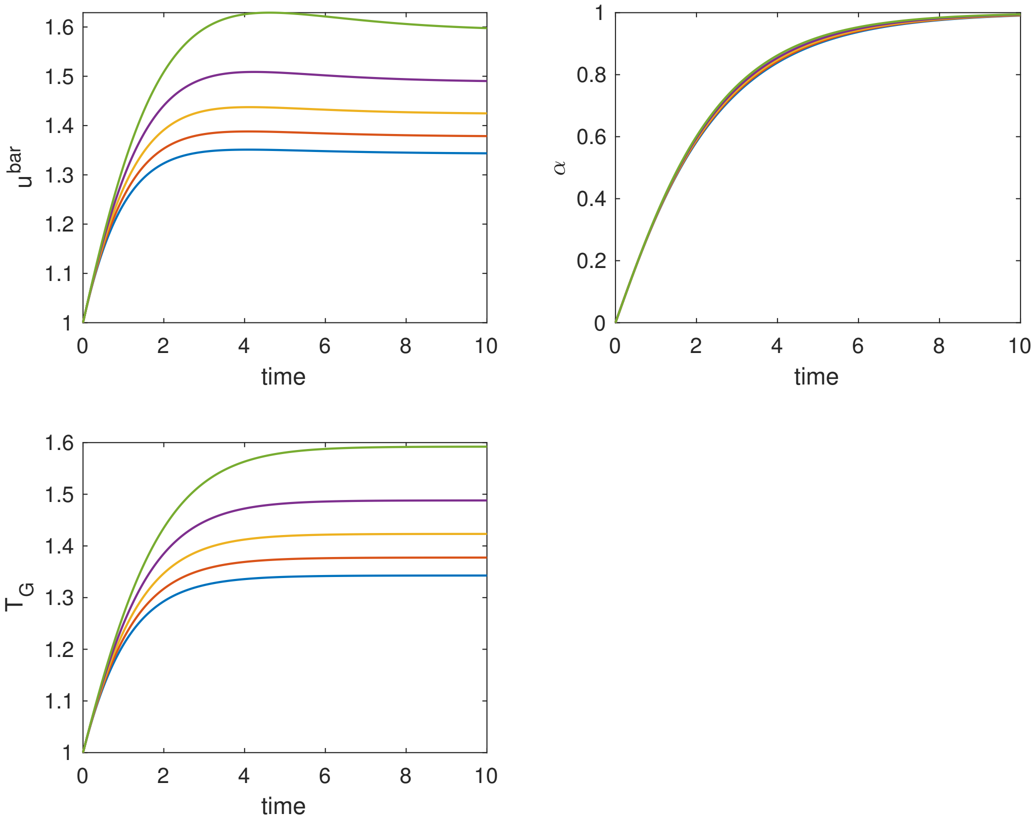

Figure 8.8: Solutions of equations (8.13)–(8.15) for $\bar{u}$, α and $\bar{T}_G$ respectively. Here we have used mild parameters with varying $\bar{\lambda}$ values starting at $\bar{\lambda} = 1$ (blue) and increasing to $\bar{\lambda} = 5$ (green). The parameter $\bar{\Omega} = 1$ is fixed, as is the ratio $\rho_S/\rho_G = 5$.

(8.18) becomes after some manipulation

$$\frac{d\bar{T}_G}{d\alpha} = \frac{5}{\alpha}(\bar{\Omega}\alpha + \bar{C} - \bar{T}_G). \tag{8.19}$$

where the ratio $\rho_S/\rho_G = 5$ in equation (8.18), $V_G(t) = 2A(\alpha + \varepsilon)$ but with ε set to zero since we are now focussing on the case of $\bar{T}_G, \bar{u}$ being equal initially and $\frac{dV_G(t)}{d\bar{t}} = 2A\frac{\partial\alpha}{\partial\bar{t}}$. We will use the value 5 for the density ratio ρ_S/ρ_G for convenience and also to provide more explicit results.

We can solve equation (8.19) both analytically and numerically. Solving ana-

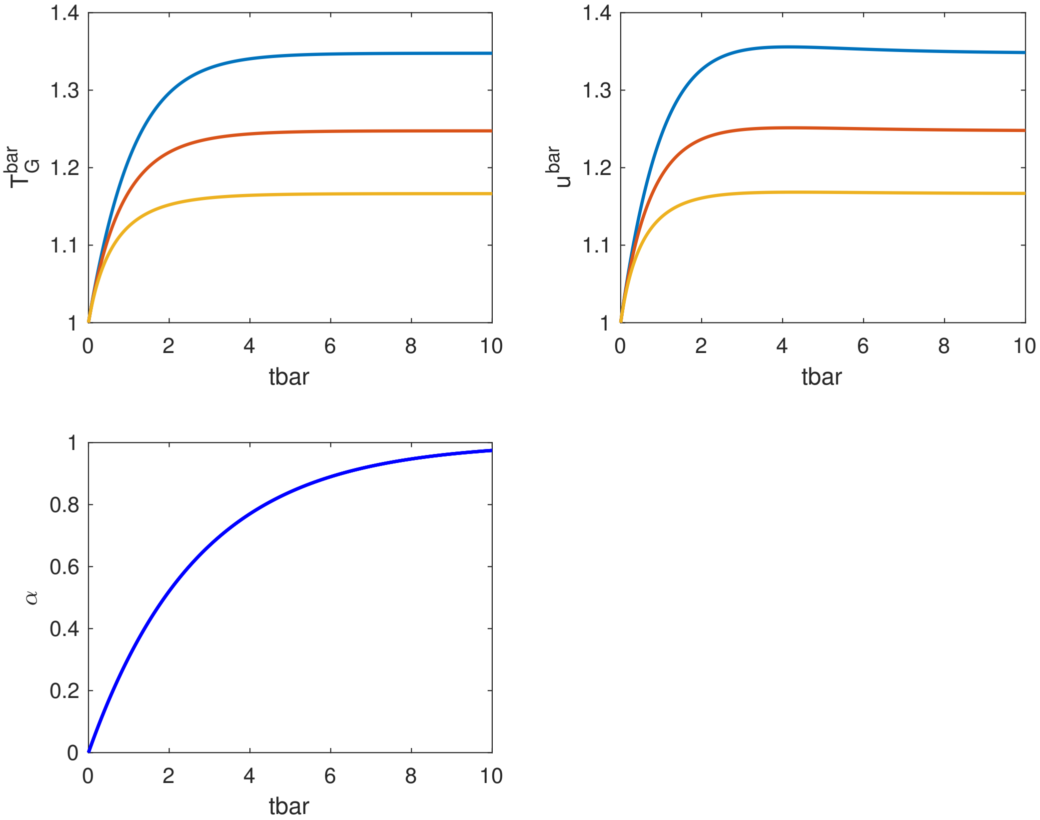

Figure 8.9: Solutions of full problem, given by equations (8.7)–(8.9) for T_G, u and α respectively. Here we have used very mild parameter values, $\Omega = R = C_v = E = A = 1$ and the ratio $\rho_S/\rho_G \approx 5$ as well as $T_G(0) = u(0) = 1$ initially. The blue line corresponds to $\bar{\lambda} = 5$, the red $\bar{\lambda} = 10$ and the yellow $\bar{\lambda} = 20$.

lytically, using the integrating factor method, yields the solution

$$\bar{T_G} = \bar{C} + \frac{5}{6}\bar{\Omega}\alpha. \tag{8.20}$$

To solve (8.19) numerically, we derive the following first and second-order accurate finite difference schemes

$$\bar{T_G}(\alpha) = \frac{\bar{T_G}(\alpha - \Delta\alpha) + 5\Delta\alpha(\bar{\Omega} + \frac{\bar{C}}{\alpha})}{1 + \frac{5\Delta\alpha}{\alpha}},$$
$$\bar{T_G}(\alpha) = \frac{4\bar{T_G}(\alpha - \Delta\alpha) - \bar{T_G}(\alpha - 2\Delta\alpha) + \frac{5}{\alpha}2\Delta\alpha(\bar{\Omega}\alpha + \bar{C}) + 2\Delta\bar{t}\bar{\lambda}}{3 + \frac{5}{\alpha}2\Delta\alpha}.$$

Comparing the analytical solution given by (8.20) with the numerical solution, presented in figure 8.10, we observe very close agreement between the two. One way

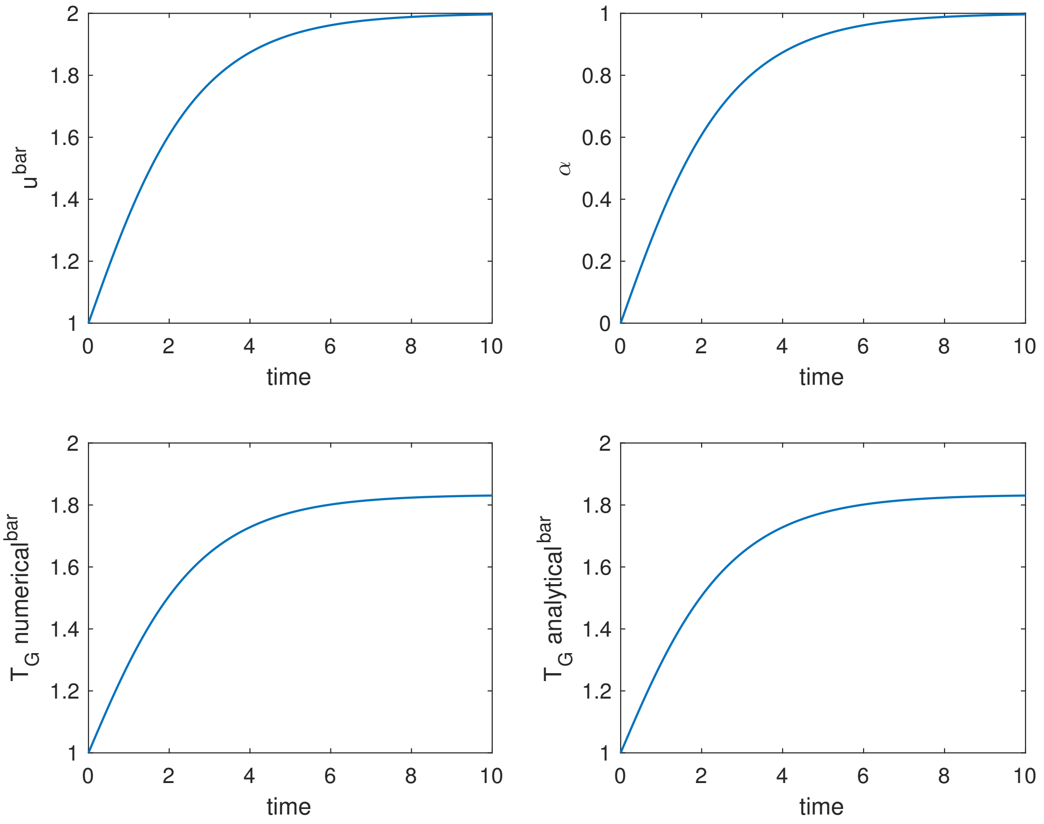

Figure 8.10: Solutions of equations (8.16)–(8.18), with comparison of analytical (8.20) and numerical solutions of equation (8.19); close agreement is demonstrated between the two methods. Here we have used mild parameter values, including $\bar{T}_G = 1$ initially and set $\bar{\lambda} = 0$.

in which we may verify the relationship given by equation (8.20) is demonstarted in figure 8.11. Here we observe that at early times the relationship between T_G and α is linear.

8.3.1.2 $\bar{t} = \mathscr{O}\left(\frac{1}{\bar{\lambda}}\right)$

The second time scale which arises when considering the effects of $\bar{\lambda} \ll 1$ is $\bar{t} = \mathscr{O}\left(\frac{1}{\bar{\lambda}}\right)$. Over a longer time scale $\alpha \rightarrow 1$ which implies that $\frac{\partial \alpha}{\partial \bar{t}} \rightarrow 0$ and hence the

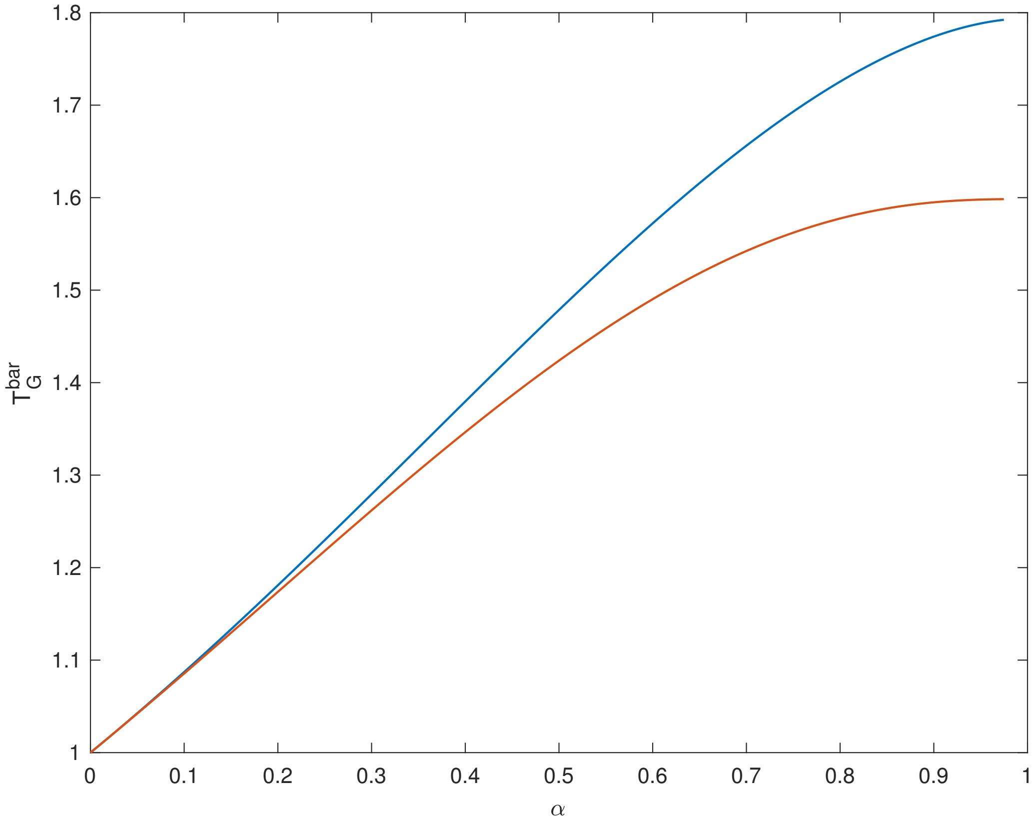

Figure 8.11: Solutions of equations (8.14)–(8.15) for $\bar{\lambda} = 1$ (red) and $\bar{\lambda} = 0.1$ (blue).

system (8.13)–(8.15) becomes

$$\frac{\partial \bar{u}}{\partial \bar{t}} = \bar{\lambda}\left(\bar{T}_G(\bar{t}) - \bar{u}(\bar{t})\right), \tag{8.21}$$

$$\frac{d\bar{T}_G}{d\bar{t}} = \frac{5}{\alpha}\left(\bar{u}(\bar{t}) - \bar{T}_G(\bar{t})\right)\frac{\partial \alpha}{\partial \bar{t}}, \tag{8.22}$$

since $\rho_S/\rho_G = 5$, $V_G(t) = 2A\alpha$ and $\frac{dV_G(t)}{d\bar{t}} = 2A\frac{\partial \alpha}{\partial \bar{t}}$. Therefore since $\frac{\partial \alpha}{\partial \bar{t}}$ is negligible, $\bar{T}_G$ is constant and equal to

$$\bar{T}_G = \frac{5\bar{\Omega}}{6} + \bar{C}, \tag{8.23}$$

throughout this time scale. The solution of (8.21) then gives

$$\bar{u} = \frac{5\bar{\Omega}}{6} + \bar{C} + \exp(-\bar{\lambda}\bar{t})\frac{\bar{\Omega}}{6}, \tag{8.24}$$

showing that the solid temperature gradually reduces to the gas temperature over the present long time scale. This trend agrees with that seen in figure 8.7 as $\bar{\lambda}$ is decreased.

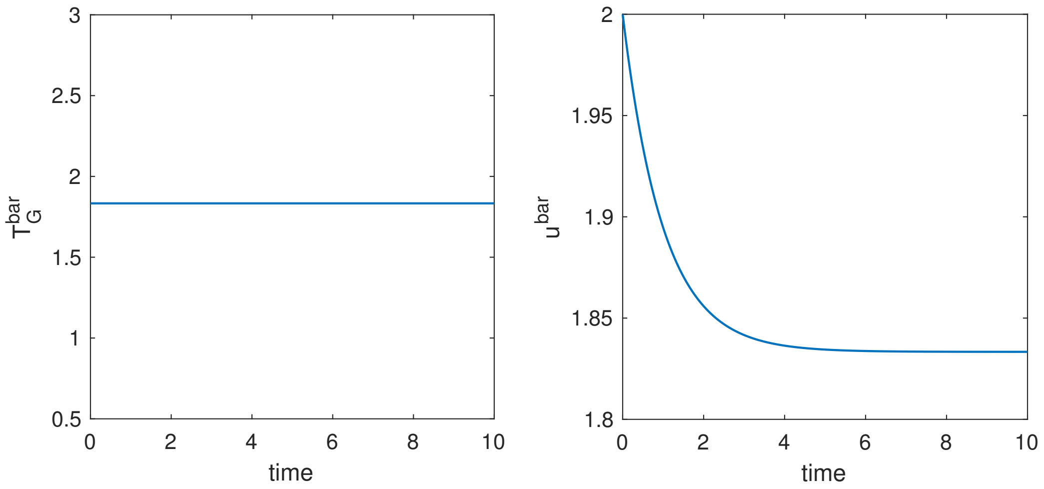

Figure 8.12: Solutions of equations (8.23)–(8.24) for $\bar{T}_G$ and $\bar{u}$ respectively. Here we have used mild parameter values, including $\bar{T}_G = 1$ initially and set $\bar{\lambda} = 1$.

8.3.2 $\bar{\lambda} \gg 1$

On the other hand, if we now consider $\bar{\lambda} \gg 1$ the first time scale which arises is $\bar{t} \sim \frac{1}{\bar{\lambda}}$ in the first instance, with say $\bar{t} = \bar{\lambda}^{-1} t^*$. The second time scale which occurs is $\bar{t} = \mathcal{O}(1)$. These are discussed in the subsections below.

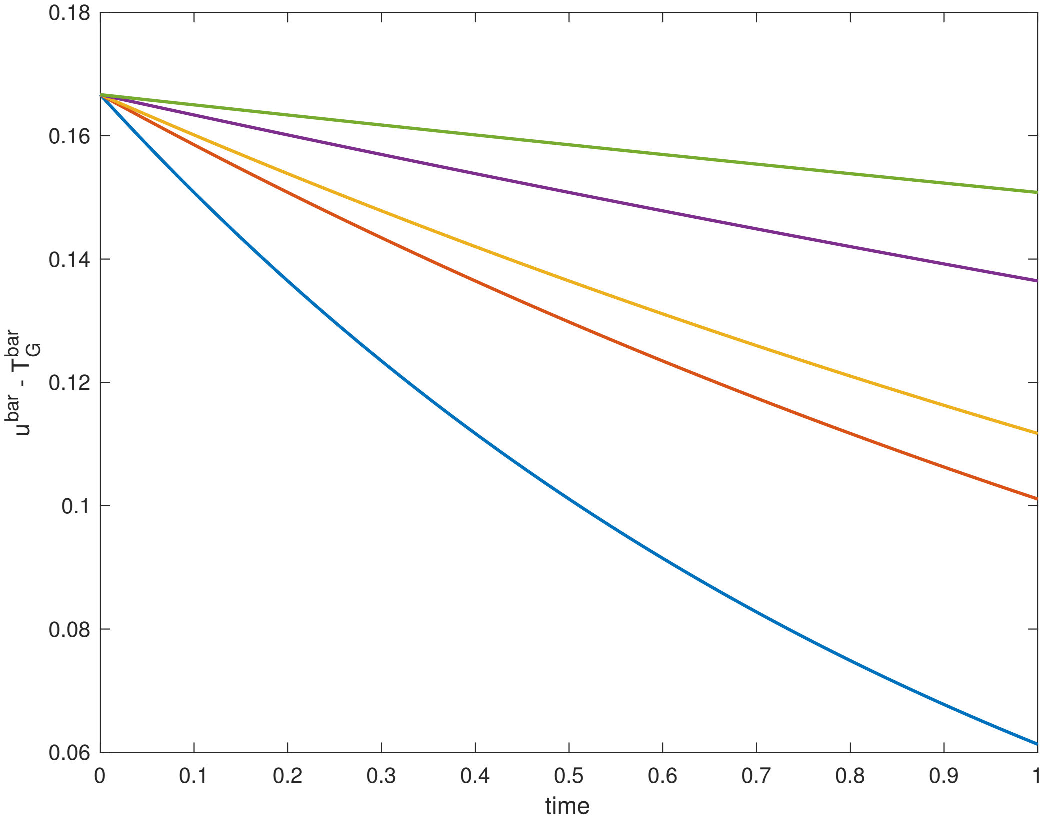

Figure 8.13: Solution of $\bar{u} - \bar{T}_G$ from equations (8.23)–(8.24). Here we have used mild parameter values, including $\bar{T}_G = 1$ initially and set $\bar{\lambda} = 1, 0.5, 0.4, 0.2, 0.1$ (blue, red, yellow, purple, green).

8.3.2.1 $\bar{t} = \bar{\lambda}^{-1} t^*$

The first time scale which arises is a short time scale. Let $\bar{t} = \bar{\lambda}^{-1} t^*$ and

$$\bar{u} = s + \bar{\lambda}^{-1} u_1^* + \dots,$$

$$\bar{T}_G = s + \bar{\lambda}^{-1} T_{G1}^* + \dots,$$

$$\alpha = \bar{\lambda}^{-1} \alpha^* + \dots$$

then equations (8.13)–(8.15) become

$$\frac{\partial u_1^*}{\partial t^*} = \bar{\Omega}\frac{\partial \alpha^*}{\partial t^*} + (T_{G1}^* - u_1^*), \tag{8.25}$$
$$\frac{\partial \alpha^*}{\partial t^*} = k, \tag{8.26}$$
$$\frac{\partial T_{G1}^*}{\partial t^*} = \frac{5}{\alpha^*}(u_1^* - T_{G1}^*)\frac{\partial \alpha^*}{\partial t^*}, \tag{8.27}$$

where $k = \exp\left(-\frac{1}{s}\right)$ and s is some constant. Equation (8.26) can be solved analytically to give

$$\alpha^* = kt^*. \tag{8.28}$$

Hence, equations (8.25)–(8.27) become

$$\frac{\partial u_1^*}{\partial t^*} = \bar{\Omega}k + (T_{G1}^* - u_1^*), \tag{8.29}$$
$$\frac{\partial T_{G1}^*}{\partial t^*} = \frac{5}{t^*}(u_1^* - T_{G1}^*), \tag{8.30}$$

Taking the difference between (8.29) and (8.30) gives

$$\begin{aligned}\frac{\partial u_1^*}{\partial t^*} - \frac{\partial T_{G1}^*}{\partial t^*} &= \bar{\Omega}k + (T_{G1}^* - u_1^*) - \frac{5}{t^*}(u_1^* - T_{G1}^*), \\ &= \bar{\Omega}k - (u_1^* - T_{G1}^*)(1 + \frac{5}{t^*}).\end{aligned}$$

If we now let $\psi = (u_1^* - T_{G1}^*)$ this implies $\frac{\partial u_1^*}{\partial t^*} - \frac{\partial T_{G1}^*}{\partial t^*} = \psi_{t^*}$ and hence we get

$$\psi_{t^*} = \bar{\Omega}k - \psi(1 + \frac{5}{t^*}). \tag{8.31}$$

Equation (8.31) can now be solved analytically to give

$$\psi = \exp(-t^*)t^{*-5}\bar{\Omega}k\left[\int_0^{t^*} \exp(t^*)t^{*5}dt^* + c_1\right], \tag{8.32}$$

where $c_1 = 0$ (since $u_0^* = T_{G0}^* \implies \psi_0 = 0$). We note here that from equation (8.31), $\psi \to \bar{\Omega}k$ as $t^* \to \infty$. Figure 8.14 shows the profile of ψ against t^*.

Figure 8.17 demonstrates the close agreement between the solutions given by

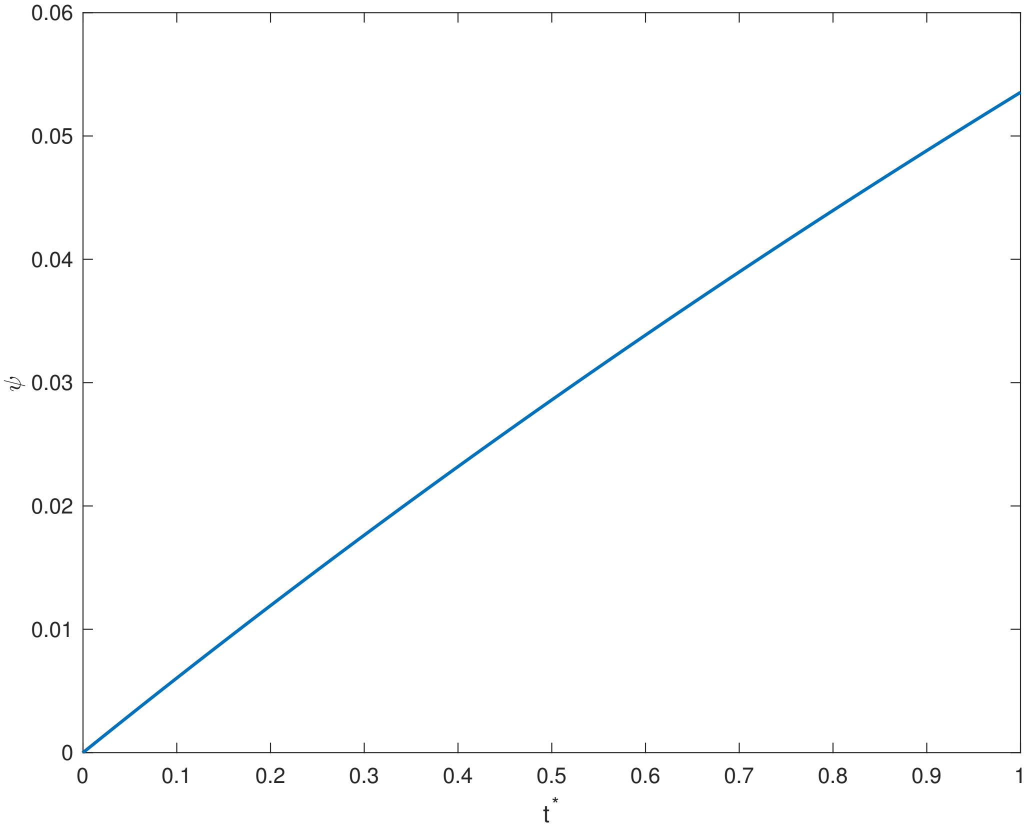

Figure 8.14: ψ vs t^*

$\psi = u_1^* - T_{G1}^*$ and $\bar{u} - \bar{T}_G$ for small time. We observe from Figure 8.16 that as $\bar{\lambda}$ gets larger, the solutions converge i.e. $u_1^* - T_{G1}^* \to \bar{u} - \bar{T}_G$ as $\bar{\lambda} \to \infty$. The results in figure 8.16 show clearly there is an inner time scale if $\bar{\lambda}$ is large.

Equation (8.29) can be rewritten as

$$\frac{\partial u_1^*}{\partial t^*} = \bar{\Omega}k - \psi,$$

and substituting in the expression for ψ given by (8.32) gives

$$\frac{\partial u_1^*}{\partial t^*} = \bar{\Omega}k - \frac{\bar{\Omega}k}{\exp(t^*)t^{*5}} \int_0^{t^*} \exp(t^*)t^{*5}dt^*. \tag{8.33}$$

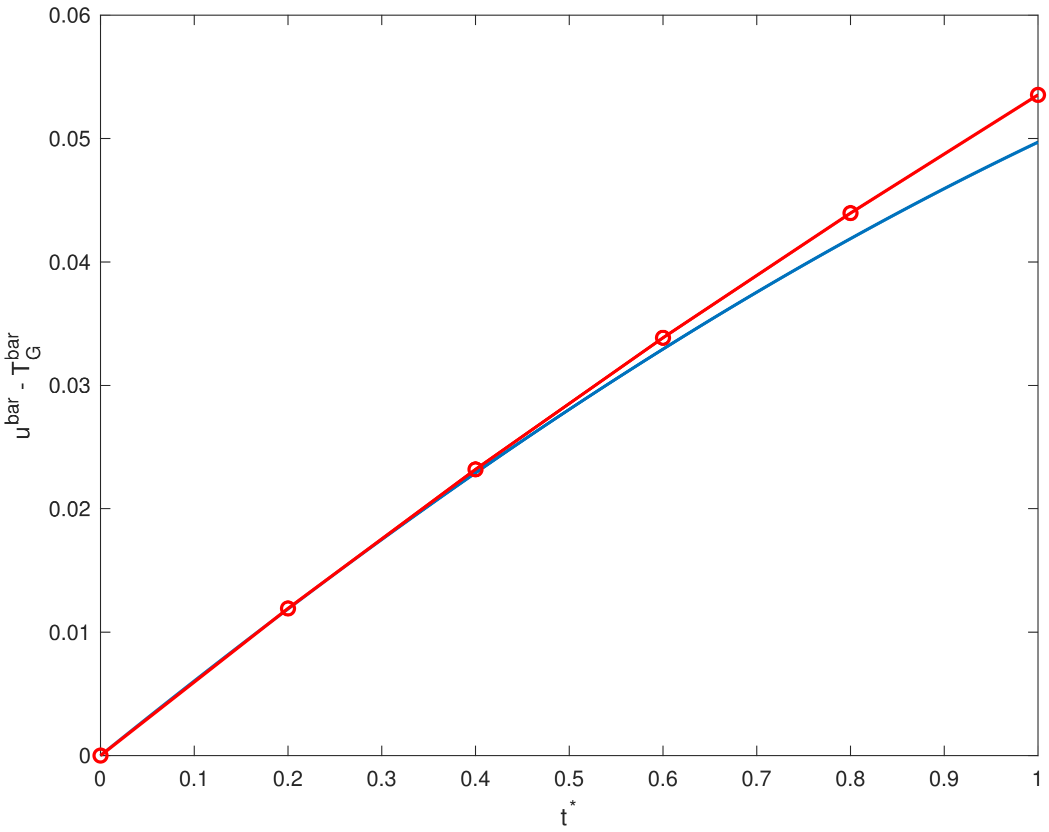

Figure 8.15: Solutions of equation (8.32) for $\psi = u_1^* - T_{G1}^*$ represented by the lines with circles, compared with $\bar{u} - \bar{T}_G$ from equations (8.7) and (8.9) represented by the solid lines. Here we have used the fixed ratio $\rho_S/\rho_G \approx 5$ and set $\bar{\lambda} = 1$.

By rewriting equation (8.33) as

$$\frac{\partial u_1^*}{\partial t^*} = \bar{\Omega}k - \frac{\bar{\Omega}k}{g} f \tag{8.34}$$

where $g = e^{t^*} t^{*5}$ and $f = \int_0^{t^*} e^{t^*} t^{*5} dt^*$ we can now apply L'Hôpital's Rule $\lim_{t^* \to \infty} \frac{f}{g} = \lim_{t^* \to \infty} \frac{f'}{g'}$ such that

$$\begin{aligned} \lim_{t^* \to \infty} \frac{\int_0^{t^*} e^{t^*} t^{*5} dt^*}{e^{t^*} t^{*5}} &= \lim_{t^* \to \infty} \frac{e^{t^*} t^{*5}}{e^{t^*} t^{*4} (t^* + 5)}, \\ &= 1. \end{aligned}$$

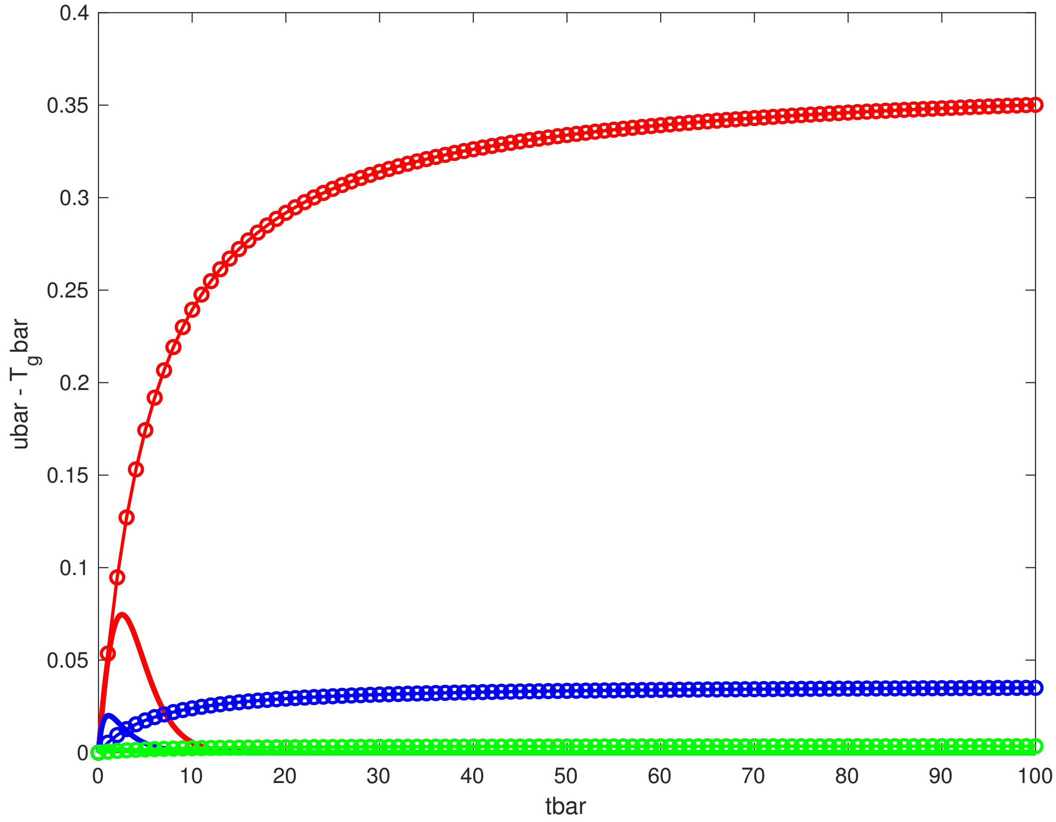

Figure 8.16: Solutions of equation (8.32) for $\psi = u_1^* - T_{G1}^*$ represented by the lines with circles, compared with the full solution $\bar{\lambda}(\bar{u} - \bar{T}_G)$ from equations (8.7) and (8.9) represented by the solid lines. Here we have used the fixed ratio $\rho_S/\rho_G \approx 5$ and set $\bar{\lambda} = 1, 10, 100$ depicted by the red, blue and green lines respectively.

Hence we may solve equation (8.33) analytically by rewriting it as

$$\frac{\partial u_1^*}{\partial t^*} = \bar{\Omega}k - \frac{\bar{\Omega}k}{t^{*5}}\left(t^{*5} - 5t^{*4} + 20t^{*3} - 60t^{*2} + 120t^* - 120 + 120e^{-t^*}\right), \qquad (8.35)$$

where we have used integration by parts. Integrating both sides with respect to t^* gives, apart from an added constant of integration,

$$u_1^* = 5\bar{\Omega}k\left(\frac{4}{t^*} - \frac{6}{t^{*2}} + \frac{8}{t^{*3}} - \frac{6}{t^{*4}} + \log(t^*)\right) - 120\bar{\Omega}k\int^{t^*} e^{-t^*}t^{*-5}dt^*$$

where the integral term can be written as

$$\int^{t^*} e^{-t^*} t^{*-5} dt^* = e^{-t^*}\left(\frac{\log(t^*)}{24} + \frac{1}{24t^*} - \frac{1}{24t^{*2}} + \frac{1}{12t^{*3}} - \frac{1}{4t^{*4}}\right) + \frac{1}{24}\int^{t^*} e^{-t^*}\log(t^*)dt^*.$$

Hence we have, with B_1 being a constant to be determined,

$$\begin{aligned} u_1^* = {} & 5\bar{\Omega}k\left(\frac{4}{t^*} - \frac{6}{t^{*2}} + \frac{8}{t^{*3}} - \frac{6}{t^{*4}} + \log t^*\right) \\ & - 120\bar{\Omega}k\left[e^{-t^*}\left(\frac{\log(t^*)}{24} + \frac{1}{24t^*} - \frac{1}{24t^{*2}} + \frac{1}{12t^{*3}} - \frac{1}{4t^{*4}}\right)\right. \\ & \left. + \frac{1}{24}\int^{t^*} e^{-t^*}\log(t^*)dt^*.\right] + B_1. \end{aligned} \tag{8.36}$$

For $t^* \ll 1$, taking the expansion $e^{-t^*} \sim (1 - t^* + \frac{t^{*2}}{2} - \frac{t^{*3}}{6} + \frac{t^{*4}}{24} + \dots)$ gives

$$\begin{aligned} u_1^* \sim {} & 5\bar{\Omega}k\Big(\frac{4}{t^*} - \frac{6}{t^{*2}} + \frac{8}{t^{*3}} - \frac{6}{t^{*4}} + \log t^*\Big) \\ & - 120\bar{\Omega}k\left[(1 - t^* + \frac{t^{*2}}{2} - \frac{t^{*3}}{6} + \frac{t^{*4}}{24} + \dots)\left(\frac{\log(t^*)}{24} + \frac{1}{24t^*} - \frac{1}{24t^{*2}} + \frac{1}{12t^{*3}} - \frac{1}{4t^{*4}}\right)\right. \\ & \left. + \frac{1}{24}\int_0^{t^*} e^{-t^*}\log(t^*)dt^*\right] + B_1 \end{aligned} \tag{8.37}$$

which, when expanded and simplified, gives

$$\begin{aligned} u_1^* \sim {} & \bar{\Omega}k\Big(\frac{125}{12} - \frac{15t^*}{4} + \frac{25t^{*2}}{24} - \frac{5t^{*3}}{24} + 5t\log(t^*) - \frac{5}{2}t^{*2}\log(t^*) + \frac{5}{6}t^{*3}\log(t^*) - \frac{5}{24}t^{*4}\log(t^*) \\ & + \int_0^{t^*} e^{-t^*}\log(t^*)\Big) + B_1. \end{aligned} \tag{8.38}$$

Comparing coefficients of this expression for u_1^* above with equation (8.36) gives $B_1 = -\frac{125}{5}\bar{\Omega}k$, satisfying $u_1^*(0) = 0$. Therefore from equation (8.36), we have

$$u_1^* \sim 5\bar{\Omega}k\left(\log(t^*) - \frac{25}{12} - \Gamma\right), \tag{8.39}$$

as t^* tends to infinity, where $\Gamma = \int_0^\infty e^{-t^*} \log(t^*) dt^* (\approx -0.577216)$.

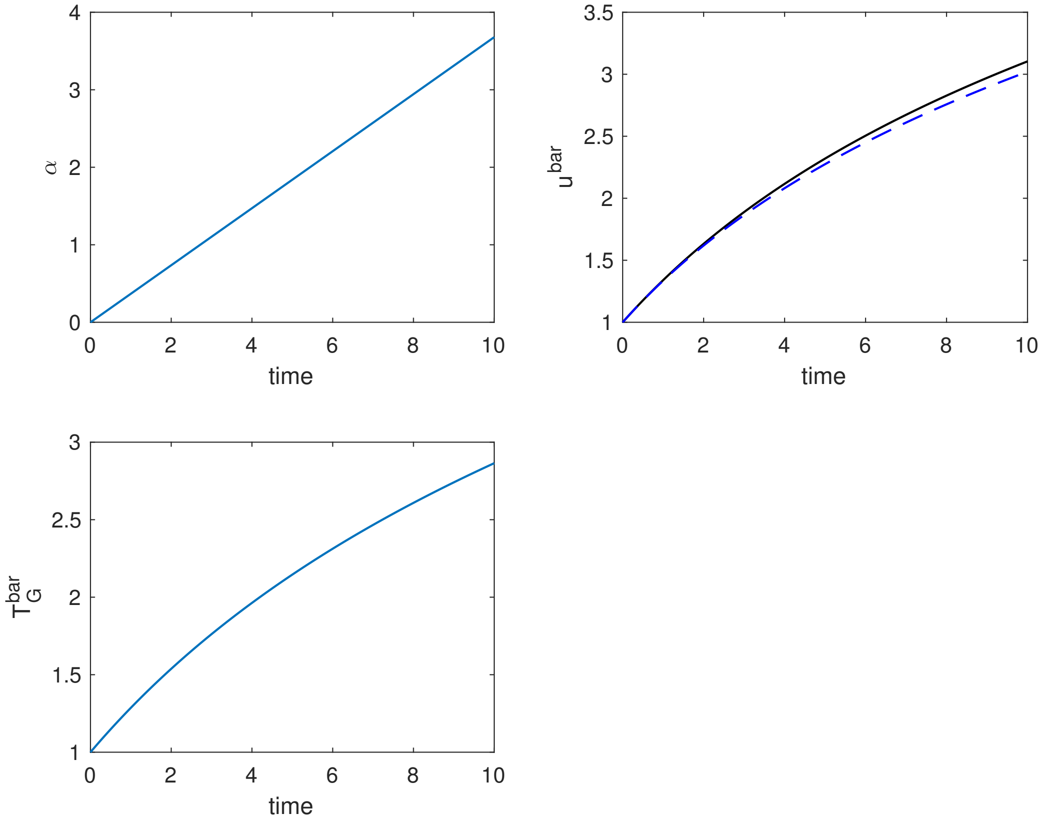

Figure 8.17: Comparison of asymptotic solution given by (8.39) (black dashed line) and numerical solution of equation (8.29)–(8.30) (blue). Here we have used very mild parameters. The parameter $\bar{\Omega} = \bar{C} = 1$ is fixed, as is the ratio $\rho_S/\rho_G = 5$ and we have set $T_G(0) = u(0) = s = 1$.

Similarly, substituting the expression for ψ, given by equation (8.32), equation (8.30) may be rewritten as

$$\frac{dT_{G1}^*}{dt^*} = \frac{5}{t^*}\psi,$$

or equivalently

$$\frac{dT_{G1}^*}{dt^*} = \frac{5}{t^*}\frac{\bar{\Omega}k}{e^{t^*}t^{*5}}\int_0^{t^*} e^{t^*}t^{*5}dt^*. \tag{8.40}$$

We may now solve equation (8.40) using integration by parts which gives,

$$\frac{dT^*_{G1}}{dt^*} = \frac{5\bar{\Omega}k}{t^{*6}}\left(t^{*5} - 5t^{*4} + 20t^{*3} - 60t^{*2} + 120t^* - 120 + 120e^{-t^*}\right). \tag{8.41}$$

Integrating both sides yields,

$$T^*_{G1} = 5\bar{\Omega}k\left(\log(t^*) + \frac{5}{t^*} - \frac{10}{t^{*2}} + \frac{20}{t^{*3}} - \frac{30}{t^{*4}} + \frac{24}{t^{*5}}\right) + 600\bar{\Omega}k\int^{t^*} e^{-t^*}t^{*-6}dt^* + B_2, \tag{8.42}$$

where B_2 is an unknown constant of integration and

$$\int^{t^*} e^{-t^*}t^{*-6}dt^* = e^{-t^*}\left(\frac{\ln(t^*)}{120} + \frac{1}{120t^*} - \frac{1}{120t^{*2}} + \frac{1}{60t^{*3}} - \frac{1}{20t^{*4}} + \frac{1}{5t^{*5}}\right) + \dots$$
$$\dots + \frac{1}{120}\int^{t^*} e^{-t^*}\ln(t^*)dt^*.$$

Hence we have

$$T^*_{G1} == 5\bar{\Omega}k\Bigg(\log(t^*)(1-e^{-t^*}) + t^{*-1}(5-e^{-t^*}) + t^{*-2}(e^{-t^*}-10) + 2t^{*-3}(10-e^{-t^*}) + \dots$$
$$\dots + 6t^{*-4}(e^{-t^*}-5) + 24t^{*-5}(1-e^{-t^*}) - \int_0^{t^*} e^{-t^*}\log(t^*)dt^*\Bigg) + B_2. \tag{8.43}$$

To determine the constant c_2 we begin by rewriting equation (8.43) such that

$$T^*_{G1} = 5\bar{\Omega}k\left(\log(t^*) + \frac{5}{t^*} - \frac{10}{t^{*2}} + \frac{20}{t^{*3}} - \frac{30}{t^{*4}} + \frac{24}{t^{*5}}\right) + \dots$$
$$\dots + 5\bar{\Omega}ke^{-t^*}\Bigg(-\log(t^*) - t^{*-1} + t^{*-2} - 2t^{*-3} + 6t^{*-4} - 24t^{*-5}\Bigg) + \dots$$
$$\dots - 5\bar{\Omega}k\int_0^{t^*} e^{-t^*}\log(t^*)dt^* + B_2$$

then taking the expansion $e^{-t^*} \sim (1 - t^* + \frac{t^{*2}}{2} - \frac{t^{*3}}{6} + \frac{t^{*4}}{24} + \dots)$ for small t^* ($t^* \ll 1$)

yields

$$\begin{aligned} T^*_{G1} &\sim 5\bar{\Omega}k\log(t^*) + \dots \\ &\cdots + 5\bar{\Omega}k(1 - t^* + \frac{t^{*2}}{2} - \frac{t^{*3}}{6} + \frac{t^{*4}}{24} + \dots)\left(-\log(t^*) - t^{*-1} + t^{*-2} - 2t^{*-3} + 6t^{*-4} - 24t^{*-5}\right) + \dots \\ &\dots - 5\bar{\Omega}k\int_0^{t^*} e^{-t^*}\log(t^*)dt^* + B_2. \end{aligned}$$

Comparing coefficients gives $B_2 = -\frac{125}{12}$. As $t^* \to \infty$ we get

$$T^*_{G1} \sim 5\bar{\Omega}k\left(\log(t^*) - \frac{25}{12} - \Gamma\right), \tag{8.44}$$

where $\Gamma = \int_0^\infty e^{-t^*}\log(t^*)dt^* (\approx -0.577216)$.

In the next stage we let $t^* = \bar{\lambda}\bar{t}$ in the expression for u^* such that equation (8.39) becomes

$$u^*_1 \sim 5\bar{\Omega}k\left(\log(\bar{\lambda}\bar{t}) - \frac{25}{12} - \Gamma\right),$$

and hence $\bar{u}$ becomes

$$\bar{u} \sim s + \frac{5\bar{\Omega}k}{\bar{\lambda}}\left(\log(\bar{\lambda}\bar{t}) - \frac{25}{12} - \Gamma\right), \tag{8.45}$$

which gives logarithmic growth at early times $\bar{t}$. Similarly, substituting $t^* = \bar{\lambda}\bar{t}$ in the expression for T^*_{G1}, equation (8.44) becomes

$$T^*_{G1} \sim 5\bar{\Omega}k\left(\log(\bar{\lambda}\bar{t}) - \frac{25}{12} - \Gamma\right),$$

and hence $\bar{T}_G$ becomes

$$\bar{T}_G = s + \frac{5\bar{\Omega}k}{\bar{\lambda}}\left(\log(\bar{\lambda}\bar{t}) - \frac{25}{12} - \Gamma\right), \tag{8.46}$$

8.3.2.2 $\bar{t} = \mathscr{O}(1)$

A second, longer time scale arises when $\bar{\lambda} \gg 1$, that is $\bar{t} = \mathscr{O}(1)$, $\alpha = \mathscr{O}(1)$ and $\bar{u} = \mathscr{O}(1)$, $\bar{T}_G = \mathscr{O}(1)$. Taking the expansions

$$\begin{aligned}
\bar{u} &= s + \bar{\lambda}^{-1}\log(\bar{\lambda})c_3 + \bar{\lambda}^{-1}\bar{u}_1 + \dots, \\
\bar{T}_G &= s + \bar{\lambda}^{-1}\log(\bar{\lambda})c_4 + \bar{\lambda}^{-1}\bar{T}_{G1} + \dots, \\
\alpha &= \alpha_1 + \bar{\lambda}^{-1}\alpha_2 + \dots
\end{aligned}$$

where s is a constant (initial condition of u or T_G, both are equal initially), $c_3 = c_4 = 5\bar{\Omega}k$ from equation (8.45) and equation (8.46), we find from equations (8.7)–(8.9)

$$0 = \bar{\Omega}\frac{\partial \alpha_1}{\partial \bar{t}} + (\bar{T}_{G1} - \bar{u}_1), \tag{8.47}$$

$$\frac{\partial \alpha_1}{\partial \bar{t}} = (1-\alpha_1)\exp\left(-\frac{1}{s}\right), \tag{8.48}$$

$$\frac{d\bar{T}_{G1}}{d\bar{t}} = \frac{5}{\alpha_1}(\bar{u}_1 - \bar{T}_{G1})\frac{\partial \alpha_1}{\partial \bar{t}}. \tag{8.49}$$

Solving equation (8.48) analytically gives

$$\alpha_1 = 1 - e^{-k\bar{t}}, \tag{8.50}$$

where $k = \exp\left(-\frac{1}{s}\right)$, and s is constant. Equation (8.47) can be rearranged for $\bar{u}_1$ which gives

$$\bar{u}_1 = \bar{T}_{G1} + \bar{\Omega}ke^{-k\bar{t}}. \tag{8.51}$$

Taking the difference gives

$$\bar{u}_1 - \bar{T}_{G1} = \bar{\Omega}ke^{-k\bar{t}}, \tag{8.52}$$

which agrees with equation (8.31) when compared for large time. We observe from equation (8.51) that $\bar{u}_1$ and $\bar{T}_{G1}$ are different, however as $\bar{t} \to \infty$ we get $\bar{u}_1 \approx \bar{T}_{G1}$ since we see exponential decay from the exponential term in equation (8.51).

Equation (8.49) can be solved by integrating directly such that

$$\frac{d\bar{T}_{G1}}{d\bar{t}} = 5\left(\bar{u}_1 - \bar{T}_{G1}\right)\frac{\frac{\partial \alpha_1}{\partial \bar{t}}}{\alpha_1},$$

and substituting equation (8.51) into the above gives

$$\frac{d\bar{T}_{G1}}{d\bar{t}} = 5\bar{\Omega}\frac{k^2 e^{-2k\bar{t}}}{1-e^{-k\bar{t}}}, \tag{8.53}$$

which, upon integration gives

$$\bar{T}_{G1} = 5\bar{\Omega}k\left(\log(1-e^{-k\bar{t}}) + e^{-k\bar{t}} - 1\right) + B_3, \tag{8.54}$$

where B_3 is a constant of integration to be determined. Substituting equation (8.54) into equation (8.51) gives

$$\bar{u}_1 = \bar{\Omega}ke^{-k\bar{t}} + 5\bar{\Omega}k\left(\log(1-e^{-k\bar{t}}) + e^{-k\bar{t}} - 1\right) + B_3.$$

Expanding for small $\bar{t}$ gives

$$\begin{aligned}\bar{u}_1 &= \bar{\Omega}k + 5\bar{\Omega}k\log(k\bar{t}) + B_3,\\ &= \bar{\Omega}k + 5\bar{\Omega}k(\log(k) + \log(\bar{t})) + B_3\end{aligned}$$

which we match with equation (8.39) such that we get $B_3 = 5\bar{\Omega}k\left(-\frac{25}{12} - \Gamma - \log(k)\right) - \bar{\Omega}k$.

Alternatively, we may transform equation (8.49) such that we get

$$\frac{d\bar{T}_{G1}}{d\alpha_1} = \frac{5\bar{\Omega}k}{\alpha_1}\left(1-\alpha_1\right) \tag{8.55}$$

integrating with respect to α_1 gives $\bar{T}_{G1}(\alpha_1)$

$$\bar{T}_{G1}(\alpha_1) = 5\bar{\Omega}k\left(\log(\alpha_1) - \alpha_1\right) + B_4, \tag{8.56}$$

where α_1 is given by equation (8.50). Expanding for small $\bar{t}$ in equation (8.50) then gives us

$$\alpha_1 \sim k\bar{t} + \mathscr{O}(\bar{t}^2), \tag{8.57}$$

which implies that equation (8.56) becomes, for small $\bar{t}$

$$\bar{T}_{G1} \sim 5\bar{\Omega}k\left(\log(k\bar{t}) - k\bar{t}\right) + B_4, \tag{8.58}$$

where from matching with (8.44), (8.46) we find $B_4 = 5\bar{\Omega}k\left(-\frac{25}{12} - \Gamma - \log(k)\right) - \bar{\Omega}k$ and $\Gamma = -0.5772$ as before.

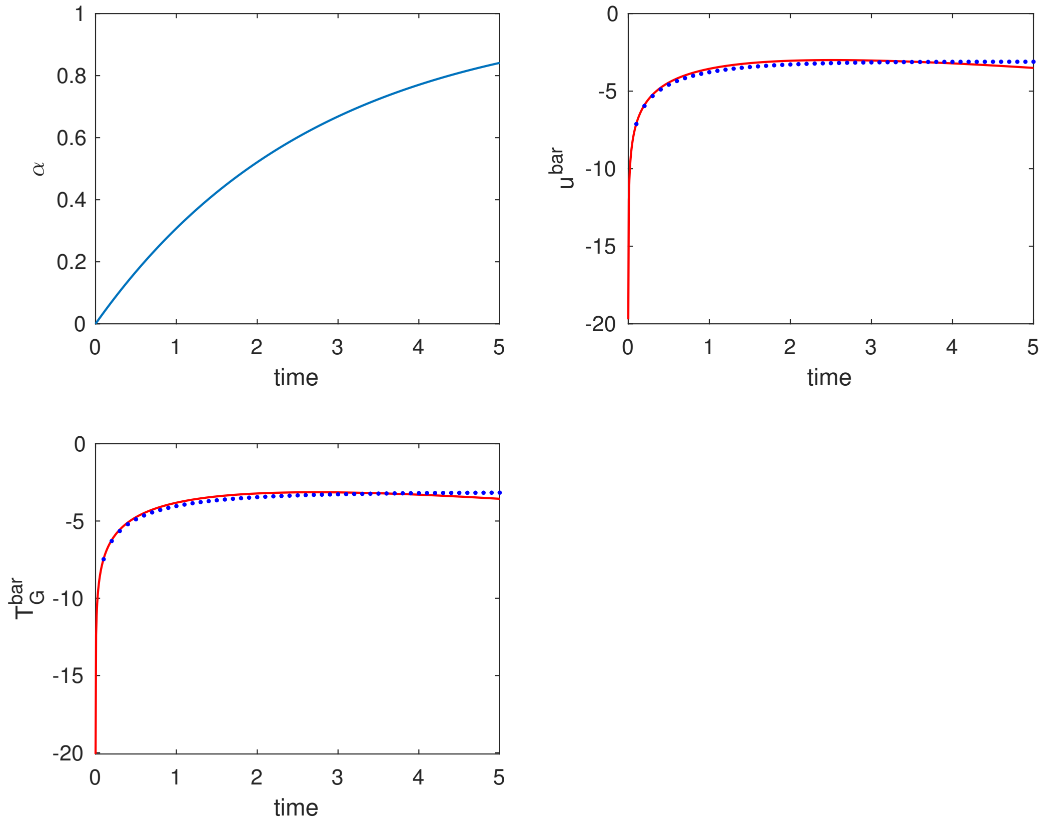

Figure 8.18: Solutions of equations (8.50), (8.51) and (8.58) for α_1, $\bar{u}_1$ and $\bar{T}_{G1}$ respectively. Here $k = e^{-1/s}$ and we have used mild parameter values, including $s = \bar{\Omega} = 1$. Here the dashed blue lines represent the solutions to $\bar{u}$ and $\bar{T}_G$ derived from equation (8.54) and the red line represent the solutions to $\bar{u}$ and $\bar{T}_G$ from equation (8.58).

Comparing results from $t = \mathscr{O}(1)$ with the full problem for $\lambda = 5, 10, 20$ we get the results in figure 8.19. We predict that the difference $\bar{u} - \bar{T}_G$ from the full core problem (equations (8.7)–(8.9)) can be given by subtracting the following

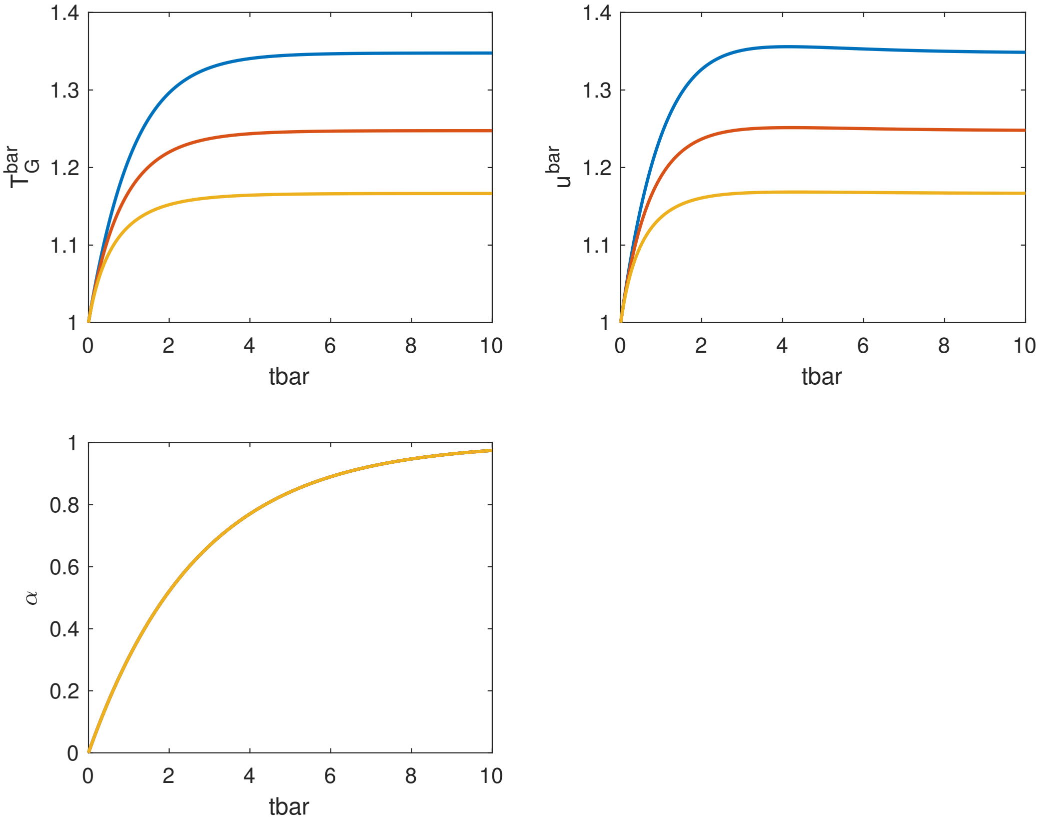

Figure 8.19: Solutions of full system given by equations (8.7)–(8.9) for α, $\bar{u}$ and $\bar{T}_G$ respectively. Here we have used mild parameter values, including $s = \bar{\Omega} = 1$. Here the blue lines represent the solutions with $\bar{\lambda} = 5$, the red lines $\bar{\lambda} = 10$ and the yellow lines show the solutions when $\bar{\lambda} = 20$.

$$\bar{u} = s + \bar{\lambda}^{-1}\log(\bar{\lambda})c_3 + \bar{\lambda}^{-1}\bar{u}_1 + \dots,$$

$$\bar{T}_G = s + \bar{\lambda}^{-1}\log(\bar{\lambda})c_4 + \bar{\lambda}^{-1}\bar{T}_{G1} + \dots,$$

such that

$$\bar{u} - \bar{T}_G = \bar{\lambda}^{-1}(\bar{u}_1 - \bar{T}_{G1}),$$

where from equation (8.51) we have

$$\bar{u} - \bar{T}_G = \bar{\lambda}^{-1}\bar{\Omega}ke^{-k\bar{t}}. \tag{8.59}$$

Comparing equation (8.59) with $\bar{u} - \bar{T}_G$ from equations (8.7)–(8.9) gives the following comparison below in figure 8.20 for varying values of $\bar{\lambda}$.

We see in figure 8.20 that the agreement between the full solutions and the reduced-system solutions improves as $\bar{\lambda}$ is increased, as should be expected.

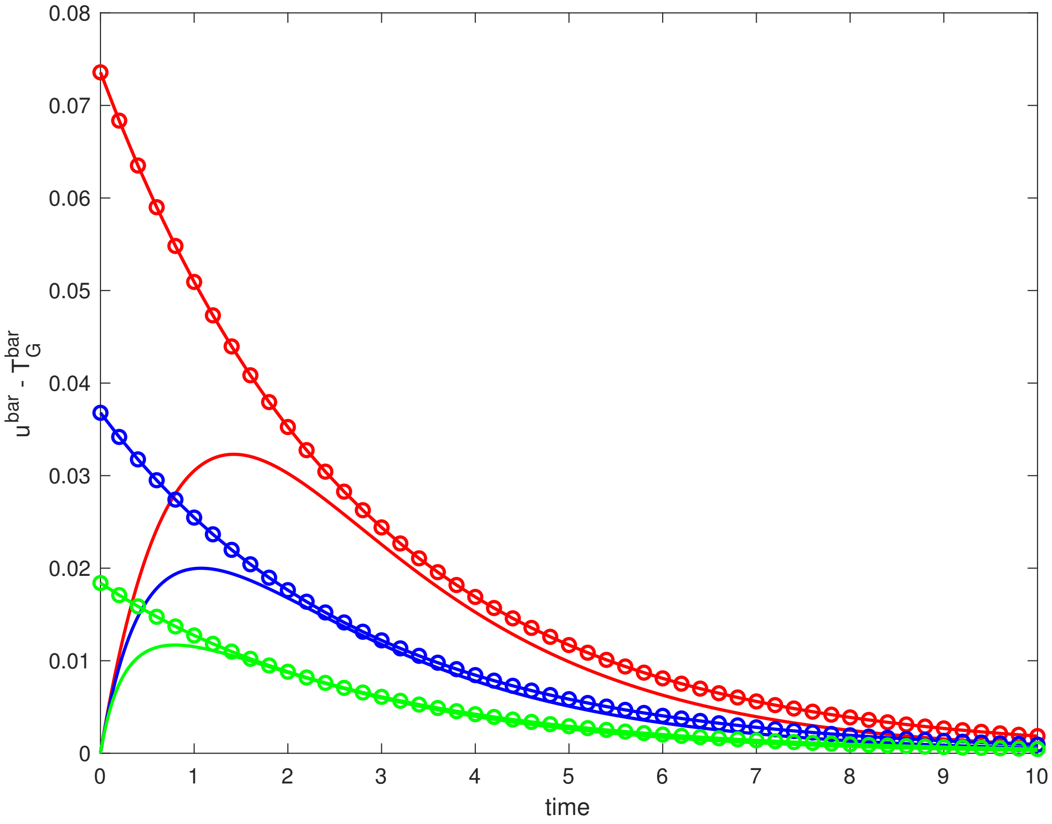

Figure 8.20: Difference $\bar{u} - \bar{T}_G$ against $\bar{t}$. Here we have used mild parameter values, including $k = e^{-1/s}$ where $s = \bar{\Omega} = 1$. The dashed lines with circles represent our prediction for $\bar{u} - \bar{T}_G$ from the reduced system given by equation (8.59) and the solid lines represent the true values of $\bar{u} - \bar{T}_G$ from the full system given by equations (8.7)–(8.9). Here the colours red, blue and green represent the values $\bar{\lambda} = 5, 10, 20$ respectively.

8.4 Varying densities

In section 8.2, we varied the temperature of the gas and investigated the feedback effect of this on the solid. In this section we consider varying the densities of both the solid and gas as well as varying the gas temperature for the fully non-dimensional case in the core region. We remove any dimensionality from the governing equations by introducing the following scaled variables

$$
\begin{aligned}
T_G(t) &= \frac{E}{R}\bar{T}_G(\bar{t}), & u(t) &= \frac{E}{R}\bar{u}(\bar{t}),\\
V_G(t) &= A\bar{V}_G(\bar{t}), & \rho_G(t) &= \left(\frac{E}{Ac_1}\right)^{1/\gamma}\bar{\rho}_G(\bar{t}),\\
V_S(t) &= A\bar{V}_S(\bar{t}), & P_G(t) &= \frac{E}{A}\bar{P}_G(\bar{t}).\\
\rho_S(t) &= \left(\frac{E}{Ac_1}\right)^{1/\gamma}\bar{\rho}_S(\bar{t}) & &
\end{aligned}
$$

Substituting the above into our system of equations yields the non-dimensional system

$$\frac{\partial \bar{u}}{\partial \bar{t}} = \bar{\Omega}\frac{\partial \alpha}{\partial \bar{t}} + \bar{\lambda}(\bar{T}_G(t) - \bar{u}(t)), \tag{8.60}$$

$$\frac{\partial \alpha}{\partial \bar{t}} = (1-\alpha)\exp\left(-\frac{1}{\bar{u}}\right), \tag{8.61}$$

$$\frac{d\bar{T}_G}{d\bar{t}} = \frac{\bar{\rho}_S(\bar{t})}{\bar{\rho}_G(\bar{t})\bar{V}_G(t)}\left(\bar{u}(t) - \bar{T}_G(\bar{t})\right)\frac{d\bar{V}_G(t)}{d\bar{t}}, \tag{8.62}$$

$$\bar{V}_G(\bar{t}) = 2\alpha, \tag{8.63}$$

$$\bar{V}_S(\bar{t}) = 2 - \bar{V}_G(\bar{t}), \tag{8.64}$$

$$\bar{P}_G(\bar{t}) = \frac{n\bar{T}_G(\bar{t})}{\bar{V}_G(\bar{t})}, \tag{8.65}$$

$$\bar{\rho}_G(\bar{t}) = \bar{P}_G(\bar{t})^{\frac{1}{\gamma}}, \tag{8.66}$$

$$\bar{\rho}_S(\bar{t}) = \bar{M}_T - \frac{\bar{\rho}_G(\bar{t})\bar{V}_G(\bar{t})}{\bar{V}_S(\bar{t})}, \tag{8.67}$$

where $\bar{M}_T = \frac{M_T}{\bar{V}_S(\bar{t})A\left(\frac{E}{Ac_1}\right)^{\frac{1}{\gamma}}}$.

To solve the system (8.60)–(8.67) we can take equations (8.61) and (8.63)–(8.67) and substitute these into equation (8.62) which, after some manipulation, gives

$$\frac{d\bar{T}_G}{d\bar{t}} = \frac{\bar{u}-\bar{T}_G}{\alpha^{1-\frac{1}{\gamma}}\bar{T}_G^{\frac{1}{\gamma}}c_3}\left(\frac{M_T}{2(1-\alpha)Ac_2} - \frac{\alpha^{1-\frac{1}{\gamma}}\bar{T}_G^{\frac{1}{\gamma}}c_3}{(1-\alpha)}\right)\frac{d\alpha}{d\bar{t}}. \tag{8.68}$$

This can be rewritten in terms of α as

$$\frac{d\bar{T}_G}{d\alpha} = \frac{\bar{u}-\bar{T}_G}{\alpha^{1-\frac{1}{\gamma}}\bar{T}_G^{\frac{1}{\gamma}}c_3}\left(\frac{M_T}{2(1-\alpha)Ac_2} - \frac{\alpha^{1-\frac{1}{\gamma}}\bar{T}_G^{\frac{1}{\gamma}}c_3}{(1-\alpha)}\right), \tag{8.69}$$

where $c_2 = \left(\frac{E}{Ac_1}\right)^{\frac{1}{\gamma}}$ and $c_3 = \left(\frac{n}{2}\right)^{\frac{1}{\gamma}}$. Finally we have

$$\frac{d\bar{T}_G}{d\alpha} = \frac{\bar{u}-\bar{T}_G}{(1-\alpha)}\left(\frac{M_T}{2Ac_2c_3\alpha^{1-\frac{1}{\gamma}}\bar{T}_G^{\frac{1}{\gamma}}} - 1\right). \tag{8.70}$$

The results of the solution to equation (8.70) are presented in figure 8.21, where we have used mild parameter values.

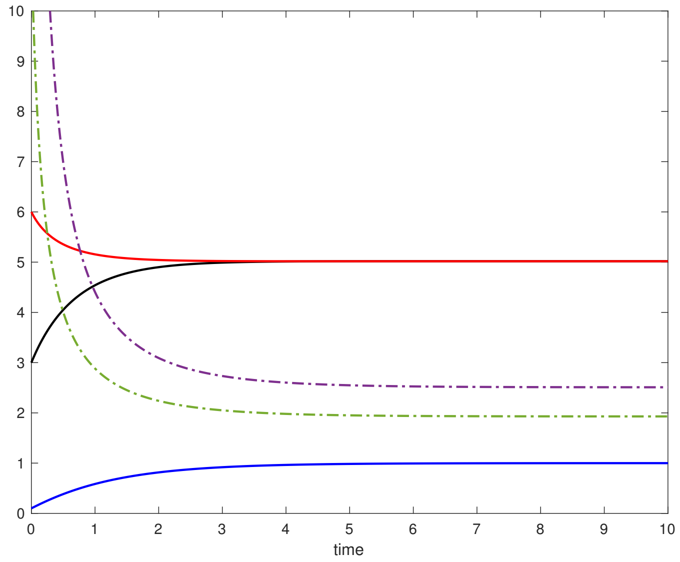

Figure 8.21: Solutions of equations (8.60)–(8.61), (8.65)–(8.66) and (8.70) for $\bar{u}$ (black), α(blue), $\bar{P}_G$ (purple dashed), $\bar{\rho}_G$ (green dashed) and $\bar{T}_G$ (red) respectively. Here we have used mild parameters including $\bar{\Omega} = 0.16$, $\bar{\lambda} = 1$, $E = A = n = c_2 = c_1 = 1$ and $M_T = 5$. We have taken the initial values to be $\bar{T}_G(0) = 6$, $\bar{u}(0) = 3$ and $\alpha(0) = 0.1$.

Moving from mild parameter values towards realistic physical values, we obtain the results displayed in figure 8.22.

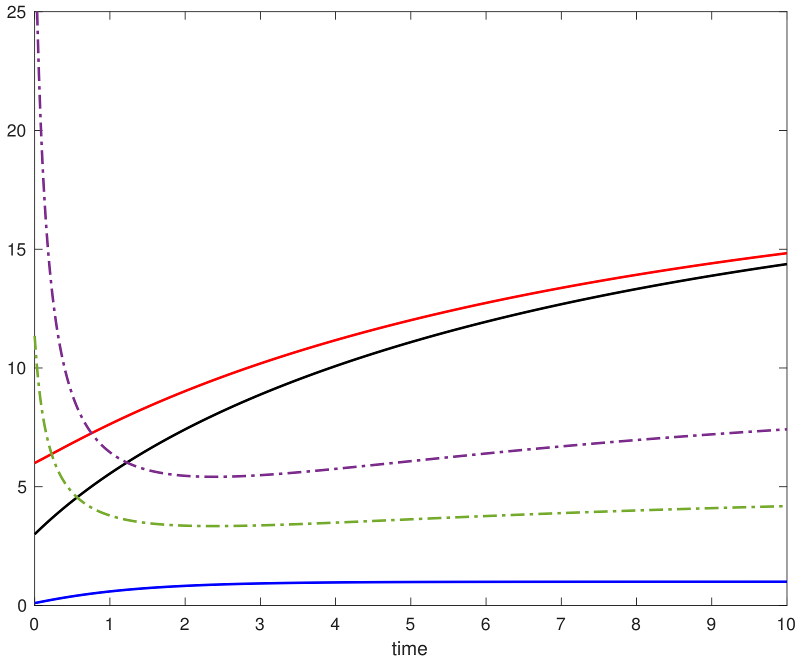

Figure 8.22: Solutions of equations (8.60)–(8.61), (8.65)–(8.66) and (8.70) for $\bar{u}$ (black), α (blue), $\bar{P}_G$ (purple dashed), $\bar{\rho}_G$ (green dashed) and $\bar{T}_G$ (red) respectively. Here we have used the same parameters as those used in figure 8.21 with $E = 2.2 \times 10^5$ and $M_T = 3600$. We have also used the same initial values.

Next, we investigate the effect of particular parameters individually, first by considering the effect of reducing the parameter n which represents the number of moles of gas. We use the physical parameter value of the activation energy E (shown in figure 8.22) and reduce the value of n. Results of this are displayed in figure 8.23.

Continuing our investigation of parameter value effects, we now consider how reducing the extent of reaction α affects the solution. This is depicted in figure 8.24 and again in figure 8.25 for various values of $\bar{\lambda}$.

In figure 8.26 the effective temperature T_2 plotted is given by

$$T_2 = \left(\frac{1}{M_T}(2A^* c_2 c_3 \alpha^{1-\frac{1}{\gamma}})\right)^{\gamma}. \tag{8.71}$$

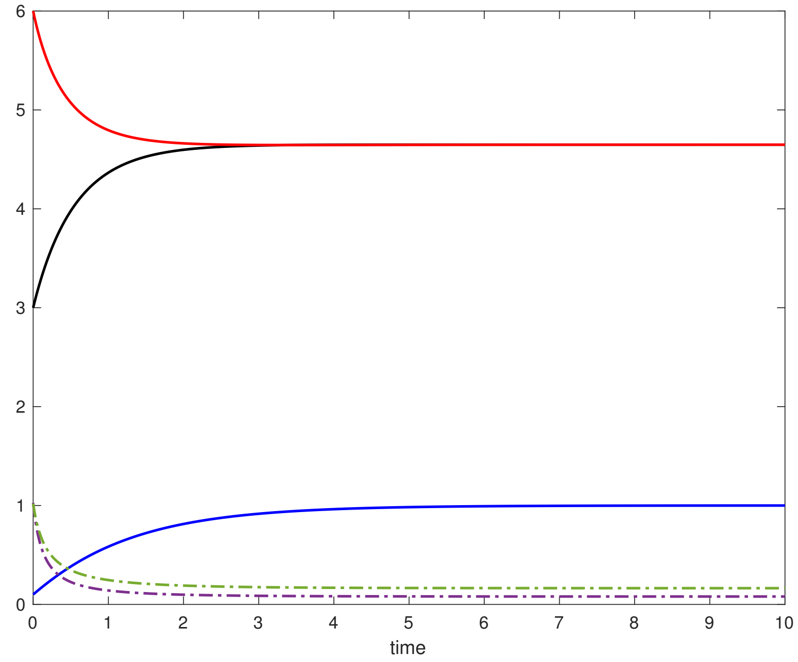

Figure 8.23: Solutions of equations (8.60)–(8.67) for $\bar{u}$ (black), α (blue), $\bar{P}_G$ (purple dashed), $\bar{\rho}_G$ (green dashed) and $\bar{T}_G$ (red) respectively. Here we have used the same parameters as in figure 8.22 with $n = 0.0342$.

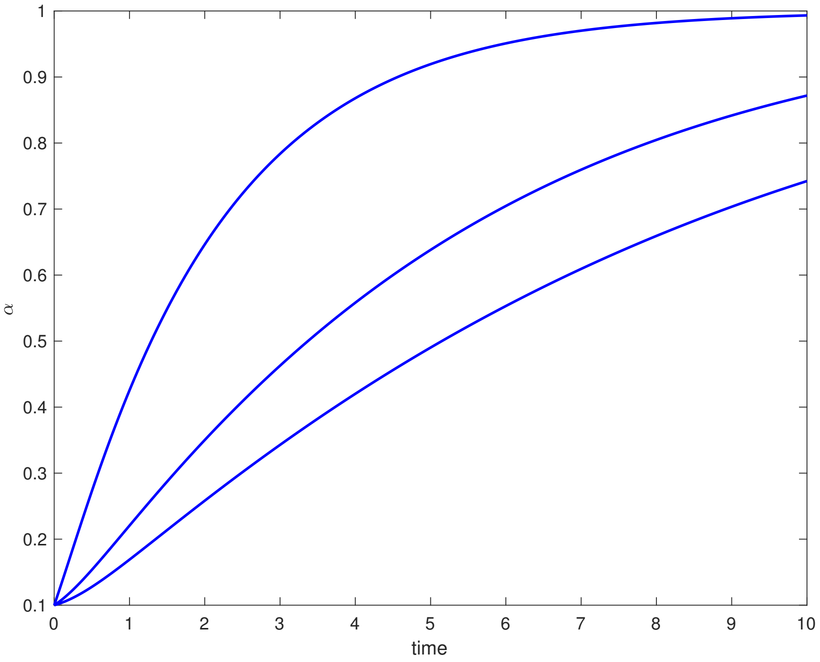

Figure 8.24: Solutions of equations (8.60)–(8.67) for α. Here we have used the same parameters as in figure 8.23 with $\bar{T}_G(0) = 2, 0.8, 0.6$ and $\bar{u}(0) = 1, 0.4, 0.3$.

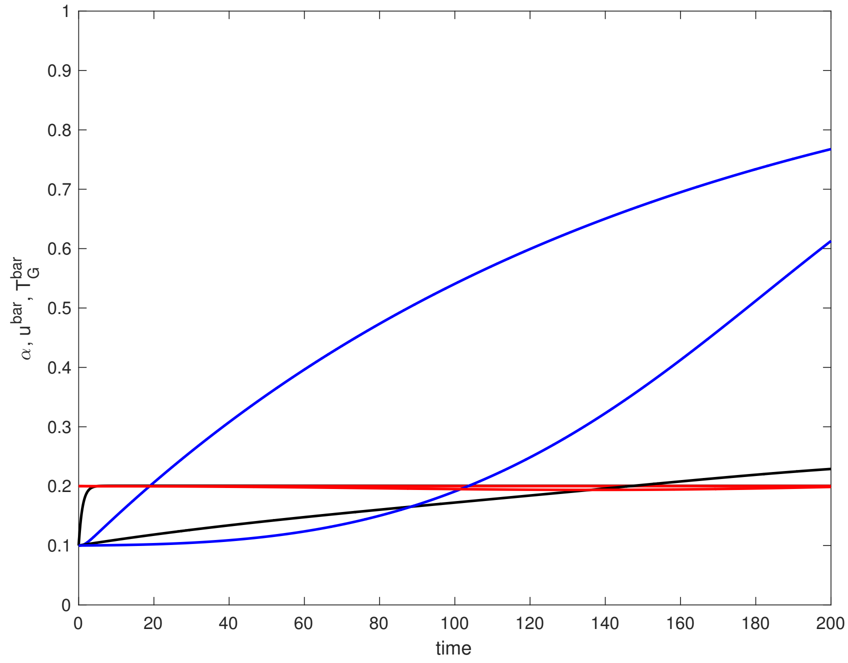

Figure 8.25: Solutions of equations (8.60)–(8.62) for $\bar{u}$ (black), α (blue) and $\bar{T}_G$ (red). Here we have used the same parameters as in figure 8.24 with $\bar{T}_G(0) = 0.2$, $\bar{u}(0) = 0.1$ in both cases presented. We have repeated the same set up using $\bar{\lambda} = 1$ and $\bar{\lambda} = 0.01$.

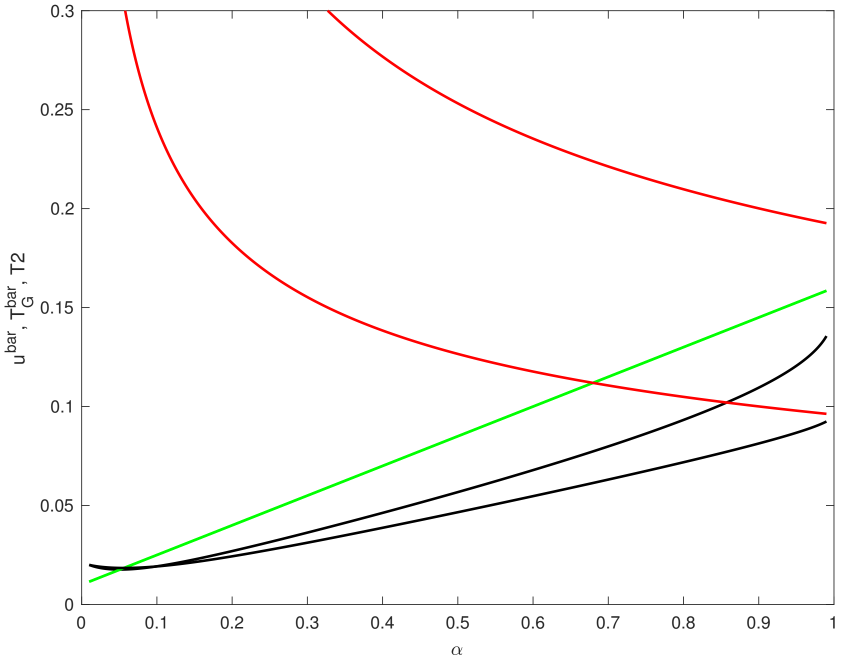

Figure 8.26: Solutions of equation (8.70), for $\bar{u}$ (green), $\bar{T}_G$ (black) and T_2 (red). Here we have used the same initial conditions for $\bar{u}$, $\bar{T}_G$ as those in figure 8.25 as well as $c_1 = 0.01$ and $c_1 = 0.02$.

8.5 Summary of chapter

In this chapter we considered the effects of internal heating on the problem using an asymptotic framework. Specifically, we considered the core region of the problem. To begin, we took the temperature of the gas T_G to be constant which resulted in little to no effect on the solid temperature $\bar{u}$ and hence on the extent of reaction α. There was also little improvement from the previous chapter (chapter 7) on the profile of the volume of gas V_G. Hence we proceeded to consider a variable gas temperature by taking $T_G = T_G(t)$. We noticed some improvement in the temperature profiles however the dominant driver of the profiles was shown to be $\bar{\lambda}$. Thus in the next section 8.3 we investigated the effects of $\bar{\lambda}$ on the system. We found various time scales arose for both small and large $\bar{\lambda}$. When varying the parameter $\bar{\lambda}$ we observe no qualitative change in the evolution of the reaction term α.

Next we considered varying the densities of the solid ρ_S and gas ρ_G. In this section we considered a fully non-dimensional system by scaling the variables in the system of equations. This resulted in a single equation to be solved which highlighted interesting behaviours within the system.

There are interesting follow-on questions: for example two heating contributions Q say, could be present, probably hotter but possibly colder than the explosive, depending on the temperature of the gas.

In the next chapter we consider the effects of internal heating on the full physical problem, initially using mild parameter values.

Chapter 9

Full problem - internal heating

In this chapter we investigate the effects of internal heating on the full problem. To begin we use mild parameters and consider a constant temperature of gas T_G in the first instance.

9.1 Constant Gas Temperature

In the case of constant gas temperature T_G we also assume constant densities ρ_S and ρ_G. Hence the resulting equations to solve are

$$\rho_S C_V \frac{\partial u}{\partial t} = \kappa \frac{\partial^2 u}{\partial x^2} + \Omega \rho_S \frac{\partial \alpha}{\partial t} + \lambda H(T_G - u(t)), \tag{9.1}$$

$$\frac{\partial \alpha}{\partial t} = A(1-\alpha)\exp\left(-\frac{E}{Ru}\right), \tag{9.2}$$

$$\frac{dV_G}{dt} = A\int_{-x_0}^{x_0} \frac{\partial \alpha}{\partial t} dx, \tag{9.3}$$

$$V_S(t) = 2 - V_G(t), \tag{9.4}$$

$$P_G(t) = \frac{nRT_G}{V_G(t)}. \tag{9.5}$$

We also note here that the pressure of the gas P_G is driven by the temperature of the gas T_G. Since we are treating T_G as constant, the resulting P_G is nonsensical but has been plotted for completeness.

In figure 9.1a we have displayed the final temperature of the solid u and final extent of reaction α for a fixed gas temperature $T_G = 10$. Figure 9.1b shows these final values near the boundary. Similar considerations apply to figures 9.2–9.4b. We

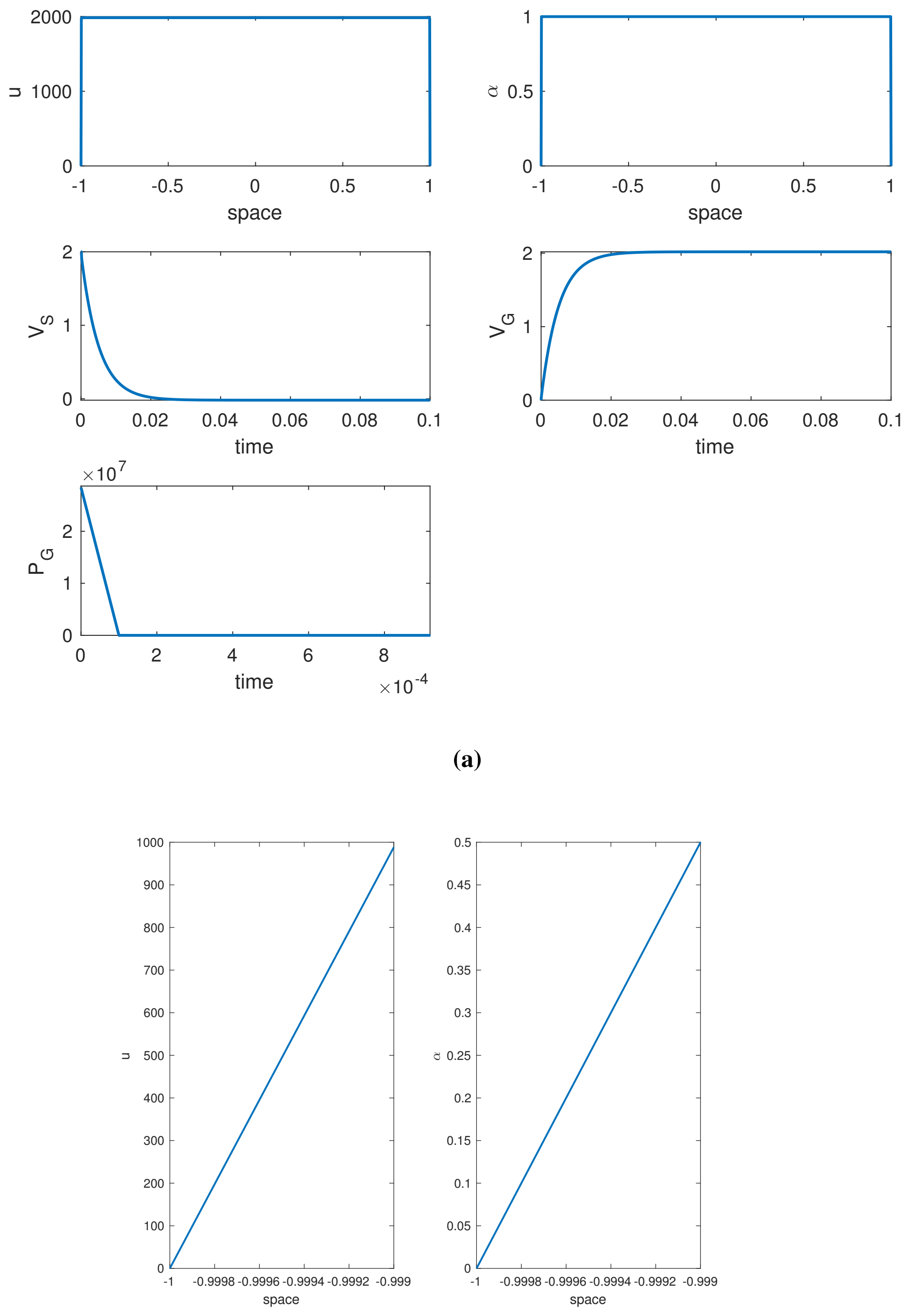

(a)

(b)

Figure 9.1: Numerical solutions of equations (9.1)–(9.5) with mild parameters. Here $\lambda H = 1$, $T_G = 10$ and we have zoomed in on the behaviour of the pressure at early time t in figure 9.1a. Figure 9.1b focuses on behaviour at boundary for the final values of u and α.

note however that the temperature profile of the solid remains unchanged for $T_G = 1, 10, 100$ and hence we conclude that the temperature of the gas (whilst constant) has little to no effect on the temperature of the solid (and thus the volumes and pressure). We also observe from figure 9.1a a sharp decline in pressure at very early time. As noted earlier, this profile is not physically realistic.

9.2 Variable Gas Temperature

In this section we consider how a variable gas temperature, $T_G(t)$, might impact the solutions of the system of equations. Here we maintain constant densities ρ_S and ρ_G but vary the temperature of gas with respect to time such that $T_G = T_G(t)$. Hence our system of equations given in section 9.1 becomes

$$\rho_S C_V \frac{\partial u}{\partial t} = \kappa \frac{\partial^2 u}{\partial x^2} + \Omega \rho_S \frac{\partial \alpha}{\partial t} + \lambda H(T_G(t) - u(t)), \tag{9.6}$$

$$\frac{\partial \alpha}{\partial t} = A(1-\alpha)\exp\left(-\frac{E}{Ru}\right), \tag{9.7}$$

$$\frac{dV_G}{dt} = A \int_{-x_0}^{x_0} \frac{\partial \alpha}{\partial t} dx, \tag{9.8}$$

$$V_S(t) = 2 - V_G(t), \tag{9.9}$$

$$\frac{dT_G}{dt} = \frac{\rho_S}{\rho_G V_G(t)} (u(t) - T_G(t)) \frac{dV_G(t)}{dt}, \tag{9.10}$$

$$P_G(t) = \frac{nRT_G(t)}{V_G(t)}. \tag{9.11}$$

We observe little to no difference between figures 9.1a and 9.2 other than a profile for T_G in figure 9.2. This could be a result of using mild parameters or using fixed densities in the analysis. We explore the effects of fixed densities by varying the densities over time in the following section.

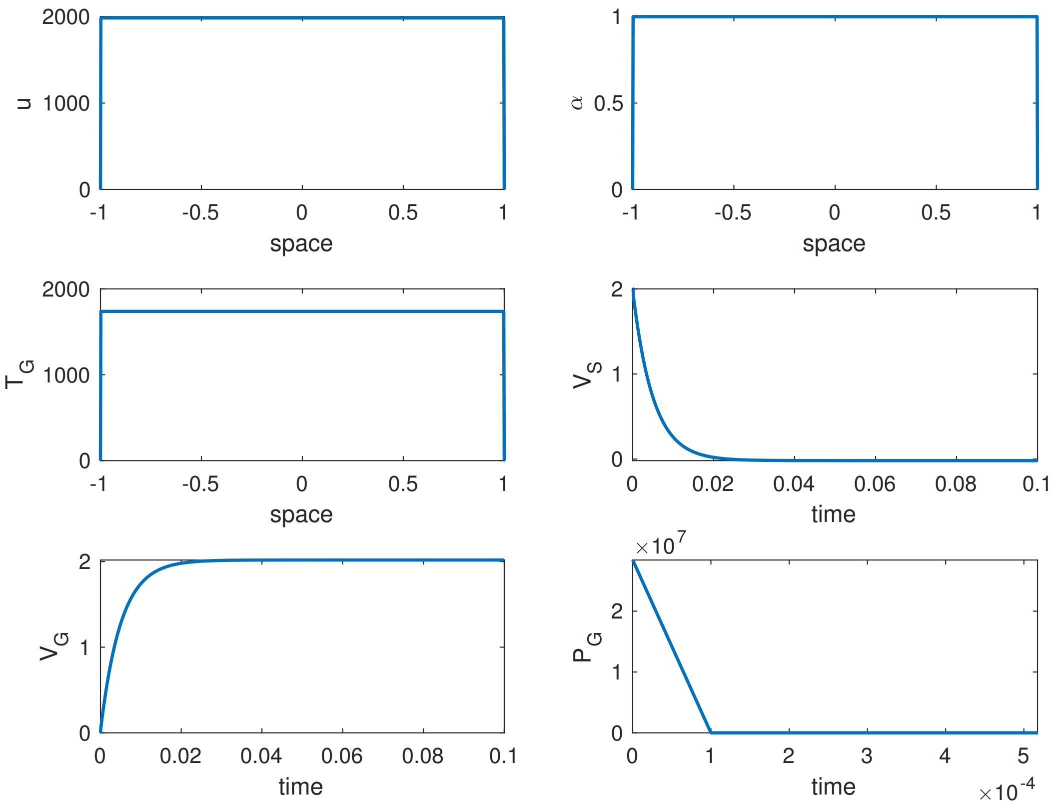

Figure 9.2: Numerical solutions of equations (9.6)–(9.11) with mild parameters. Here $\lambda H = 1$ and $T_G(0) = 10$.

9.3 Varying densities

In this section we consider varying both the densities of the solid and gas along with the temperature of the gas as before in the previous section 9.2. We use mild parameter values in the first instance and later consider the effects of the physical parameter values on the system.

Taking $T_G = T_G(t)$ as before in section 9.2, with $\rho_G = \rho_G(t)$ and $\rho_S = \rho_S(t)$

now, yields the following system of equations

$$\rho_S(t)C_V\frac{\partial u}{\partial t} = \kappa\frac{\partial^2 u}{\partial x^2} + \Omega\rho_S(t)\frac{\partial \alpha}{\partial t} + \lambda H(T_G(t) - u(t)), \tag{9.12}$$

$$\frac{\partial \alpha}{\partial t} = A(1-\alpha)\exp\left(-\frac{E}{Ru}\right), \tag{9.13}$$

$$\frac{dV_G}{dt} = A\int_{-x_0}^{x_0}\frac{\partial \alpha}{\partial t}dx, \tag{9.14}$$

$$V_S(t) = 2 - V_G(t), \tag{9.15}$$

$$\frac{dT_G}{dt} = \frac{\rho_S(t)}{\rho_G(t)V_G(t)}\left(u(t) - T_G(t)\right)\frac{dV_G(t)}{dt}, \tag{9.16}$$

$$P_G(t) = \frac{nRT_G(t)}{V_G(t)}, \tag{9.17}$$

$$\rho_G(t) = \left(\frac{P_G(t)}{c_1}\right)^{\frac{1}{\gamma}}, \tag{9.18}$$

$$\rho_S(t) = \frac{M_T - \rho_G(t)V_G(t)}{V_S(t)}. \tag{9.19}$$

9.3.1 Mild parameters

Here we solve the system 9.12–9.19 using the mild parameter values given in table 8.1. We also use the initial conditions given by $u(0) = 15, T_G(0) = 10, V_G(0) = 1\times 10^{-7}, \rho_G(0) = 372$ and $\rho_S(0) = 1800$. The initial condition for V_S is given by equation (9.15) using the initial conditions for V_G given above. Similarly the initial condition for P_G is given by equation (9.17) using the initial conditions for T_G and V_G given above.

9.3.2 Physical parameters

In this subsection we repeat the analysis from the previous subsection 9.3.1 using physical parameter values here. Solving equations (9.12)–(9.19) with the physical parameter values given in table 9.1 gives the results in figure 9.4a–.9.4b

We observe from figure 9.4a relatively low solid temperature u and little change in the density of solid ρ_S over the time span. This could be a result of the reaction not reaching full extent, as demonstrated in the plot for α. Since α has not reached $\alpha = 1$ i.e. fully reacted, the resulting quantities u and ρ_S have not peaked. Due to the extremely large physical parameters present in table 9.1 the system would

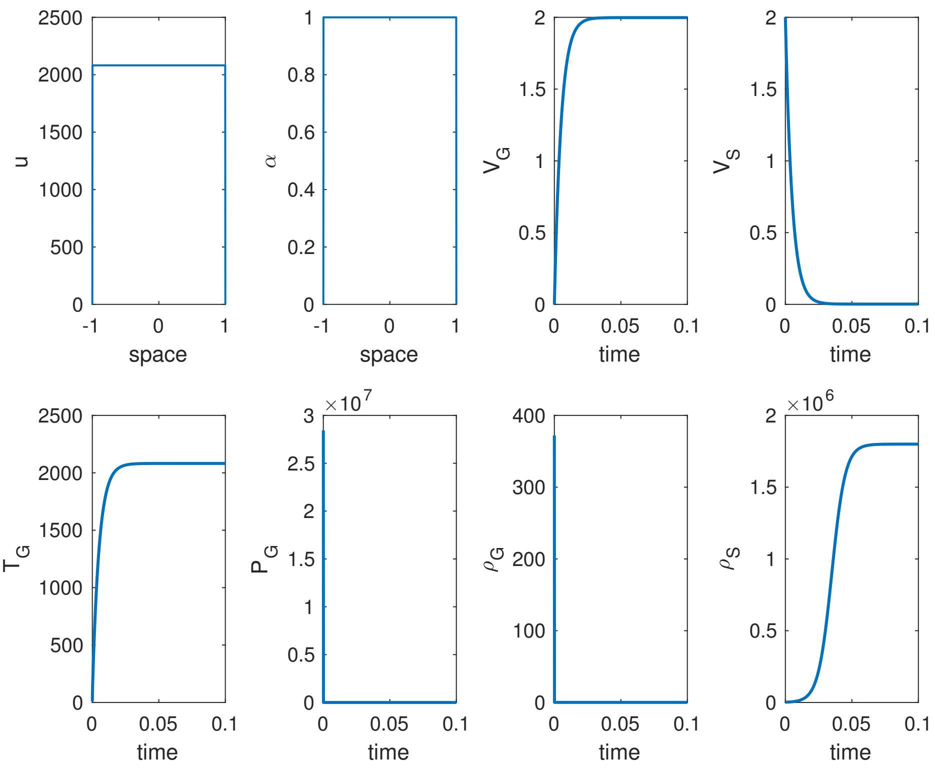

Figure 9.3: Numerical solutions of equations (9.12)–(9.19) with mild parameters given in table 8.1.

Table 9.1: Physical parameters used in model.

Parameter with units	**Symbol**	**Value**
Conductivity (W/m/K)	κ	0.44
Specific Heat (J/kg/K)	c_v	1255.0
Heat of Reaction (J/kg)	Ω	$5.0208e6$
Molar Gas Constant (J/mol/K)	R	8.314
Activation Energy (J/mol)	E	$2.2e5$
Pre-exponential Constant (s^{-1})	A	$5.011872336e19$
Initial solid temperature $^\circ K$	C	293
Number of moles of gas ($\frac{M}{mw}$)	n	0.0342
Specific surface area×Heat transfer coefficient	λH	1

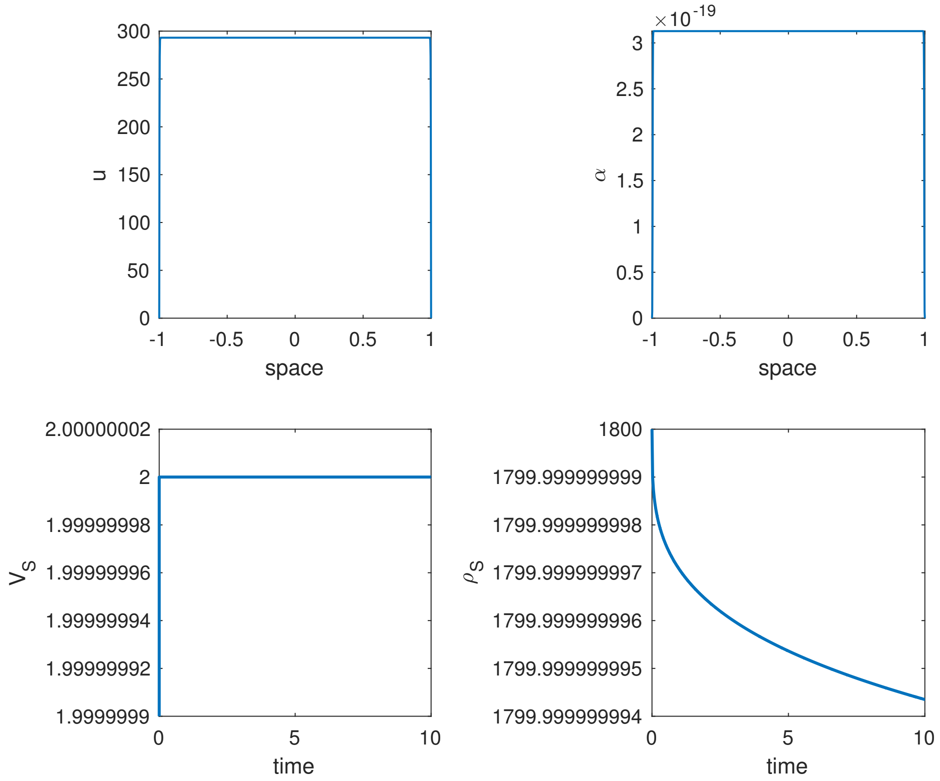

(a) Solid quantities

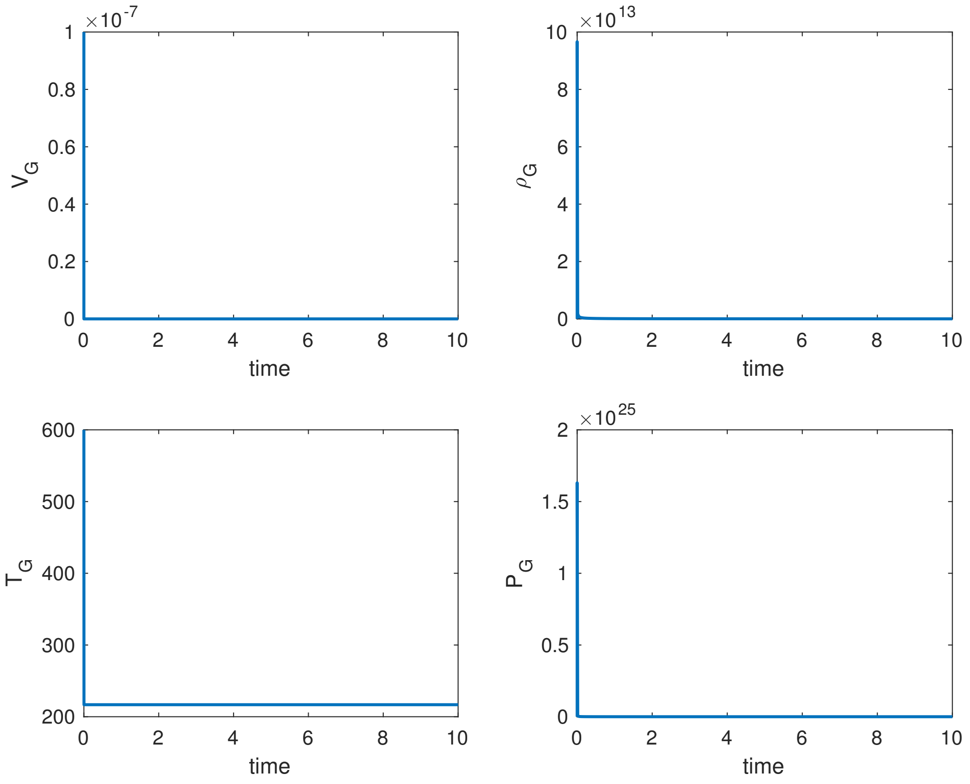

(b) Gas quantities

Figure 9.4: Numerical solutions of equations (9.12)–(9.19) with physical parameters given in table 9.1.

require a much longer time period before the reaction process has significant effect on the system. Similarly in figure 9.4b we observe a low gas temperature T_G and extremely small gas volume V_G.

9.4 Summary of chapter

In this chapter we investigated the effects of internal heating on the full problem using the physical parameters. We began by considering a constant gas temperature which resulted in physically unrealistic results, in particular for the pressure and temperature of gas. This initial investigation using a constant gas temperature allowed us to verify the numerical scheme worked well for the problem and was able to handle the large physical parameters involved.

Next we considered a variable gas temperature, as is physically realistic, however we maintained constant densities of both solid and gas. This approach proved to be more insightful with regards to the numerical treatment of the problem and the temperatures reached (of the gas in particular) were more realistic than previous analysis. Since the densities were kept constant in this section, the feedback within the solid was neglected and hence the internal temperature of the solid u was not accurately calculated.

In the final section of this chapter we allowed densities of both solid and gas to vary over time. Since this affects the solid calculations, we began by considering mild parameters. We observed an increase in gas temperature by allowing the densities to vary. When considering the physical parameters with internal heating and varying densities, we were able to solve the system accurately however due to computational run-time, it was difficult to obtain insightful results. The time and computational memory required for the extent of reaction α to reach unity is beyond that of standard computers. Given the results demonstrated in subsection 9.3.1 however, we are confident that if allowed to run for long enough, the results using the physical parameter values would be accurate.

The trends in the numerical results in the present chapter are consistent with the analytical trends described near the end of chapter 8.

As a broad conclusion, gas feedback has bee included but in the parameter range studied here, it has produced only small effects.

Part III

Wedge Analysis

Chapter 10

Heating of material in squeezed wedge flow

The work presented in this part of the thesis could be regarded as separate from the previous work, but on the other hand there is a close connection to some of the previous chapters. The intention here is to begin the build-up of an overall large-scale model involving fluid dynamics together with heat production, reaction and interaction; this chapter 10 is thus in preparation for such a large-scale model. There is very little available in the literature on the particular Jefferey-Hamel flow problem which we consider in this part of the thesis. However the paper by Riley [64] considers heating in similar geometry and hence provides useful insights.

Having looked at purely thermal boundary layers, where hot gas provides the initial heating source, we now consider a situation where a mechanical stimulus causes the dissipation and hence heating. This chapter considers the explosive reaction as a result of heat arising from a mechanical insult or impact. Specifically, explosive material which is able to move inside a hollow slender wedge is addressed with the contained material being squeezed by the inward movement of one of the two walls of the wedge, as depicted in figure 10.1. The fixed wall of the wedge is taken as the x-axis in Cartesian coordinates.

The modelling is based on considering a viscous fluid within the wedge rather than a precise HE, along with a spatial assumption of two-dimensionality in coordinates x, y in the horizontal and vertical directions respectively: again see figure

10.1. The present approach begins with an unsteady version in section 10.1 of the classical steady Jeffery-Hamel flow solution [65], which holds inside a diverging channel with a fluid source present and constitutes an exact solution of the Navier-Stokes equations with appropriate boundary conditions. We consider the boundary-layer limit since the contained material is confined in a relatively thin wedge of small angle; the boundary layer form has the advantage of being readily able to incorporate non-simple wall shapes and non-simple wall velocities for example, in addition to being more tractable in general. Here, in the case of a flat-walled wedge, the Jeffery-Hamel solution can hold very close to the origin or pivot of the wedge at $(x,y) = (0,0)$, in contrast with our concern which is on the broader scale at increased distance x where extreme temperatures are found to be generated, according to section 10.2. This is followed by analysis, results and further discussion in sections 10.3–10.6.

10.1 The Fluid Flow and Temperature

We start with the continuity, Navier-Stokes and thermal equations written in dimensional form,

$$\begin{aligned}
u_x + v_y &= 0,\\
u_t + uu_x + vu_y &= -p_x + \nu\nabla^2 u,\\
v_t + uv_x + vv_y &= -p_y + \nu\nabla^2 v,\\
\hat{\theta}_t + u\hat{\theta}_x + v\hat{\theta}_y &= (Pr)^{-1}\nu\nabla^2\hat{\theta}.
\end{aligned}$$

For now we are omitting dissipation but this will be incorporated later. Here u, v are the flow velocities in the x, y directions in turn, t denotes time, p is the fluid pressure variation and $\hat{\theta}$ is the temperature, while ν is the kinematic viscosity of the fluid and Pr is the Prandtl number. Suppose that the typical normal $(y-)$velocity W of the upper wall of the wedge and the typical $x-$length L are given for the slender wedge. We assume the ratio $\delta = \frac{\nu}{WL}$ is small, this ratio representing an inverse Reynolds number in effect, and substitute the scales

$$x = LX, \qquad y = \delta LY, \qquad t = L\delta W^{-1}T,$$
$$v = WV, \qquad u = \delta^{-1}WU, \qquad p = \delta^{-2}W^{2}P, \tag{10.1}$$

and

$$\text{temperature}\hat{\theta} = \theta_{REP}\theta, \tag{10.2}$$

(here 'θ_{REP}' is a reference temperature such as an imposed wall temperature) into the Navier-Stokes equations. From this we obtain the boundary-layer equations for the fluid flow:

$$U = \Psi_Y, \quad V = -\Psi_X, \tag{10.3}$$
$$U_T + UU_X + VU_Y = -P_X + U_{YY}, \tag{10.4}$$
$$0 = -P_Y, \quad \text{implying } P = P(X,T). \tag{10.5}$$

The relevant boundary conditions include

$$U = 0, \quad V = E(T)X \quad \text{at } Y = F(X,T), \tag{10.6}$$
$$U = V = 0 \quad \text{at } Y = 0. \tag{10.7}$$

Here the prime case of interest has the straight-walled wedge shape

$$F(X,T) = X\alpha(t) \quad \text{together with } E(T) = \frac{d\hat{\alpha}}{dT}, \tag{10.8}$$

where the scaled angle $\alpha(T)$ is prescribed as a function of time T and its derivative is expected to be negative in order to represent a squeezing of the contained material. In addition we have, for the temperatures produced by the flow of the material, the equation with dissipation included

$$\theta_T + U\theta_X + V\theta_Y = (Pr)^{-1}\theta_{YY} + C\Phi + r, \tag{10.9}$$

where the constant Pr is the Prandtl number, to repeat, estimated values of which are to be described below. The constant C is a non-dimensionalisation factor and the definition of the scaled dissipation Φ is to be given in ssection 10.3, while r is a reaction term similar to that introduced in chapter 2. The role of r will be discussed later. The thermal boundary conditions are

$$\vartheta = \vartheta_{UW}(x,t) \quad \text{at the upper wall } Y = F(X,T), \tag{10.10}$$

$$\vartheta = \vartheta_{AXIS}(x,t) \quad \text{at the axis } Y = 0. \tag{10.11}$$

The contributions on the right hand sides of (10.10), (10.11) are prescribed temperatures at the walls in the present model. Alternatives to the given wall and axis values $\vartheta(x,t)$ imposed in (10.10), (10.11) are constraints of no heat transfer $\vartheta_Y = 0$ or a Robin condition or although perhaps less likely to be relevant, a radiative condition where the heat transfer rate involves the fourth power of the absolute temperature.

The formulation (10.3)-(10.9) applies in a viscous/inviscid interaction region surrounding the origin. We would anticipate that for small X the solution becomes quasi-steady, with the time dependence in (10.4), (10.9) becoming secondary there because X-derivatives are relatively large; this possibly yields the classical Jeffery-Hamel flow response, depending on whether there is a source of fluid at the origin or not. An alternative situation at small X corresponds to the presence of a dynamically negligible void or gap between the origin and the material. In either case the main flow forcing of interest in this study is the forcing due to the movement (the squeezing) of the upper wall of the wedge.

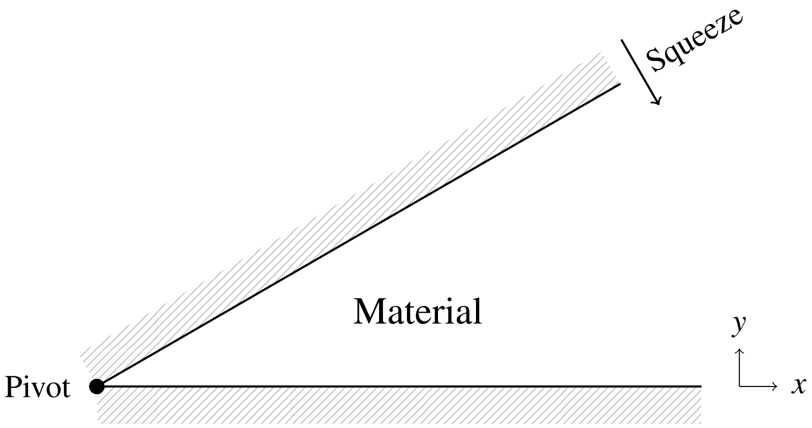

Figure 10.1: Sketch of the squeezed wedge configuration with material (fluid) contained between moving and fixed walls able to flow in x and y directions. The wedge angle is of order δ. Sketch is not to scale.

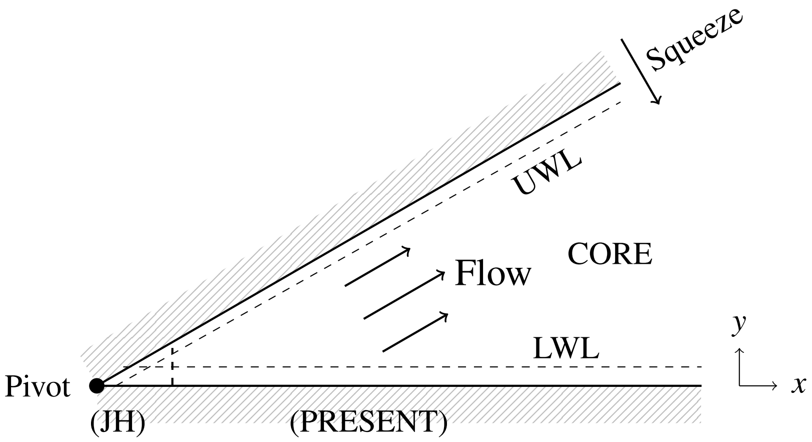

Figure 10.2: Solution structure for slender cases. JH is region of either classical source flow or a void. PRESENT is region of current study especially for large X downstream where UWL (upper wall layer), core and LWL (lower wall layer) emerge with thickness of order X^{-1}, X, 1 respectively.

10.2 Downstream Response

The material (fluid) is expected to flow away from the origin, in the positive X direction. We find that for large positive X an interesting multi-structure arises as indicated in figure 10.2 and described as follows.

First, a quasi-inviscid core emerges in which the typical (Y,V,U) vlaues grow like distance X. Hence in (10.4) the viscous term U_{YY} is $\mathcal{O}(X^{-1})$, which is seen to become negligible in comparison with the inertia terms which are $\mathcal{O}(X)$, and thus after some manipulation the solution by John Curtis [66] is then found. The main detail required for the analysis below is the property that the dominant velocity component U grows linearly with X and is positive.

Second, there has to be a comparatively thin lower-wall layer (LWL) along $Y=0$ to satisfy the no-slip condition, in view of the slip that is present in the inviscid core solution. Here the slip velocity due to the core is given by

$$U = kX \quad (\text{for } X \gg 1), \tag{10.12}$$

where k is a known positive constant. The wall layer then, which surprisingly happens to be the same as for a front stagnation point on an air-foil, takes the form

$$\Psi \sim Xg(Y) + \ldots (\text{for } X \gg 1), \tag{10.13}$$

as suggested by (10.12) in conjunction with (10.3), (10.4), with ψ being the scaled stream function associated with $U = d\psi/dY$, $V = -d\psi/dX$. Substitution into (10.3)-(10.5) is found to lead to the classical (Hiemenz flow) solution [65], satisfying the nonlinear ordinary differential equation

$$(g')^2 - gg'' = k^2 + g''' \quad \text{subject to } g'(\infty) = k, \quad g(0) = g'(0) = 0, \tag{10.14}$$

where the prime denotes the operator d/dY. The numerical solution derived by use of a shooting method is presented in figure 10.3 and is in agreement with the classical result. It is significant that the thickness of this wall layer remains $\mathcal{O}(1)$

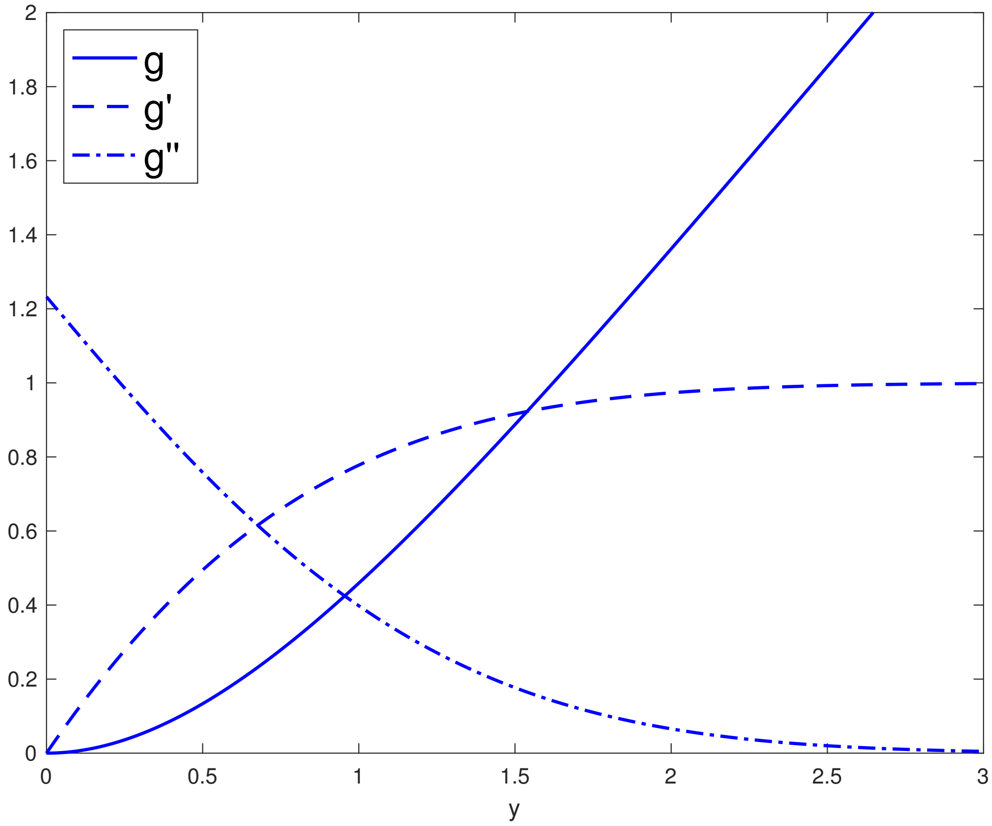

Figure 10.3: Solution g, g', g'' of equation (10.14) in the lower wall layer (LWL).

even though the gap grows spatially downstream.

Third, an upper wall layer (UWL) is also induced close to the moving wall of (10.8). An argument based on orders of magnitude suggests that near the upper wall $Y - \hat{\alpha}X$ is $\mathscr{O}(X^m)$ say, with the power m being less than unity, while V is $\mathscr{O}(X)$ from the moving-wall boundary condition (10.6) and the stream function ψ is $\mathscr{O}(1)$ by virtue of (10.3). Balancing effects in the boundary layer equations (10.4) implies that $m = -1$. This indicates that the appropriate scales and expansions are

$$Y = X\alpha(T) + X^{-1}Y^*, (U, V, \Psi) = (XU^*, XV^*, \Psi^*) + \dots . \tag{10.15}$$

After substituting (10.15) into (10.3)–(10.5) we find the linear governing equation

$$-B(T)U^*_{Y^*} = U^*_{Y^*Y^*}, \tag{10.16}$$

to leading order, where $B(T) = d\hat{\alpha}/dT$ is used for convenience. Since only derivatives with respect to Y^* are present in (10.16), the upper-wall layer solution is thus

$$U^*(Y^*) = 1 - \exp(-B(T)Y^*)A \tag{10.17}$$

where the positive constant A is known from the core solution: cf (10.12). Thus we have $A = k$. We remark that Y^* tends to $-\infty$ as the wall layer matches with the core and repeat that $B(T)$ is taken to be negative for the squeezing effect due to the upper wall of the wedge.

The next section, section 10.3 below, establishes that the largest dissipation occurs in the upper wall layer (UWL). So we need to treat the scaled dissipation Φ and then the equation (10.9) for the scaled temperature θ in a similar way to (10.15). Section 10.4 below tackles the temperature part of the model in the UWL. Then section 10.5 examines the lower wall layer (LWL) and section 10.6 provides a summary.

10.3 The Dissipation in the Lower and Upper Wall Layers

Concerning thermal effects induced by the fluid motion, the scaled dissipation Φ is defined in classical tensor notation e.g. [65] by

$$\frac{\Phi}{2\mu} = e_{ij}e_{ij} \quad \text{where } e_{ij} = \frac{1}{2}\left(\frac{\partial u_i}{\partial x_j} + \frac{\partial u_j}{\partial x_i}\right), \tag{10.18}$$

where μ denotes the viscosity of the material. Hence for our two-dimensional wedge configuration we have

$$\frac{\Phi}{2\mu} = u_x^2 + \frac{1}{2}(u_y + v_x)^2 + v_y^2 \tag{10.19}$$

and therefore in the thin-wedge setting of (10.1), (10.2) this becomes

$$\frac{\Phi}{2\mu} = \frac{1}{2}W^2\delta^{-4}L^{-2}\left(\frac{\partial U}{\partial Y}\right)^2 + h.o.t. \tag{10.20}$$

since the ratio δ is small; *h.o.t.* denotes higher order terms.

We then consider X becoming large downstream, based on the findings for the flow in section 10.2. Here in the lower wall layer (LWL) the asymptotic behaviour is $U \sim Xg'(Y)$ from (10.13) whereas in the upper wall layer (UWL) $U \sim XU^*$, to leading order. In consequence the $\frac{\partial U}{\partial Y}$ contribution induced is $Xg''(Y)$ in the LWL but $X^2\frac{dU^*}{dY^*}$ in the UWL. The latter clearly dominates when X is large.

Hence the maximum of the scaled dissipation Φ is encountered within the UWL and it has a value given by

$$\frac{\Phi}{2\mu} \sim \frac{1}{2}W^2\delta^{-4}L^{-2}\left(\frac{\partial U^*}{\partial Y^*}\right)^2 X^4, \tag{10.21}$$

from (10.20) combined with (10.15). This suggests we should focus first on the thermal response in the UWL, as follows.

10.4 The Resulting Temperature in the Upper Wall Layer

In section 10.3 we found that $\Phi \sim \Gamma X^4$ as $X \to \infty$, where the function Γ is given by

$$\Gamma(Y^*,T) = \mu W^2\delta^{-4}L^{-2}\left(\frac{\partial U^*}{\partial Y^*}\right)^2, \tag{10.22}$$

in the UWL. Here $\frac{\partial U^*}{\partial Y^*}$ is given by $AB(T)\exp(-B(T)Y^*)$ from (10.17) and so since $B(T)$ is negative the function Γ decays exponentially in the outer reaches of the wall layer where $Y^* \to -\infty$, i.e. on approach to the core. We now wish to consider the thermal equation (10.9) when X is large with time T of order unity and with the reaction r taken to be zero as a main case. The behaviour of U,V,Y is given by (10.15). The governing equations (10.3)–(10.9) with (10.15) suggest that the temperature in the wall layer must therefore expand in the form

$$\theta = X^2\theta^*(Y^*,T) + \ldots, \tag{10.23}$$

due to the forcing term involving Φ in (10.9); the substantial growth of temperature with distance downstream according to (10.23) is notable.

Substitution of (10.23) into (10.9) shows that the main balance occurs between the contributions of order X^4 and these yield the equation

$$-B(T)\frac{\partial\theta^*}{\partial Y^*} = (Pr)^{-1}\frac{\partial^2\theta^*}{\partial Y^{*2}} + C\Gamma \tag{10.24}$$

for $\theta^*(Y^*,T)$. We observe that a significant cancellation between V^* and αU^* is involved in the derivation of (10.24). The boundary conditions now become

$$\theta^* = 0 \quad \text{at } Y^* = 0, \tag{10.25}$$

$$\theta^* \to 0 \quad \text{as } Y^* \to \infty. \tag{10.26}$$

The zero thermal values in the boundary conditions here arise because of the large scaling of θ in (10.23) compared with (10.10) and the reasonable assumption (given the exponential decay of Γ at large negative Y^*) of less large temperatures in the inviscid core outside the wall layer(s). The final task here in the UWL then is to solve (10.24)–(10.26). We now proceed to solve Equation (10.24) subject to the boundary conditions (10.25)-(10.26). For completeness we show much of the detail below. We begin by dividing (10.25) through by $-B(T)$ such that we have

$$\frac{\partial\theta^*}{\partial Y^*} = \frac{(Pr)^{-1}}{-B(T)}\frac{\partial^2\theta^*}{\partial Y^{*2}} + \frac{C\Gamma}{-B(T)},$$

or equivalently

$$\frac{\partial\theta^*}{\partial Y^*} = k_1(Y)\frac{\partial^2\theta^*}{\partial Y^{*2}} + k_2(Y),$$

where $k_1(Y) = -\frac{1}{PrB(T)}$ and $k_2(Y) = -\frac{C\Gamma(Y)}{B(T)}$. If we let $\frac{\partial\theta}{\partial Y} = \hat{v}(Y)$ such that $\frac{\partial^2\theta}{\partial Y^2} = \frac{\partial\hat{v}}{\partial Y}$. Dividing through by $-k_1(Y)$ gives

$$-\frac{\hat{v}(Y)}{k_1(Y)} + \frac{\partial\hat{v}}{\partial Y} = -\frac{k_2(Y)}{k_1(Y)}.$$

Now, using the integrating factor method, we let $\hat{\mu}(Y) = \exp\left(\int -\frac{1}{k_1(Y)}dY\right) =$

$\exp\left(-\int \frac{1}{k_1(Y)}dY\right)$ and multiply both sides of the above by $\hat{\mu}(Y)$ such that

$$\exp\left(-\int \frac{1}{k_1(Y)}dY\right)\frac{\partial \hat{v}}{\partial Y} - \exp\left(-\int \frac{1}{k_1(Y)}dY\right)\frac{\hat{v}(Y)}{k_1(Y)} = -\exp\left(-\int \frac{1}{k_1(Y)}dY\right)\frac{k_2(Y)}{k_1(Y)}.$$

Substituting $-\exp\left(-\int \frac{1}{k_1(Y)}dY\right)/k_1(Y) = \frac{d}{dY}\left(\exp\left(-\int \frac{1}{k_1(Y)}dY\right)\right)$ gives

$$\exp\left(-\int \frac{1}{k_1(Y)}dY\right)\frac{\partial \hat{v}}{\partial Y} + \frac{d}{dY}\left(\exp\left(-\int \frac{1}{k_1(Y)}dY\right)\right)\hat{v}(Y) = -\exp\left(-\int \frac{1}{k_1(Y)}dY\right)\frac{k_2(Y)}{k_1(Y)},$$

and applying the product rule to the left hand side

$$\frac{d}{dY}\left(\exp\left(-\int \frac{1}{k_1(Y)}dY\right)\hat{v}(Y)\right) = -\exp\left(-\int \frac{1}{k_1(Y)}dY\right)\frac{k_2(Y)}{k_1(Y)}.$$

Now we integrate with respect to Y and dividing through by $\hat{\mu}(Y)$ gives

$$\hat{v}(Y) = \exp\left(\int \frac{1}{k_1(Y)}dY\right)\left(-\int \exp\left(-\int \frac{1}{k_1(Y)}dY\right)\frac{k_2(Y)}{k_1(Y)}dY + c_1\right).$$

Recall, we made the substitution $\frac{\partial \theta}{\partial Y} = \hat{v}(Y)$, and so we have

$$\frac{\partial \theta}{\partial Y} = \exp\left(\int \frac{1}{k_1(Y)}dY\right)\left(-\int \exp\left(-\int \frac{1}{k_1(Y)}dY\right)\frac{k_2(Y)}{k_1(Y)}dY + c_1\right),$$

which, integrating with respect to Y, gives

$$\theta(Y) = \int \exp\left(\int \frac{1}{k_1(Y)}dY\right)\left(-\int \exp\left(-\int \frac{1}{k_1(Y)}dY\right)\frac{k_2(Y)}{k_1(Y)}dY + c_1\right)dY + c_2.$$

From the boundary conditions (10.25)-(10.26) we have that $\theta = 0$ at $Y = 0$ and $\theta \to 0$ as $Y \to \infty$; hence we can obtain $c_2 = 0$ and c_1 provided the limits on the integral are set where c_1 is a constant of integration. See also the numerical solution below (figure 10.4) where we used a finite difference method instead of the integrating factor method.

Alternatively, we may solve (10.24)-(10.26) by normalising (10.24) such that substituting (10.22) into (10.24) gives

$$-B(T)\frac{\partial\theta^*}{\partial Y^*} = (Pr)^{-1}\frac{\partial^2\theta^*}{\partial Y^{*2}} + CBAB(T)^2\exp(-2B(T)Y^*)$$

where $B = \mu W^2\delta^{-4}L^{-2}$. If we let $\theta^* = a\theta$ and $Y^* = bY$ and substitute into the above we get

$$-B(T)\frac{a}{b}\frac{\partial\theta}{\partial Y} = \frac{1}{Pr}\frac{a}{b^2}\frac{\partial^2\theta}{\partial Y^2} + CBAB(T)^2\exp(-2B(T)bY).$$

Dividing through by $\frac{a}{b^2}$ gives

$$-B(T)b\frac{\partial\theta}{\partial Y} = \frac{1}{Pr}\frac{\partial^2\theta}{\partial Y^2} + \frac{b^2}{a}CBAB(T)^2\exp(-2B(T)bY).$$

Taking $B(T)b = 1$ implies $b = \frac{1}{B(T)}$, substitution into the above yields

$$-\frac{\partial\theta}{\partial Y} = \frac{1}{Pr}\frac{\partial^2\theta}{\partial Y^2} + \frac{CBA}{a}\exp(-2Y),$$

which when setting $\frac{CBA}{a} = 1$ gives $a = CBA$ and finally we have

$$-\frac{\partial\theta}{\partial Y} = \frac{1}{Pr}\frac{\partial^2\theta}{\partial Y^2} + \exp(-2Y). \tag{10.27}$$

The equation of interest is therefore in a convenient normalized form.

Results are shown in figure 10.4. As regards $Pr = 0.1$, the trend of the scaled temperature θ to zero as Y tends to infinity is found to occur on a larger Y scale, consistent with reduced diffusion for such a low Prandtl number. The same point applies to $Pr = 0.01$ although in that case the magnitude of the variation of θ is diminished for the entire Y range.

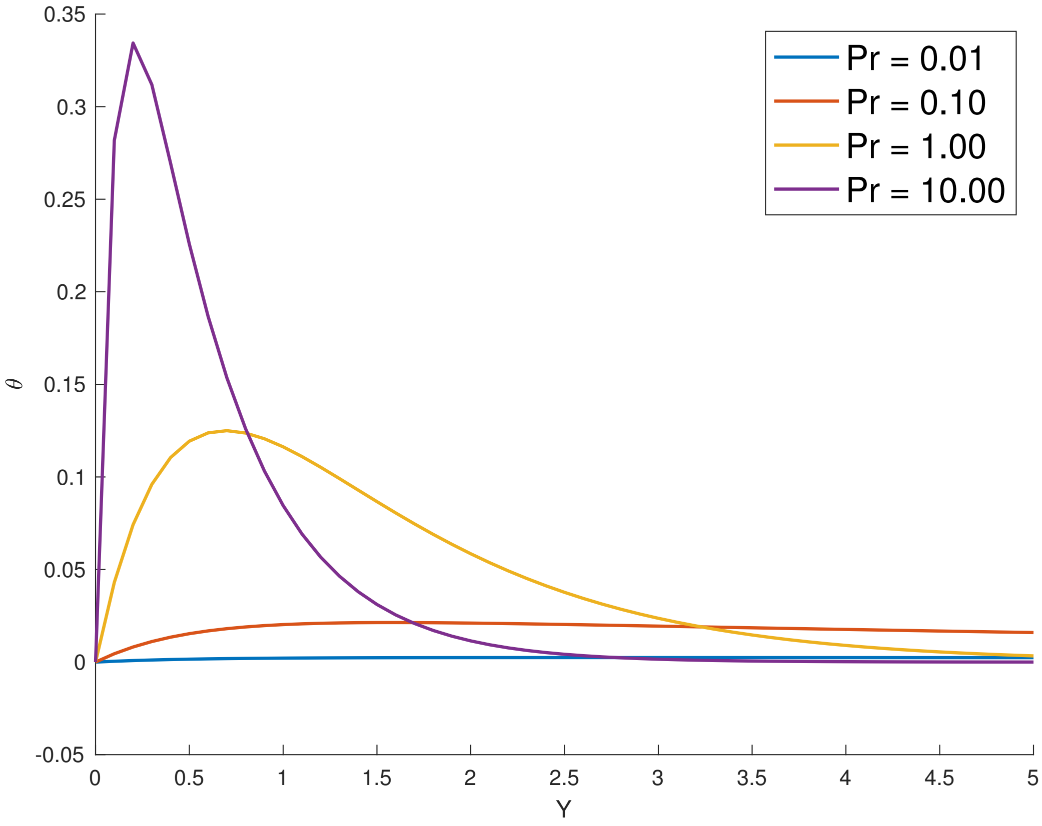

Figure 10.4: Solution θ of Equation (10.27) for varying values of Pr.

10.5 The Temperature in the Lower Wall Layer

An analysis based on order of magnitude similar to that in section 10.3 shows that in the LWL the dissipation function grows like X^2, say $\Phi \sim \Gamma_2 X^2$ as $X \to \infty$, because of the form of the fluid dynamical behaviour in (10.13). Here the function Γ is given by

$$\Gamma_2(Y,T) = \mu W^2 \delta^{-4} L^{-2} g''(Y)^2, \tag{10.28}$$

in the LWL, with the prime again denoting a Y-derivative. Here $g(Y)$ is the Heimenz solution of figure 10.5 and it gives Γ_2 decaying exponentially in the outer reaches of the LWL where $Y \to \infty$, i.e. on approach to the core. The governing equations including (10.9) suggest that the temperature in the LWL expands as

$$\theta = X^2 \theta_2(Y,T) + \dots, \tag{10.29}$$

due to the forcing term involving Φ in (10.9). The comparatively large size of the temperature is noticeable again.

The growth of temperature according to (10.29) in the LWL is of the same order as that in the UWL (see (10.23)), which is perhaps surprising in view of the larger dissipation in the UWL. The explanation for this lies in the balancing within (10.9) of the diffusion term which is of order θ/Y^2 and the dissipation term which in non-dimensional form has the order U^2/Y^2 from (10.20). Hence the expectation is that θ must be $\mathscr{O}(U^2)$: this is exactly $\mathscr{O}(X^2)$ for both the LWL and the UWL since both layers are subject to the slip velocity defined in (10.12).

Substitution of (10.29) into (10.9) gives the linear differential equation

$$2g'\theta_2 - g\theta_2' = (Pr)^{-1}\theta_2'' + C_2\Gamma_2 \tag{10.30}$$

for the scaled temperature $\theta_2(Y,T)$. The boundary conditions now become

$$\theta_2 = 0 \quad \text{at } Y = 0, \tag{10.31}$$

$$\theta_2 \to 0 \quad \text{as } Y \to \infty. \tag{10.32}$$

The zero thermal values here arise because of the large scaling of θ in (10.29) compared with (10.10) and the reasonable assumption (given the exponential decay of Γ_2 at large Y) of less large temperatures in the inviscid core outside the wall layer(s). The task here in the LWL then is to solve (10.30)-(10.32), which is effectively an ordinary differential equation problem. Normalising (10.30) such that $C_2\Gamma_2 = 1$ by letting $\theta_2 = a\theta_2^*$ we obtain

$$2g'a\theta_2^* - ga\theta_2^{*\prime} = \frac{a}{Pr}\theta_2^{*\prime\prime} + C_2Bg''(Y)^2,$$

where $\Gamma_2 = Bg''(Y)^2$ and $B = \mu W^2\delta^{-4}L^{-2}$. Dividing through by a gives

$$2g'\theta_2^* - g\theta_2^{*\prime} = \frac{1}{Pr}\theta_2^{*\prime\prime} + \frac{C_2B}{a}g''(Y)^2,$$

then we take $\frac{C_2 B}{a} = 1$ which implies $a = C_2 B$ and hence

$$2g'\theta_2^* - g\theta_2^{*\prime} = \frac{1}{Pr}\theta_2^{*\prime\prime} + g''(Y)^2. \tag{10.33}$$

We used the solution of (10.14) for g and then solved (10.33). Both (10.14) and (10.33) were solved numerically using a shooting method and the solutions of the latter are displayed in figure 10.5 below for a fairly wide range of Prandtl numbers.

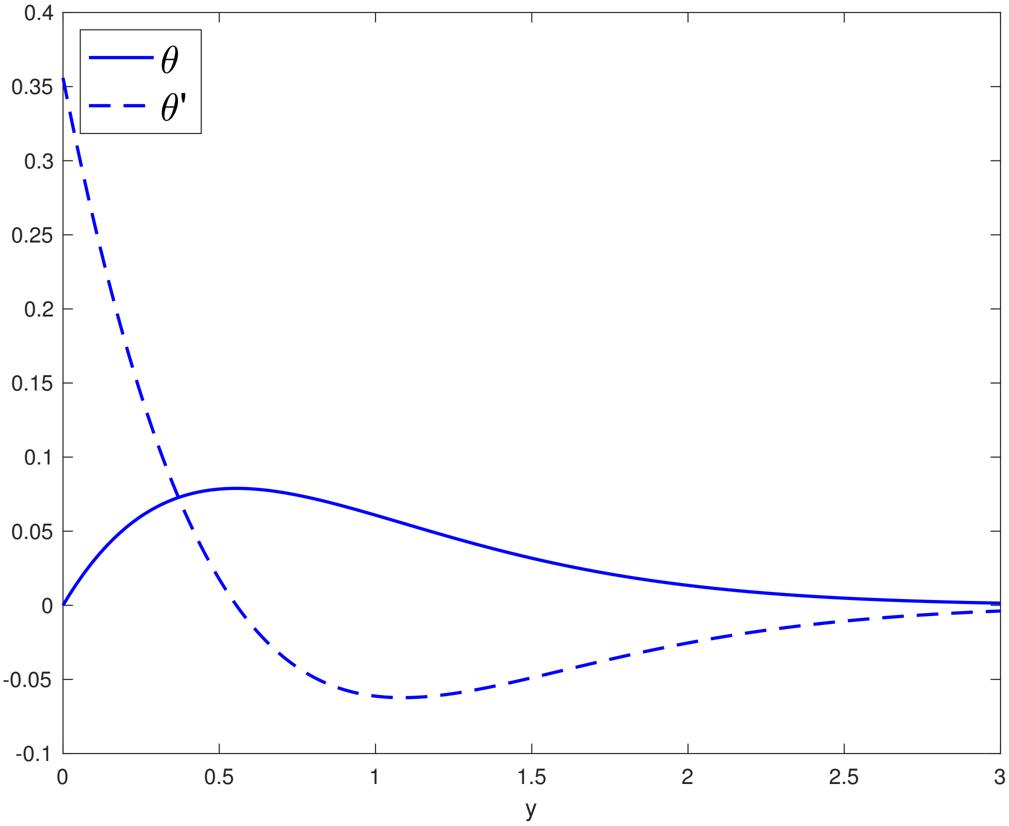

Figure 10.5: Solutions θ_2, θ_2' of equation (10.33) for $Pr = 0.7$.

10.6 Summary of chapter

This part of the thesis, consisting of only the present chapter, considered mechanical stimulus as a means of heating. From the work presented in this chapter we observed that overall, the structure of the flow and heating problem appears to be both logical and sensible.

There are however certain details of the work presented in this chapter which are incomplete. These include the constant factors C, C_2 in particular. We also note that here we have only examined the reaction contribution r being zero and future work could explore the case of r being nonzero. The role of such a reaction, similar to that involving the reaction fraction alpha in chapters 2, 3, or several reactions examined in chapter 4, should be of much interest in future investigations. It would provide a means for a full two-way interaction between the material flow and the material temperature by way of nonlinear feedback effects.

From the analysis presented in this chapter, we conclude from (10.15) the flow thickness in the lower wall layer is $Y = \mathscr{O}(1)$, consistent with the Heimenz solution at leading order. In the upper wall layer the flow thickness is of order X^{-1} which is approximately 1% of the wedge thickness ($\mathscr{O}(X)$ where X is some large number number which we take to be 10 as a representative value).

The thermal thickness on the other hand can be obtained from equation (10.24). We adjust Y^* according to the magnitude of Pr. Suppose Pr is large, then $Y^* \sim \frac{1}{Pr}$ of the flow thickness in the upper wall layer, for example $Pr = 60$ would give $Y^* \sim \frac{1}{60}$. In the lower wall layer, from equation (10.30) we scale Y with Pr in a similar way.

When considering the thermal and mechanical cases and how these compare with crystal sizes of $50\mu m$ we must first take into account the size of the wedge. Since we are dealing with small angles, we consider a wedge which is somewhat larger in length (x) than in width (y). Take for example 10cm as the Y-coordinate (vertical) width of the wedge, then the flow thickness of the upper wall layer is 1% of that (thus giving 1mm or 10^{-3}m) which is 1000 microns. This is 20 times the maximum crystal size. If we take $Pr = 20$ say, then the thermal flow thickness is reduced by a factor of $1/20$ which takes the 1mm estimate down to 50 microns. Hence, provided $Pr < 20$, the current analysis is outside the range where we need to consider crystals.

Part IV

Conclusions

Chapter 11

General Conclusions

In this chapter we review the main findings of the work presented in the thesis. We conclude by highlighting areas of potential further research. We first draw conclusions on part I of the thesis consisting of chapters 2–4.

In chapter 2 we considered the one reactant problem and its computational properties. We introduced the non-dimensional system based on the scaled parameters $\bar{u}$ and $\bar{t}$ which when investigated highlighted the emergence of boundary layers.

We proceeded in chapter 3 to consider non-dimensional variables for simplicity. We included a variation of the Arrhenius reaction equation into our model in the first instance. Our numerical scheme coped well with the non-linear system of equations. However, when considering the actual physical parameters, the numerical method was unable to produce sensible/informative results. This is due to the extreme nature of the parameters involved. To address this, we introduced mild parameters in place of the physical ones. We compared the results of the mild parameter case with the corresponding asymptotic case and observed excellent agreement between the two. Chapter 4 extended the model presented in chapters 2–3 by including multiple reactants. Here, we first solved the full equations with mild parameters and then turned to asymptotics following the promising results of chapter 3. Again, we observed excellent agreement between the full problem and reduced asymptotic problem for mild parameter values.

The verification of the asymptotic model described above makes tractable the solution of the reaction diffusion problem over the parameter ranges of real concern without the need for the extremely fine spatial resolution to capture the behaviour near the wall that is needed in direct treatment of the full problem. This has important implications for the application of the model to real problems, where often it is desired to perform parametric studies within a reasonable timescale. Such studies can be greatly hampered by the computational times needed, so this is a significant potential benefit of the work.

In the second part of the thesis (part II) we introduced the effects of gas into the model. We began first by introducting in chapter 5 gas via a discrete scheme which we then extended to a continuous framework. The model developed here unrealistically assumes the gas which is created in the system immediately leaves, having no effect whatsoever on the temperature of the solid. Chapter 6 aimed to address this by allowing feedback in the system. In the first instance, we allowed feedback only at the boundaries of the solid by taking the gas temperature as the solid boundary condition once it exceeds the prescribed boundary condition. We also considered the effects of a moving boundary on the system in chapter 6. This model allows the gas produced to fill the space which was once occupied by solid explosive through a moving boundary. The results of this model however, insufficiently capture the behaviour of the physical problem. This is mainly because the position of the boundary (calculated by (6.2)) did not tend to zero as expected and thus the volume of gas did not tend to 2 (i.e. fill the whole domain).

To further address the lack of feedback in the system, chapter 7 considered the effects of varying the densities of both solid and gas such that the solid matrix calculation of temperature takes these into account. This model proved to be a significant improvement of the previous one described in chapter 6. This model was also considered in an asymptotic framework. Finally, to consider the effects of gas on the system, we considered, in chapter 8, internal heating. Here we built on the previous model in chapter 7 by allowing for internal heating as well as boundary heating by the gas produced. The results of this model agree closely with those presented in previous chapters; however one key difference is that due, to the internal heating by the gas produced in the system, the temperature of the solid reaches the peak temperature, albeit the same as without internal heating, much quicker than before. The extent of reaction also reaches its maximum much sooner. The analysis in this chapter also identified some key parameters, namely $\bar{\lambda}\left(=\frac{\lambda H}{\rho_S C_v A}\right)$ which we investigated in detail. Finally in chapter 9, for completeness, we repeated the analysis done in chapters 7–8 for the full problem with both mild and physical parameters.

The third and final part of the thesis consisted only of chapter 10. In this chapter we considered an alternative heating method: mechanical stimulus produced by a squeezing wedge. This chapter serves as a starting point for future work. We also conclude that much like with thermal stimulus, the majority of the behaviour in the mechanical system takes place within the thin boundary layers as well.

11.1 Future work

Here we briefly outline the main areas of future potential research which may follow on from the work presented in the thesis. The first and perhaps most obvious extension of this work could be to repeat the analysis presented in chapters 7–9 but with three reactants present as explored in chapter 4.

Second, the model of interaction evolving between thermal diffusion effects and a number of reactants has been considered for one spatial dimension only. The present approach, especially the asymptotic treatment but to some extent the direct treatment also, indicates that reliable predictions for two- and three-dimensional configurations should be quite possible [20].This second avenue of future work could therefore explore the extension of the model to higher dimensions. Using the asymptotic methodology developed throughout the present work, the potential for savings in computational resources is possibly even greater for two-and three-dimensional cases, which, of course, are prevalent in reality.

Finally, in the wedge problem described in chapter 9, a clear area of future work is considering the presence of a reaction term where 'r' is non-zero. The form of the reaction term required would most likely be based on that discussed in the first few chapters of the present thesis.

Appendix A

Further features of the core problem

This addresses the core problem (in altered notation)

$$\frac{d\alpha}{dt^*} = (1-\alpha)\exp(-1/(\delta + W\alpha)) \tag{A.1}$$

subject to $\alpha = 0$ at $t^* = 0$. ((2))

When δ is small but W is of order unity, the RHS of (A.1) increases very rapidly when plotted against α. This increase takes place where α becomes $\mathscr{O}(\delta)$; so there the RHS of (A.1) is $\mathscr{O}(\varepsilon)$ say where $\varepsilon = \exp(-1/\delta)$ is very small.

The corresponding time scale t^* is $t^* = \mathscr{O}(\delta^{-1}\exp(-1/\delta))$, very small, from (A.1). Hence $dt^*/d\alpha$ is very large, about $\exp(1/\delta)$, whereas α is about $\mathscr{O}(D)$ here. On integration with respect to α therefore t^* is about $\mathscr{O}(\exp(1/\delta))$ and so is large. It follows that the curve of α versus t^* shows slow evolution at first, remaining low for a long time until t^* reaches $\mathscr{O}(\exp(1/\delta))$, at which stage α begins to rise, heading towards 1 eventually.

When does the change occur? Well, it is when α becomes $\mathscr{O}(1)$ but

$$t^* = \exp(1/\delta) + t^{**}. \tag{A.2}$$

Then we have the equation

$$d\alpha/dt^{**} = (1-\alpha)\exp(-1/W\alpha), \tag{A.3}$$

from (A.1).

Equation ((A.3) can be integrated in principle to give $t^{**}(\alpha)$ and thus $\alpha(t^{**})$. We expect that (A.3) also yields the property that α tends to 1 as t^{**} tends to infinity. ((4))

Further, the match with the previous stage takes place as t^{**} tends to $-$ infinity: then (A.3) gives us $d\alpha/dt^{**} = \exp(-1/W\alpha)$ approximately and hence $\alpha = W - 1(\ln(mod(t^{**})) - 1$ approximately as t^{**} tends to $-$ infinity. ((5)) The slow evolution prior to the present stage is evident in the logarithmically-like slow decay in ((5)).

Here the two time scales t^{*} of order $\exp(1/\delta)$ and order unity involved in this scenario appear to reflect well the features of the direct solutions of the core problem (A.1), ((2)) calculated for decreasing δ in chapter 3. In addition it is notable that the core α evolves slowly as well as the wall layer α doing so. Consequently the direct numerical solution of the wall layer described in chapter 3 strictly has to continue for a long time t^{*} of order $\exp(1/\delta)$ in order for the entire wall layer properties to emerge.

Bibliography

[1] R. R. McGuire and C. M. Tarver, "Chemical Decomposition Models for the Thermal Explosion of Confined HMX, TATB, RDX, and TNT Explosives," *Symposium on Detonation*, no. June, p. 11, 1981.

[2] P. W. Cooper and S. R. Kurowski, *Introduction to the Technology of Explosives*. 1996.

[3] P. W. Cooper, *Explosives engineering*. 1996.

[4] S. Said, F. SMITH, and J. CURTIS, "Modelling, computation and analysis on combustion of explosives," *European Journal of Applied Mathematics*, vol. 33, no. 1, pp. 27–57, 2022.

[5] M. Ward, S. Son, and M. Brewster, "Steady deflagration of hmx with simple kinetics: A gas phase chain reaction model," *Combustion and Flame*, 1997.

[6] J. Curtis, "A new analytical model of the one-dimensional time to explosion experiment," *Unpublished AWE Report*, October 2018.

[7] D. Breshears, "One dimensional time-to-explode (odtx) in hmx spheres," *Los Alamos National Lab. Technical Report*.

[8] A. C. Victor, "Simple calculation methods for munitions cookoff times and temperatures," *Propellants, Explosives, Pyrotechnics*, vol. 20, no. 5, pp. 252–259, 1995.

[9] J. J. Yoh, M. A. McClelland, J. L. Maienschein, A. L. Nichols, and C. M. Tarver, "Simulating thermal explosion of octahydrotetranitrotetrazine-based

explosives: Model comparison with experiment," *Journal of Applied Physics*, vol. 100, no. 7, p. 073515, 2006.

[10] K. W. Morton and D. Mayers, *Numerical Solution of Partial differential Equations*. 2005.

[11] M. Ã-zisik, M. Özısık, and M. Özışık, *Heat Conduction*. Wiley-Interscience publication, Wiley, 1993.

[12] J. M. Groocock, "Griffiths and groocock : The burning to detonation of solid explosives," *Journal of the Chemical Society.*, no. 4154, 1958.

[13] M. L. Blanford, "Jas3d—a multi-strategy iterative code for solid mechanics analysis," *Sandia National Laboratories.*, 1998.

[14] C. Tarver, T. Tran, and R. Whipple, "Thermal decomposition of pentaerythritol tetranitrate," *Propellants, Explosives, Pyrotechnics*, vol. 28, no. 4, pp. 189–193, 2003.

[15] A. L. Nichols, "Improving the material response for slow heat of energetic materials," *Lawrence Livermore National Laboratory (LLNL)*.

[16] J. Bdzil and S. Son, "Engineering models of deflagration-to-detonation transition," *Los Alamos National Laboratory, LA-12794-MS*, 1995.

[17] J. Bear, *Dynamics of fluids in porous media*. New York : American Elsevier, 1972.

[18] M. J. K. Michael L. Hobbs, Judith A. Brown and C. Aviles-Ramos, "A micromechanics pressurization model for cookoff," *Propellants Explos. Pyrotech*, vol. 38, pp. 779–781, 2021.

[19] M. Baer and J. Nunziato, "A two-phase mixture theory for the deflagration-to-detonation transition (ddt) in reactive granular materials," *International Journal of Multiphase Flow*, vol. 12, no. 6, pp. 861 – 889, 1986.

[20] J. P. Curtis, J. E. Reaugh, and C. A. Handley, "On Modelling the Evolution of Specific Surface Area in the Burning of Explosives," *Proceedings of the Forty-Fourth International Pyrotechnics Seminar*, 2019.

[21] P. C. Hsu, G. Hust, M. Howard, and J. L. Maienschein, "The odtx system for thermal ignition and thermal safety study of energetic materials," *Lawrence Livermore National Laboratory (LLNL).*

[22] F. Williams, *Combustion Theory*. Addison-Wesley series in engineering sciences, Addison-Wesley Publishing Company, 1965.

[23] J. E. Reaugh, B. W. White, J. P. Curtis, and H. K. Springer, "A computer model to study the response of energetic materials to a range of dynamic loads," *Propellants, Explosives, Pyrotechnics*, vol. 43, no. 7, pp. 703–720, 2018.

[24] J. Yoh, M. McClelland, J. Maienschein, and C. Tarver, "Test-based thermal explosion model for hmx," *Proceedings of the Combustion Institute*, vol. 31, no. 2, pp. 2353 – 2359, 2007.

[25] P. E. Luebcke, P. M. Dickson, and J. E. Field, "Deflagration-to-Detonation Transition in Granular Pentaerythritol Tetranitrate," *J. Appl. Phys.*, vol. 79, no. 7, pp. 3499–3503, 1996.

[26] C. M. Tarver and S. K. Chidester, "On the violence of high explosive reactions," *Journal of Pressure Vessel Technology*, vol. 127, 2 2004.

[27] M. Baer, M. Hobbs, R. Gross, and R. Schmitt, "Cookoff of energetic materials," *11th Detonation Symposium.*

[28] C. Tarver, R. McGuire, E. Lee, E. Wrenn, and K. Brein, "The thermal decomposition of explosives with full containment in one-dimensional geometries," *Symposium (International) on Combustion*, vol. 17, no. 1, pp. 1407 – 1413, 1979. Seventeenth Symposium (International) on Combustion.

[29] D. Zerkle, "Multiphase treatment of odtx in hmx spheres," *Los Alamos National Lab. Technical Report.*

[30] M. Becker, *Heat Transfer Analysis and Design Problems*. Boston, MA: Springer US, 1986.

[31] A. L. N. III and K. W. Westerberg, “Modification of a thermal transport code to include chemistry with thermally controlled kinetics,” *Numerical Heat Transfer, Part B: Fundamentals*, vol. 24, no. 4, pp. 489–509, 1993.

[32] C. M. Tarver, S. K. Chidester, and A. L. Nichols, “Critical conditions for impact- and shock-induced hot spots in solid explosives,” *The Journal of Physical Chemistry*, vol. 100, no. 14, pp. 5794–5799, 1996.

[33] R. McGuire and C. Tarver, “Seventh symposium (international) on detonation,” *Naval Surface Weapons Center NSWC MP82-334, Annapolis, MD.*

[34] C. M. Tarver, R. R. McGuire, E. L. Lee, E. W. Wrenn, and K. R. Brein, “Seventeenth symposium (international) on combustion,” *The Combustion Institute: Pittsburgh.*

[35] E. Catalano, R. McGuire, E. Lee, E. Wrenn, D. Ornellas, and J. Walton, “Thermal decomposition and reaction of confined explosives. [tnt, tatb, lx-04, lx-10],” *Proceedings of Sixth Symposium (International) on Detonation*, pp. 214–222, 1976.

[36] T. Boggs, “Thermal behavior of cyclotrimethylenetrinitramine (rdx) and cyclotetramethylenetetranitramine (hmx).,” *Progress in Astronautics and Aeronautics.*, vol. 90, pp. 121–175, 01 1984.

[37] A. M Renlund, J. C Miller, W. M Trott, K. L Erickson, M. Hobbs, R. G Schmitt, G. W Wellman, and M. Baer, “Characterization of thermally degraded energetic materials.,” *Sandia National Labs Technical Report*, 01 1997.

[38] B. Asay, S. Son, and J. Bdzil., “The role of gas permeation in convective burning,” *International Journal of Multiphase Flow*, vol. 22, no. 5, pp. 923 – 952, 1996.

[39] L. Taylor and D. Flanagan, “Pronto 3d: A three-dimensional transient solid dynamics program.,” *Sandia National Labs. Technical Report*, 03 1989.

[40] R. Schmitt and T. Baer, “Millisecond burning of confined energetic materials during cookoff.,” *16th JANNAF PSHS Meeting*, 11 1997.

[41] M. Hobbs, M. Baer, and R. Gross, “A constitutive mechanical model for energetic materials.,” *Proceedings of the 20th International Pyrotechnics Seminar*, 06 1994.

[42] M. Kipp, D. Grady, and J. Swegle, “Experimental and numerical studies of high-velocity impact fragmentation,” *International Journal of Impact Engineering*, vol. 14, 08 1993.

[43] M. Baer, R. Gross, D. Gartling, and M. Hobbs, “Multidimensional thermal-chemical cookoff modeling,” *JANNAF Propulsion Systems Hazards Subcommittee Meeting*, 08 1994.

[44] B. Harold H., Jr and T. L. Boggs, “Convective burning in propellant defects: A literature review.,” *Naval Weapons Center Technical Information Department*, p. 105, 02 1978.

[45] R. Behrens, “Thermal decomposition of energetic materials: Temporal behaviors of the rates of formation of the gaseous pyrolysis products from condensed-phase decomposition of octahydro-1,3,5,7-tetranitro-1,3,5,7-tetrazocine,” *Journal of Physical Chemistry*, vol. 94, 08 1990.

[46] S. Y. Ho, “Thermomechanical properties of rocket propellants and correlation with cookoff behavior,” *Propellants, Explosives, Pyrotechnics*, vol. 20, pp. 206 – 214, 08 1995.

[47] J. McGlaun, S. Thompson, and M. Elrick, “Cth: A three-dimensional shock wave physics code,” *International Journal of Impact Engineering*, vol. 10, pp. 351–360, 01 1989.

[48] K. Alexander and K. Gibson, “Variable confinement cookoff test,” *Naval Surface Warfare Center*, 11 1994.

[49] H. W. Sandusky and R. R. Bernecker, “Compressive reaction in porous beds of energetic materials„” *Eight Symposium (International) on Detonation.*, p. 881–891, 08 1985.

[50] M. R. Baer, E. S. Hertel, and R. L. Bell, “Multidimensional ddt modeling of energetic materials,” *APS Topical Conference on Shock Compression of Condensed Matter.*, 1995.

[51] C. Peletski and K. Gibson, “Variable confinement cookoff test,” *JANNAF Prop.ulsion Sys. Haz. Sub. Mtg., Monterey, CA.*, 08 1996.

[52] R. J. Gross, “A direct fortran coupling of coy-oteii and jas3d to perform thermal/chemical/mechanical analyses,” *Sandia National Laboratories.*, 1995.

[53] D. K. Gartling, R. E. Hogan, , and M. W. Glass, “Coyote–a finite element computer program for nonlinear heat conduction problems,” *Sandia National Laboratories.*, vol. 94, 1998.

[54] A. L. Nichols, R. Couch, J. D. Maltby, R. Mccallen, and I. Otero, “Coupled thermal/chemical/mechanical modeling of energetic materials in ale3d.,” *JANNAF Combustion Subcommittee & Propulsion Systems Hazards Subcommittee Joint Meeting*, 11 1996.

[55] J. Curtis, “Modelling spigot impact in the presence of an air gap,” *Proceedings of the Forty-Third International Pyrotechnics Seminar*, July 2018.

[56] H. S. Carslaw, J. C. Jaeger, and J. E. Morral, *Conduction of Heat in Solids, Second Edition*, vol. 108. 1986.

[57] C. AB, “Comsol multiphysics® v. 5.4.”

[58] S. Bullett, T. Fearn, and F. Smith, *Advanced Techniques in Applied Mathematics*. WORLD SCIENTIFIC (EUROPE), 2016.

[59] D. A. Anderson, *Computational fluid mechanics and heat transfer*. Series in computational methods in mechanics and thermal sciences, Washington: Hemisphere Pub. Corp., 1984.

[60] D. Anderson, J. Tannehill, and R. Pletcher, "Computational fluid mechanics and heat transfer,"

[61] M. E. Brown, "The Prout-Tompkins rate equation in solid-state kinetics," *Thermochimica Acta*, vol. 300, no. 1-2, pp. 93–106, 1997.

[62] F. Morrison, "Transient gas flow in a porous column," *I&EC Fundamentals*, vol. 11, pp. 191–197, 1972.

[63] M. Cook, P. Haskins, and C. Stennett, "Development and implementation of an ignition and growth model for homogeneous and heterogeneous explosives," in *Proceedings of the Eleventh Symposium (International) on Detonation, Snowmass, Colorado*, vol. 30, 1998.

[64] N. RILEY, "HEAT TRANSFER IN JEFFERY-HAMEL FLOW," *The Quarterly Journal of Mechanics and Applied Mathematics*, vol. 42, pp. 203–211, 05 1989.

[65] G. K. Batchelor, *An introduction to fluid dynamics*. Cambridge university press, 2000.

[66] J. Curtis, "Private communications," 2021.